



الجمهورية الجزائرية الديمقراطية الشعبية
وزارة التعليم العالي و البحث العلمي
جامعة تيسمسيلت



THÈSE

En vue de l'obtention du Diplôme de Doctorat LMD

Présentée par : *Fatima SOFRANI*

**Intitulé: Propriétés structurales, électroniques, magnétiques et
mécaniques des alliages Heusler : calcul de premier principe.**

<i>Faculté</i>	: <i>Sciences et de la Technologie</i>
<i>Département</i>	: <i>Sciences de la matière</i>
<i>Domaine</i>	: <i>Sciences de la matière</i>
<i>Filière</i>	: <i>Physique</i>
<i>Spécialité</i>	: <i>Physique des Matériaux et Nanostructures</i>

Devant le Jury Composé de :

<i>Membres de Jury</i>	<i>Grade</i>	<i>Qualité</i>	<i>Domiciliation</i>
<i>BOUCHARFE Mohamed</i>	<i>MCA</i>	<i>Président</i>	<i>U. Tissemsilt</i>
<i>BOUDIA Keltouma</i>	<i>Pr</i>	<i>Encadreur</i>	<i>U. Tissemsilt</i>
<i>MOKHTARI Mohamed</i>	<i>Pr</i>	<i>Examineur</i>	<i>U. Tissemsilt</i>
<i>ADJADJ Aze Eddine</i>	<i>MCA</i>	<i>Examineur</i>	<i>Université Ibn khaldoun TIARET</i>
<i>BERRAHAL Mokhtar</i>	<i>MCA</i>	<i>Examineur</i>	<i>Ecole normale Supérieur d'ORAN</i>
<i>BOUMIA Lakhdar</i>	<i>MCA</i>	<i>Examineur</i>	<i>U. Tissemsilt</i>

Année Universitaire : **2022/2023**



الجمهورية الجزائرية الديمقراطية
الشعبية
وزارة التعليم العالي و البحث العلمي
جامعة تيسمسيلت



THESIS

With the View to Obtaining
the LMD Doctoral Diploma

Presented by : Fatima SOFRANI

Entitled: Structural, electronic, magnetic and mechanical properties of Heusler alloys: first principle calculation.

Faculty	: <i>Sciences and Technology</i>
Departement	: <i>Sciences of Matter</i>
Domain	: <i>Sciences of Matter</i>
Filière	: <i>Physics</i>
Spécialité	: <i>Physics of Materials and Nanostructures</i>

In front of the jury composed of:

Members of the Jury	Grade	Position	Affiliation
BOUCHARE Mohamed	MCA	Chairman	U. Tissemsilt
BOUDIA Keltouma	Prof.	Supervisor	U. Tissemsilt
MOKHTARI Mohamed	Prof.	Examiner	U. Tissemsilt
ADJADJ Aze Eddine	MCA	Examiner	Ibn Khaldoun TIARET University
BERRAHAL Mokhtar	MCA	Examiner	Higher Normal School of ORAN
BOUMIA Lakhdar	MCA	Examiner	U. Tissemsilt

Academic Year : 2022/2023

Dedication

To my mother's soul...

To my father...

Who always encouraged me and gave me hope and never stopped

God save him.

To my brothers and my sisters

All my friends

To all my colleagues

Acknowledgments

I want to express my deepest respect and gratitude to **Professor Keltouma BOUDIA** .for agreeing to be my dissertation rapporteur and express my sincere gratitude to her for her evidence and these suggestions throughout. These four years of dissertation also for the time and attention you have given me to this work, especially these constructive criticisms. Her scientific knowledge, extreme kindness, and constant support she gave me allowed me to acquire a rich knowledge of materials science and lead this work toward common sense.

I am greatly indebted to **Doctor Abderrahmane CHERIET** at the Laghouat University for his great amounts of encouragement, advice, and help.

I would like to further thank my colleague **Miss. Soumia ZEFFANE** for everything she has done for me.

Special thanks are due to **Doctor Mohamed BOUCHARF**, **Doctor Mohamed MOKHTARI**, **Doctor ADJADJ Aze Eddine** , **Doctor BERRAHAL Mokhtar**, and **Doctor BOUMIA Lakhdar** for accepting being part of the panel of examination and judging the research work to be complete for its defense.

Abstract

In this research study, we investigated the properties of the double-half Heusler alloy (**DHH**), **K₂NaRbAs₂**. We utilized the full-potential linearized augmented plane wave method (**FP-LAPW**) with the generalized gradient **GGA** approximation and the GGA+ Modified Becke-Johnson (**mBJ**) correlation potential to investigate the alloy's structural, elastic, electronic, magnetic, and thermoelectric properties. Our findings indicate that the alloy possesses resistance to distortion and can endure reversible deformation. The calculated elastic constants suggest that **K₂NaRbAs₂** is mechanically stable, ductile, and anisotropic, which is supported by a three-dimensional representation of its elastic moduli. The total magnetic moment of $2\mu_B$ demonstrates its half-metallic behavior primarily attributed to the presence, of arsenic atoms. Furthermore, we conducted an analysis of the equilibrium structural parameters, as well as the electronic, magnetic, and elastic properties of half-Heusler compounds **VMSb (M=Pd, Pt)** using density functional theory (**DFT**). The theoretical results revealed that both **VMSb (M=Pd, Pt)** compounds exhibit half-metallic behavior, characterized by a total magnetic moment of $2\mu_B$ consistent with the Slater-Pauling rule. These half-Heusler compounds show promise as potential candidates for spintronic devices.

Keywords: Heusler alloy. FP-LAPW. mBJ. mechanically stable. half-metallic. magnetic properties

Résumé

Dans cette étude de recherche, nous avons étudié les propriétés de l'alliage Heusler à double moitié (**DHH**), $K_2NaRbAs_2$. Nous avons utilisé la méthode des ondes planes augmentées linéarisées à plein potentiel (**FP-LAPW**) avec l'approximation **GGA** à gradient généralisé et le potentiel de corrélation Becke-Johnson modifié **GGA + (mBJ)** pour étudier les propriétés structurales, élastiques, électroniques, magnétiques et thermoélectriques de l'alliage. Nos résultats indiquent que l'alliage possède une résistance à la distorsion et peut supporter une déformation réversible. Les constantes élastiques calculées suggèrent que $K_2NaRbAs_2$ est mécaniquement stable, ductile et anisotrope, ce qui est soutenu par une représentation tridimensionnelle de ses modules élastiques. Le moment magnétique total de $2 \mu_B$ démontre son comportement semi-métallique principalement attribué à la présence d'atomes d'arsenic. De plus, nous avons effectué une analyse des paramètres structuraux d'équilibre, ainsi que des propriétés électroniques, magnétiques et élastiques des composés demi-Heusler **VMSb** (**M = Pd, Pt**) en utilisant la théorie de la fonctionnelle de la densité (**DFT**). Les résultats théoriques ont révélé que les deux composés **VMSb** (**M = Pd, Pt**) présentent un comportement semi-métallique, caractérisé par un moment magnétique total de $2\mu_B$ conforme à la règle de Slater-Pauling. Ces composés semi-Heusler sont prometteurs en tant que candidats potentiels pour les dispositifs spintroniques.

Mots clés: Alliage Heusler. FP-LAPW. mBJ. mécaniquement stable. demi-métallique. Propriétés magnétiques.

ملخص

في هذه الدراسة البحثية ، درسنا خصائص سبيكة Heusler ذات النصف المزدوج (DHH) ، $K_2NaRbAs_2$ استخدمنا طريقة الموجة المستوية المعززة ذات الإمكانيات الكاملة (FP-LAPW) مع تقريب GGA المنترج المعمم وإمكانية ارتباط + GGA المعدلة Becke-Johnson (mBJ) للتحقيق في الخصائص الهيكلية والمرنة والإلكترونية والمغناطيسية والكهروحرارية للسبيكة. تشير النتائج التي توصلنا إليها إلى أن السبيكة تمتلك مقاومة للتشوه ويمكن أن تتحمل التشوه القابل للانعكاس. تشير الثوابت المرنة المحسوبة إلى أن $K_2NaRbAs_2$ مستقر ميكانيكيًا ، ومرن ، ومتباين الخواص ، وهو مدعوم بتمثيل ثلاثي الأبعاد لمعاملاته المرنة. يوضح إجمالي العزم المغناطيسي البالغ $2\mu_B$ سلوكه نصف المعدني الذي يُعزى أساسًا إلى وجود ذرات الزرنيخ. علاوة على ذلك ، أجرينا تحليلًا للمعلومات الهيكلية للتوازن ، بالإضافة إلى الخصائص الإلكترونية والمغناطيسية والمرنة لمركبات نصف Heusler $VMSb$ (M = Pd, Pt) ، باستخدام نظرية الكثافة الوظيفية (DFT). كشفت النتائج النظرية أن كلا المركبين $VMSb$ (M = Pd, Pt) ، يظهران سلوكًا نصف معدني ، يتميز بعزم مغناطيسي إجمالي قدره $2\mu_B$ بما يتوافق مع قاعدة Slater-Pauling. تظهر مركبات نصف Heusler هذه واعدة كمرشحين محتملين للأجهزة spintronic.

الكلمات الرئيسية: سبيكة FP-LAPW. Heusler. م. مستقر ميكانيكيًا. نصف معدني. الخواص المغناطيسية

Table of Contents

Dedication	i
Acknowledgments	ii
Abstract	iii
Résumé	iv
ملخص.....	v
Table of Contents	vi
List of Tables	x
List of Figures	xi
List of Abbreviations	xiii

GENERAL INTRODUCTION

INTRODUCTION.....	1
-------------------	---

CHAPTER I: MAGNETISM AND HEUSLERS ALLOYS

I. 1. Introduction.....	4
I.2. Origins of magnetic moments	5
I.3. The different forms of magnetism.....	5
I.3.1. Diamagnetism.....	6
I.3.2. Paramagnetism.....	6
I.3.3.Ferromagnetism	6
I.3.4.Ferrimagnetism	7
I.3.5.Antiferromagnetism	7
I.4. Magnetic interactions	7
I.4.1. Direct exchange	8
I.4.2.Super-exchange interaction	8
I.4.3 Double exchange interaction	9
I.5. Spin polarization	11
I.6.Semi-metallic materials	11
I.6.1.Definition of a half-metal	11
I.7.Heuslers alloys	12
I.8. Heuslers Alloys Information General.....	13
I.9. Nomenclature of Heuslers alloy.....	14
I.9.1. Half-Heuslers alloys.....	14

I.9.2. Full-Heuslers alloys	14
I.9.3. Quaternary alloys- Heuslers	15
I.9.4. double half-Heuslers	16
I.10. Classification and crystal structure of Heuslers alloys	16
I.10.1 Crystal structure of half-Heusler alloys	17
I.10.2. Crystal structure of full-Heusler alloys	18
I.11. Structural properties and order-disorder phenomena	19
I.11. 1. Half-Heusler compounds.....	19
I.11. 2. Full-Heusler compounds	21
I.12. Magnetism and Heusler alloys	23
I.12.1. Ferromagnetism in half-metals	25
I.12.2. The Slater–Pauling rule	26
I.13. Origin of the gap in half-Heusler alloys	28
I.14. Applications	29
I.14.1. Spintronics	30
I.14.2. Tunnel Magnetoresistance (TMR).....	30
I.14.3. Giant Magnetoresistance (GMR).....	31
References	33

CHAPTER II: OVERVIEW OF CALCULATION METHODS

II.1. Introduction	38
II.2. Schrödinger equation of a crystal	38
II.3. Born–Oppenheimer approximation	40
II.4. Hartree approximation.....	41
I.5. Hartree–Fock approximation	41
I.6. Density Functional Theory	42
I.6.1. Hohenberg's and Kohn's theorems.....	42
I.6.2. Kohn–Sham equations	43
I.6.2.1. Solving Kohn-Sham equations	45
I.6.3. Functionality of the exchange and correlation	46
I.6.3.1. Local Density Approximation (LDA).....	47
I.6.3.2. Generalized Gradient Approximation (GGA)	48
I.6.3.3. The LDA and GGA approximations with spin polarization	48
I.6.3.4. The DFT + U approximation (L(S)DA+U and GGA+U)	49

I.6.3.5. The modified Becke-Johnson potential (mBJ)	50
I.7. Calculation Methods.....	51
I.7.1.The augmented plane wave (APW) method	51
I.7.2.Full Potential Linearized Augmented Plane Wave Method (FP-LAPW).....	54
I.7.2.1.Multiple energy windows	55
I.8.The WIEN2k Code.....	56
I.8.1.Code initialization.....	56
I.8.2.Self-consistent calculation.....	57
I.8.3.Determination of properties.....	58
References	58

CHAPTER III: RESULTS AND DISCUSSIONS

III.1. Introduction	63
III.2.Computational method:.....	64
III.3. Results and discussion:	65
III.3.1. double-half Heusler $K_2NaRbAs_2$	65
III.3.1.1 Structural Properties	65
III.3.1.1.1The Crystal Structure of Heusler Alloys and Preferred Sites:	65
III.3.1.1.2 Structural optimizations and magnetic order	66
III.3.1.1.3 Energy of formation (or enthalpy of formation) and energy of cohesion.....	67
III.3.2.1 Elastic properties	69
III.3.2.1.1 Debye temperature Θ_D and elastic wave velocities	74
III.3.3.1 Electronic properties.....	75
III.3.3.1.1 Band structures:.....	75
III.3.3.1.2 Densities of electronic states:.....	76
III.3.4.1 Magnetic properties:	77
III.3.5.1 Thermoelectric properties:	78
III.3.2. half-Heusler $VMSb$ ($M = Pd, Pt$).....	82
III.3.2.1 Structural Properties	82
III.3.2.1.1The Crystal Structure of Heusler Alloys and Preferred Sites	82
III.3.2.1.2 Structural optimizations and magnetic order:	82
III.3.2.2 Elastic properties:	84
III.3.2.2.1 Debye temperature Θ_D and elastic wave velocities	87
III.3.2.3 Magnetic properties	89

III.3.2.4 Electronic properties.....	90
III.3.2.4.1 Electronic band structure	90
III.3.2.4.2 Densities of states:.....	91
III.3.2.4.3 Effect of pressure on band structure properties.....	93
References	96

GENERAL CONCLUSION

Conclusion	98
------------------	----

List of Tables

Table.I.1 The different possibilities of occupation of non-equivalent sites in the half- Heusler structure C_{1b}	18
Table.I.2 Occupation of sites, general formula, type of structure (according to different databases) for different atomic orders and group space of compounds half-Heuslers.....	20
Table.I. 3 The different structures of full-Heuslers compounds	22
Table.III.1 The valence states and RMT radii of the atoms in the investigated materials.	64
Table.III.2 The different possibilities of occupation of non-equivalent sites in the Hlef-Heusler C_{1b} structure, for the studied compounds KNaAs, KRbAs.....	66
Table.III.3 Calculated lattice parameter (\AA), bulk modulus (GPa), its derivative pressure, and formation energies $E_{\text{formation}}(\text{Ry})$ for $K_2\text{NaRbAs}_2$ in their FM phase with structure type I.	69
Table.III.4 Calculated elastic constants $C_{11}, C_{12}, C_{13}, C_{33}, C_{44}, C_{66}$, bulk B , machinability index B/C_{44} , Shear G , Young E moduli, hardness H (in GPa), anisotropic parameter A , B/G , Poison's ratio ν , for $K_2\text{NaRbAs}_2$ in its structural and magnetic ground states. ...	70
Table.III.5 Calculated total, atom-resolved and interstitial magnetic moments (in μ_B) in the unit cell for $K_2\text{NaRbAs}_2$ in its structural and magnetic ground states.	78
Table.III.6 Possible atomic arrangements of the half- Heusler compounds VMSb ($M= \text{Pd}, \text{Pt}$).	82
Table.III.7 The calculated values of lattice parameter (\AA), bulk modulus (GPa), and its pressure derivative, the minimum energy (Ry) of both compounds VMSb ($M=\text{Pd}, \text{Pt}$)...84	84
Table.III.8 The elasticity constants C_{ij} (in GPa), the calculated elasticity constants: bulk B , shear G and Young moduli E (in GPa), anisotropy parameter A , B/G ratio, and Poison's ratio ν , θ_D temperature of Debye for VMSb ($M = \text{Pd}$ and Pt) compounds.	86
Table.III.9 The calculated transverse and longitudinal elastic wave velocities, the average wave velocity (m.s^{-1}), the temperature of Debye (K), and the melting temperature for VPdSb and VPtSb (K) compounds.	88
Table.III.10 Total and partial magnetic moments (WC- GGA, LSDA+U, TB-mBJ) in (μ_B) per unit cell.	89
Table.III.11 The calculated lattice constant(\AA), electronic band gaps for spin down (eV) and the electronic band structure nature of VPdSb and VPtSb compounds.	93

List of Figures

Figure.I.1 demonstration of the magnetic moment associated with (a)an orbiting electron and (b)a spinning electron.....	5
Figure.I.2 the different types of magnetic behaviour.	6
Figure.I.3 The Bethe-Slater curve presents the relationship of the exchange integral and the ratio of the interatomic distance r_{ij} to the radius of the orbital “ r_d ”	8
Figure.I.4 The semi-empirical Goodenough-Kanamori-Anderson super-exchange rules.	9
Figure.I.5 Double exchange between Mn^{+3} and Mn^{+4}	10
Figure.I. 6 schematic representation of the densities of states and spin polarization of a non-ferromagnetic metal (A), a ferromagnetic material (B) and a half-metallic material (C). 12	
Figure.I.7 Periodic table of Heusler compounds. The huge number of full Heusler compounds can be formed by combination of the different elements according to the color scheme. X and X' are in yellow, Y is blue, and Z is green	14
Figure.I.8 Representative of the cubic meshes of a Heusler (Full-Heusler) and a half Heusler (half-Heusler) alloys	15
Figure.I.9 Crystal structure of quaternaryHeusler alloys.....	16
Figure.I.10 Crystal structure of double half-Heusler alloys	16
Figure.I.11 Composition of the C_{1b} crystal structure of the Heusler alloy.	17
Figure.I.12 The two structures (regular and inverse) for Heusler alloys based on Mn_2 depending on the position of the element Y.	19
Figure.I.13 Reverse Heusler structure $CuHg_2Ti$ (a), quaternary structure $LiMgPdSn$ (b) [53].	19
Figure.I.14 Overview of the most important types of disorder that can occur in the semi-Heusler structure: (a) CaF_2 -like disorder, (b) $NaTl$ -like disorder, (c) Cu_2MnAl -like disorder, (d) $CsCl$ -like disorder , and (e) tungsten-like disorder.	21
Figure.I.15 Crystal structures of full-Heusler compounds.corresponding to the various types of structures[58].	23
Figure.I. 16 (a) XYZ half-Heusler alloys with only one magnetic sub-lattice since only the atoms in the octahedral locations carry a localized magnetic moment.a magnetic moment. In (b) Heusler alloys of the X_2YZ type, we have two magnetic sub-lattices. There are ma sub-lattices where we can find a ferromagnetic or antiferromagnetic coupling.	24
Figure.I.17 Band structure for (a) conventional ferromagnetic and (b) half-metallic material.	25
Figure.I.18 Schematic illustration of the density of states for: (a) metal, (b) half-metal, (c) a metal (spin-polarized), (d) ferromagnetic compound, (e) half-metallic ferromagnetic compound, and (f) half-metallic ferromagnetic compound. (\uparrow) majority spin, (\downarrow)minority spin.	26
Figure.I.19 The Slater-Pauling curve for 3d transition metals and their alloys. Experimental values are given for some Co2-based Heusler alloys for comparison. (A_1-xB_x alloys are abbreviated as AB).	27
Figure.I.20 The Slater-Pauling curve, (a) the total magnetic moment of half-Heusler alloys (b) of Full-Heusler alloys as a function of the total number of valence electrons.	28
Figure.I.21 Density of states of the half Heusler $NiMnSb$ alloy	29

Figure.I.22 Schematic illustration of the origin of the gap in the spin down channel in half-Heusler alloys.....	29
Figure.I.23 Schematic of the TMR effect in an MTJ. During tunneling, electron spin.	31
Figure.I.24 Giant magnetoresistance junction (the two states, parallel and antiparallel).....	32
Figure.II.1 Self-consistent iteration process used to solve Kohn Sham equations.....	46
Figure.II.2 Representation of Muffin-Tin “MT” potential. Diagram of the distribution of the unit cell in the atomic sphere and in the interstitial region.....	53
Figure.II.3 Multiple energy windows.....	55
Figure.II.4 Diagram of the Wien2K code.....	58
Figure.III.1 Structure representation of $K_2NaRbAs_2$ compound.....	65
Figure.III.2 Calculated total energy of KRbAs and KNaAs compounds as a function of the volume for FM, NM, and AFM phases.	66
Figure.III.3 Calculated total energy of $K_2NaRbAs_2$ compound as a function of the volume.....	67
Figure.III.4 Phonon dispersion curve of the $K_2NaRbAs_2$ compound.	68
Figure.III.5 3D graphical representation of (a) bulk, (b) Young's and (c) shear moduli and (d) Poisson's ratio of DHH $K_2NaRbAs_2$	73
Figure.III.6 Calculated band structure of $K_2NaRbAs_2$ compound in both (a, c) spin-up and (b, d) spin-down states by (a,b) GGA and (c,d) GGA+mBJ approximations.....	76
Figure.III.7 Calculated DOS of $K_2NaRbAs_2$ compound in both spin-up and spin-down states by GGA and GGA+mBJ approximations.....	77
Figure.III.8 Temperature dependence of the Seebeck coefficient of the spin up and spin down channels of $K_2NaRbAs_2$	80
Figure.III.9 Temperature dependence of the electrical conductivity for the spin up and spin down channels of $K_2NaRbAs_2$	81
Figure.III.10 Temperature dependence of the electronic thermal conductivity in the spin-up and spin-down channels of $K_2NaRbAs_2$ DHH alloy.	81
Figure.III.11 Different types of half-Heusler structures.	82
Figure.III.12 Calculated total energy of VPdSb and VPtSb compounds in their FM and NM phases as a function of the volume.....	83
Figure.III.13 3D-representation of Young's modulus of both compounds: a) VPdSb and b) VPtSb.....	87
Figure.III.14 The band structure of the VPdSb compound using: WC- GGA, LSDA+U, and TB-mBJ.....	91
Figure.III.15 The band structure of the VPtSb compound using: WC- GGA, LSDA+U, and TB-mBJ.....	91
Figure.III.16 Total and Partial DOS of the VPdSb and VPtSb compounds obtained by the TB-mBJ approach.....	92
Figure.III.17 Band structure of VPdSb alloy (in the 0–20 GPa range) at optimized lattice constant.	94
Figure.III.18 Band structure of VPtSb alloy (in the 0–20 GPa range) at optimized lattice constant.	94

List of Abbreviations

GMR giant magneto resistance.

TMR Tunnel magneto resistance.

T_c Curie temperature.

P spin polarization.

M_{tot} Total magnetic moment.

DFT Theory of density functional (densityfunctionaltheory)

LSDA+U approximation of local spin density (Local Spin Density Approximation)

GGA approximation of the generalized gradient (generalized gradient approximation)

MBJ Beck-Johnson modified (modified Beck-Johnson)

E_F Energy of Fermi.

DOS States density (Density of States)

TDOS/PDOS Total/Partial States Density (Total/Partial Density of States)

FP-LAPW Linearized augmented plane waves at full potential.

SCF self-consistent cycle.

ZB Brillouin Zone

B Modulus of compressibility.

Up/Dn Spin Up/Spin Down.

FM Ferromagnetic.

AFM Antiferromagnetic.

GENERAL INTRODUCTION

INTRODUCTION

Technological and industrial development depends heavily on the search for new materials and alloys from the periodic table of elements based on the natural law, which affirms that the combination of two different materials does not present a combination of their properties but rather gives rise to new characteristics physics specific to the alloy [1].

Heusler alloys have been known for their unique properties and potential applications in various fields. These alloys are made up of three different elements, and their composition can be manipulated to create specific properties that make them ideal for various applications. They were discovered in the late 19th century by a German mining engineer named Friedrich Heusler. Heusler was investigating the properties of certain minerals when he discovered an unusual compound made up of **Co**, **Mn**, and **Al**. He found that this compound is a ferromagnetic material, Whereas its elementary constituents are not ferromagnetic [2].

Researchers have been attempting to deepen their knowledge of the behavior of **HMF**, in order to understand, predict, and create new half-metallic materials due to their promising potential applications in spintronic devices [3], magnetic tunnel junctions, magnetic disk drives, spin injection devices, and nonvolatile magnetic random access memories [4]. Ideal HM ferromagnets exhibit a metallic nature in one spin channel ("up" or "down") and a semiconducting (or insulating) nature in the other spin channel, thereby revealing a 100% spin polarization at the Fermi level [5] with an integer value of the magnetic moment. The **HMF** nature was first determined in half-Heusler alloys such as NiMnSb and PtMnSb [6, 7].

The general formula for these alloys is X_2YZ , which crystallizes in the L_{21} structure. In addition, the half-Heusler type XYZ compounds, which crystallize in the C_{1b} phase, has also been widely investigated. These compounds have Wyckoff positions, with X in position 4a, Y in position 4c, and Z in position 4b [8, 9]. The half-Heusler-phase has attracted the attention of many researchers due to its ability to easily accommodate a ternary composition.

Recently, a novel class of Heusler alloys, named double half-Heusler alloys (DHH), has been discovered, inspired by the conception of double perovskites $A_2B'B''O_6$. They could be thought of as a collection of two half Heuslers of formula. It is worth noting that the first prediction of this class of materials was made by Anand et al. [10]. They investigated a large class of relatively unexplored DHH compounds, which have substantially lower lattice thermal conductivities due to their crystal chemistry. Their work presented a reliable method

for identifying low-thermal-conductivity half-Heuslers and highlighted a broad composition space for their potential applications.

Simulation methods have added a new dimension to scientific investigation of physical or chemical phenomena. Ab-initio methods have become a fundamental tool for calculating properties of complex systems, replacing expensive or dangerous experiments. These calculations methods are based on the density functional theory, theory (DFT) . Among these methods is the FP-LAPW (augmented plane wave) method [11], which has been highly successful in predicting structural, magnetic, electronic, thermoelectric, thermodynamic, and optical properties.

The objective of our work is to present the structural, elastic, electronic, magnetic, and thermoelectric properties of the $K_2NaRbAs_2$ DHH alloy and compare them with those of its parent HH alloys, $KNaAs$ and $KRbAs$ [12]. In the second part of this study, we used full potential linearized extended plane wave (FP-LAPW) and generalized gradient approximation (GGA) within density functional theory (DFT) to investigate the structural, electronic, elastic, and magnetic properties of two half-Heusler VMSb compounds ($M = Pd, Pt$)

The work that we present in this dissertation consists of three chapters:

- In the first chapter we recall certain notions related to magnetism as well as the different types of magnetism. and presents generalities on Heusler alloys. We also present some applications related to ferromagnetic compounds in technology such as GMR and TMR.
- The second chapter is dedicated to the density functional theory (DFT) which constitutes the basis of the ab initio calculation, to the FP-LAPW methods, and to the different approximations used in our study. Finally, an overview of the functionalities of the different programs implemented in the Wien2K code, which we used, is presented.
- The third chapter will be devoted to the results of our work on the double half-Heusler $K_2NaRbAs_2$ compounds and two half-Heusler VMSb compounds ($M = Pd, Pt$). We will present all the properties, in particular the structural, electronic, elastic and magnetic properties obtained by using the GGA method (the General Gradient Approximation) for the exchange and correlation interactions.

References

- [1]. Zarouali, Z. and Y. Nougali, Study of the electronic and magnetic structural properties of Half-heusler LiCaB for application in spintronics, 2021.
- [2]. Heusler, F., Magnetic-chemical studies Verh. Dtsch. Phys. Ges. 1903; **5**: p. 219.
- [3]. Wolf S, Awschalom D, Buhrman R, Daughton J, von Molnár vS, Roukes M, et al. Spintronics: a spin-based electronics vision for the future. Science. 2001;294(5546):1488-95.
- [4]. Terkhi S, Bentata R, Bendahma F, Lantri T, Bentata S, Aziz Z, et al. Half-metallic ferromagnetic behavior of cubic lanthanide based on perovskite-type oxide NdCrO₃: first-principles calculations. Indian Journal of Physics. 2021 ;**95**: p. 833-839.
- [5]. Vargas-Hernández, C. and R.B. Cruz, Half-metallic ferromagnetism of Zn_xMn_{1-x}O compounds: a first-principles study. computational condensed Matter. 2015: **4**: p. 1-5.
- [6]. Bona G, Meier F, Taborelli M, Bucher E, Schmidt P. Spin polarized photoemission from NiMnSb. Solid state communications.1985;56(4):391-4.
- [7]. Watanabe, K., On new ferromagnetic intermetallic compounds PtMnSn and PtMnSb. Journal of the Physical Society of Japan. 1970;**28**(2): p. 302-307.
- [8]. Neumann K-U, Crangle J, Smith J, Zayer N, Ziebeck K. Magnetic order in ternary intermetallic compounds containing palladium and titanium. Journal of magnetism and magnetic materials. 1995;140:185-6.
- [9]. Prokeš K, Diviš M, Mohn P, Schwarz K, Sechovský V, Svoboda P, et al. Reduced magnetic moments in UNiSi. Journal of alloys and compounds. 1998;269(1-2):43-9.
- [10]. Anand S, Wood M, Xia Y, Wolverton C, Snyder GJ. Double half-heuslers. Joule. 2019;3(5):1226-38.
- [11]. Schwarz, K., DFT calculations of solids with LAPW and WIEN2k. Journal of Solid State Chemistry, 2003. **176**(2): p. 319-328.
- [12]. Lorf A, Boudia K, Khelfaoui F, Amara K, Sadouki O, Ameri M, editors. Structural and Half-Metallic Stabilities of the Half-Heusler Alloys KNaAs, KRbAs and NaRbAs: First Principles Method. Spin; 2021: World Scientific.

CHAPTER I

MAGNETISM AND HEUSLERS ALLOY

I. 1. Introduction

Heusler alloys materials that possess magnetic properties, such as the ability to attract or repel other magnets. these properties arise from the presence of magnetic domains within the material, with are regions where the atomic moments are aligned. Magnetic materials are of great economic importance, with applications ranging from information storage and energy conversion to medical imaging and sensing

Recent research has focused on the synthesis of new materials with superior magnetic performance. An important discovery was the observation that the resistance an electron faces when passing through a polarized layer depends on its spin relative to the magnetization of the layer. This phenomenon, called spin-dependent transport, allows electron currents to be filtered according to their spin configuration

The atomic structure of a material determines its magnetic characteristics. In particular, the magnetic moment of each atom is influenced by its electron configuration, which in turn is influenced by the arrangement of its constituent subatomic particles. By manipulating the atomic structure of a material, researchers can control its magnetic properties and design materials with specific applications in mind.

Magnetic materials have many applications in modern technology. For example, they are used in the construction of hard drives, which store digital data by magnetizing regions of thin film. Magnetic materials are also used in electric motors, where they convert electrical energy into mechanical motion, and in transformers, where they convert electrical energy from one voltage level to another. Magnetic materials are also important for medical applications, such as magnetic resonance imaging (MRI), which uses strong magnetic fields to produce detailed images of the human body.

In conclusion, the study of magnetic materials is a dynamic and important field with many potential applications. By understanding the science behind these materials, researchers can design new materials with improved magnetic performance and explore new applications for these materials in various fields of science and engineering.

I.2. Origins of magnetic moments

The term "magnetism" refers to the set of phenomena exhibited by materials that are attracted or repelled by an external magnetic field. Magnetism is a general property of matter, but it is particularly pronounced in certain materials called magnetic materials. The cause of this phenomenon is the spins of the electrons, and to a lesser extent, their magnetic moment orbitals. Generally, the electrons of an atom tend to organize themselves according to the Pauli exclusion principle and Hund's laws, which give rise to magnetism. The orbital motion of the electrons is analogous to the current in a loop of wire. In addition, a magnetic spin instant is associated with a rotating electron.

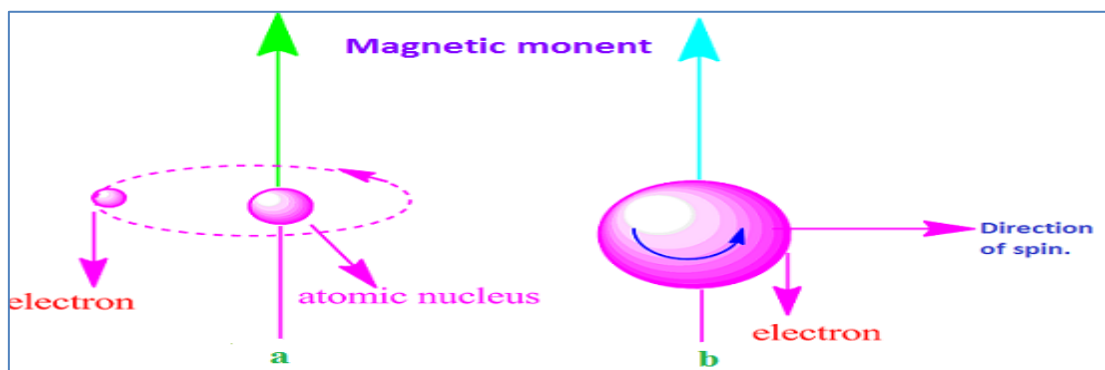


Figure.I.1 demonstration of the magnetic moment associated with (a)an orbiting electron and (b)a spinning electron.

I.3. The different forms of magnetism

Most of the magnetism in atoms within matter arises from their incomplete electronic shells. In condensed matter, the spin moments of atoms are coupled through exchange interactions that have an electrostatic origin. These interactions are a result of the overlapping of electrons' orbitals around the nucleus. A magnetic field tends to align the magnetic moments in the direction of the field. The order of the moments is determined by the competition between exchange interactions and thermal agitation, resulting in a collective behavior responsible for various magnetic behaviors such as diamagnetism, paramagnetism, ferromagnetism, ferrimagnetism, and antiferromagnetism. We will outline the characteristics of each of these categories of materials.

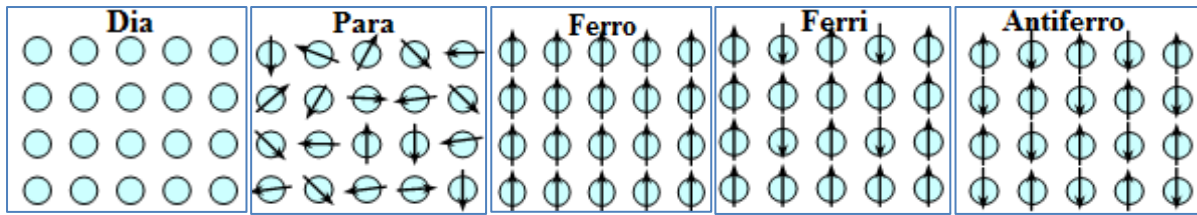


Figure.I.2 the different types of magnetic behaviour[1].

I.3.1. Diamagnetism

Diamagnetic materials consist of atoms that all have complete electronic shells and do not possess a permanent magnetic moment. If a diamagnetic material is subjected to a magnetic field (H), all of its electrons are oriented in the opposite direction of the magnetic field because the spinning electrons generate a type of electric charge. This diamagnetic phenomenon appears in all materials, but it is sometimes masked by other effects such as paramagnetism, ferromagnetism, and antiferromagnetism when they coexist in the material [2].

I.3.2. Paramagnetism

If a material medium does not exhibit spontaneous magnetization, but has weak interactions between the magnetic moments compared to thermal agitation, these interactions become negligible when subjected to an external magnetic field. In the absence of a magnetic field, the moments can point in any direction. However, the magnetic moments tend to orient themselves according to the field direction when subjected to a magnetic field. The magnetization is proportional to the excitation H applied: $M = xH$, where x is the magnetic susceptibility. Paramagnetism is temperature-sensitive. The initial susceptibility is positive and becomes infinite at absolute zero. It decreases as the temperature increases [3].

I.3.3. Ferromagnetism

The theory of how atoms in a lattice can interact to create magnetic moments, known as ferromagnetism, was first proposed by Fritz Weiss in 1907. In quantum mechanics, the Heisenberg model describes the parallel alignment of magnetic moments in terms of the exchange interaction between neighboring moments. In classical theory, the presence of a molecular field within the material determines how the material responds to a magnetic field. At room temperature, Fe, Co, and Ni are ferromagnetic, but above their respective Curie-Weiss temperatures (T_C), the susceptibility varies according to the Curie-Weiss law [3, 4]. As thermal agitation increases, the degree of alignment of the atomic magnetic moments decreases, and the material becomes paramagnetic.

I.3.4.Ferrimagnetism

A ferrimagnetic body is an antiferromagnet with two sublattices carrying unequal moments [5, 6]. This results in a spontaneous magnetization of the material. It differs from antiferromagnetism, for which the resulting magnetic moment is zero, and from ferromagnetism, for which it is zero. Spontaneous magnetization results at the microscopic level from a parallel arrangement of magnetic moments.

In the absence of a magnetic field, the magnetic moments of the crystal ions align antiparallel inside the Weiss domain, but the opposite magnetic moments are unequal and do not completely compensate for each other. In the presence of an external magnetic field, the magnetic moments tend to align in the direction of the magnetic field. As for ferromagnetic materials, ferrimagnetic materials have a spontaneous magnetization below the Curie-Weiss temperature and become paramagnetic above this temperature.

I.3.5.Antiferromagnetism

Antiferromagnets are often ceramic materials made of transition metal oxides, oxygen, or other compounds. The exchange contact between nearby atoms produces an antiferromagnetic alignment of atomic magnetic moments in antiferromagnetic materials, in contrast to ferromagnetic materials. The material's overall magnetization is then zero. These materials have a positive magnetic susceptibility. However, it is typically smaller than ferromagnetic materials. At present, only one element in the atomic number that is antiferromagnetic at ambient temperature is chromium.

I.4. Magnetic interactions

Diluted magnetic materials do not interact with magnetic moments. Paramagnetic materials are used. Interactions, however, appear to be conceivable as the density of magnetic moments grows. The magnetic properties of manganites are controlled via direct exchange interactions (super-exchange and double exchange) between the spins of Mn ions via oxygen ions. This contact, known as Heisenberg's exchange interaction, is important for organizing the spins into parallel (ferromagnetic material) or antiparallel (antiferromagnetic material). The mechanism most often employed to understand magnetic exchange interactions will be presented in the next section.

I.4.1. Direct exchange

The exchange integral $J_{(i,j)}$ is the strength of the interaction between the localized spins S_i and S_j . It depends on the distance between the two atoms, the overlap between the electron wave functions of the atoms, and the electron configuration of the atoms. The indirect exchange interaction arises from the virtual hopping of electrons between neighboring atoms via non-magnetic atoms or through delocalized states [7]. This mechanism is known as superexchange interaction and is a key mechanism for the magnetic properties of many materials, including manganites. In some cases, the superexchange interaction can be mediated by mobile charge carriers, as in the case of double exchange interaction. The Heisenberg Hamiltonian is a simple model used to describe magnetic interactions in materials, but more complex models are often needed to capture the full range of magnetic phenomena in real materials.

$$\mathbf{H} = -2 \sum_{i,j} J_{i,j} \mathbf{S}_i \cdot \mathbf{S}_j \quad (\text{I.1})$$

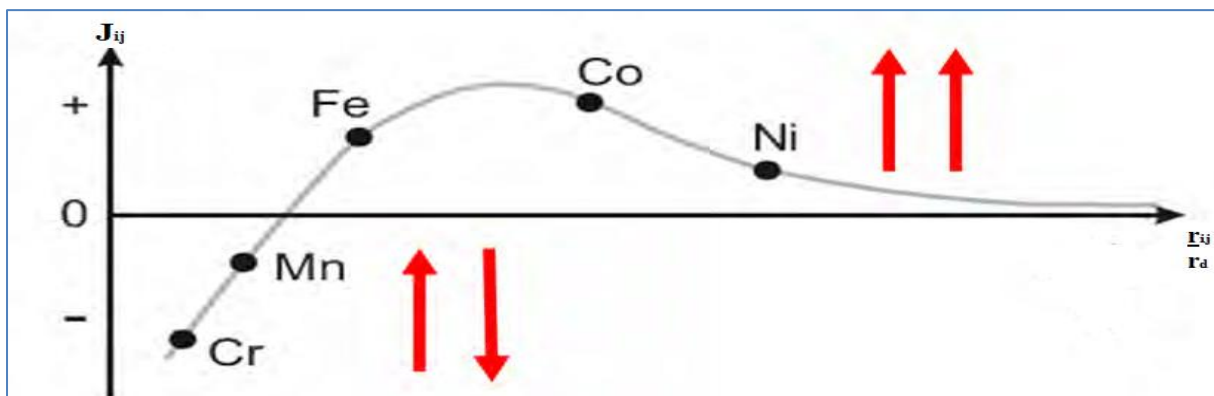
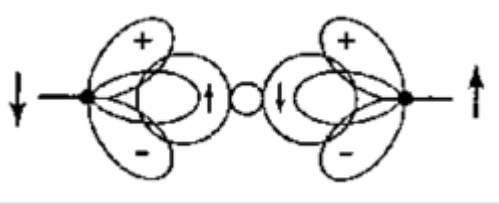
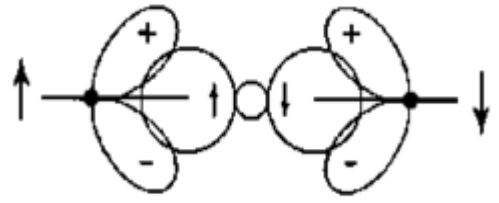
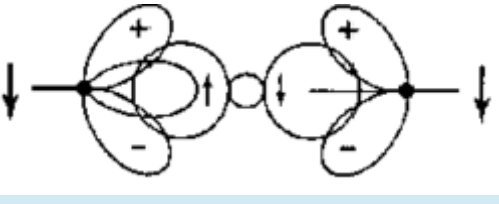


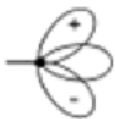
Figure.I.3 The Bethe-Slater curve presents the relationship of the exchange integral and the ratio of the interatomic distance r_{ij} to the radius of the orbital “ r_d ” [8].

I.4.2. Super-exchange interaction

Super-exchange is a type of interaction between two neighboring magnetic ions, mediated by an intervening non-magnetic ion, such as oxygen. This interaction is based on the exchange of electrons between the two magnetic ions via the intervening ion. In contrast to direct exchange, the strength of the super-exchange interaction depends on the distance between the magnetic ions and the strength of the intervening ion's coupling to the magnetic ions. Super-exchange interactions are usually antiferromagnetic, as in the case of LaMnO_3 [9, 10] crystals, where the interaction between two manganese ions is mediated by an oxygen ion. The crystal field In **Figure I.4**.splitting of the 3d electronic levels of transition metal ions can also play a role in determining the strength and nature of the super-exchange interaction.

Case	orbital configuration	super-exchange coupling
1		strong antiferromagnetic coupling
2		weak antiferromagnetic coupling
3		weak ferromagnetic coupling

Cation Mn^{+3}



Half-filled t2g orbitals and one eg orbital at

.half filled pointing in the direction of the O^{-2} anion

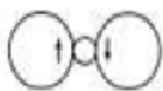
Cation Mn^{+4}



Half-filled t2g orbitals and one empty eg orbital

.Pointing in the direction of the O^{-2} anion

Anion O^{-2}



Orbital 2p.

Figure.I.4 The semi-empirical Goodenough-Kanamori-Anderson super-exchange rules.

I.4.3 Double exchange interaction

In transition metal oxides, the exchange interaction between ions is primarily due to the hybridization of transition metal d-orbitals with the p-orbitals of the neighboring oxygen ions.

The nature of this interaction depends on the relative energies and electron configurations of the d and p orbitals involved.

In the case of transition metal oxides like $\text{La}_{1-x}\text{Ca}_x\text{MnO}_3$ or $\text{La}_{1-x}\text{Sr}_x\text{MnO}_3$, the Mn ions can exist in two different valence states, Mn^{3+} and Mn^{4+} , depending on the doping level. The Mn^{3+} ions have a total spin of 2, while the Mn^{4+} ions have a total spin of 3/2. **Figure I.5**

Due to the hybridization of the d and p orbitals, the Mn^{3+} and Mn^{4+} ions can interact via a ferromagnetic double exchange interaction. This arises from the alignment of the spins of the Mn^{3+} and Mn^{4+} ions, which leads to a lowering of the total energy of the system. This interaction is essential for the ferromagnetic behavior observed in these materials.

In addition to the double exchange interaction[11], there can also be antiferromagnetic superexchange interactions between ions of the same valence. These interactions arise due to the exchange of electrons between neighboring ions via an intermediate oxygen ion. The strength and nature of the superexchange interaction depend on the geometry and electron configuration of the ions involved.

Therefore, in the $\text{La}_{1-x}\text{Ca}_x\text{MnO}_3$ alloy, both antiferromagnetic superexchange interactions between ions of the same valence and ferromagnetic double exchange interactions between ions of different Valen.

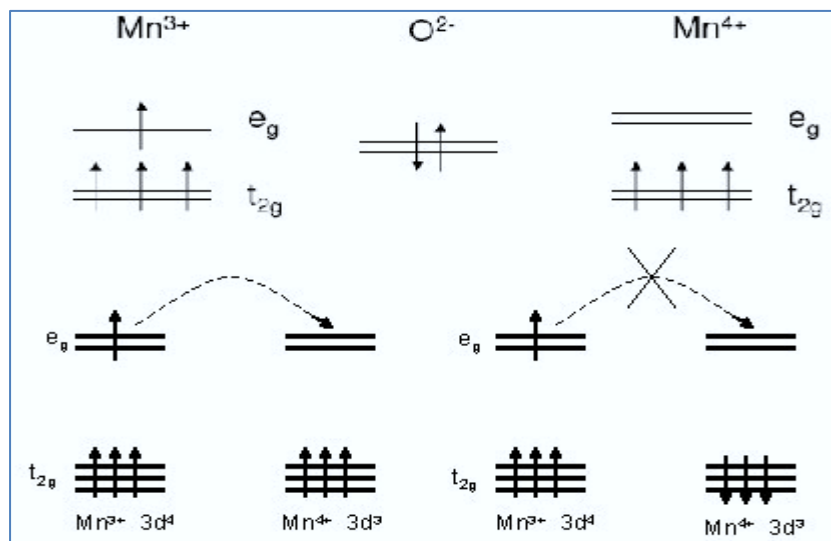


Figure.I.5 Double exchange between Mn^{3+} and Mn^{4+} .

I.5. Spin polarization

Spin polarization, or the difference between the density of states for the spins "up" and "down," has not yet been explained by a model, but one may have tried to assume that it is a property of the material. Because the processes of spin polarisation are so complex, no model has yet been able to adequately describe them. Its discovery enables practical uses of this phenomenon. The ferromagnetic/insulator [12] interface determines the spin polarization of an electrode, and the kind of barrier can alter the value of the spin polarization. A superconducting tip can be used to measure Andreev's reflection to measure spin polarization, or junctions can be used to measure conductance or magnetoresistance. Speaking of the spin polarisation of material only makes sense if the nature of the barrier is specified. The value of the polarisation depends on the method of measurement and also on the temperature. It is therefore necessary to strictly use the same measurement technique and devices for different materials to determine their spin polarization.

I.6.Semi-metallic materials

I.6.1.Definition of a half-metal

De Groot and his collaborators [13] discovered the concept of a ferromagnetic half-metal whose definition is relatively simple. It is a material characterized by the fact that at the Fermi level, there is only one spin population. Therefore, conduction is ensured only by "up" or "down" spins. In a half-metal, according to de Groot, only the electrons of a given spin orientation (up or down) are metallic, while the electrons of the opposite spin orientation exhibit insulating behavior. In other words, half-metals have a spin polarization of 100% since they contribute only to the conduction of either spin "up" or spin "down" electrons **Figure I.6.**

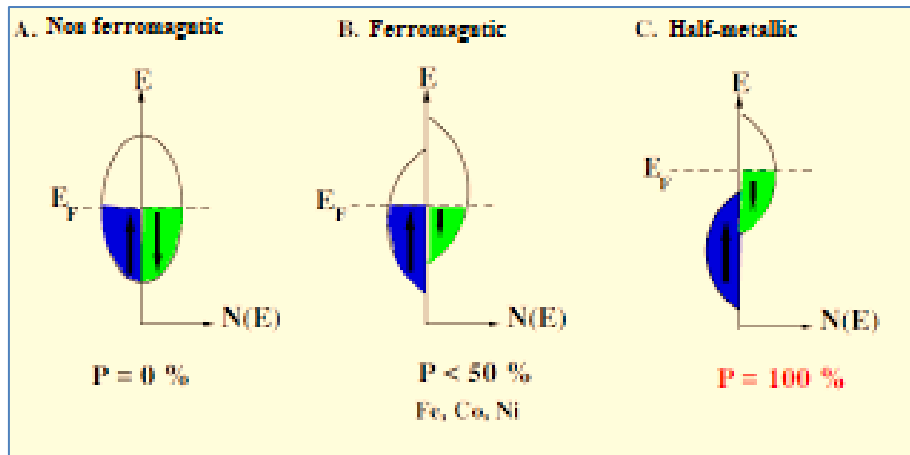


Figure.I. 6 schematic representation of the densities of states and spin polarization of a non-ferromagnetic metal (A), a ferromagnetic material (B) and a half-metallic material (C).

For a half-metallic material, the Fermi level passes through the gap energy for one spin direction and an energy band for the other direction. A half-metallic material can be considered magnetic for the majority of spins and a semiconductor for the minority spin. This discovery was made by performing band calculations on compounds from the half-Heusler family, specifically on NiMnSb. Researchers predicted the band structures, which were consistent with predictions made from earlier work on PtMnSb [14]. A research project was conducted to discover new half-metallic materials using band calculations.

Some examples of half-metals include CrO_2 [15], Fe_3O_4 [16], $\text{La}_{0.7}\text{Ca}_{0.3}\text{MnO}_3$ [17], $\text{Fe}_x\text{Co}_{1-x}\text{S}_2$ [18], Co_2MnX ($X = \text{Si, Ge}$) [19], CuV_2S_4 , and CuTi_2S_4 [20] CrAs[21], as well as compounds from various crystallographic families, including half-Heusler, Zn-blende compounds [22], and others with similar structures. Of particular interest is their potential integration into semiconductor structures.

I.7.Heuslers alloys

The combination of Heusler alloys exhibits a wide range of electronic and magnetic properties. They are of particular importance in the context of this thesis due to their excellent characteristics for spin electronics. Furthermore, they are being investigated for various applications, including thermoelectric and solar. In this chapter, we will provide a brief review of Heusler alloys, which are part of the series of alloys covered in this study. We will

discuss their various structures, principal features, and possible applications. We will also define the numerous elements that constitute Heusler alloys.

I.8. Heuslers Alloys Information General

Heusler alloys were first developed by Friedrich Heusler, a German scientist, in 1903 [23]. He discovered that adding an "sp" element (Al, In, Sn, Sb, or Bi) to a Cu-Mn alloy renders it ferromagnetic, even in the absence of magnetic elements. This discovery gave rise to a new class of materials, paving the way for future technologies [24, 25]. In 1963, it was determined that pure Mn, which has an antiferromagnetic order, is the major component that contributes to the magnetic moment of spin in this alloy [26]. This class of materials, known as Heusler compounds or alloys, presently consists of a vast collection of over 1000 discovered compounds exhibiting a broad range of magnetic properties.

The first class of Heusler alloys comprises ternary semiconductor or metallic materials with a 1:1:1 type stoichiometry (also known as half-Heusler "Half-Heusler") that have a band gap around the Fermi level in the energy band diagram solely for spin up or spin down. This type of material has been extensively studied as it can optimize the effectiveness of spintronic devices. The second type, represented by the general chemical formula X_2YZ , where X and Y are transition elements and Z is a semiconductor or a non-magnetic material, is of the 2:1:1 type (known as "Full-Heusler"). The following diagrams illustrate the unlimited number of compounds that can be formed by combining practically any element from the periodic table.

1																	2				
H 2.20																	He				
3 Li 0.98	4 Be 1.57															5 B 2.04	6 C 2.55	7 N 3.04	8 O 3.44	9 F 3.98	10 Ne
11 Na 0.93	12 Mg 1.31															13 Al 1.61	14 Si 1.90	15 P 2.19	16 S 2.58	17 Cl 3.16	18 Ar
19 K 0.82	20 Ca 1.00	21 Sc 1.36	22 Ti 1.54	23 V 1.63	24 Cr 1.65	25 Mn 1.55	26 Fe 1.83	27 Co 1.88	28 Ni 1.91	29 Cu 1.90	30 Zn 1.85	31 Ga 1.81	32 Ge 2.01	33 As 2.18	34 Se 2.55	35 Br 2.96	36 Kr 3.00				
37 Rb 0.82	38 Sr 0.95	39 Y 1.22	40 Zr 1.33	41 Nb 1.60	42 Mo 2.16	43 Tc 1.90	44 Ru 2.20	45 Rh 2.28	46 Pd 2.20	47 Ag 1.93	48 Cd 1.69	49 In 1.78	50 Sn 1.96	51 Sb 2.05	52 Te 2.10	53 I 2.66	54 Xe 2.80				
55 Cs 0.79	56 Ba 0.89	57-71 LANTHANIDE	72 Hf 1.30	73 Ta 1.50	74 W 1.70	75 Re 1.90	76 Os 2.20	77 Ir 2.20	78 Pt 2.20	79 Au 2.40	80 Hg 1.90	81 Tl 1.80	82 Pb 1.80	83 Bi 1.90	84 Po 2.00	85 At 2.20	86 Rn				
87 Fr 0.70	88 Ra 0.90	89-103 ACTINIDE																			
LANTHANIDE																					
57 La 1.10	58 Ce 1.12	59 Pr 1.13	60 Nd 1.14	61 Pm 1.13	62 Sm 1.17	63 Eu 1.20	64 Gd 1.20	65 Tb 1.10	66 Dy 1.22	67 Ho 1.23	68 Er 1.24	69 Tm 1.25	70 Yb 1.10	71 Lu 1.27							
ACTINIDE																					
89 Ac 1.10	90 Th 1.30	91 Pa 1.50	92 U 1.70	93 Np 1.30	94 Pu 1.25	95 Am 1.13	96 Cm 1.28	97 Bk 1.30	98 Cf 1.30	99 Es 1.30	100 Fm 1.30	101 Md 1.30	102 No 1.30	103 Lr 1.30							

X_2YZ	Full Heusler*
XYZ	Half Heusler#

Figure.I.7 Periodic table of Heusler compounds. The huge number of full Heusler compounds can be formed by combination of the different elements according to the color scheme. X and X' are in yellow, Y is blue, and Z is green [25].

I.9. Nomenclature of Heuslers alloy

I.9.1. Half-Heuslers alloys

Alloys in this family have a chemical composition of XYZ. In 1983, de Groot and his colleagues [27] discovered a half-Heusler alloy of the NiMnSb type [28]. Half-Heusler compounds can be viewed as consisting of two parts, one covalent and the other ionic. Therefore, the X and Y atoms exhibit distinct cationic properties, while Z is the anionic counterpart [29]. The X and Y elements can be main group elements, transition metals, or rare earth elements, while the element Z belongs to the second half of the classification period and includes elements such as Ge, Sn, and Sb. Examples of half-Heusler compounds include LiAlSi, ZrNiSn, and LuAuSn [30, 31].

I.9.2. Full-Heuslers alloys

Full Heusler alloys have a cubic structure and a high degree of chemical flexibility, which allows for the possibility of tailoring their electronic and magnetic properties. They exhibit a wide range of magnetic and electronic properties, including ferromagnetic, antiferromagnetic, and spin-gapless semiconducting behavior [32]. The use of Full Heusler alloys in spintronics

has gained significant attention due to their excellent spin polarization and spin injection efficiency. These materials have been used in various spintronic devices such as magnetic tunnel junctions, spin valves, and magnetic sensors. Additionally, Full Heusler alloys are being investigated for other applications such as thermoelectric devices, catalysis, and solar energy conversion [33,34].

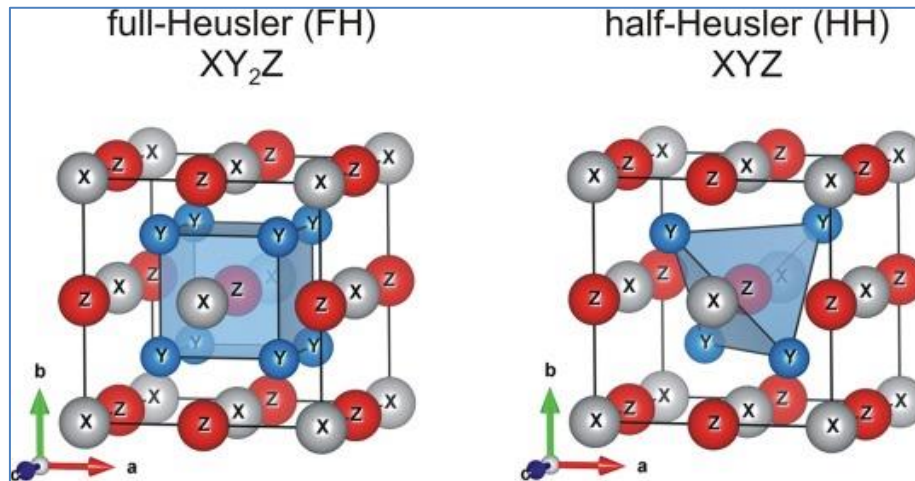


Figure.I.8 Representative of the cubic meshes of a Heusler (Full-Heusler) and a half Heusler (half-Heusler) alloys .

I.9.3.Quaternary alloys- Heuslers

A new series of quaternary Heusler alloys with a stoichiometry of type 1:1:1:1 can be created by exchanging another X atom for one of the X atoms in the formula X_2YZ . These alloys have the LiMgPbSb type structure [35] with the space group F-43m (No 216) and the structural formula $XX'YZ$, where X, X', and Y are transition metals and Z is an sp element. X' atoms have a lower valence than X atoms, while Y atoms have a valence that is strictly lower than both (X and X'). The LiMgPdSn structure can indeed be classified into three types [36-38] Y-(I), Y-(II), and Y-(III).

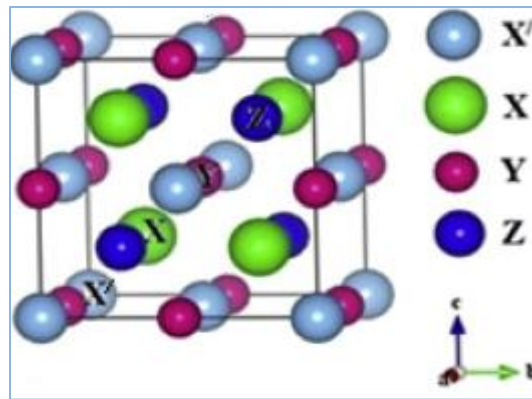


Figure.I.9 Crystal structure of quaternary Heusler alloys.

I.9.4. double half-Heuslers

The half-Heusler semiconductors have been studied extensively as three-component systems. Here, we explore the phase space of quaternary double ($X'X''Y_2Z_2$), compositions that are 10 times larger in size. Using a reliable double half-Heusler composition, the compositions studied here are divided into three classes ($X'X''Y_2Z_2$, $X_2Y'Y''Z_2$, $X'X''Y_2Z_2$) based on the site of substitution in the XYZ structure.

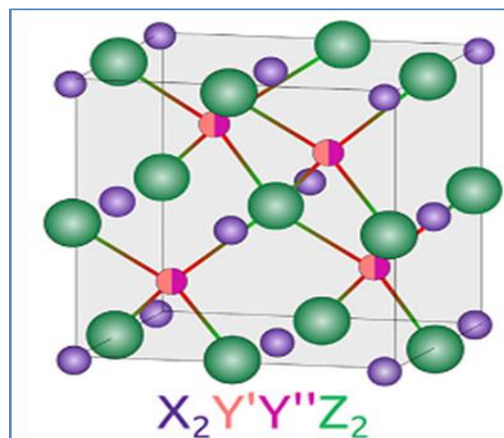


Figure.I.10 Crystal structure of double half-Heusler alloys[39].

I.10. Classification and crystal structure of Heuslers alloys

Heusler alloys are classified into two categories based on their crystal structure and their disordered atomic structure. The order of the atoms within the crystal lattice is the basis for this new categorization. Small quantities of disorder within the distribution of atoms at the lattice sites create notable differences in their electronic structure, and also changes in magnetic and transportation characteristics [40, 41]. For half-Heuslers, their atoms are arranged in a perfect arrangement according to the structures C_{1b} , L_{21} ,

I.10.1 Crystal structure of half-Heusler alloys

Half-Heusler alloys have a general formula and stoichiometry (1:1:1) XYZ, and they crystallize in the space group (F-43m No. 216) [42] as a non-centrosymmetric C_{1b} cubic structure. The structure of the Half-Heuslers is defined by the interpenetration of three face-centered cubics (fcc) sub-lattices, as exemplified by the prototype MgAgAs, where atoms X and Y create a NaCl-type lattice, and elements Y and Z form a ZnS-type sub-network [43]. However, the majority of Half-Heusler alloys are structured according to the combination MgCuSb [44], where elements Y and Z form a ZnS-type covalent sub-lattice, while the most electropositive X elements and the most electronegative Y elements form a NaCl-type lattice.

The face-centered cubic (fcc) structure has three full sublattices and one unoccupied interpenetrating sub-lattice in the C_{1b} structure. In the third structure of fcc, the transverse of the rock-salt structure is moved by half a unit cell [45]. Generally, the Half-Heusler structure can be thought of as a ZnS sub-lattice (with Wyckoff positions at sites 4a and 4c) with busy octahedral sites (4b). This description emphasizes the importance of the covalent bonding interaction between two confined elements in the material's electrical characteristics. On the other hand, atoms on sites 4a and 4b form a NaCl-like sublattice, indicating that their interaction has a strong ionic nature [46]. **Figure I.11** depicts the correlation between these different crystal lattices.

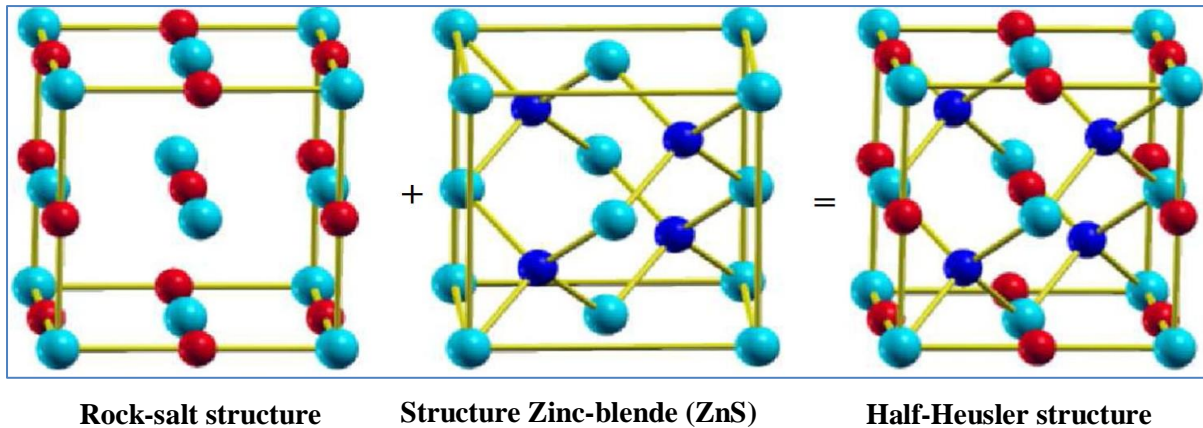


Figure.I.11 Composition of the C_{1b} crystal structure of the Heusler alloy.

Depending on the occupied positions: 4a (0, 0, 0), 4b (1/2, 1/2, 1/2), and 4c (1/4, 1/4, 1/4), several possibilities of association of the three atomic arrangements not equivalent to this type of structure (C_{1b}) as shown in table (I.1) [47], or, the most observed atomic order and that of both types I, II and III.

Atoms	X	Y	Z
Type I (α)	4c (1/4,1/4,1/4)	4a (0,0,0)	4b (1/2,1/2,1/2)
Type II (β)	4c (1/4,1/4,1/4)	4b (1/2,1/2,1/2)	4a (0,0,0)
Type III (γ)	4a (0,0,0)	4c (1/4,1/4,1/4)	4b (1/2,1/2,1/2)

Table.I.1 The different possibilities of occupation of non-equivalent sites in the half-structure Heusler C_{1b} .

I.10.2. Crystal structure of full-Heusler alloys

Heusler alloys have a general formula of X_2YZ and a stoichiometry of 2:1:1, also known as "full-Heusler". They crystallize in the cubic space group $Fm-3m$ (space group No. 225) with a prototype Cu_2MnAl denoted as L_{21} [48, 49]. In L_{21} , X atoms occupy position 8c (1/4, 1/4, 1/4), Y atoms are at position 4a (0, 0, 0), and Z atoms are located at position 4b (1/2, 1/2, 1/2). Two sub-cells are occupied by X while the other two are occupied by Y and Z elements. The L_{21} structure is completely ordered. In some cases, an inverse structure is observed when the atomic number of Y is greater than that of X ($Z(Y) > Z(X)$). This inverse structure is often referred to as XA, and the prototype is $CuHg_2Ti$, which crystallizes in the cubic space group $F-43m$ (space group No. 216) [50]. In all cases, X is more electropositive than Y, and thus, X and Z form a rock salt structure to achieve octahedral coordination for X. The remaining X and Y atoms occupy the symmetrical tetrahedral sites. The structure is described by four interconnected cubic sub-networks, but X atoms do not form a simple cubic network. Instead, they are placed at positions 4a (0, 0, 0) and 4d (3/4, 3/4, 3/4), while Y and Z atoms are located at positions 4b (1/2, 1/2, 1/2) and 4c (1/4, 1/4, 1/4), respectively. Inverse Heusler alloys are often distinguished from normal Heusler alloys by the formula $(XY) X'Z$. Mn_2 -based materials with $Z(Y) > Z(Mn)$ often exhibit this inverse Heusler structure, such as Mn_2CoSn or $(Mn Co)Mn Sn$ [51, 52]. Another family of Heusler alloys is quaternary Heusler compounds, where four different chemical atoms with two different X and X elements are located at positions 4a and 4d, respectively. The Y element is placed in position 4b while the Z element is placed in position 4c. This structure presents the $LiMgPdSn$ prototype and crystallizes in the cubic space group $F-43m$ (space group No. 216). The reverse Heusler structure and the quaternary Heusler alloy are illustrated in **FigureI.12**.

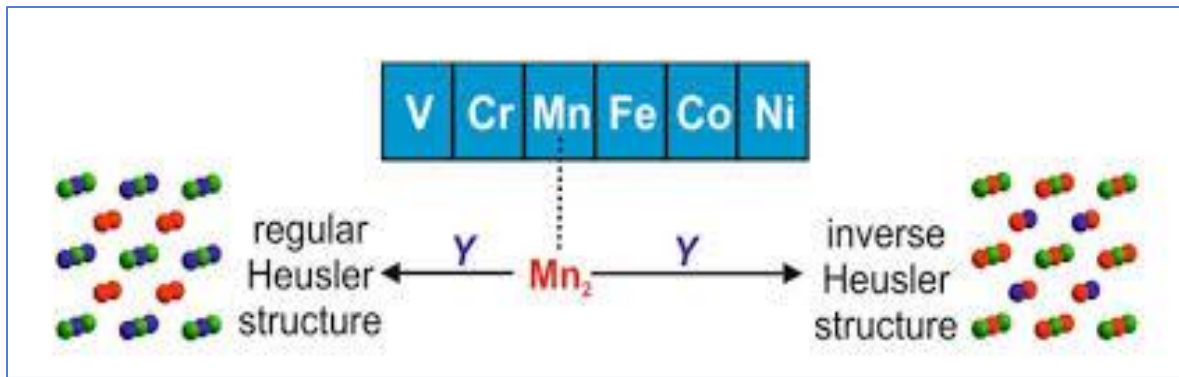


Figure.I.12 The two structures (regular and inverse) for Heusler alloys based on Mn_2 depending on the position of the element Y.

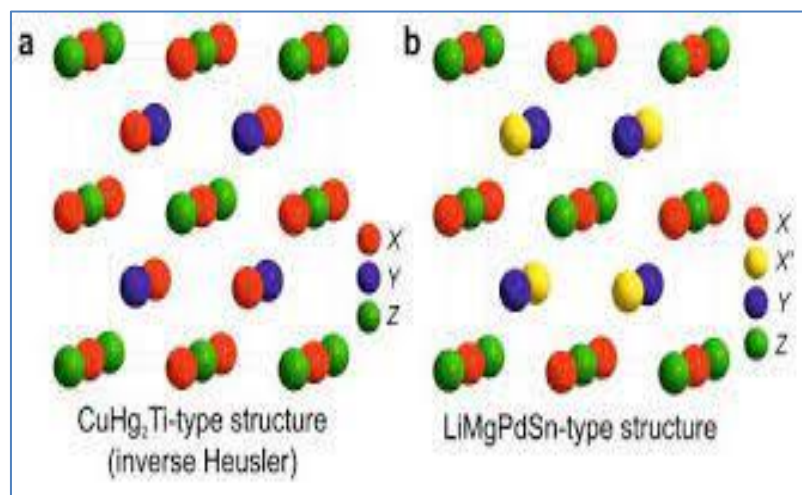


Figure.I.13 Reverse Heusler structure $CuHg_2Ti$ (a), quaternary structure $LiMgPdSn$ (b) [53].

I.11. Structural properties and order-disorder phenomena

The properties of Heusler materials are strongly influenced by their atomic arrangements. Even a partial mixing of atoms can significantly alter the electronic structure of the material. Half-Heusler compounds are tetrahedrally coordinated structures that are closely related to binary semiconductors. They maintain their crystalline order at the composition temperature [54]. In contrast, X_2YZ phases often exhibit substantial atomic disorder, leading to the occupation of vacant network sites. This disorder is much less common in half-Heusler compounds..

I.11. 1. Half-Heusler compounds

A mixture of atoms in the Wyckoff 4a and 4b positions results in a CaF_2 -type structure ($C1$, $Fm-3m$ space group, n° 225). However, vacant sites may also become partially occupied, introducing vacancies in other subnets. For instance, partial occupation of 4d sites

accompanied by voids on the 4c sites results in a Cu_2MnAl -type structure (L_{21} , Fm-3m space group, n° 225). If there is an additional mixture of atoms in the 4a and 4b positions, it leads to a type of disorder called CsCl (B_2 , Pm-3m, #221). On the other hand, if the vacant network site is partially occupied by atoms from the 4b site and accompanied by the mixing of positions of 4a and 4c, we obtain a structure of type NaTl (B_{32a} , Fd-3m, n° 227). Finally, a totally random distribution of the three atoms over the four possible positions gives rise to a tungsten disorder (W, Im-3m, n° 229). Table I.2 provides a summary of the different types of structures and notations based on the Inorganic Crystal Structure Database (ICSD), Structure Reports (Strukturberichte), the Pearson database, as well as the space group [44].

Different forms of the atomic disorder are possible in the half-Heusler structure **Table I.2**. **Figure I.14** provides an overview of the numerous forms of disorder while providing a detailed description of all possible atomic configurations.

occupation of Site	Formula General	Structure type			Groupe d'espace
		ICSD	SB	Pearson	
4a, 4b, 4c	XYZ	LiAlSi	C1 _b	cF16	F-43m (N°. 216)
4a= 4b, 4c	XZ ₂	CaF ₂	C1	cF12	Fm-3m (N°. 225)
4a, 4b, 4c=4d	X ₂ YZ	Cu ₂ MnAl	L ₂₁	cF16	Fm-3m (N°. 225)
4a= 4b, 4c=4d	XZ	CsCl	B ₂	cP2	Pm-3m (N°. 221)
4a= 4c, 4b=4d	YZ	NaTl	B _{32a}	cF16	Fd-3m (N°. 227)
4a= 4b= 4c=4d	X	W	A ₂	cI2	Im-3m (N°. 229)

Table.I.2 Occupation of sites, general formula, type of structure (according to different databases) for different atomic orders and group space of compounds half-Heuslers.

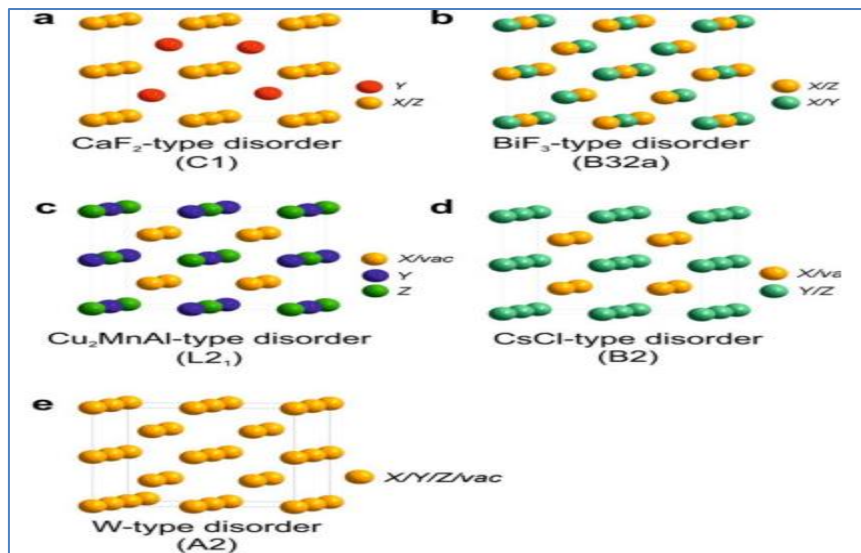


Figure.I.14 Overview of the most important types of disorder that can occur in the semi-Heusler structure: (a) CaF_2 -like disorder, (b) NaTi -like disorder, (c) Cu_2MnAl -like disorder, (d) CsCl -like disorder, and (e) tungsten-like disorder.

I.11. 2. Full-Heusler compounds

The properties of full-Heusler compounds are strongly dependent on the atomic order. Band structure calculations show that small amounts of disorder within the distribution of atoms at lattice sites cause noticeable changes in their electronic structure, and thus also in their properties. This structural disorder can affect the electrical structure as well as the magnetic and transport properties [55]. In full-Heuslers, disordered structures including structures L_{21} , Y , A_2 , DO_3 , and B_2 have been discovered. **Table I.3** summarizes the many potential structures for full-Heusler alloys based on the Inorganic Crystal Structure Database (ICSD), the Strukturberichte Data System (SB), and the Pearson Databases [56].

occupation of Site	Formula General	Structure type			Groupe d'espace
		ICSD	SB	Pearson	
X, X', Y, Z	XX'YZ	LiMgPdSn	Y	cF16	F-43m (N°. 216)
X=X', Y, Z	X ₂ YZ	Cu ₂ MnAl	L2 ₁	cF16	Fm-3m (N°. 225)
X, X'=Y, Z	XX' ₂ Z	CuHg ₂ Ti	X	cF16	F-43m (N°. 216)
X=X'=Y, Z	X ₃ Z	BiF ₃	DO ₃	cF16	Fm-3m (N°. 225)
X=X', Y=Z	X ₂ Y ₂	CsCl	B2	cP2	Pm-3m (N°. 221)
X=Y, X'=Z	X ₂ X' ₂	NaTl	B32a	cF16	Fd-3m (N°. 227)
X=X'=Y=Z	X ₄	W	A2	cI2	Im-3m (N°. 229)

Table.I. 3 The different structures of full-Heuslers compounds [48].

The transition from the most disordered structures to the ordered Heusler structures is shown in **Figure I.15** [57, 58]. When the arrangement of Y and Z atoms is uniform, positions 4a and 4b become equivalent, resulting in a replaced CsCl structure, also known as a B2-like disorder. On the other hand, a BiF₃ type disorder (space group Fm3m, n°216, DO3) occurs due to the dispersion of X and Y or X and Z. Other types of disorder, such as the NaTl-style structure, are rare. In this type of structure, one of the fcc sublattices is covered by X and the other by Y atoms. Depression B32a is another name for a type of condition (space group Fd-3m, #227). In the tungsten-like structure with a bcc lattice and decreased symmetry, all positions become equal, as opposed to these partial disorder phenomena. The various structures of Heusler compounds are listed in **Table I.3**, and the related general formula is connected to the site occupancy rate.

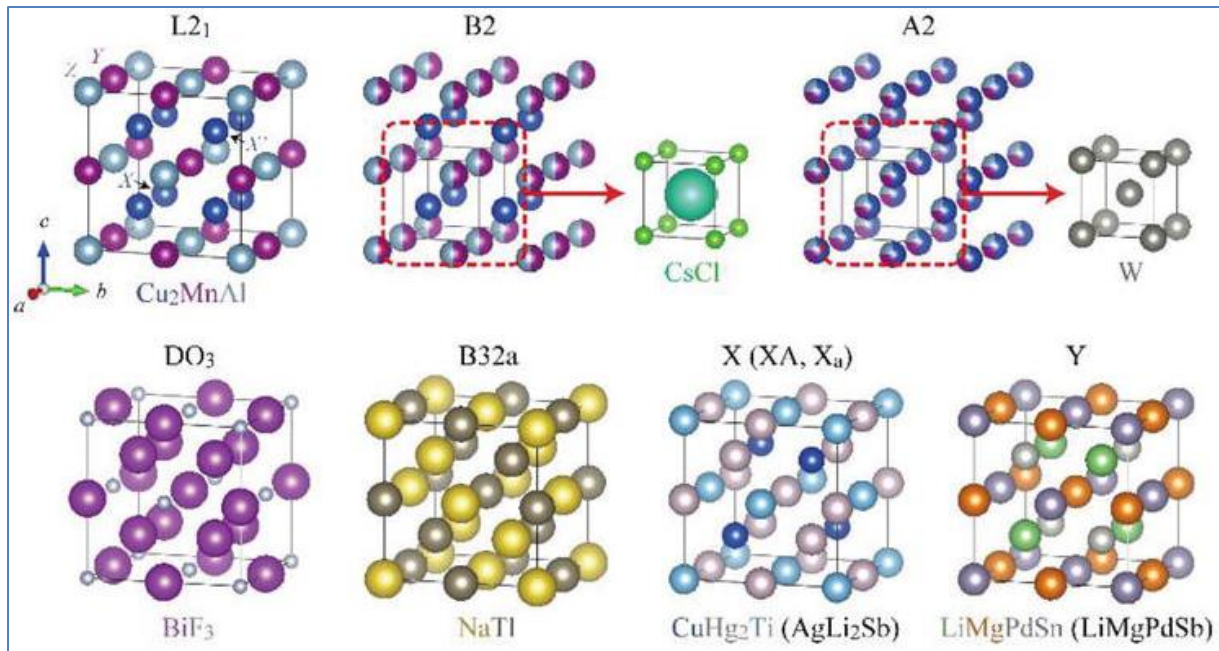


Figure I.15 Crystal structures of full-Heusler compounds corresponding to the various types of structures [58].

I.12. Magnetism and Heusler alloys

Friedrich Heusler discovered that the compound Cu_2MnAl exhibits ferromagnetism despite its constituent elements not being magnetic. However, it took thirty years to determine that the crystal structure of the compound was face-centered cubic [59, 60]. Unfortunately, in the following decades, the compound was largely forgotten, and only a few reports were published in the 1970s [58, 61].

In Heusler XYZ compounds, the magnetic sublattice is exhibited only by the atoms on the octahedral sites, as shown in **Figure I.16**. Among the Heusler compounds containing Re that are known in the literature, most of the semiconductor or metalloid systems exhibit antiferromagnetism and have a low Neel temperature [62]. Only a few ferromagnetic half-Heusler compounds have been described in the literature, such as NdNiSb and VCoSb [63].

In Heusler X_2YZ compounds, the two X atoms occupying the tetrahedral sites are responsible for the magnetic interaction between X atoms. This interaction leads to the formation of a second, more delocalized magnetic sub-lattice, as shown in **Figure I.16**. Due to their different magnetic properties, these compounds can exhibit various types of magnetic phenomena, such as half-metallic ferromagnetism and electric field phenomena.

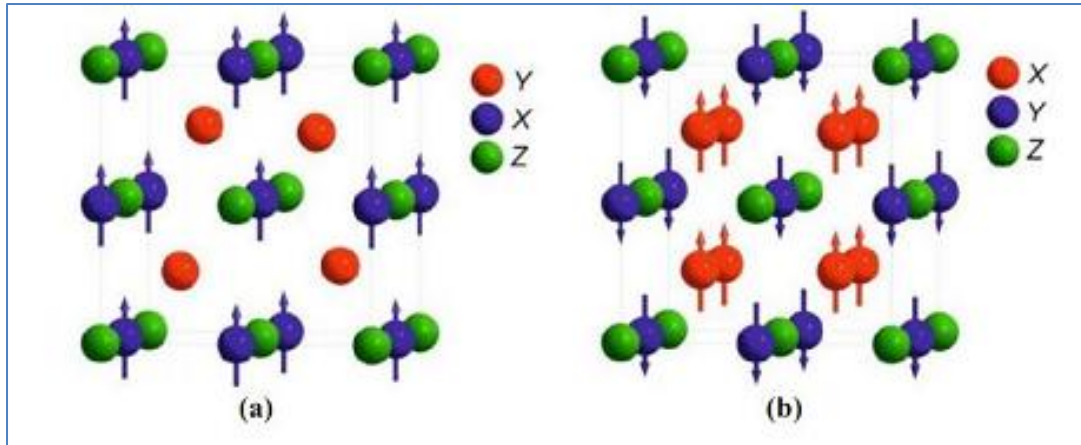


Figure.I. 16. (a) XYZ half-Heusler alloys with only one magnetic sub-lattice since only the atoms in the octahedral locations carry a localized magnetic moment. In (b) Heusler alloys of the X₂YZ type, we have two magnetic sub-lattices. There are two sub-lattices where we can find a ferromagnetic or antiferromagnetic coupling.

The term "half-metallicity" was first introduced by de Groot et al. [64] in their study of half-Heusler alloys, specifically NiMnSb. In conventional ferromagnetic materials, both majority spin (Up: $N_{\uparrow}(E_F)$) and minority spin (Down: $N_{\downarrow}(E_F)$) electrons have a density of states of $N(E_F)$ at the Fermi level. The spin polarization P , which measures the spin asymmetry, can be calculated using the equation [64]:

$$P = \frac{N_{\uparrow}(E_F) - N_{\downarrow}(E_F)}{N_{\uparrow}(E_F) + N_{\downarrow}(E_F)} \quad (\text{I.2})$$

Half-metallic materials, on the other hand, exhibit completely different conductive properties for minority and majority spins. They possess metallic properties for one spin direction (i.e., a non-zero density of states at the Fermi level) and semiconductor or even insulating properties for the other spin direction, resulting in a spin polarization rate of 100%. **Figure I.17** illustrates this phenomenon. Half-metallicity has been observed in Heusler cobalt-based alloys since the 1970s, including Co_2MnAl , Co_2MnSn , Co_2MnSi , Co_2MnGe [65], and Co_2FeSi [66].

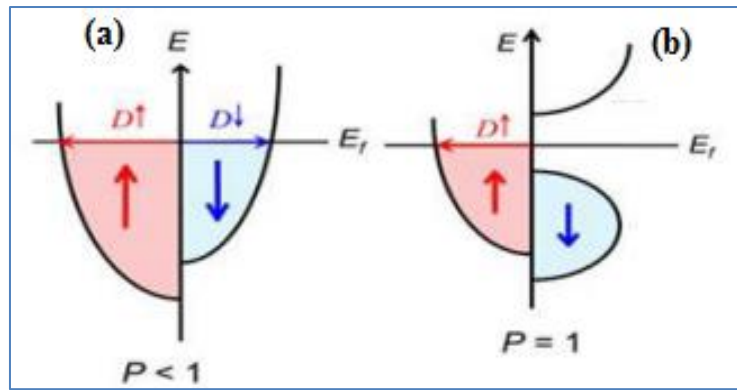


Figure.I.17 Band structure for (a) conventional ferromagnetic and (b) half-metallic material.

I.12.1. Ferromagnetism in half-metals

Heusler compounds are materials with a specific crystal structure that exhibits remarkable magnetic properties. One such property is semi-metallic ferromagnetism[13, 28], where the material behaves like a metal in one spin orientation but behaves like an insulator in the opposite spin orientation. This property is characterized by the density of states (DOS) of the material.

De Groot developed a classification system to differentiate between three different forms of semi-metallic ferromagnetism. **Figure I.18** shows the DOS of various materials:

- (a) A metal with a localized density of states at the Fermi level.
- (b) A half-metal with minor gap densities of states around the Fermi level.
- (c) A representation of a metal that takes into account the spin polarization of two states that are similar along the two spin directions.
- (d) The density of states of a ferromagnetic material in which the majority and minority states are offset from one another, which is explained by the formation of measurable magnetism.
- (e) The case of a ferromagnetic half-metal (HMF), which behaves like an insulator or a metal for the opposing spin direction. HMF materials exhibit 100% spin polarization, which makes them promising candidates for use in spintronics and optical devices.

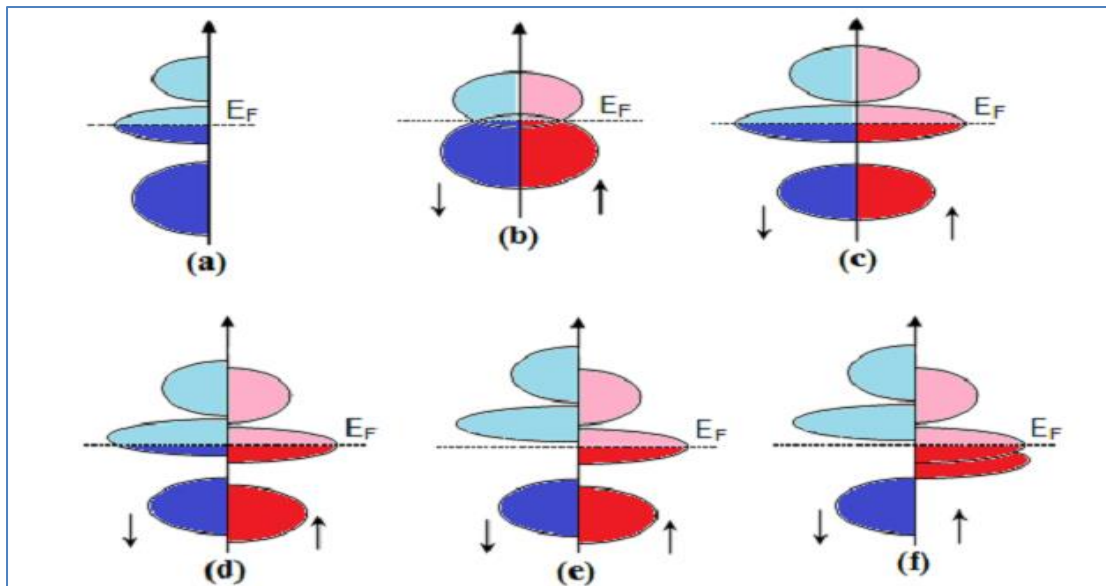


Figure.I.18 Schematic illustration of the density of states for: (a) metal, (b) half-metal, (c) a metal (spin-polarized), (d) ferromagnetic compound, (e) half-metallic ferromagnetic compound, and (f) half-metallic ferromagnetic compound. (↑) majority spin, (↓) minority spin.

I.12.2. The Slater–Pauling rule

After the discovery of Slater-Pauling, the magnetic moment of 3d elements and their binary alloys can be predicted or estimated through the average number of valence electrons (Z_t) per atom [67, 68]. Slater and Pauling established a curve that presents two zones based on $m(Z_t)$, the average number of valence electrons per atom. The first zone is the domain of weak valence electron concentrations ($Z_t \leq 8$) and localized magnetism, with bcc structures. The second zone is the domain of high concentrations of valence electrons ($Z_t \geq 8$) and itinerant magnetism, with fcc and hcp structures. In the middle of this curve lies iron with $Z_t = 8$, between localized and itinerant magnetism.

The Slater-Pauling curve for transition metals and some alloys is shown in Figure I.19. The region of this curve's localized magnetism, where Heusler alloys are found, is of interest. The magnetic moment per atom can be estimated using the equation [69] :

$$m \approx Z_t - 6 \quad (\text{I.3})$$

where the magnetic moment is simply the average number of valence electrons minus six.

For ferromagnetic half-metals, which have a gap in the minority densities of states at the Fermi level, the number of occupied minority states must be an integer, which is perfectly satisfied for the situation $m=Z_t-6$ [70, 71].

The Slater-Pauling rule is presented for half-Heusler XYZ alloys with three atoms per unit formula as:

$$m_{XYZ} = Z_t - 18 \tag{I.4}$$

The interaction between the magnetic moment and valence electron concentration in ferromagnetic alloys can be studied using the Slater-Pauling curve. The spin magnetic moments of Co₂-based Heusler compounds can be determined using the Slater-Pauling rule, which varies linearly with the number of valence electrons. These compounds can be found in regions of localized magnetism on the Slater-Pauling graph[71, 72], where the magnetic moment rises as the number of valence electrons decreases.

In the case of Heusler X₂YZ alloys, where there are four atoms per unit formula, the magnetic moment can be estimated using the equation

$$m_{X_2YZ} = Z_t - 24 \tag{I.5}$$

where Z_t is the number of valence electrons present in each unit cell containing the four atoms. For a half-metal compound in both cases (C_{1b} and L₂₁), the total magnetic moment must be an integer, as shown in **Figure I.20**.

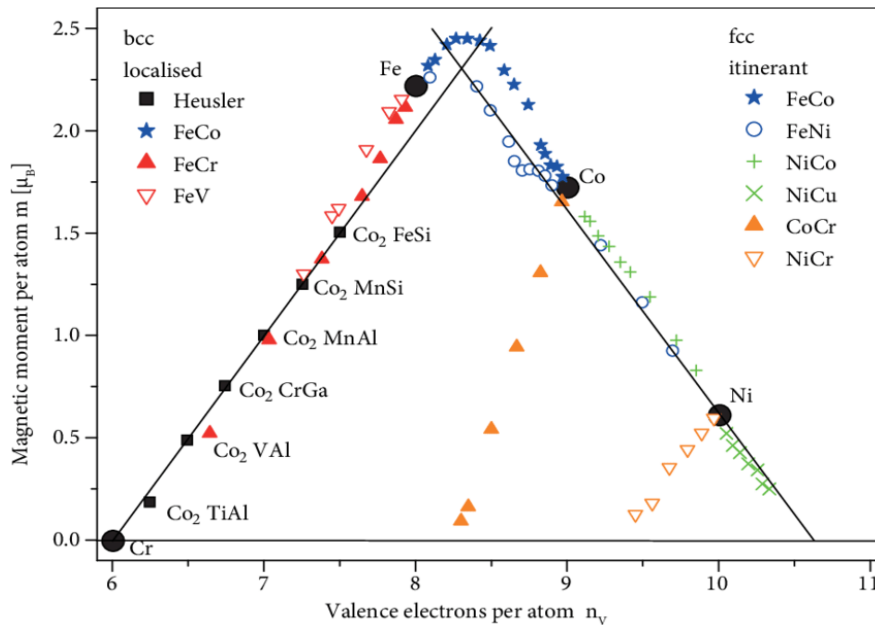


Figure.I.19 The Slater-Pauling curve for 3d transition metals and their alloys. Experimental values are given for some Co₂-based Heusler alloys for comparison. (A_{1-x}B_x alloys are abbreviated as AB) [73].

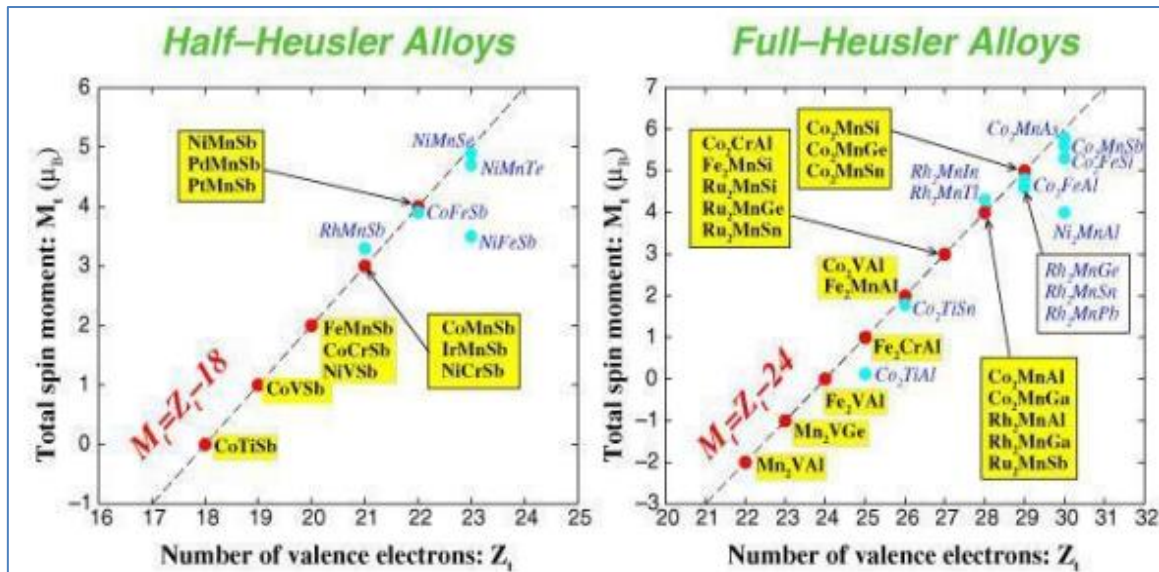


Figure.I.20 The Slater-Pauling curve, (a) the total magnetic moment of half-Heusler alloys (b) of Full-Heusler alloys as a function of the total number of valence electrons [74].

I.13. Origin of the gap in half-Heusler alloys

This strong hybridization leads to the formation of two separate electronic bands, one for majority spins and one for minority spins, with the Fermi level located in the gap between them. The majority-spin band is metallic and contributes to the electrical conductivity of the material, while the minority-spin band is insulating due to the gap at the Fermi level. As a result, half-metal materials exhibit 100% spin polarization, meaning that only one spin orientation is conducting while the other is insulating. This unique property makes them promising candidates for spintronic and magnetic storage applications, as they can potentially improve device efficiency and reduce energy consumption.

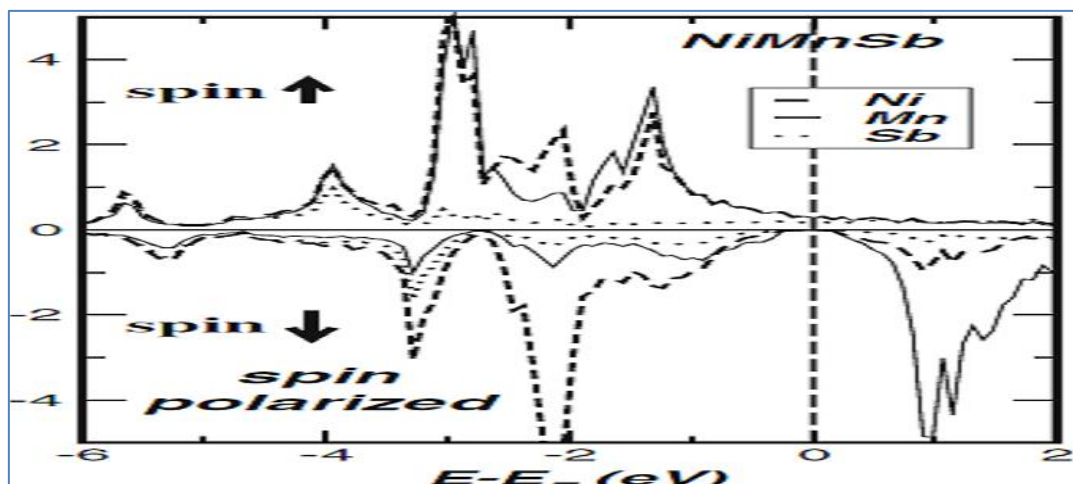
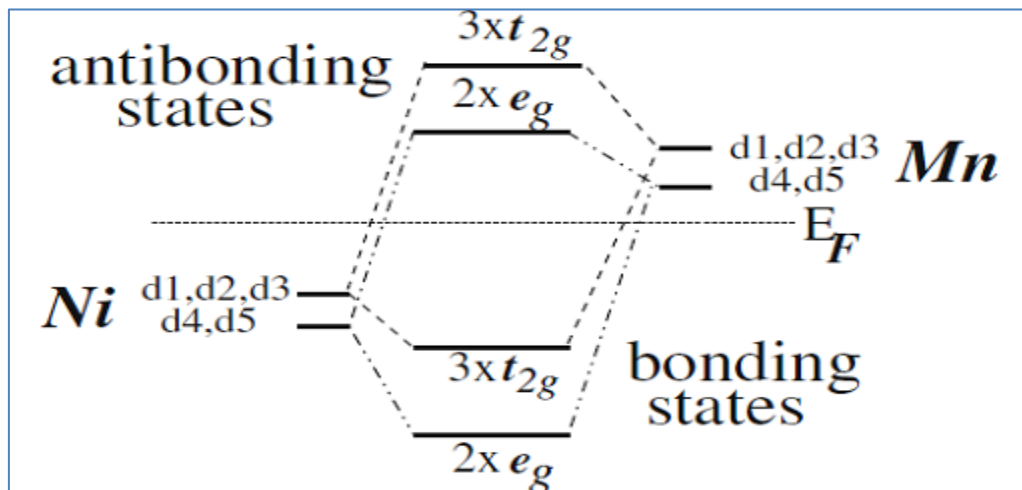


Figure.I.21 Density of states of the half HeuslerNiMnSb alloy [74].**Figure.I.22** Schematic illustration of the origin of the gap in the spin down channel in half-Heusler alloys [74].

To summarize, the origin of the gap in the density of states of half-metallic compounds like NiMnSb is due to the strong hybridization between the d states of high and low valence transition metals, which results in bonding and anti-bonding orbitals separated by a gap at the Fermi level. In the case of half-Heusler alloys, the gap is typically located between the maximum of the valence band at point Γ and the minimum of the conduction band at point X in the Brillouin zone. The gap in the spin-down channels is what makes these materials unique and useful for spintronics applications.

I.14. Applications

1. Spintronics: The half-metallic nature of Heusler alloys makes them excellent candidates for spintronics, a field that deals with the manipulation of electron spin in electronic devices [75, 76]. These alloys have the potential to be used as spin injectors and spin detectors in spintronic devices.

2. Magnetic memory: Due to their high Curie temperature [77], Heusler alloys are ideal for magnetic memory applications. The Curie temperature is the temperature above which a material loses its magnetic properties, and Heusler alloys can maintain their magnetic properties at high temperatures, making them suitable for use in high-temperature applications.

3. Thermoelectric applications: Heusler alloys have shown promising thermoelectric properties, which means they can convert heat into electricity and vice versa. This makes them suitable for use in thermoelectric generators and refrigeration devices.

4. Catalysis: Heusler alloys have been shown to exhibit excellent catalytic properties in various chemical reactions, including hydrogenation and dehydrogenation reactions. This makes them suitable for use as catalysts in the chemical industry.

5. Solar energy conversion: Heusler alloys have also been explored for use in solar energy conversion applications. They have shown promising properties for use in photovoltaic. Overall, the unique properties of Heusler alloys make them promising candidates for various technological applications, and their development and exploration continue to be an active area of research. devices and solar thermal energy conversion systems.

I.14.1. Spintronics

Spintronics is a rapidly evolving field that utilizes the spin of electrons to process, store, and transmit data. This field has revolutionized information and communication technology and has led to the development of new materials and devices. One of the key materials used in spintronics is Heusler alloys, which possess magnetic properties that make them ideal for spintronics applications. Co_2MnGe , in particular, has attracted attention due to its high Curie temperature and the magnetic moment [78], making it a promising candidate for spintronics applications. The development of new materials and devices based on Heusler alloys is essential for advancing the field of spintronics and meeting the demands of modern technology [79].

I.14.2. Tunnel Magnetoresistance (TMR)

Tunneling magnetoresistance (TMR) is a quantum mechanical effect where the resistance of a tunnel junction made of two ferromagnetic electrodes separated by an insulating barrier depends on the relative orientation of their magnetic moments. This effect was first observed by Julliere in 1975 [79]. The magnetic tunnel junction (MTJ), which is composed of two ferromagnetic electrodes separated by an insulator for a spin valve, is an example of a device that makes use of TMR. In an MTJ, electrons tunnel through the insulating barrier, and the resistance of the junction depends on the relative orientation of the magnetic moments of the electrodes. When the magnetic moments are parallel, the resistance is smaller than when they are antiparallel.

Heusler alloys are often used in magnetic tunnel junctions because of their high TMR values at room temperature. For example, Co_2FeAl and $\text{Co}_2\text{MnGe}/\text{MgO}/\text{Co}_{0.75}\text{Fe}_0$ are commonly used in magnetic tunnel junctions [80,81]. The TMR values can reach up to 200% at room temperature and 600% in some cases. In a recent study, an MTJ made with Co_2MnSi electrodes and a MgO barrier resulted in a TMR value of 182%. These high TMR values make Heusler alloys promising candidates for spintronic applications.

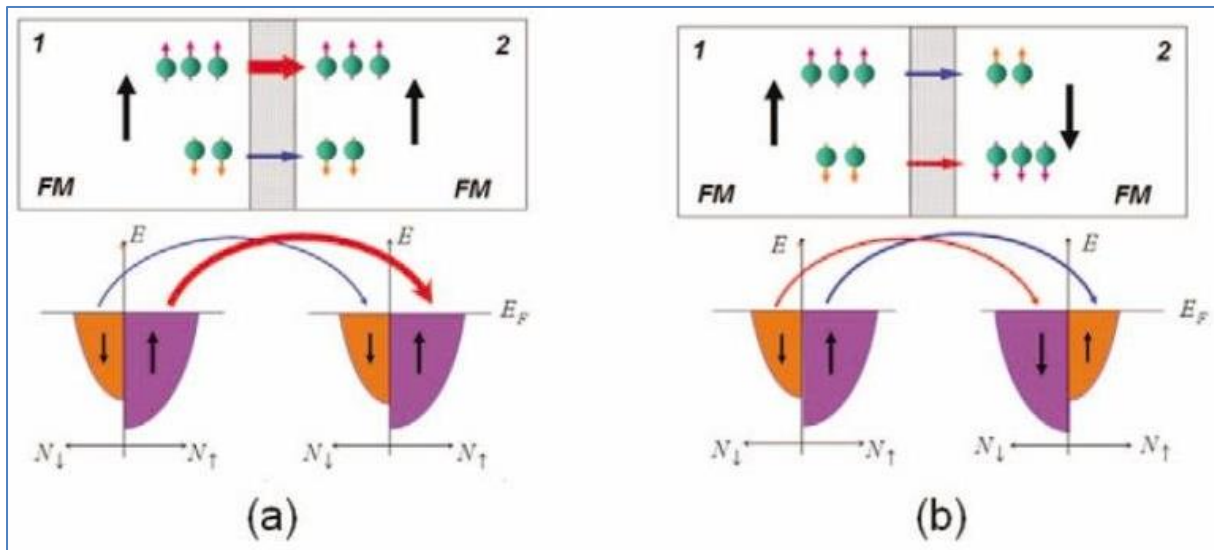


Figure.I.23 Schematic of the TMR effect in an MTJ. During tunneling, electron spin [82].

I.14.3. Giant Magnetoresistance (GMR)

Heusler alloys have been identified as excellent materials for use as magnetic electrodes in spin valves due to their high Curie temperatures and 100% spin polarization at the Fermi level. Spin valves are complex structures designed to increase the sensitivity of magnetoresistive components, and Co_2MnGe -based spin valves have been shown to be promising devices [83]. The GMR phenomenon is the basis for these devices, and it is a quantum mechanical effect that is exploited to measure changes in resistance due to changes in magnetic fields. Overall, Heusler alloys have shown great potential for use in spintronics applications, which aim to utilize the spin of electrons in addition to their electric charge for information processing and storage. The GMR working concept is depicted in **Figure .I.20**.

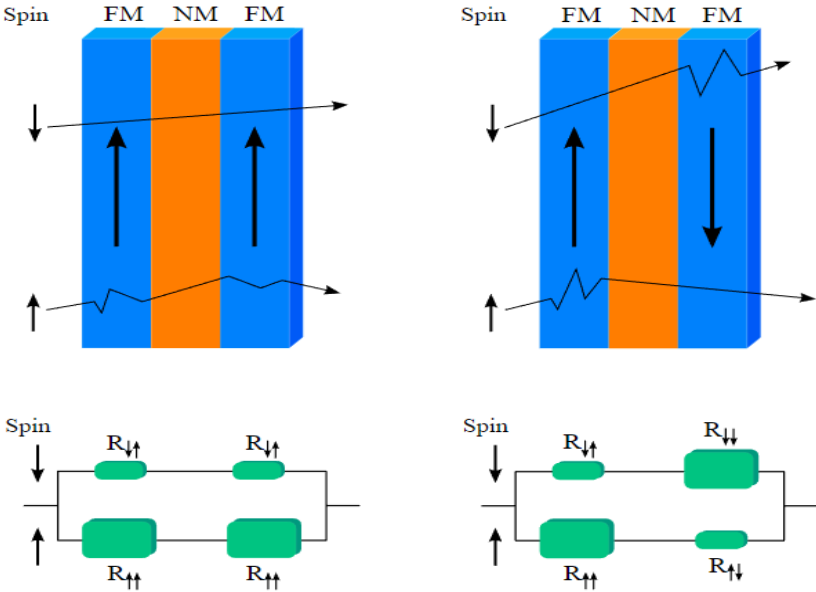


Figure.I. 24 Giant magnetoresistance junction (the two states, parallel and antiparallel) [84]

References

- [1]. Bradford, P., The aggregation of iron oxide nanoparticles in magnetic fields, 2012, University of Birmingham.
- [2]. Pérez, J.-P., et al., Electromagnétisme: fondements et applications avec 300 exercices et problèmes résolus 2002: Dunod.
- [3]. Duc, N., et al., Exchange interactions in rare earth—transition metal compounds. Journal of magnetism and magnetic materials, 1993. **124**(3): p. 305-311.
- [4]. Radwanski, R., J. Franse, and S. Sinnema, Effective anisotropy constants in rare earth-3d intermetallics. Journal of magnetism and magnetic materials, 1987. **70**(1-3): p. 313-315.
- [5]. Hu, J., et al., Determination of magnetocrystalline anisotropy constants from a hard magnetic material with polycrystalline structure. Solid state communications, 1994. **89**(9): p. 799-801.
- [6]. Li, Z. and A. Morrish, Negative exchange interactions and Curie temperatures for Sm₂Fe₁₇ and Sm₂Fe₁₇N_ys. Physical Review B, 1997. **55**(6): p. 3670.
- [7]. KAHAL, L., Etude des propriétés électroniques des matériaux ferromagnétiques, 2011, USTO.
- [8]. Chikazumi, S., Magnetism—from fundamentals to nanoscale dynamics. New York: Oxford University Press, 1999.
- [9]. Jonker, G. and J. Van Santen, Ferromagnetic compounds of manganese with perovskite structure. physica, 1950. **16**(3): p. 337-349.
- [10]. Goodenough, J.B., et al., Relationship between crystal symmetry and magnetic properties of ionic compounds containing Mn³⁺. Physical Review, 1961. **124**(2): p. 373.
- [11]. De Gennes, P.-G., Effects of double exchange in magnetic crystals. Physical Review, 1960. **118**(1): p. 141.
- [12]. Lakdja, A., et al., Ferromagnetism in the half-Heusler XC₃Ba compounds from first-principles calculations (X= C, Si, and Ge). Journal of alloys and compounds, 2013. **564**: p. 8-12.
- [13]. De Groot, R., et al., New class of materials: half-metallic ferromagnets. Physical Review Letters, 1983. **50**(25): p. 2024.
- [14]. De Groot, R., et al., Half-metallic ferromagnets and their magneto-optical properties. Journal of Applied Physics, 1984. **55**(6): p. 2151-2154.
- [15]. Schwarz, K., CrO₂ predicted as a half-metallic ferromagnet. Journal of Physics F: Metal Physics, 1986. **16**(9): p. L211.

- [16]. Hu, G. and Y. Suzuki, Negative Spin Polarization of Fe_3O_4 in Magnetite/Manganite-Based Junctions. *Physical Review Letters*, 2002. **89**(27): p. 276601.
- [17]. Bowen, M., et al., Nearly total spin polarization in $\text{La}_{2/3}\text{Sr}_{1/3}\text{MnO}_3$ from tunneling experiments. *Applied Physics Letters*, 2003. **82**(2): p. 233-235.
- [18]. Mazin, I., Robust half metallicity in $\text{Fe}_x\text{Co}_{1-x}\text{S}_2$. *Applied Physics Letters*, 2000. **77**(19): p. 3000-3002.
- [19]. Cheng, S., et al., Growth and magnetic properties of single crystal Co_2/MnX (X= Si, Ge) Heusler alloys. *IEEE transactions on magnetics*, 2001. **37**(4): p. 2176-2178.
- [20]. Park, M.S., S. Kwon, and B. Min, Half-metallic antiferromagnets in thiospinels. *Physical Review B*, 2001. **64**(10): p. 100403.
- [21]. Galanakis, I. and P. Mavropoulos, Zinc-blende compounds of transition elements with N, P, As, Sb, S, Se, and Te as half-metallic systems. *Physical Review B*, 2003. **67**(10): p. 104417.
- [22]. Xie, W.-H., et al., Half-metallic ferromagnetism and structural stability of zincblende phases of the transition-metal chalcogenides. *Physical review letters*, 2003. **91**(3): p. 037204.
- [23]. Heusler, F., Magnetic-chemical studies *Verh. Dtsch. Phys. Ges*, 1903. **5**: p. 219.
- [24]. Chadov, S., et al., Tunable multifunctional topological insulators in ternary Heusler compounds. *Nature materials*, 2010. **9**(7): p. 541-545.
- [25]. Bai, Z., et al. Data storage: review of Heusler compounds. in *Spin*. 2012. World Scientific.
- [26]. End, K., T. Ohoyama, and i.K. Ren, On the magnetic moment of Mn in aluminum Heusler alloy. *Journal of the Physical Society of Japan*, 1964. **19**(8): p. 1494-1495.
- [27]. Kohn, W., Electronic structure of matter-wave functions and density functionals. *Rev. Mod. Phys.*, 1999. **71**(5): p. 1253-1266.
- [28]. Kohn, W. and L.J. Sham, Self-consistent equations including exchange and correlation effects. *Physical review*, 1965. **140**(4A): p. A1133.
- [29]. Zunger, A. and A. Freeman, Ground-state electronic properties of diamond in the local-density formalism. *Physical Review B*, 1977. **15**(10): p. 5049.
- [30]. Schuster, H., et al., Investigations on neutron diffraction of the phases LiAlSi and LiAlGe . *Z. Naturforsch., B*, 1976. **31**(11): p. 1540-1541.
- [31]. Hohl, H., et al., Efficient dopants for ZrNiSn -based thermoelectric materials. *Journal of Physics: Condensed Matter*, 1999. **11**(7): p. 1697.

- [32]. Cheriet, A., S. Khenchoul, et al. (2021). "First-principles calculations to investigate structural, magnetic, electronic and elastic properties of full-Heusler alloys Co_2MB ($\text{M} = \text{V}, \text{Mn}$)." *Solid State Communications* **337**: 114426.
- [33]. Samant, M.G. and S.S. Parkin, *Magnetic tunnel junctions—Principles and applications*. Vacuum, 2004. **74**(3-4): p. 705-709.
- [34]. Mott, N., *A discussion of the transition metals on the basis of quantum mechanics*. Proceedings of the Physical Society (1926-1948), 1935. **47**(4): p. 571.
- [35]. Feng, Y., et al., The effect of disorder on electronic and magnetic properties of quaternary Heusler alloy CoFeMnSi with LiMgPbSb -type structure. *Journal of Magnetism and Magnetic Materials*, 2015. **378**: p. 7-15.
- [36]. Xiong, L., L. Yi, and G. Gao, Search for half-metallic magnets with large half-metallic gaps in the quaternary Heusler alloys CoFeTiZ and CoFeVZ ($\text{Z} = \text{Al}, \text{Ga}, \text{Si}, \text{Ge}, \text{As}, \text{Sb}$). *Journal of magnetism and magnetic materials*, 2014. **360**: p. 98-103.
- [37]. Halder, M., et al., Electronic, structural, and magnetic properties of the quaternary Heusler alloy NiCoMnZ ($\text{Z} = \text{Al}, \text{Ge}, \text{and Sn}$). *Journal of Magnetism and Magnetic Materials*, 2015. **377**: p. 220-225.
- [38]. Gao, Q., et al., A first-principle study on the properties of a new series of quaternary Heusler alloys CoFeScZ ($\text{Z} = \text{P}, \text{As}, \text{Sb}$). *Journal of Magnetism and Magnetic Materials*, 2015. **379**: p. 288-293.
- [39]. Anand, S., et al., Double half-heuslers. *Joule*, 2019. **3**(5): p. 1226-1238.
- [40]. Miura, Y., K. Nagao, and M. Shirai, Atomic disorder effects on half-metallicity of the full-Heusler alloys $\text{Co}_2(\text{Cr}_{1-x}\text{Fe}_x)\text{Al}$: A first-principles study. *Physical Review B*, 2004. **69**(14): p. 144413.
- [41]. Picozzi, S., A. Continenza, and A. Freeman, Role of structural defects on the half-metallic character of Co_2MnGe and Co_2MnSi Heusler alloys. *Physical Review B*, 2004. **69**(9): p. 094423.
- [42]. ABBASSA, H., *Contribution à l'étude des propriétés physico-chimiques des alliages d'Heusler*. Université de Mostaganem, Thèse, 2015.
- [43]. Casper, F., et al., Half-Heusler compounds: novel materials for energy and spintronic applications. *Semiconductor Science and Technology*, 2012. **27**(6): p. 063001.
- [44]. Graf, T., et al., Magnetic heusler compounds, in *Handbook of magnetic materials* 2013, Elsevier. p. 1-75.
- [45]. Tritt, T., *Recent trends in thermoelectric materials research: part three* 2001: Elsevier.
- [46]. Wang, C., et al., Heusler nanoparticles for spintronics and ferromagnetic shape memory alloys. *Journal of Vacuum Science & Technology B, Nanotechnology and*

- Microelectronics: Materials, Processing, Measurement, and Phenomena, 2014. **32**(2): p. 020802.
- [47]. Becke, A.D. and M.R. Roussel, Exchange holes in inhomogeneous systems: A coordinate-space model. *Physical Review A*, 1989. **39**(8): p. 3761.
- [48]. Graf, T., et al., Crystal structure of new Heusler compounds. *Zeitschrift für anorganische und allgemeine Chemie*, 2009. **635**(6-7): p. 976-981.
- [49]. Wollmann, L., et al., Magnetism in cubic manganese-rich Heusler compounds. *Physical Review B*, 2014. **90**(21): p. 214420.
- [50]. Pušelj, M. and Z. Ban, The crystal structure of TiCuHg_2 . *Croatica Chemica Acta*, 1969. **41**(2): p. 79-83.
- [51]. Surikov, V., V. Zhordochkin, and T.Y. Astakhova, Hyperfine fields in a new Heusler alloy Mn_2CoSn . *Hyperfine Interactions*, 1990. **59**: p. 469-472.
- [52]. Lakshmi, N., A. Pandey, and K. Venugopalan, Hyperfine field distributions in disordered Mn_2CoSn and Mn_2NiSn Heusler alloys. *Bulletin of Materials Science*, 2002. **25**: p. 309-313.
- [53]. Graf, T., C. Felser, and S.S. Parkin, Simple rules for the understanding of Heusler compounds. *Progress in solid state chemistry*, 2011. **39**(1): p. 1-50.
- [54]. Skovsen, I., et al., Multi-temperature synchrotron PXRD and physical properties study of half-Heusler TiCoSb . *Dalton transactions*, 2010. **39**(42): p. 10154-10159.
- [55]. Miura, Y., M. Shirai, and K. Nagao, Ab initio study on stability of half-metallic Co-based full-Heusler alloys. *Journal of applied physics*, 2006. **99**(8): p. 08J112.
- [56]. Picozzi, S., A. Continenza, and A. J. Freeman, Role of structural defects on the half-metallic character of heusler alloys and their junctions with Ge and GaAs, in *Half-metallic Alloys: Fundamentals and Applications 2006*, Springer. p. 41-66.
- [57]. Bacon, G. and J. Plant, Chemical ordering in Heusler alloys with the general formula A_2BC or ABC . *Journal of Physics F: Metal Physics*, 1971. **1**(4): p. 524.
- [58]. Webster, P., Magnetic and chemical order in Heusler alloys containing cobalt and manganese. *Journal of Physics and Chemistry of Solids*, 1971. **32**(6): p. 1221-1231.
- [59]. Heusler, O., Crystal structure and the iron magnetism of manganese-aluminium-copper alloys. *Ann. Phys*, 1934. **19**: p. 155-201.
- [60]. Bradley, A.J. and J. Rodgers, The crystal structure of the Heusler alloys. *Proceedings of the royal society of london. Series A, Containing Papers of a Mathematical and Physical Character*, 1934. **144**(852): p. 340-359.

- [61]. Brooks, J. and J. Williams, Magnetic Hyperfine Interactions in the Ferromagnetic Heusler-Type Alloy Co_2TiSn Studied by Means of the Mössbauer Effect in ^{119}Sn . *physica status solidi (a)*, 1975. **32**(2): p. 413-417.
- [62]. Gofryk, K., et al., Magnetic and transport properties of the rare-earth-based Heusler phases R Pd Z and $\text{R Pd}_2\text{Z}$ ($\text{Z} = \text{Sb, Bi}$). *Physical Review B*, 2005. **72**(9): p. 094409.
- [63]. Heyne, L., et al., Atomic and magnetic order in the weak ferromagnet CoVSb : is it a half-metallic ferromagnet? *Journal of Physics: Condensed Matter*, 2005. **17**(33): p. 4991.
- [64]. HEHN, M., F. MONTAIGNE, and A. SCHUHL, Magnétorésistance géante et électronique de spin. *Techniques de l'ingénieur. Electronique*, 2002. **3**(E2135): p. 1-15.
- [65]. Ishida, S., et al., Theoretical search for half-metallic films of Co_2MnZ ($\text{Z} = \text{Si, Ge}$). *Physica B: Condensed Matter*, 1998. **245**(1): p. 1-8.
- [66]. Inomata, K., et al., Structural and magnetic properties and tunnel magnetoresistance for $\text{Co}_2(\text{Cr, Fe})\text{Al}$ and Co_2FeSi full-Heusler alloys. *Journal of Physics D: Applied Physics*, 2006. **39**(5): p. 816.
- [67]. Fang, C.M., G. De Wijs, and R. De Groot, Spin-polarization in half-metals. *Journal of Applied Physics*, 2002. **91**(10): p. 8340-8344.
- [68]. Slater, J.C., The ferromagnetism of nickel. *Physical Review*, 1936. **49**(7): p. 537.
- [69]. Pauling, L., The nature of the interatomic forces in metals. *Physical Review*, 1938. **54**(11): p. 899.
- [70]. Balke, B., et al., Rational design of new materials for spintronics: Co_2FeZ ($\text{Z} = \text{Al, Ga, Si, Ge}$). *Science and Technology of advanced Materials*, 2008.
- [71]. Galanakis, I., Theory of Heusler and full-Heusler compounds, in *Heusler Alloys: Properties, Growth, Applications 2015*, Springer. p. 3-36.
- [72]. Kübler, J., Chap. 1, 2000, Oxford University Press Oxford, UK.
- [73]. Kübler, J., First principle theory of metallic magnetism. *Physica B+ C*, 1984. **127**(1-3): p. 257-263.
- [74]. Galanakis, I., P. Dederichs, and N. Papanikolaou, Slater-Pauling behavior and origin of the half-metallicity of the full-Heusler alloys. *Physical Review B*, 2002. **66**(17): p. 174429.
- [75]. Ishikawa, T., et al., Half-metallic electronic structure of Co_2MnSi electrodes in fully epitaxial $\text{Co}_2\text{MnSi}/\text{MgO}/\text{Co}_2\text{MnSi}$ magnetic tunnel junctions investigated by tunneling spectroscopy. *Journal of Applied Physics*, 2009. **105**(7): p. 07B110.

- [76]. Finley, J., et al., Spin-orbit torque switching in a nearly compensated Heusler ferrimagnet. *Advanced Materials*, 2019. **31**(2): p. 1805361.
- [77]. Prinz, G.A., Magnetoelectronics. *Science*, 1998. **282**(5394): p. 1660-1663.
- [78]. Munekata, H., et al., Diluted magnetic III-V semiconductors. *Physical Review Letters*, 1989. **63**(17): p. 1849.
- [79]. Ikeda, S., et al., Tunnel magnetoresistance of 604% at 300 K by suppression of Ta diffusion in Co Fe B/ Mg O/ Co Fe B pseudo-spin-valves annealed at high temperature. *Applied Physics Letters*, 2008. **93**(8): p. 082508.
- [80]. Wang, W., et al., Giant tunneling magnetoresistance up to 330% at room temperature in sputter deposited Co₂FeAl/MgO/CoFe magnetic tunnel junctions. *Applied Physics Letters*, 2009. **95**(18): p. 182502.
- [81]. Jin, Y., *Novel Half-Metallic and Spin-Gapless Heusler Compounds*, 2017, The University of Nebraska-Lincoln.
- [82]. Baibich, M.N., et al., Giant magnetoresistance of (001) Fe/(001) Cr magnetic superlattices. *Physical review letters*, 1988. **61**(21): p. 2472.
- [83]. Binasch, G., et al., Enhanced magnetoresistance in layered magnetic structures with antiferromagnetic interlayer exchange. *Physical review B*, 1989. **39**(7): p. 4828.
- [84]. Carey, M., et al., Co₂MnGe-based current-perpendicular-to-the-plane giant-magnetoresistance spin-valve sensors for recording head applications. *Journal of Applied Physics*, 2011. **109**(9): p. 093912.

CHAPTER II

OVERVIEW OF CALCLUATION METHOD

II.1. Introduction

Density functional theory (DFT) is a successful theory for calculating the electronic structure of atoms, molecules, and solids. In principle, DFT can deal with both molecules and large systems, and it allows for the exact study of the properties of an electronic system using only the density of the system. Moreover, the calculation of the density does not require knowledge of the many-body wave function, which greatly simplifies its calculation. DFT has its origins in the model developed by Llewellyn Thomas and Enrico Fermi in the late 1920s [1] and 30s [2]. Nevertheless, it was not until the mid-1960s and the contributions of Pierre Hohenberg, Walter Kohn, and Li Sham that the theoretical formalism on which the current method is based was established [3]. The density $n(\mathbf{r})$ can be calculated even for massive systems. The density depends only on three spatial variables and shows no sign of mass or radiation.

This chapter will briefly cover the fundamentals of DFT. The various degrees of approximation that were employed in its implementation will then be thoroughly discussed. Finally, we will provide a brief overview of the computing tools used in this study, such as Wien2K.

II.2. Schrödinger equation of a crystal

Schrödinger's equation is the fundamental equation of quantum physics. It describes the motion of electrons and nuclei much like Newton's laws in classical physics. A complete description of a quantum system with N electrons requires the calculation of the corresponding wave function. This can be obtained from the time-independent Schrödinger equation [4]. The Schrödinger equation can be written as follows.

$$\hat{H}\psi = E\psi \quad (\text{II.1})$$

Where:

\hat{H} : is the Hamiltonian operator of the studied system,

ψ : is the eigenfunction of the system,

E : represents the total energy associated with this same system.

Schrödinger's equation is the fundamental equation of quantum physics. It describes the motion of electrons and nuclei much like Newton's laws in classical physics. A complete description of a quantum system with N electrons requires the calculation of the corresponding wave function. This can be obtained from the time-independent Schrödinger equation [4]. The Schrödinger equation can be written as follows:

$$\hat{H} = \hat{T}_e + \hat{T}_n + V_{e-e} + \hat{V}_{n-n} + \hat{V}_{e-n} \quad (\text{II.2})$$

The operators that form the Hamiltonian can be written:

$$\hat{T}_e = -\frac{\hbar^2}{2m} \sum_i \nabla_i^2$$

$$\hat{T}_n = -\frac{\hbar^2}{2M_a} \sum_a \nabla_a^2$$

$$V_{e-e} = \frac{1}{2} \sum_{i \neq j} \frac{e^2}{4\pi\epsilon_0 |\vec{r}_i - \vec{r}_j|}$$

$$\hat{V}_{n-n} = \frac{1}{2} \sum_{I \neq J} \frac{Z_I Z_J e^2}{4\pi\epsilon_0 |\vec{R}_I - \vec{R}_J|}$$

$$\hat{V}_{e-n} = -\sum_{i,j} \frac{Z_j e^2}{4\pi\epsilon_0 |\vec{r}_i - \vec{R}_j|}$$

Where $\hbar = h/2\pi$ and h the Planck constant, m The mass of an electron is m, the mass of the nucleus is M, and the charge is Z. The Hamiltonian operator can be decomposed into two contributions, one kinetic and the other potential. The kinetic part is composed of terms \hat{T}_e for electrons and \hat{T}_n nuclei. The contribution to the potential energy is attractive between electrons and nuclei (\hat{V}_{e-n}), and repulsive between electrons-electrons (V_{e-e}) and nuclei-nuclei (\hat{V}_{n-n}).

In the same way, if we replace the Hamiltonian in equation (II.1), we will have:

$$[\hat{T}_e + \hat{T}_n + V_{e-e} + \hat{V}_{n-n} + \hat{V}_{e-n}] \psi = E \psi \quad (\text{II.3})$$

The objective of the majority of quantum chemical methods is to approximate and approximate the analytical solution of the non-relativistic Schrödinger equation independent of time. To devices, this job is completed in steps: The first approximation is the Born-Oppenheimer approximation, which is the point of departure from all other approaches.

II.3. Born–Oppenheimer approximation

The approximations used in quantum mechanics consider the electrons and nuclei of a given system as distinct objects, i.e., atoms and molecules, rather than their respective masses. The first historically significant approximations were made by Max Born (1882–1970) and Robert Oppenheimer (1904–1967) [5], who made contributions to the theory of relativity and the Manhattan Project, respectively. The Born-Oppenheimer approximation [6] is based on the fact that there is a significant mass difference between electrons and nuclei [7]. The movement of nuclei is considered negligible compared to that of electrons, so their kinetic energies are zero, and the potential energies of interaction between the nuclei become constant [8].

$$\hat{H}_e = \hat{T}_e + \hat{V}_e + \hat{V}_{e-n} \quad (\text{II.4})$$

With:

\hat{H}_e : Electronic Hamiltonian.

\hat{T}_e : The operator of the kinetic energy of the electrons.

\hat{V}_e : The repulsive energy operator between electrons.

\hat{V}_{e-n} : The operator of the nucleus-electron attraction energy.

Including the Schrödinger equation for electronics is:

$$\hat{H}_e \psi_e(r, R) = [\hat{T}_e + \hat{V}_e + \hat{V}_{e-n}] \psi_e(r, R) \quad (\text{II.5})$$

Schrödinger's equation can only be solved if all terms of the Hamiltonian involving nuclei are eliminated. This is why it is very often coupled with the Hartree approximation, which reduces the number of variables needed to describe the function.

II.4.Hartree approximation

A method for calculating wave functions and the approximative energy of ions and atoms was first developed by Douglas Hartree in 1927 [9]. The fundamental tenet of this approximation is to think of the electrons as fast movements of one another. Such a system's Hamiltonian is as follows [10]:

$$\hat{H} = \sum_{i=1}^N H_i \quad (\text{II.6})$$

Where: H_i is the single-electron Hamiltonian

$$\hat{H} = \sum_{i=1}^N H_i = \sum -\frac{1}{2} \nabla_i^2 + \hat{V}_{e-n}(\vec{r}_i, \vec{R}) + V_{e-e}(\vec{r}_i) \quad (\text{II.7})$$

The product of Hartree [10] presents the electronic wave function that allows solving this Hamiltonian which consists of a single-electron product [11].

$$\psi(\vec{r}_1, \vec{r}_2, \vec{r}_3, \dots, \vec{r}_n) = \psi(\vec{r}_1) \psi(\vec{r}_2) \dots \psi(\vec{r}_n) \quad (\text{II.8})$$

This approximation is based on the assumption of free electrons, which does not take into account the interactions between electrons and spin states. A significant advantage of this approach is that it proposes a self-consistent solution to the problem of the electronic system. However, it also has important limitations: The total Coulomb repulsion V_{e-e} of the electronic system is overestimated, and it is simple to solve but does not yield very accurate results. Additionally, the Pauli exclusion principle is not taken into account.

I.5.Hartree-Fock approximation

The Hartree-Fock theory is one of the simplest approximations for solving the many-body Hamiltonian [12]. It is an extension of the Hartree approximation that includes the permutation symmetry of the wave function, which leads to the exchange interaction. The Pauli exclusion principle states that the total wave function for a system must be antisymmetric under particle exchange. The wave function is given by a single Slater determinant [13] of N spin-orbitals:

$$(\vec{r}_1, \vec{r}_2, \dots, \vec{r}_n) = \frac{1}{\sqrt{n!}} \begin{vmatrix} \psi(\vec{r}_1) & \psi(\vec{r}_1) & \dots & \psi_N(\vec{r}_1) \\ \psi(\vec{r}_2) & \psi(\vec{r}_2) & \dots & \psi_N(\vec{r}_2) \\ \psi(\vec{r}_n) & \psi(\vec{r}_n) & \dots & \psi_N(\vec{r}_n) \end{vmatrix} \quad (\text{II.9})$$

$\psi_i(\vec{r}_i)$: is the mono-electron wave function, also known as the spin-orbital, that is dependent on the spatial coordinates and the spin of the electrons. $\frac{1}{\sqrt{n!}}$ is used to normalize data. The results from this approach are promising, particularly in molecular physics. Therefore, it is limited to systems containing a few electrons, such as tiny molecules. It is difficult to apply to the handling of extended systems like solids and ignores the impact of electronic correlations.

For larger molecules or solids, methods using Density Functional Theory (DFT) are much more effective. adapted.

I.6. Density Functional Theory

The DFT theory allows us to reformulate the many-body problem into a one-body problem in an effective field, taking into account all the interactions using electron density as a basis function. This theory is the result of two theorems developed by Hohenberg and Kohn [13] in 1964, which demonstrated the possibility of determining the properties of a system using electron density, and Kohn and Sham [3] in 1965, which turned DFT into a practical tool in quantum chemistry.

I.6.1. Hohenberg's and Kohn's theorems

The approach developed by Walter Kohn and Pierre Hohenberg was to reformulate the density functional theory proposed by Thomas and Fermi into an exact theory of a many-body system. The formulation, which applies to any system of interacting particles evolving in an external potential, is based on two fundamental theorems stated and demonstrated by Hohenberg and Kohn in their 1964 paper [14].

Theorem 1:

For a given exterior potential $V_{\text{ext}}(\mathbf{r})$, the total ground state energy E is a unique function of the particle density $\rho(\vec{r})$. This is used to establish a correspondence between the charge density of a system of N interacting particles in the ground state and the external potential of its nuclei, $U_{\text{ext}}(\mathbf{r})$. The total energy of the ground-state system is also unique in functional terms; that is,

$$E = E[\rho(\vec{r})] \quad (\text{II.10})$$

With:

$$E[\rho(\vec{r})] = F[\rho(\vec{r})] + \int \rho(\vec{r}) U_{ext}(\vec{r}) d\vec{r} \quad (\text{II. 11})$$

Where:

$F[\rho(\vec{r})]$: is a density functional.

$\int \rho(\vec{r}) U_{ext}(\vec{r}) d\vec{r}$: represents the nucleus-electron interaction.

$\rho(\vec{r})$ independent of external potential U_{ext}

$$F[\rho(\vec{r})] = T_e[\rho(\vec{r})] + U_{ee}[\rho(\vec{r})] = T_e[\rho(\vec{r})] + E_{Hartree}[\rho(\vec{r})] + E_{XC}[\rho(\vec{r})] \quad (\text{II. 12})$$

Where $T_e[\rho(\vec{r})]$ is the kinetic energy of the electronic system and $U_{ee}[\rho(\vec{r})]$ is the electron-electron interaction term that includes the Hartree energy $E_{Hartree}[\rho(\vec{r})]$ (the Coulomb electron-electron repulsion) and the exchange and correlation energy. $E_{XC}[\rho(\vec{r})]$ Expressions for kinetic energy $T_e[\rho(\vec{r})]$ and energy of exchange and correlation $E_{XC}[\rho(\vec{r})]$ are not known exactly.

Theorem 2:

The total energy functional of any multiparticle system has a minimum that corresponds to the ground state. Ground state particle density check:

$$E[\rho_0] = \min E[\rho] \quad (\text{II.13})$$

$$\left[\frac{\partial F[\rho(\vec{r})]}{\partial [\rho(\vec{r})]} \right]_{\rho(\vec{r})=\rho_0(\vec{r})} = 0 \quad (\text{II. 14})$$

The function $F[\rho(\vec{r})]$ is universal for any multi-particle system. If the function $F[\rho(\vec{r})]$ is known, then it will be relatively easy to use the variational principle to determine the total energy and electron density of the ground state for a given external potential. However, the Hohenberg and Kohn theorem does not indicate the form of $F[\rho(\vec{r})]$.

I.6.2.Kohn-Sham equations

The equations developed by Kohn and Sham in 1965 represent a significant step towards making DFT applicable[3]. They showed that it is possible to replace the real, interacting system with a fictitious, non-interacting system of N electrons moving in an effective potential $V_{eff}(\mathbf{r})$. Consequently, Hohenberg and Kohn's theorems apply to the non-interacting system in the same way as they do to the real system. To write the function in the form of a

set of coupled equations that can be solved, the notion of an effective potential is introduced, such that

$$V_{eff}[\rho(\mathbf{r})] = V_{ext} + \int \frac{\rho(\mathbf{r}')}{|\mathbf{r}-\mathbf{r}'|} d\mathbf{r}' + V_{xc}[\rho(\mathbf{r})] \quad (\text{II.15})$$

With

$V_H = \int \frac{\rho(\mathbf{r}')}{|\mathbf{r}-\mathbf{r}'|} d\mathbf{r}'$:is the Hartree potential.

$V_{xc}[\rho(\mathbf{r})]$: is the exchange and correlation potential given by:

$$V_{xc}[\rho(\mathbf{r})] = \frac{\partial E_{xc}[\rho(\mathbf{r})]}{\partial \rho(\mathbf{r})} \quad (\text{II.16})$$

In equation (II.17) , E_{xc} is The exchange-correlation energy that brings together everything unknown in the system, namely the effects of correlations due to the quantum nature of electrons. The second uses the effective potential in the N mono-Schrödinger equations to obtain:

$$\left[-\frac{1}{2} \nabla^2 + V_{eff}(\mathbf{r}) \right] \varphi_i(\mathbf{r}) = \varepsilon_i \varphi_i(\mathbf{r}) \quad (\text{II.17})$$

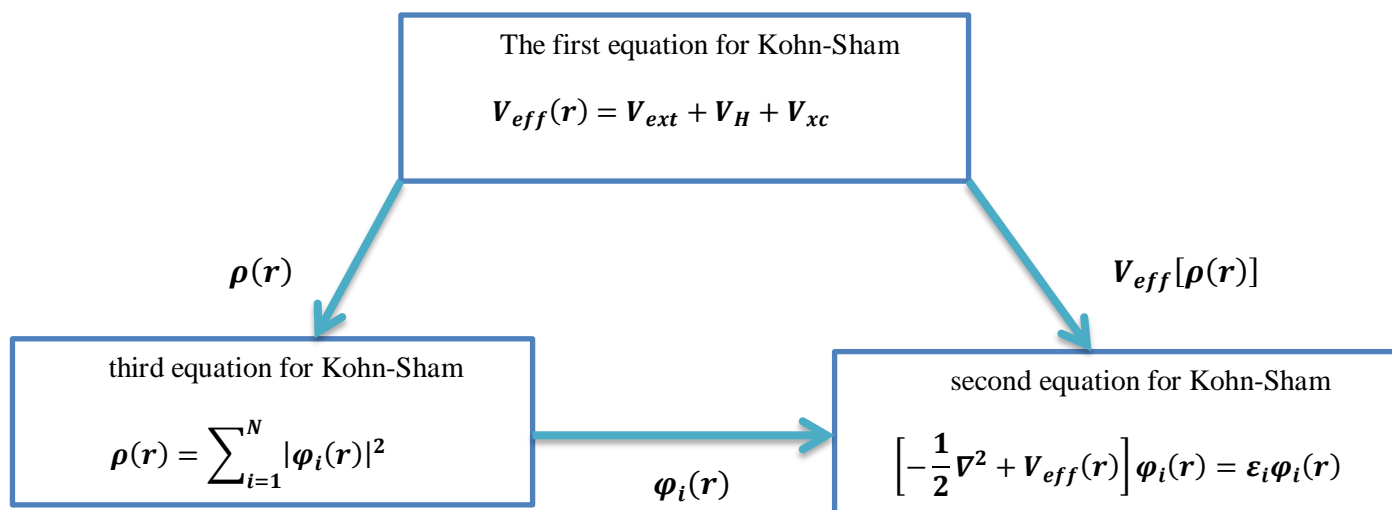
With:

$$V_{eff}(\mathbf{r}) = V_{ext} + V_H + V_{xc} \quad (\text{II.18})$$

The third indicates how to access the density from the N single-electron functions [15]:

$$\rho(\mathbf{r}) = \sum_{i=1}^N |\varphi_i(\mathbf{r})|^2 \quad (\text{II.19})$$

Let's summarize the interrelated Kohn Sham equations:



The exchange-correlation energy, \mathbf{E}_{xc} , represents the contribution to the total energy of a system that arises from the exchange and correlation interactions between the electrons. Unfortunately, the exact form of \mathbf{E}_{xc} is unknown, and this is where approximations are required. There are many proposed approximations for \mathbf{E}_{xc} , ranging from simple local density approximations to more sophisticated functionals that take into account the non-local nature of exchange and correlation effects. These approximations are often based on physical insights, empirical fitting to experimental data, or even machine learning techniques.

I.6.2.1. Solving Kohn-Sham equations

The self-consistent field (SCF) method is used to solve the Kohn-Sham equations and obtain the ground state electron density of a system. The process involves starting with an initial guess of the electron density, calculating the effective potential based on this density, and solving the Kohn-Sham equations to obtain a new set of orbitals and eigenvalues. The electron density is then updated based on the new orbitals, and the process is repeated until convergence is achieved. The SCF procedure can be repeated for different numbers of electrons to study the behavior of the system under different conditions.

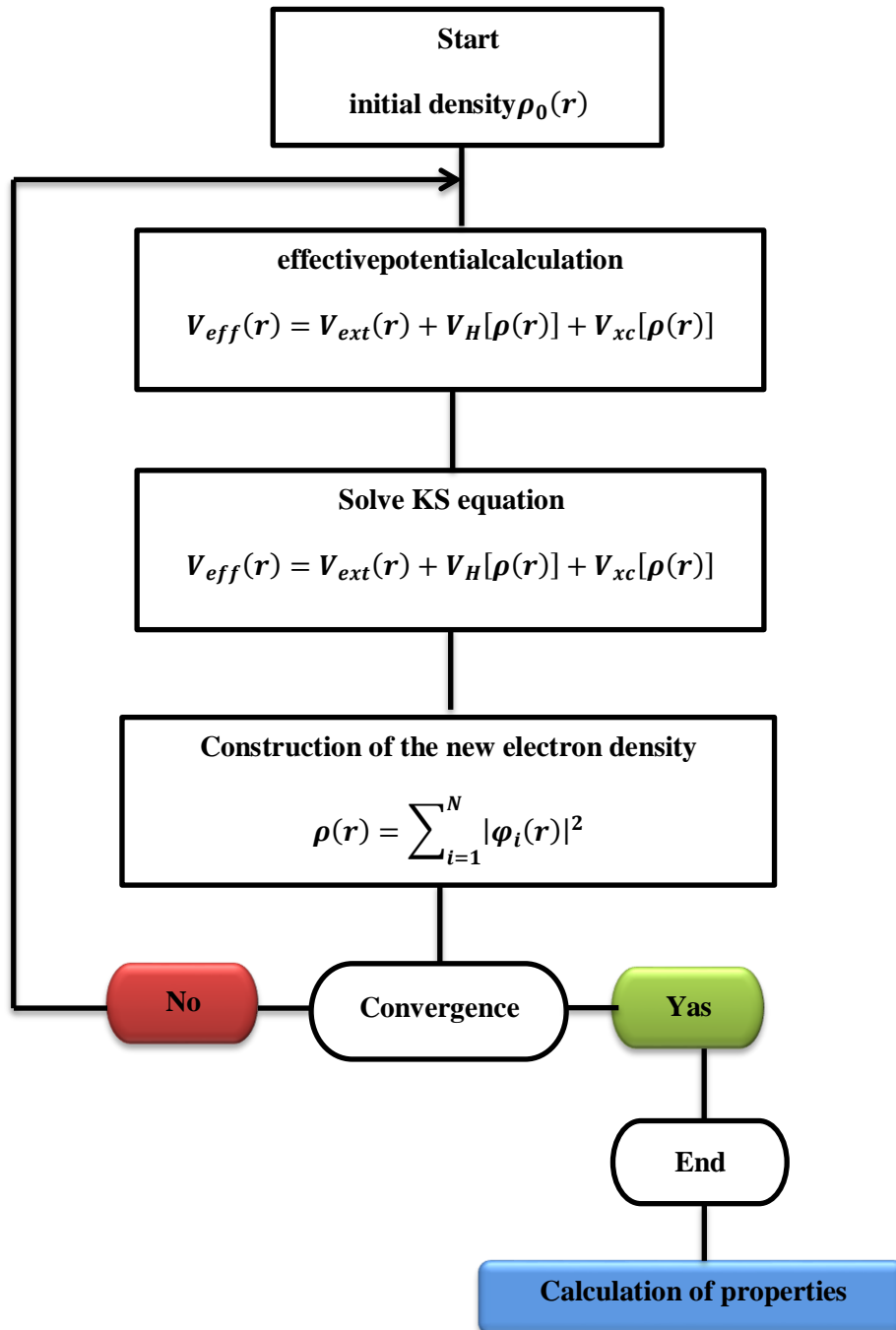


Figure.II.1 Self-consistent iteration process used to solve Kohn Sham equations.

I.6.3. Functionality of the exchange and correlation

The generalized gradient approximation (GGA) and the local density approximation (LDA) are two commonly used approximations to estimate the exchange-correlation energy in DFT calculations. The LDA assumes that the exchange-correlation energy density is a function of the local electron density only. On the other hand, the GGA includes not only the local

electron density but also its gradient in the estimation of the exchange-correlation energy density.

These approximations are still not exact, and errors can arise in the calculated properties of the system. Therefore, there is ongoing research to develop more accurate approximations for the exchange-correlation energy. The development of new functionals is an active area of research in computational chemistry and physics.

I.6.3.1. Local Density Approximation (LDA)

$$E_{xc}^{LDA}[\rho(\mathbf{r})] = \int \rho(\mathbf{r}) \epsilon_{xc}^{LDA}[\rho(\mathbf{r})] d^3r \quad (\text{II.20})$$

where E_{xc} is the exchange-correlation energy per electron in a uniform gas of electron density $\rho(\vec{r})$. This means that the exchange-correlation energy for a non-uniform electron density can be determined by integrating the uniform electron density over space, weighted by the local density at each point.

The LDA is a local approximation, meaning that the exchange-correlation energy is only dependent on the density at each point in space and not on the gradient or curvature of the density [16]. While the LDA has been successful in predicting many properties of atoms and molecules, it can still be inaccurate in some cases, particularly for systems with strongly correlated electrons or in systems with significant non-local effects.

where ϵ_{xc}^{LDA} is the exchange-correlation energy per particle in a homogeneous electron system (i.e. a uniform gas of interacting electrons) of density $\rho(\mathbf{r})$.

The exchange and correlation functions can be divided into an exchange-related term and a correlation-related term

$$\epsilon_{xc}^{LDA}[\rho(\mathbf{r})] = \epsilon_x^{LDA}[\rho(\mathbf{r})] + \epsilon_c^{LDA}[\rho(\mathbf{r})] \quad (\text{II.21})$$

According to the Dirac exchange functional [17], we write the term relating to the exchange:

$$\epsilon_x^{LDA}[\rho(\mathbf{r})] = -\frac{3}{4} \left(\frac{3\rho(\vec{r})}{\pi} \right)^{1/3} \quad (\text{II.22})$$

Many works on the parametrization of ϵ_{xc}^{LDA} have been published, including those by Vosko, Wilk, and Nusair, [18], Perdew and Zungar, and [19]. The local density approximation (LDA) produces good results for systems where the density varies slowly. It is less good for more

inhomogeneous density systems. For this reason, many developments have been made to improve the results obtained.

I.6.3.2. Generalized Gradient Approximation (GGA)

The exchange and correlation energy in GGA is written as a functional of the electron density and its gradient, expressed as $\epsilon_{xc}^{GGA}[\rho(\mathbf{r})|\nabla\rho(\mathbf{r})|]$. This approach takes into account the non-locality of the density, which makes it more accurate than the LDA. The GGA is more complex and computationally demanding than the LDA, but it has been shown to provide more accurate results for many systems. There are several types of GGA functionals, such as the Perdew-Burke-Ernzerhof (PBE) functional, which is one of the most widely used GGA functionals.

$$E_{xc}^{GGA}[\rho(\mathbf{r})] = \int \rho(\mathbf{r}) \epsilon_{xc}^{GGA}[\rho(\mathbf{r})|\nabla\rho(\mathbf{r})|] d^3r \quad (\text{II.23})$$

Where ϵ_{xc}^{GGA} represents the exchange-correlation energy per electron in an electron system inhomogeneous density in mutual interaction.

In the case where a spin polarization is taken into account, the energy of exchange and the correlation is described as follows:

$$E_{xc}^{GGA}[\rho_{\uparrow}(\mathbf{r}), \rho_{\downarrow}(\mathbf{r})] = \int \rho(\mathbf{r}) \epsilon_{xc}^{GGA}[\rho_{\uparrow}\rho_{\downarrow}\nabla\rho_{\uparrow}(\mathbf{r})\nabla\rho_{\downarrow}(\mathbf{r})] d^3r \quad (\text{II.24})$$

There are several forms of energy and the exchange and correlation potential, the most used is that of Perdew-Burke-Ernzerhof in 1996 [20] and WC-GGA introduced by Wu and Cohen [21].

I.6.3.3. The LDA and GGA approximations with spin polarization

In magnetic systems, the electron densities depend on the spin polarization, ρ_{\uparrow} which is different from ρ_{\downarrow} the exchange and correlation energies given by the following expression depending on whether gradient corrections are introduced or not [22, 23].

The local spin density approximation (LSDA)

$$E_{xc}^{LSDA}[\rho_{\uparrow}(\mathbf{r}), \rho_{\downarrow}(\mathbf{r})] = \int [\rho_{\uparrow}(\mathbf{r}), \rho_{\downarrow}(\mathbf{r})] \epsilon_{xc}^{LSDA}[\rho_{\uparrow}, \rho_{\downarrow}] d^3r \quad (\text{II.25})$$

and the generalized gradient approximation (GGA) [14]:

$$E_{xc}^{GGA}[\rho_{\uparrow}(\mathbf{r}), \rho_{\downarrow}(\mathbf{r})] = \int \rho(\mathbf{r}) \epsilon_{xc}^{GGA}[\rho_{\uparrow}\rho_{\downarrow}\nabla\rho_{\uparrow}(\mathbf{r})\nabla\rho_{\downarrow}(\mathbf{r})] d^3r \quad (\text{II.26})$$

ρ_{\uparrow} and ρ_{\downarrow} respectively symbolize the electronic densities of majority and minority spin.

I.6.3.4. The DFT + U approximation (L(S)DA+U and GGA+U)

The structures of strongly correlated systems [24] contain transition metals or rare earth ions. The L(S)DA and GGA approaches are incapable of accurately describing correlated systems. So to improve the results, an attempt was made by Dudarev et al. [25] called DFT +U (LSDA+U, GGA+U). The fundamental principle of this approximation is to add the additional term U to the LSDA or GGA potential for each d and f orbit in order to obtain the correct gap and magnetic properties for magnetic materials.

DFT+U introduces an energy correction to the standard functional DFT given by:

$$E^{DFT+U} = E^{DFT} + E_{Hub} - E_{dc} \quad (\text{II.27})$$

With:

E^{DFT} : represents the energy contribution of the standard DFT (LSDA or GGA),

E_{Hub} : is a correction of the electron-electron interaction energy.

E_{dc} is a double-counted term that corrects for contributions to the total energy included in both E_{Hub} and E_{dc} .

Evaluating energy with (II.27) requires expressions for E_{Hub} and E_{dc} . [26] used the Mott-Hubbard Hamiltonian to calculate the energy of the DFT+U function in electron spin polarization. After subtracting the terms counted twice from the energy given by the classical DFT method, the energy of this functional is obtained.

$$E^{DFT+U} = E^{DFT} + \sum_{m,\sigma} \frac{(U-J)}{2} (n_{m,\sigma} - n_{m,\sigma}^2) \quad (\text{II.28})$$

Where $n_{m,\sigma}$ is the operator that gives the number of electrons occupying an orbital of the magnetic quantum number m and spin σ at a particular site. U is the spherically averaged Hubbard parameter, which describes the energy cost of placing an extra electron at a particular site. The screened exchange energy is represented by.

$$U = E(F^{n+1}) + E(F^{n-1}) - 2E(F^n) \quad (\text{II.29})$$

U depends on the spatial extension of the wave functions and screening. The effective Coulomb exchange interaction, $U_{\text{eff}} = U - J$, was used here for the calculation, where U is the Coulomb-energetic cost of placing two electrons at the same site, and J is an approximation of

the Stoner exchange parameter. The key to performing an accurate DFT+U calculation lies in selecting a suitable value for U_{eff} .

1.6.3.5. The modified Becke-Johnson potential (mBJ)

The exchange potential, which was initially put out by Becke and Johnson [27], has been updated by Tran and Blaha. The MBJ "modified Becke Johnson Potential" is what is being described (also known as the TB potential, Tran-Blaha)[28]. It has been incorporated into the most recent Wien2k code version. The LDA and GGA potentials reproduce the band structure of metallic systems relatively well, but they fail to procreate the gap energy in semiconductors. Tran and Blaha introduced a simple modification of the Becke and Johnson potential and obtained good agreement with other more expensive approaches. The modified mBJ potential has the following form [29]:

$$V_{x,\sigma}^{\text{mBJ}} = cV_{x,\sigma}^{\text{mBJ}}(\vec{r}) + (3c - 2) \frac{1}{\pi} \sqrt{\frac{5}{12}} \sqrt{\frac{2t_{\sigma}(\vec{r})}{\rho_{\sigma}(\vec{r})}} \quad (\text{II.30})$$

$V_{x,\sigma}^{\text{mBJ}}$ is the semi-local Becke-Roussel potential (BR) [30], which was proposed to model the Coulomb potential created by the exchange holes, it is defined as follows:

$$V_{x,\sigma}^{\text{mBJ}}(\vec{r}) = -\frac{1}{b_{\sigma}(\vec{r})} \left(1 - e^{-x_{\sigma}(\vec{r})} - \frac{1}{2} x_{\sigma}(\vec{r}) e^{-x_{\sigma}(\vec{r})} \right) \quad (\text{II.31})$$

The function $x_{\sigma}(\vec{r})$ can be calculated from the following nonlinear equation:

The function $x_{\sigma}(\vec{r})$ can be calculated from the following nonlinear equation:

$$\frac{x_{\sigma}(\vec{r}) e^{-\frac{2x_{\sigma}(\vec{r})}{3}}}{x_{\sigma}(\vec{r}) - 2} = \frac{12}{3} \pi^{2/3} \frac{\rho_{\sigma}^{5/3}(\vec{r})}{\left(\nabla^2 \rho_{\sigma}(\vec{r}) - \left(4t_{\sigma}(\vec{r}) - \frac{|\nabla \rho_{\sigma}(\vec{r})|^2}{2\rho_{\sigma}(\vec{r})} \right) \right)} \quad (\text{II.32})$$

$t_{\sigma}(\vec{r})$ is the kinetic energy density, given by:

$$t_{\sigma}(\vec{r}) = \frac{1}{2} \sum_{i=1}^{N_{\sigma}} \nabla \psi_{i,\sigma}^* \nabla \psi_{i,\sigma} \quad (\text{II.33})$$

As well as the term $b_{\sigma}(\vec{r})$ was calculated using the following relationship:

$$b_{\sigma}(\vec{r}) = \left(\frac{x_{\sigma}^3(\vec{r}) e^{-x_{\sigma}(\vec{r})}}{8\pi \rho_{\sigma}(\vec{r})} \right)^{1/3} \quad (\text{II.34})$$

In equation (II.34) it is a parameter that depends linearly on the ratio $\frac{\nabla\rho_{\sigma}(\vec{r})}{\rho_{\sigma}(\vec{r})}$, it is written in the form:

$$c = \alpha + \beta \left(\frac{1}{\Omega} \int \frac{\nabla\rho_{\sigma}(\vec{r})}{\rho_{\sigma}(\vec{r})} d\vec{r} \right)^{1/2} \quad (\text{II.35})$$

α and β are adjustable parameters and Ω is the unit cell volume.

I.7. Calculation Methods

These methods you mentioned are all different computational approaches to solve the Kohn-Sham equations in DFT calculations. LCAO [31, 32] (linear combination of atomic orbitals) is a basis set approach that approximates the wavefunction as a linear combination of atomic orbitals. It is often used to describe the electronic structure of molecules and solids containing transition metals.

On the other hand, OPW (orthogonalized plane waves) [32, 33] is a basis set approach that uses a set of orthogonalized plane waves as a basis set to expand the wavefunction. It is well-suited for simple metals where the conduction bands are mainly composed of s and p orbitals.

KKR (Korringa-Kohn-Rostoker) [34, 35] is a method that uses Green's functions to solve the Kohn-Sham equations. It is well-suited for calculating the electronic structure of complex materials, such as alloys and surfaces.

APW (augmented plane wave) [36] is another basis set approach that expands the wavefunction in a set of plane waves and local orbitals. It is often used to describe the electronic structure of semiconductors and insulators.

LAPW (linearized augmented plane wave) and LMTO (linearized muffin-tin orbitals) [37] are two linearized techniques developed by Andersen. They provide significant computational time savings and are widely used to study the electronic structure of materials.

I.7.1. The augmented plane wave (APW) method

The Muffin-Tin approximation was introduced by Slater in 1937 when he created the novel APW (Augmented Plane Wave) approach [36], in which he offered a radial step to represent the crystal potential. This approximation predicts that the unit cell will be split into two categories of regions:

1) "Muffin-tin" spheres with a radius of r_0 that are centered on each atom and do not overlap (Region I).

2) An area of interstitial tissue separating the remaining space from the spheres see **Figure II.2**. (Region II).

which uses the following two appropriate base categories:

- ❖ In the "muffin-tin" atomic spheric region (region I), there are radial functions multiplied by spherical harmonics
- ❖ In (region II), there are plane waves for the interstitial region.

The functions of waves, which are denoted by the following notation, define the two spherical and interstellar regions:

$$\phi(r) = \begin{cases} \sum_{l m} A_{l m} U_l(r) Y_{l m}(r) & r < r_0 \\ \frac{1}{\sqrt{\Omega}} \sum_G C_G e^{i(K+G)r} & r > r_0 \end{cases} \quad (\text{II.36})$$

Represent the radius of the muffin-tin sphere.

Ω : is the volume of the elementary cell.

G : is the reciprocal lattice vector.

C_G and $A_{l m}$ are the coefficients of development in spherical harmonics $Y_{l m}$.

U_l : The regular solution of the following equation [38]:

$$\left\{ -\frac{d^2}{dr^2} + \frac{l(l+1)}{r^2} + V(r) - E_l \right\} r U_l(r) = 0 \quad (\text{II.37})$$

Where E_l : energy parameter.

$V(r)$: The spherical component of the potential in the sphere.

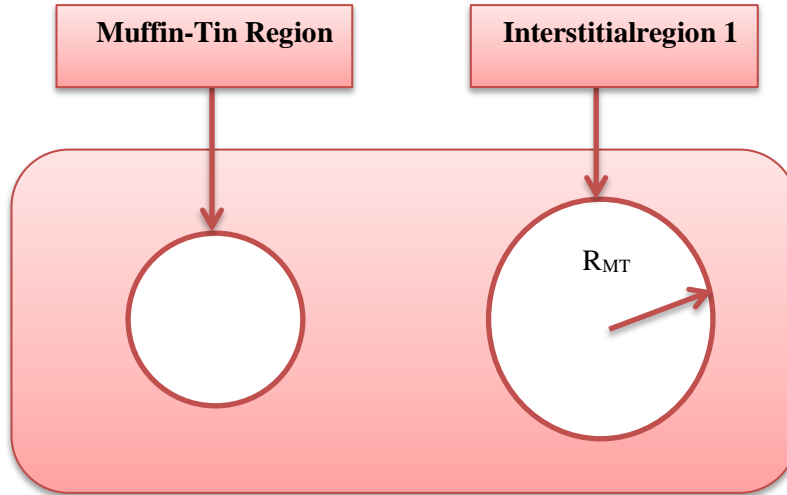


Figure.II.2 Representation of Muffin-Tin “MT” potential. Diagram of the distribution of the unit cell in the atomic sphere and in the interstitial region.

The radial functions defined by (II.38) are orthogonal to any proper state of the core. This orthogonality disappears at the limit of the sphere as shown by the Schrödinger equation

next :

$$(E_1 - E_2)rU_1U_2 = U_2 \frac{d^2rU_1}{dr^2} - U_1 \frac{d^2rU_2}{dr^2} \quad (\text{II.38})$$

With U_1 and U_2 are the radial solutions at different energies E_1 and E_2 respectively.

Slater introduces the muffin-tin (MT) approximation to justify the particular choice of these functions [39]. Presenting plane waves as solutions of Schrödinger's equation is a constant potential.

The representations defined in the expressions (II.36) and (II.37) are continued on the limits of the spheres MT, which is necessary. Of this fact, the coefficients must be defined according to the coefficient of the plane waves existing in the interstitial regions where the latter is expressed as follows:

$$A_{lm} = \frac{4\pi i^l}{\sqrt{\Omega u_l(R)}} \sum_G C_G J_l(|K + g|R) Y_{lm}^*(K + G) \quad (\text{II.39})$$

With

J_l : the Bessel function and the origin is taken at the center of the sphere.

R : is the radius of the sphere MT.

In this method (APW), the plane waves and the energy parameters are called the variational coefficients, where coefficients are determined from these two coefficients, and on the other side, the individual functions indicated by \mathbf{G} also become compatible with the radial functions in the spheres, where one can then obtain augmented plane waves (APW). The major problem caused by this method is the discontinuity of the function $\varphi_{\mathbf{G}}^K(\vec{r}, \mathbf{E})$ on the surface of the sphere MT. To ensure continuity in this limit, the coefficients A_{lm} must be expanded as a function of the coefficients $C_{\mathbf{G}}$. In this expansion, if the radial part $u_l^{\sigma}(\mathbf{r}, \mathbf{E})$ vanishes for a value of E , there will be no continuity. To address this, several modifications to the method [37, 39, 40] have been proposed: the linearized augmented plane wave method (LAPW: linearized APW), the LAPW+ method (LAPW+lo), and the full potential LAPW method (FP-LAPW: full potential LAPW). We will see these methods later.

1.7.2. Full Potential Linearized Augmented Plane Wave Method (FP-LAPW)

Anderson first developed the linearized augmented plane wave (LAPW) method in 1975 [40-42]. is a development of Slater's APW method and offers one of the most efficient foundations for calculations using crystalline solids. The basis functions inside the Muffin-Tin sphere in the Linearized Augmented Plane Wave (LAPW) method are a combination of linear functions of the radial functions $U_l(\mathbf{r})$ and $Y_{lm}(\mathbf{r})$ and their derivatives with respect to the energy $U_l(\mathbf{r})$ and $Y_{lm}(\mathbf{r})$ [43], and the functions $U_l(\mathbf{r})$ and $Y_{lm}(\mathbf{r})$ must meet the following requirements:

$$\left\{ -\frac{d^2}{dr^2} + \frac{l(l+1)}{r^2} + V(\mathbf{r}) - E_l \right\} r \dot{U}_l(\mathbf{r}, E_l) = r U_l(\mathbf{r}, E_l) \quad (\text{II.40})$$

In a non-relativistic situation, the radial functions and their derivatives ensure continuity with the plane waves coming from outside on the surface of the MT sphere. As a result, the wave functions improve the FP-LAPW method's fundamental functions (LAPW):

$$\psi(\mathbf{r}) = \begin{cases} \frac{1}{\Omega^2} \sum_{\mathbf{G}} C_{\mathbf{G}} e^{i(\mathbf{G}+\mathbf{K})\mathbf{r}} & r > R_a \\ \sum_{lm} (A_{lm} U_l(\mathbf{r}) + B_{lm} \dot{U}_l) Y_{lm} & r < R_a \end{cases} \quad (\text{II.41})$$

The coefficients B_{lm} are equivalent to the function E_l and share the same kind of A_{lm} . In general, if U_l is equal to zero at the surface of the sphere, its derivative \dot{U}_l will not be zero. As

a result, the problem of continuity at the surface of the MT sphere that was previously reported in the APW method will not be solved by this method.

1.7.2.1. Multiple energy windows

- The FP-LAPW problem[37] involves doing two independent LAPW computations with the same potential as illustrated in **Figure II.3**.
- The method that divides the energy range into windows, each of which corresponds to energy E_l , is the one that is most often used to deal with the semi-core problem. In this treatment using windows, the states of valence and semi-Core are differentiated, and a set E_l is selected for each window to process the appropriate forms.
- The FP-LAPW approach to quantum physics is based on the theory of semi-core states, which are states where there are U_l and \dot{U}_l functions parallel to any suitable condition of the heart and, in particular, to those located on the surface of the sphere. But they often do not satisfy this condition unless there are "ghost" bands between them and the valence state.

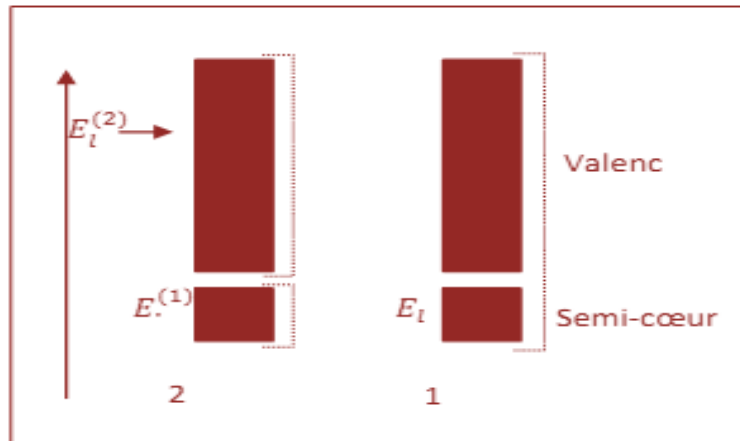


Figure.II.3 Multiple energy windows

Local orbitals are formed by modifying the orbitals of its base to avoid the use of several windows by using the third category of basic functions. The principle is to process all the bands from a single energy window (proposed by Singh in 1991) [44]. These orbitals denoted "LO," are the result of a linear combination of two radial functions corresponding to two different energies and the derivative with respect to the energy of one of these functions:

$$\varphi = \begin{cases} 0 & r > R_a \\ [A_{lm}(r, E_l) + B_{lm}\dot{U}_l(r, E_l) + C_{lm}(r, E_{LO})]Y_{ml} & r < R_a \end{cases} \quad (\text{II. 42})$$

Where: C_{lm} are its coefficients having the same nature of coefficients A_{lm} and B_{lm} .

I.8. The WIEN2k Code

Step 1: Structural Optimization - The WIEN2k code first performs a structural optimization of the crystal unit cell [45,46]. The user specifies the crystal structure in terms of lattice vectors and atomic positions, and the code uses various optimization techniques to minimize the total energy of the system.

Step 2: Electronic Band Structure Calculation - After the optimized structure is obtained, the code performs an electronic band structure calculation using the FP-LAPW method. The code solves the Kohn-Sham equations self-consistently to obtain the electronic density and energy of the system.

Step 3: Properties Calculation - Finally, the code calculates various physical properties of the system, such as the density of states, magnetic moments, and charge density. These properties are calculated using the electronic density and energy obtained in step 2.

The WIEN2k code provides a user-friendly interface for carrying out these calculations, and it is widely used in the materials science community.

I.8.1. Code initialization

Additionally, there are other auxiliary programs that can be used for specific purposes, such as generating starting magnetic configurations (MSTART), calculating the charge density of a supercell (SUPER), and creating an initial potential file (VPOTENTIAL), among others.

Once the geometry and starting densities have been defined, the main calculation is performed in three steps:

1. SCF (Self-Consistent Field) cycle: The SCF cycle starts by assuming an initial potential, which is used to calculate the electron density using the Kohn-Sham equations. This electron density is then used to recalculate the potential, which is then used to obtain a new electron density. This process is iterated until self-consistency is achieved, i.e., the potential and the electron density no longer change significantly from one iteration to the next.
2. Band structure calculation: Once the self-consistent electron density has been obtained, the program calculates the eigenvalues and eigenvectors of the Kohn-Sham

Hamiltonian in the irreducible part of the Brillouin zone. This information is used to calculate the band structure and the density of states.

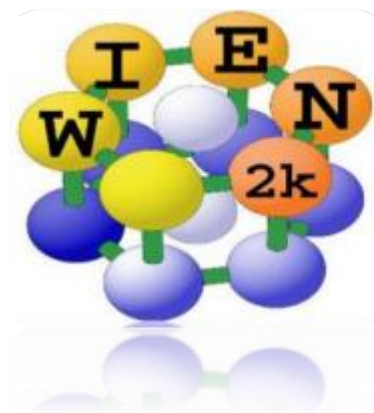
3. Total energy calculation: The total energy of the system is obtained by integrating the electron density and the potential over all space, and adding the kinetic energy and the Hartree energy. The exchange-correlation energy is calculated using one of the approximations discussed earlier.

The output files of the calculation contain information such as the band structure, density of states, electron density, and total energy, among others. These can be further analyzed using other programs or visualization tool

I.8.2. Self-consistent calculation

In this step, a self-consistent cycle is initialized and repeated until the convergence criterion is satisfied. This cycle involves the following stages [47]:

- **LAPW0:** Calculate the potential as the sum of the Coulomb potential V_C and the exchange potential and V_{xc} correlation from density.
- **LAPW1:** Find valence bands, eigenvalues and eigenvectors.
- **LAPW2:** Calculates the valence densities for the eigenvectors as well as the energy of Closed.
- **LCORE:** Computes core states and densities.
- **MIXER:** Mixes the electron densities of the core, semi-core states, and valence states to generate the input density for the next iteration. By, therefore, the input and output density will be mixed and the convergence criterion will be checked.



I.8.3.Determination of properties

Once the self-consistent calculation of the "SCF cycle" is completed, several properties can be determined, among which are the structural properties, magnetic properties, the structure of bands, density of states, charge density, and elastic properties, etc. The use of the different Wien2k programs is presented in a flowchart in **Figure II.4**.

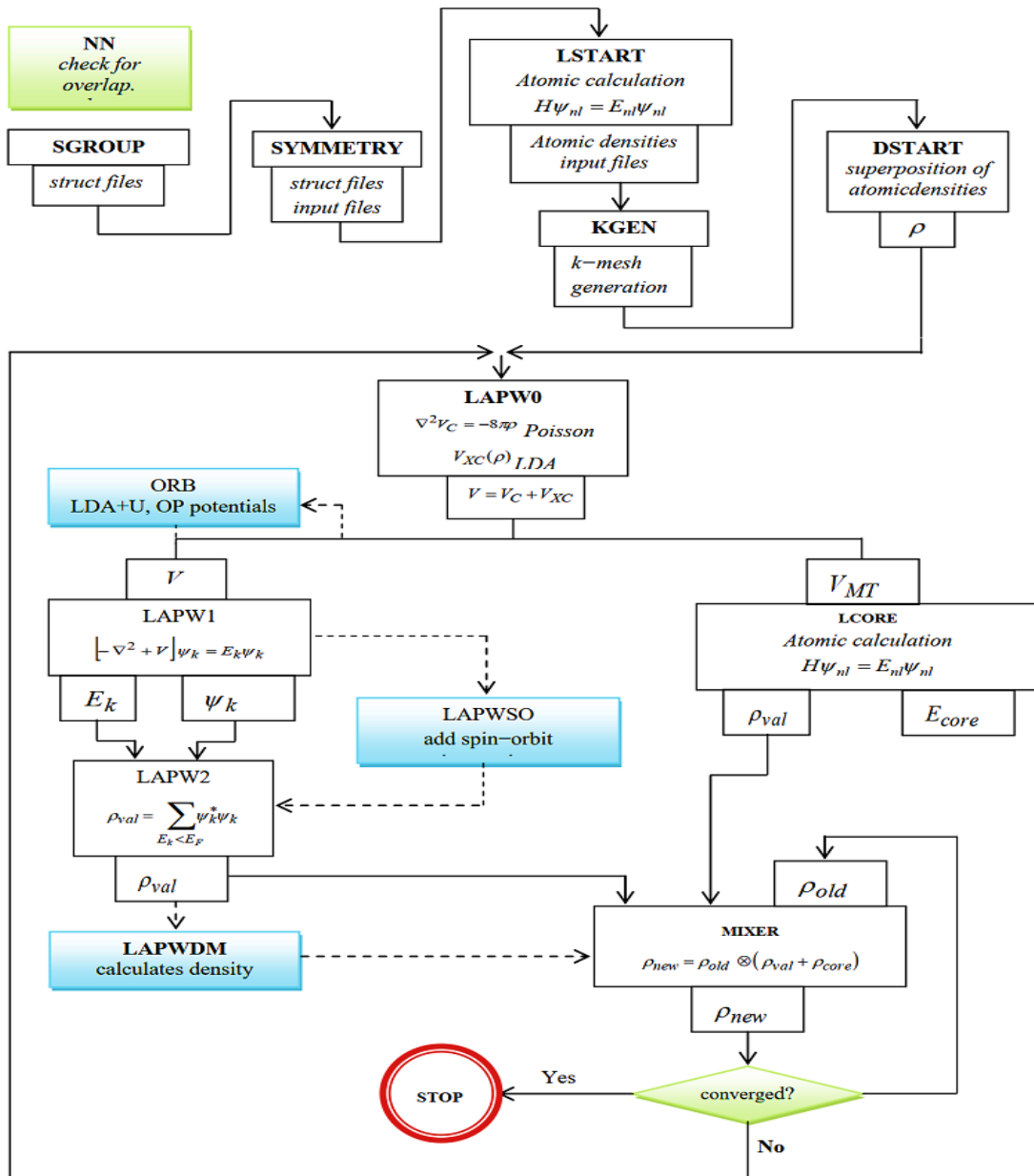


Figure.II.4 Diagram of the Wien2K code.

References

- [1]. Adams, J. and S. Priddy, Mathematical proceedings of the cambridge philosophical society. 1927.
- [2]. Fermi, E., Statistical method to determine some properties of atoms. Rend. Accad. Naz. Lincei, 1927. **6**(602-607): p. 5.
- [3]. Kohn, W. and L.J. Sham, Self-consistent equations including exchange and correlation effects. Physical review, 1965. **140**(4A): p. A1133.
- [4]. Schrödinger, E., An undulatory theory of the mechanics of atoms and molecules. Physical review, 1926. **28**(6): p. 1049.
- [5]. Parr, R.G., Density functional theory of atoms and molecules, in Horizons of quantum chemistry 1980, Springer. p. 5-15.
- [6]. Born, M., Kopplung der Elektronen- und Kernbewegung in Molekeln und Kristallen, von M. Born 1951: Vandenhoeck und Ruprecht.
- [7]. Kohn, W., Electronic structure of matter-wave functions and density functionals. Rev. Mod. Phys., 1999. **71**(5): p. 1253-1266.
- [8]. Jensen, F., Introduction to computational chemistry 2017: John Wiley & Sons.
- [9]. Cramer, C.J., Essentials of computational chemistry: theories and models 2013: John Wiley & Sons.
- [10]. Hartree, D.R. The wave mechanics of an atom with a non-Coulomb central field. Part I. Theory and methods. in Mathematical Proceedings of the Cambridge Philosophical Society. 1928. Cambridge university press.
- [11]. Fock, V., „Selfconsistent field “mit Austausch für Natrium. Zeitschrift für Physik, 1930. **62**(11): p. 795-805.
- [12]. Fock, V., Näherungsmethode zur Lösung des quantenmechanischen Mehrkörperproblems. Zeitschrift für Physik, 1930. **61**(1): p. 126-148.
- [13]. Hohenberg, P. and W. Kohn, Inhomogeneous electron gas. Physical review, 1964. **136**(3B): p. B864.
- [14]. Hohenberg, P. and W. Kohn, Density functional theory (DFT). Phys. Rev, 1964. **136**: p. B864.
- [15]. Skylaris, C.-K., The computational modelling of heavy atom chemistry, 1999, University of Cambridge.
- [16]. Herman, F., J.P. Van Dyke, and I.B. Ortenburger, Improved statistical exchange approximation for inhomogeneous many-electron systems. Physical Review Letters, 1969. **22**(16): p. 807.
- [17]. Dreizler, R. and E. Gross, Density Functional Theory Springer Verlag, 1990, Berlin New York.

- [18]. Vosko, S.H., L. Wilk, and M. Nusair, Accurate spin-dependent electron liquid correlation energies for local spin density calculations: a critical analysis. *Canadian Journal of physics*, 1980. **58**(8): p. 1200-1211.
- [19]. Perdew, J., E. McMullen, and A. Zunger, Density-functional theory of the correlation energy in atoms and ions: a simple analytic model and a challenge. *Physical Review A*, 1981. **23**(6): p. 2785.
- [20]. Perdew, J.P., K. Burke, and M. Ernzerhof, Generalized gradient approximation made simple. *Physical review letters*, 1996. **77**(18): p. 3865.
- [21]. Wu, Z. and R.E. Cohen, More accurate generalized gradient approximation for solids. *Physical Review B*, 2006. **73**(23): p. 235116.
- [22]. Liechtenstein, A., V.I. Anisimov, and J. Zaanen, Density-functional theory and strong interactions: Orbital ordering in Mott-Hubbard insulators. *Physical Review B*, 1995. **52**(8): p. R5467.
- [23]. Perdew, J.P. and A. Zunger, Self-interaction correction to density-functional approximations for many-electron systems. *Physical Review B*, 1981. **23**(10): p. 5048.
- [24]. Anisimov, V. and Y. Izyumov, Electronic Structure Calculations in One-Electron Approximation, in *Electronic Structure of Strongly Correlated Materials 2010*, Springer. p. 9-45.
- [25]. Dudarev, S.L., et al., Electron-energy-loss spectra and the structural stability of nickel oxide: An LSDA+ U study. *Physical Review B*, 1998. **57**(3): p. 1505.
- [26]. Dudarev, S., et al., Surface states on NiO (100) and the origin of the contrast reversal in atomically resolved scanning tunneling microscope images. *Physical Review B*, 1997. **56**(8): p. 4900.
- [27]. Becke, A.D. and E.R. Johnson, A simple effective potential for exchange. *The Journal of chemical physics*, 2006. **124**(22): p. 221101.
- [28]. Tran, F. and P. Blaha, Accurate band gaps of semiconductors and insulators with a semilocal exchange-correlation potential. *Physical review letters*, 2009. **102**(22): p. 226401.
- [29]. Tran, F., P. Blaha, and K. Schwarz, Band gap calculations with Becke–Johnson exchange potential. *Journal of Physics: Condensed Matter*, 2007. **19**(19): p. 196208.
- [30]. Becke, A., *Phys. Rev. A: At., Mol., Opt. Phys.* 1988.
- [31]. Bloch, F., Quantum mechanics of electrons in crystal lattices. *Z. Phys*, 1928. **52**: p. 555-600.
- [32]. Slater, J.C., *Quantum Theory of Molecules and Solids. Vol. 2: Symmetry and Energy Bands in Crystals* 1965: New York.
- [33]. Herring, C., A new method for calculating wave functions in crystals. *Physical Review*, 1940. **57**(12): p. 1169.
- [34]. Korringa, J., On the calculation of the energy of a Bloch wave in a metal. *Physica*, 1947. **13**(6-7): p. 392-400.

- [35]. Ham, F. and B. Segall, Energy bands in periodic lattices—Green's function method. *Physical Review*, 1961. **124**(6): p. 1786.
- [36]. Slater, J.C., Wave functions in a periodic potential. *Physical Review*, 1937. **51**(10): p. 846.
- [37]. Andersen, O.K., Linear methods in band theory. *Physical Review B*, 1975. **12**(8): p. 3060.
- [38]. Kanoun, M.B., First-Principles study of Structural, Elastic and Electronic Properties of AlN and GaN Semiconductors under Pressure Effect and Magnetism in AlN: Mn and GaN: Mn systems, 2004, Université de Tlemcen.
- [39]. Starkloff, T. and J. Joannopoulos, Local pseudopotential theory for transition metals. *Physical Review B*, 1977. **16**(12): p. 5212.
- [40]. Koelling, D. and G. Arman, Use of energy derivative of the radial solution in an augmented plane wave method: application to copper. *Journal of Physics F: Metal Physics*, 1975. **5**(11): p. 2041.
- [41]. Takeda, T. and J. Kubler, Linear augmented plane wave method for self-consistent calculations. *Journal of Physics F: Metal Physics*, 1979. **9**(4): p. 661.
- [42]. Kresse, G., J. Hafner, and R. Needs, Optimized norm-conserving pseudopotentials. *Journal of Physics: Condensed Matter*, 1992. **4**(36): p. 7451.
- [43]. BENSTAALI, W., ETUDE DES PROPRIETES OPTOELECTRONIQUES ET MAGNETIQUES DES COMPOSES ZnX/CdX DOPES PAR DES METAUX DE TRANSITION, Université de Mostaganem-Abdelhamid Ibn Badis.
- [44]. Singh, D., Ground-state properties of lanthanum: Treatment of extended-core states. *Physical Review B*, 1991. **43**(8): p. 6388.
- [45]. Blaha, P., K. Schwarz, and R. Augustyn, Technical University of Vienna Report No. WIEN93, 1993.
- [46]. Schwarz, K., C. Ambrosch-Draxl, and P. Blaha, Charge distribution and electric-field gradients in $\text{YBa}_2\text{Cu}_3\text{O}_{7-x}$. *Physical Review B*, 1990. **42**(4): p. 2051
- [47]. Petersen, M., et al. Improving the efficiency of FP-LAPW calculations. *Computer Physic Communications*, 2000. **126**(3): p. 294-309.

CHAPTER III

RESULTS AND DISCUSSION

II.1. Introduction

Half-Heusler materials are a class of intermetallic compounds with unique properties. They have a cubic leaf phase crystal structure and a chemical formula of XYZ, where X and Y are transition metals and Z is typically an element from group III or V. They have an electronic structure that can be semiconducting, metallic, or demi-metallic. They are named after Fritz Heusler, who discovered them in 1903[1].

Half-Heusler materials are fascinating compounds with a wide range of electronic, magnetic, and thermoelectric properties, making them ideal candidates for applications in fields such as spintronics, energy harvesting, and magnetic storage devices. They have a high Seebeck coefficient and high electrical conductivity, making them ideal candidates for applications in fields such as spintronics, energy harvesting, and magnetic storage devices. Research into these materials may uncover further potential applications and lead to the development of new and exciting technologies. In this chapter, we will explore the properties of Half Heusler materials.

The objective of this present work is to provide the maximum of information and to carry out at the same time a complementary and comparative study. This work is subdivided into two parts:

-a new double-half Heusler $K_2NaRbAs_2$.

- half-Heusler $VMSb$ ($M = Pd, Pt$).

these materials do not have many theoretical studies dealing with their physical properties. Based on the FP-LAPW method implemented in the Wien2k code [2], we have adopted as exchange and correlation functionals the generalized gradient approximation (GGA: Generalized Gradient Approximation) in the framework of (PBE: Perdew-Burke -Ernzerhof) and (WC: Wu-Cohen), and the local spin density approximation with interaction parameter U (LSDA+U) [3, 4]. Thus we used the modified Beck-Johnson exchange potential (mBJ: Modified Beck-Johnson) [5] to calculate the structural, elastic, electronic, magnetic, and thermoelectric properties of the considered $K_2NaRbAs_2$ double half Heusler (DHH) alloy are presented, and compared with those of its parent half Heusler (HH) alloys, $KNaAs$ and $KRbAs$. and investigate the structural, electronic, elastic, and magnetic properties of two half-Heusler $VMSb$ compounds ($M = Pd, Pt$).

III.2.Computational method:

In the FP-LAPW method, the space is divided into non-overlapping Muffin-Tin spheres and interstitial regions. Basis functions, electron densities, and potentials are expanded into spherical harmonics with cutoff radius $l_{max} = 10$ around atomic and Fourier series sites. The product of the smallest radius R_{MT} of the spheres MT and K_{max} determines the maximum of the wave vector ($R_{MT} \times K_{max}$) which sets the number of plane waves., the energy cut-off value of $R_{MT} * K_{max} = 8$ is used, and at 12, the Gaussian value G_{max} is performed. The choice of the values of the radii of the spheres Muffin-Tin R_{MT} is made in such a way that the interstitial region is the smallest possible, in order to ensure the speed of convergence. The number of k-points in the first Brillouin zone (BZ) is carried out for 1000 k points. and using a $15 \times 15 \times 15$ Self-consistent calculations are considered convergent when the total energy of the crystal converges to be 10^{-4} e, and 10^{-5} Ry. The Muffin-Tin rays and the valence states adopted in our work are grouped in **Table III.1**

Table.III.1 The valence states and RMT radii of the atoms in the investigated materials.

	Electronic configuration	$R_{MT}(a.u)$
K	$1s^2 2s^2 2p^6 3s^2 3p^6 4s^1$	2.35
Na	$1s^2 2s^2 2p^6 3s^1$	2.35
Rb	$1s^2 2s^2 2p^6 3s^2 3p^6 4s^2 3d^{10} 4p^6 5s^1$	2.35
As	$3d^{10} 4s^2 4p^3$	2.23
V	$3d^3 4s^2$	2.00
Pd	$1s^2 2s^2 2p^6 3s^2 3p^6 3d^{10} 4s^2 4p^6 4d^{10} 5s^0$	2.10
Pt	$1s^2 2s^2 2p^6 3s^2 3p^6 3d^{10} 4s^2 4p^6 4d^{10} 5s^2 5p^6 4f^{14} 5d^9 6s^1$	2.10
Sb	$1s^2 2s^2 2p^6 3s^2 3p^6 3d^{10} 4s^2 4p^6 4d^{10} 5s^2 5p^3$	2.30

III.3. Results and discussion:

III.3.1. double-half Heusler $K_2NaRbAs_2$

III.3.1.1 Structural Properties

III.3.1.1.1 The Crystal Structure of Heusler Alloys and Preferred Sites:

Among the materials that have garnered a lot of attention lately is the double-half Heusler alloy. This compound is a combination of three different elements and possesses a cubic crystal structure. What makes this material so fascinating is its unique structural properties, which have the potential to revolutionize many areas of technology. We'll explore the structural properties of the double-half Heusler alloy.

The studied compound $K_2NaRbAs_2$ crystallizes in a tetragonal structure with $P-4m2$ space group ($N^\circ 115$), see **Figure III.1**.

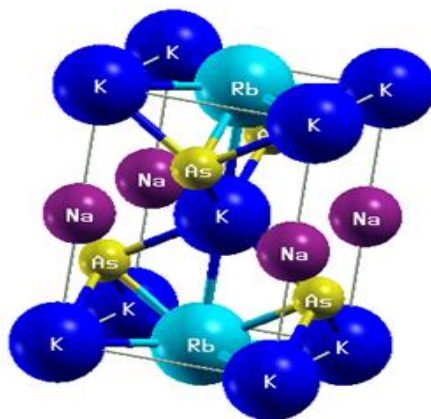


Figure.III.1 Structure representation of $K_2NaRbAs_2$ compound.

Heusler alloys are magnetic intermetallics with a face-centered cubic crystal structure and a composition of XYZ with stoichiometry 1:1:1 (half-Heusler). we have three non-equivalent atomic arrangements that are possible.

Table.III.2 The different possibilities of occupation of non-equivalent sites in the Hlef-Heusler C_{1b} structure, for the studied compounds KNaAs, KRbAs.

Type	K	Na .Rb	As
Type I	(1/2,1/2,1/2)	(0,0,0)	(1/4,1/4,1/4)
Type II	(1/2,1/2,1/2)	(1/4,1/4,1/4)	(0,0,0)
Type III	(1/4,1/4,1/4)	(1/2,1/2,1/2)	(0,0,0)

III.3.1.1.2 Structural optimizations and magnetic order

In order to check the stable magnetic phase, the optimization of both parent HH alloys was carried out within GGA in their ferromagnetic, non-magnetic, and anti-ferromagnetic phases [6] and represented in **Figure.III.2**

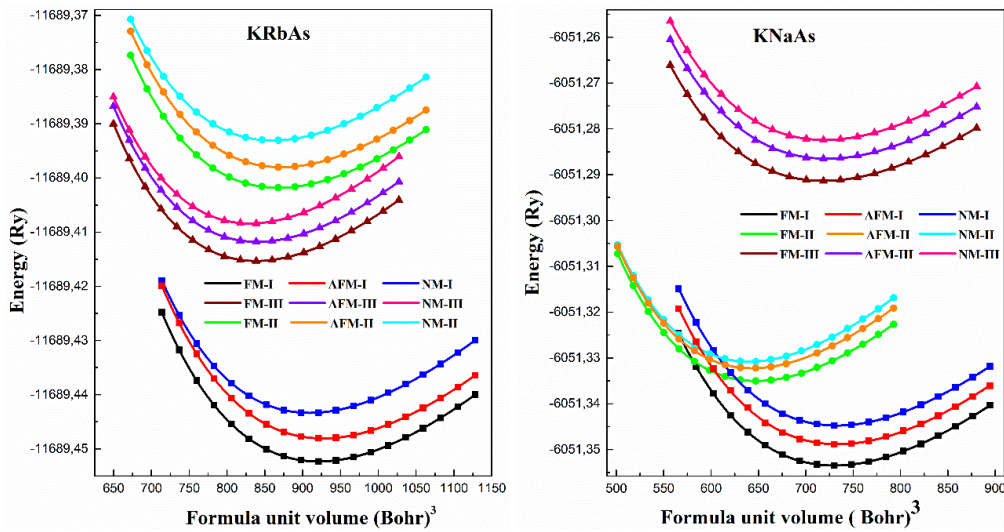


Figure.III.2 Calculated total energy of KRbAs and KNaAs compounds as a function of the volume for FM, NM, and AFM phases.

As can be seen in **Figure.III.2** the ferromagnetic phase of type I structure (FM-I) has the lowest total energy for both compounds, which suggests that it is energetically most stable compared to the other (NM) and (AFM) phases at the equilibrium volume.

From the obtained magnetic and structural ground states of KNaAs and KRbAs (FM-I), the $K_2NaRbAs_2$ structure is constructed by substituting, in the conventional lattice of KNaAs, two Na atoms with Rb atoms. Consequently, only the FM phase of this acquired DHH structure is

optimized, as shown in **Figure.III.3** the optimized volume of $K_2NaRbAs_2$ is 1649.7486 (bohr^3).

Then the structural parameters of the equilibrium are calculated by adjusting the total energy as a function of the volume, using the Birch Murnaghan equation of state [7].

$$E(V) = E_0 + \frac{9V_0B_0}{16} \left\{ \left[\left(\frac{V_0}{V} \right)^{2/3} - 1 \right]^3 B_0 + \left[\left(\frac{V_0}{V} \right)^{2/3} - 1 \right]^2 \left[6 - 4 \left(\frac{V_0}{V} \right)^{2/3} \right] \right\} \quad (\text{III.1})$$

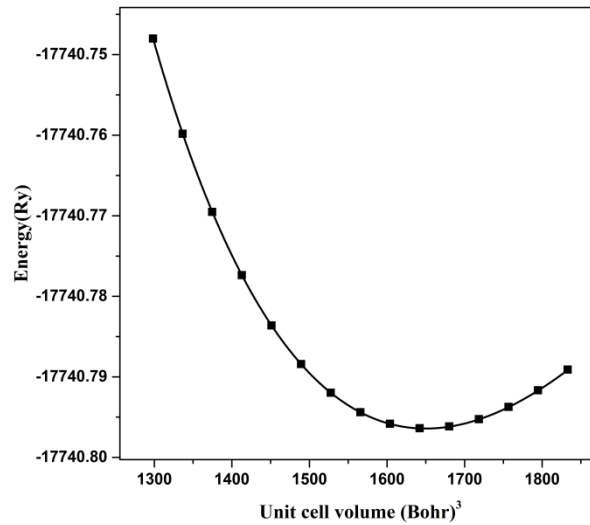


Figure.III.3 Calculated total energy of $K_2NaRbAs_2$ compound as a function of the volume.

The resulted structural ground state of DHH has a parent HH with a lattice parameter of a_{HH} , which is equal to c_{DHH} , while $a_{DHH} = b_{DHH} = \frac{a_{HH}}{\sqrt{2}}$, corresponding to a, b and c values, as presented in **Table III.3**.

The obtained parameters corresponding to the optimized structures for different magnetic phases of the equilibrium lattice parameter, bulk modulus, and its derivative, are given in **Table III 3**.

III.3.1.1.3 Energy of formation (or enthalpy of formation) and energy of cohesion

The enthalpy of the formation of a crystal is the difference between the energy of the crystal and the sum of the energies of the constituent elements in their standard states. To determine the thermodynamic stability and estimate the possibility of synthesizing these compounds, the formation energy is a useful norm. The formation energy of $K_2NaRbAs_2$ in **Table III.3** has been evaluated using the following equation:

$$E_f(K_2NaRbAs_2) = E_{tot}(K_2NaRbAs_2) - 2E_{tot}(K) - E_{tot}(Na) - E_{tot}(Rb) - 2E_{tot}(As) \quad (III.2)$$

Where, $E_{tot}(K_2NaRbAs_2)$ is the total energy of $K_2NaRbAs_2$; while, $E_{tot}(K)$, $E_{tot}(Na)$, $E_{tot}(Rb)$ and $E_{tot}(As)$ correspond to the total energy for K, Na, Rb, and As, per atom, respectively. The obtained negative formation energy of -0.0642 Ry, for the studied compound, indicates that this material is thermodynamically stable. Therefore, it can be synthesized in the DHH structure.

We calculated the phonon dispersion diagram of the $K_2NaRbAs_2$ material using the linear response method within the density functional perturbation theory (DFPT) as implemented in the CASTEP computational software[8]. The CASTEP computational code is an implementation of the pseudo-potential plane-wave method (PP-PW) in the framework of density functional theory (DFT). To ensure accurate total energy calculations, a plane-wave basis with a cut-off of 770 eV and a $6 \times 6 \times 4$ Monkhorst–Pack scheme k-point grid were applied. The obtained phonon dispersions along lines of high symmetry in BZ are shown in **Figure III.4**. The absence of soft modes (imaginary modes; negative frequencies) in a material implies its dynamic stability.

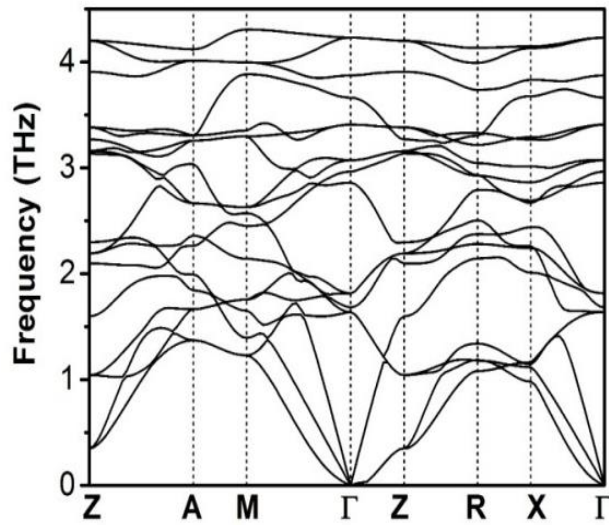


Figure.III. 4 Phonon dispersion curve of the $K_2NaRbAs_2$ compound.

The equilibrium lattice constant (a_0), bulk modulus (B), its pressure derivative (B'), and formation energies ($E_{formation}$) of the compounds are listed in TableIII.3. The results, presented in **Table III.3**, show that the bulk modulus (measure of compression resistance) diminishes as X atomic number rises.

Table.III.3 Calculated lattice parameter (Å), bulk modulus (GPa), its derivative pressure, and formation energies $E_{\text{formation}}(\text{Ry})$ for $\text{K}_2\text{NaRbAs}_2$ in their FM phase with structure type I.

Alloy	Phase	a_{HH} ($a_{\text{DHH}} = a_{\text{HH}}/\sqrt{2}$, $c_{\text{DHH}} = a_{\text{HH}}$)	B (GPa)	B'	$E_{\text{formation}}$
HH: KNaAs ^[6]	FM	7.564	14.835	4.166	-0.0381
	AFM	7.576	14.881	3.931	
	NM	7.573	14.972	4.086	
HH: KRbAs ^[6]	FM	8.173	11.117	4.253	-0.0355
	AFM	10.319	10.931	4.055	
	NM	8.138	11.056	4.443	
DHH: $\text{K}_2\text{NaRbAs}_2$	FM	5.2917	12.6115	4.164	-0.0642

III.3.2.1 Elastic properties

The mechanical behavior of crystals is strongly tied to their elastic properties, which enable us to examine crucial details about mechanical stability and comprehend the kind of forces in materials. Using the IRelast package, integrated into the WIEN2k code, the elastic constants are evaluated in order to check the mechanical stability of our compound.

Compounds that have a tetragonal structure have six independent elastic constants, denoted by; C_{11} , C_{12} , C_{13} , C_{33} , C_{44} and C_{66} , are necessary and sufficient to characterize the elastic behavior of the $\text{K}_2\text{NaRbAs}_2$ alloy. The mechanical stability of a tetragonal structure requires that Born's stability criteria be satisfied [9].

$$(C_{11} - 2C_{12}) > 0,$$

$$(C_{11} + C_{33} - 2C_{13}) > 0,$$

$$(2C_{11} + C_{33} + 2C_{12} + 4C_{13}) > 0,$$

$$C_{11} > 0, C_{33} > 0, C_{44} > 0, C_{66} > 0 \quad \text{(III.3)}$$

The obtained elastic constants satisfied all the Born's stability criteria. So; The $\text{K}_2\text{NaRbAs}_2$ alloy is confirmed to be mechanically stable. The computed C_{ij} constants are given in **Table III. 4**. The following formulae can be used to estimate various mechanical quantities such as Bulk (B), shear (G), Young's (E) moduli, anisotropic factor and Poisson's ratio:

$$B = (2C_{11} + C_{33} + 2C_{12} + 4C_{13})/9 \quad (\text{III.4})$$

$$G = \frac{2C_{11} + C_{33} - C_{12} - 2C_{13} + 6C_{44} + 3C_{66}}{15} \quad (\text{III.5})$$

$$E = \frac{9BG}{(G+3B)} \quad (\text{III.6})$$

$$\nu = \frac{(3B-2G)}{[2(3B+G)]} \quad (\text{III.7})$$

It can be observed that the bulk modulus value, determined by equation (04), calculated through the elastic constants of the studied alloy is fairly in agreement with that obtained from the total energy optimization.

The estimated data shows that $\text{K}_2\text{NaRbAs}_2$ can resist reversible deformation brought on by shear stress and can endure distortion better than its parent HHs.

Table.III.4 Calculated elastic constants C_{11} , C_{12} , C_{13} , C_{33} , C_{44} , C_{66} , bulk B , machinability index B/C_{44} , Shear G , Young E moduli, hardness H (in GPa), anisotropic parameter A , B/G , Poisson's ratio ν , for $\text{K}_2\text{NaRbAs}_2$ in its structural and magnetic ground states.

Compound	B	C_{11}	C_{12}	C_{13}	C_{33}	C_{44}	B/C_{44}	C_{66}	G	E	A	B/G	ν	H
$\text{KNaAs}^{[6]}$	14.20	16.40	13.10	//	//	4.46	3.18	//	2.99	8.39	2.70	4.74	0.40	0.20
$\text{KRbAs}^{[6]}$	12.08	17.96	9.14	//	//	4.16	2.90	//	4.26	11.43	0.94	2.84	0.34	0.45
$\text{K}_2\text{NaRbAs}_2$	12.20	18.27	7.78	9.90	18.32	5.86	2.08	3.37	4.71	12.53	0.27	2.59	0.33	0.53

To evaluate the brittleness and ductility of a material, it is necessary to present B/G ratio, where the critical value which separates the ductile and brittle behavior is equal to 1.75 (brittle $< 1.75 <$ ductile) [10]. According to Pugh, the B/G ratio for $\text{K}_2\text{NaRbAs}_2$ DHH alloy, is greater than 1.75, which leads us to classify it as a ductile material. In the previous work, The KNaAs and KRbAs HH alloys[6], from which the $\text{K}_2\text{NaRbAs}_2$ DHH alloy is derived, also showed similar feature.

Machinability is the ability of a metal to be cut to remove material with a satisfactory finish at low cost. Materials with good machinability (free machining materials) require low cutting power, obtaining a good finish and without significant tool wear. Factors that typically improve a material's performance often degrade its machinability, presenting a significant

engineering challenge. The machinability index, μ_M of a material is defined by $1/C_{44}$. The useful material, with a high machinability, should be strong (i.e. high bulk modulus) and malleable (i.e. low C_{44}) [11]. The calculated machinability indices are in the sequence: $K_2NaRbAs_2 < KRbAs < KNaAs$, as shown in **Table III.4**.

Hardness (H) is a measure of the resistance to a plastic deformation in the field of materials science (the opposite of softness). Strong intermolecular bonds typically describe a macroscopic hardness. Ductility, elastic stiffness, plasticity, deformation, strength, toughness, viscoelasticity, and viscosity are all factors that affect hardness. H is expressed by [12]:

$$H = \frac{(1-2\nu)E}{6(1+\nu)} \quad (\text{III.8})$$

The $K_2NaRbAs_2$ DHH has the highest hardness of 0.53 GPa, compared to those of their parents HHs, illustrated in **Table III.4**.

The Zener contrast factor is strongly correlated with the possibility of inducing micro cracks in materials, and it is an important physical quantity that informs us about the structural stability. For an isotropic system, A equals the unity, and the divergence from it measures the degree of elastic anisotropy. One may observe, from **Table III.4**, that the $K_2NaRbAs_2$ DHH is more anisotropic than its parent HHs. In order to comprehend the nature of a compound's bonding force, Poisson's ratio (ν) is utilized. In our case, the found ν values, which ranged between 0.25 and 0.5, suggest the presence of ionic character bonding in these compounds.

In fact, three-dimensional surfaces can also be used to describe the anisotropy of a material in specific directions. For that, the software MATrix LABoratory, which is made and published by J. Nordmann et al [13], was used to plot the 3D anisotropic surface figures of bulk, Young's and shear moduli and Poisson's ratio. It is worth mentioning that this software was used for the first time by H. Bouafia et al [14] in LuAuSn half-Heusler. For tetragonal system, the expressions of the elastic moduli in this context are as follows:

$$\frac{1}{B} = (S_{11} + S_{12} + S_{13}) - (S_{11} + S_{12} - S_{13} - S_{33})l_3^2 \quad (\text{III.9})$$

$$\frac{1}{E} = S_{11}(l_1^4 + l_2^4) + (2S_{13} - S_{44})(l_1^2l_3^2 + l_2^2l_3^2) + S_{33}l_3^4 + (2S_{12} + S_{66})l_1^2l_2^2 \quad (\text{III.10})$$

$$\frac{1}{G} = S_{44} + \left[(S_{11} - S_{12}) - \frac{S_{44}}{2} \right] (1 - l_3^2) + 2(S_{11} + S_{33} - 2S_{13} - S_{44})l_3^2 (1 - l_3^2) \quad (\text{III.11})$$

where $\begin{pmatrix} l_1 \\ l_2 \\ l_3 \end{pmatrix} = \begin{pmatrix} \sin \theta \cos \varphi \\ \sin \theta \sin \varphi \\ \cos \theta \end{pmatrix}$, and S_{ij} is compliance coefficient.

$$B_V = [2(C_{11} + C_{12}) + C_{33} + 4C_{13}]/9 \quad (\text{III.12})$$

$$G_V = [M + 3C_{11} - 3C_{12} + 12C_{44} + 6C_{66}]/30 \quad (\text{III.13})$$

$$B_R = C^2/M \quad (\text{III.14})$$

$$G_R = 15\{(18B_V/C^2) + [6/(C_{11} - C_{12})] + (6/C_{44}) + (3/C_{66})\}^{-1} \quad (\text{III.15})$$

Where $C^2 = (C_{11} + C_{12})C_{33} - 2C_{13}^2$; $M = C_{11} + C_{12} + 2C_{33} - 4C_{13}$

$$B_H = (B_V + B_R)/2 \quad (\text{III.16})$$

$$G_H = (G_V + G_R)/2 \quad (\text{III.17})$$

The Young's modulus (E), Poisson's ratio (ν) and the Zener anisotropic factor are computing with the following equations:

$$E_H = \frac{9B_H G_H}{3B_H + G_H} \quad (\text{III.18})$$

$$\nu = \frac{3B_H - 2G_H}{2(3B_H + G_H)} \quad (\text{III.19})$$

$$A^U = 5 \frac{G_V}{G_R} + \frac{B_V}{B_R} - 6 \quad (\text{III.20})$$

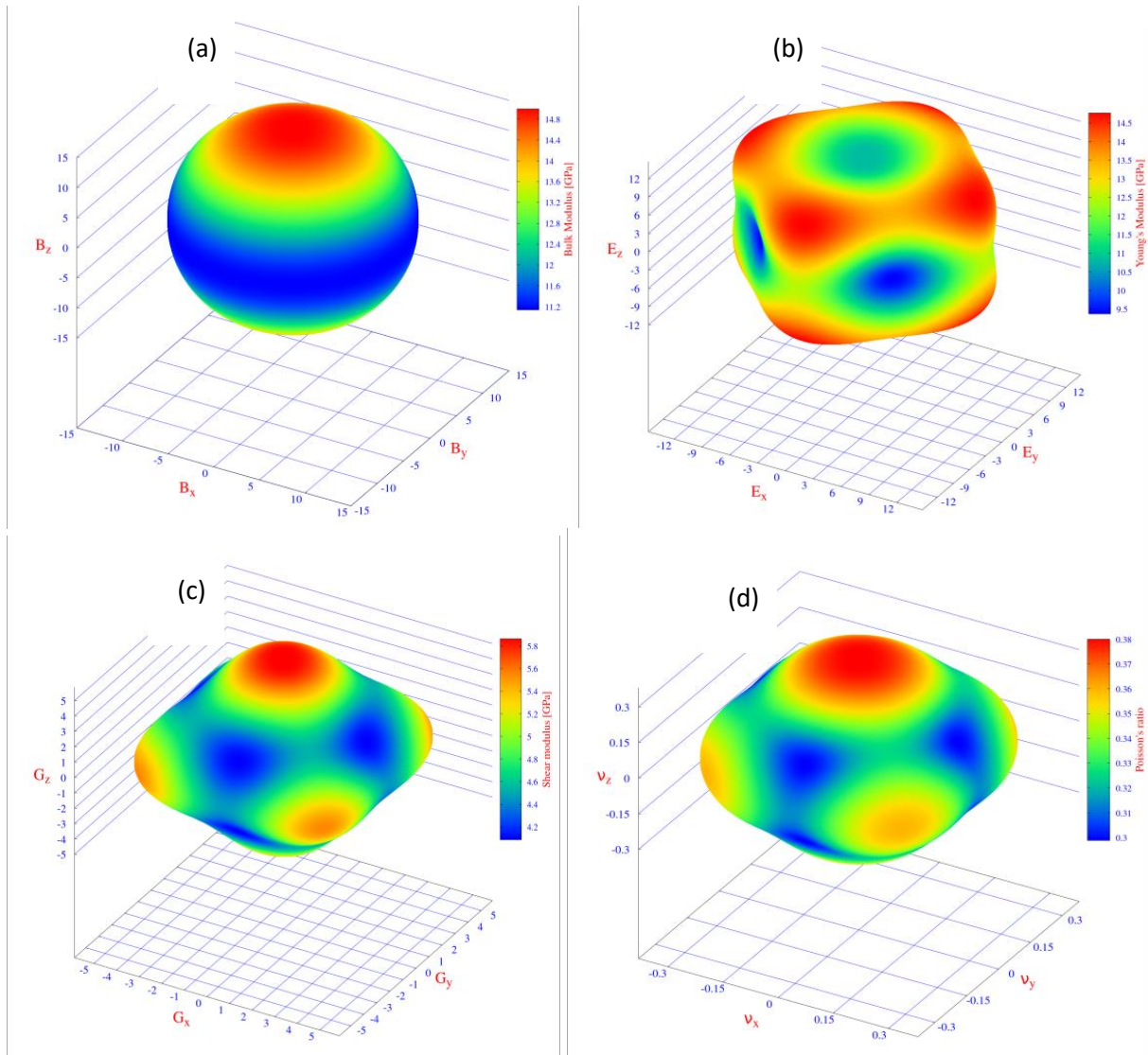


Figure.III.5 3D graphical representation of (a) bulk, (b) Young's and (c) shear moduli and(d) Poisson's ratio of DHH $K_2NaRbAs_2$.

The 3D surface of an isotropic system would have a spherical shape; therefore any deviation from that shape reflects the degree of anisotropy. As per **Figure.III.5**, the surfaces of (B), (E) and (G) moduli and (ν) clearly deviate from a spherical shape, which represents the clear elastic anisotropy of $K_2NaRbAs_2$.

Among these mechanical properties, the bulk modulus of $K_2NaRbAs_2$ is nearly isotropic. This is evident in 3D representation (refer to **Figure.III.5** (a)) which appears almost spherical (i.e. not spherical), as expected for a tetragonal structure. For the Young's modulus, we can

observe a significant deviation from the sphere shape along the $\langle 111 \rangle$ direction, whereas for the shear modulus and Poisson's ratio, the deformation is along $\langle 001 \rangle$ direction.

The universal anisotropy index A^U , which is determined by the upper and lower limits of the bulk and shear moduli, is expressed by **Eq III.20**. The crystal displays isotropic behavior when A^U is equal to zero, and any deviation from this value indicates elastic anisotropy. Our compound exhibits elastic anisotropy, as its computed value of A^U was found to be 0.27.

III.3.1.2.1 Debye temperature θ_D and elastic wave velocities

The Calculation of the elastic constants has an impact on how the materials behave when heated; as a result, we can assess several thermal properties, such as the Debye temperature and the melting temperature, which are listed in **Table III.5**. The Debye temperature (θ_D) is calculated, using the equation below[10]:

$$\theta_D = \frac{h}{k_B} \left[\frac{3}{4\pi V_0} \right]^{1/3} v_m \quad (\text{III.21})$$

where h is Planck's constant, k_B is Boltzmann's constant, V_0 is the average atomic volume, and v_m is the average sound wave velocity, which depends on the transverse (v_t) and longitudinal (v_l) sound velocities [15]:

$$v_m = \left[\frac{1}{3} \left(\frac{2}{v_t^3} + \frac{1}{v_l^3} \right) \right]^{-1/3} \quad (\text{III.22})$$

and these are given by equations (III.23) and (III.24), as follows:

$$v_l = \sqrt{\frac{3B+4G}{3\rho}} \quad (\text{III.23})$$

and

$$v_t = \sqrt{\frac{G}{\rho}} \quad (\text{III.24})$$

where ρ is the density. The outcomes of our calculations are given in **Table III.5**.

Table III.5 Calculated longitudinal (v_l), transverse elastic wave velocities (v_t), average acoustic (v_m) velocities (in m/s), Debye (θ_D) and melting (T_m) temperatures (in K) of $K_2NaRbAs_2$ in its structural and magnetic ground states.

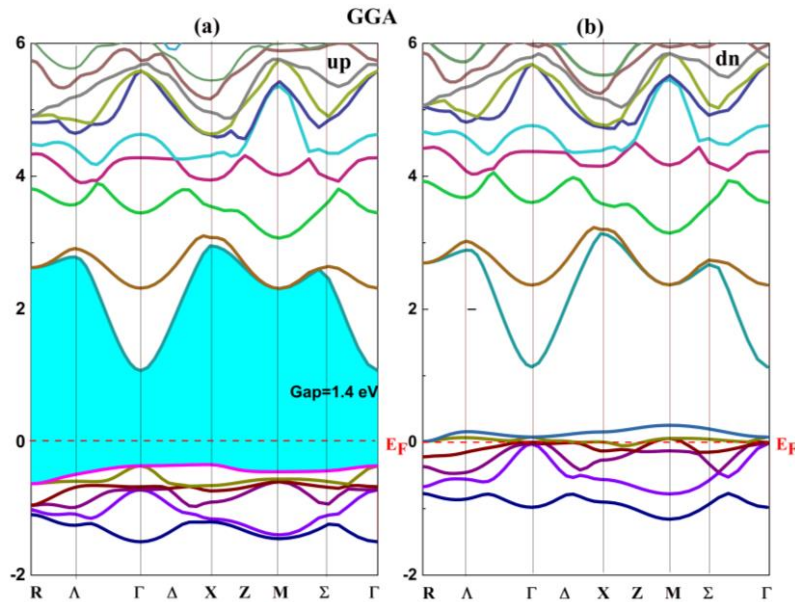
Compound	v_l	v_t	v_m	θ_D	T_m
KNaAs ^[6]	2941.36	1193.26	1351.07	121.746	649.9393
KRbAs ^[6]	2705.1	1324.81	1487.96	124.094	622.1995
K ₂ NaRbAs ₂	2843.92	1436.11	1610.09	139.307	436.297

III.3.3.1 Electronic properties

Double-half Heusler materials exhibit a variety of interesting electronic properties. Understanding their electronic properties requires that the next electronic properties are inspected at the equilibrium lattice constant using the GGA approach to describe the electron profile.

III.3.3.1.1 Band structures:

Figure III.6 shows the spin-polarized band structures for the compound K₂NaRbAs₂ calculated by GGA and TB-mBJ approximations. These are drawn along the high symmetry points in the first Brillouin zone.



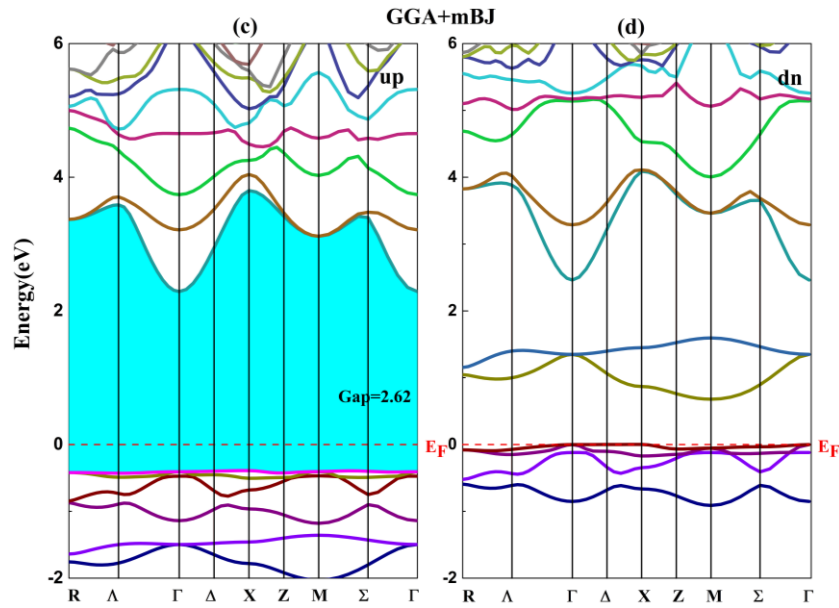


Figure.III.6 Calculated band structure of $K_2NaRbAs_2$ compound in both (a, c) spin-up and (b, d) spin-down states by (a,b) GGA and (c,d) GGA+mBJ approximations.

We can see, for the spin down states of $K_2NaRbAs_2$, a metallic character due to the intersection of the valence bands with the Fermi level. On the other hand, for the spin-up channel, the compound exhibits a semiconductor character. In this channel (spin-up), we can see that the compound $K_2NaRbAs_2$ has an indirect band gap of 1.40 eV and 2.62 eV calculated by GGA and TB-mBJ approximations. The half-metallic gap (HMGap) is inferred from the valence band maximum (VBM) which is closer than conduction band minimum (CBM) to the Fermi level. The obtained half-metallic gap values are 0.34 eV and 0.39 eV for GGA and TB-mBJ methods, respectively. Therefore, we can see that the TB-mBJ method opens the band gap, located at high symmetry points Γ and X, for the valence band maximum (VBM), and conduction band minimum (CBM), respectively.

III.3.3.1.2 Densities of electronic states:

To explain the contribution of the different electronic states to the band structures, it is also interesting to determine the total (TDOS) and partial (PDOS) densities of states. In order to find out which states are responsible for the bond. The total and partial densities of states were calculated for both spin channels (i.e. spin-up and spin-dn), as shown in the **Figure.III.7**.

From both approaches (GGA, and GGA+mBJ), The PDOSs show that spin-exchange splitting, fundamentally originated from p states of Arsenic (As) atoms, which mainly contribute to the TDOS for the spin-up and-down channels, around the Fermi level.

This exchange splitting causes the spin-polarization of 100%, as defined by equation:

$$P = \frac{|\rho_{\uparrow}(E_F) - \rho_{\downarrow}(E_F)|}{\rho_{\uparrow}(E_F) + \rho_{\downarrow}(E_F)} \quad (\text{III.25})$$

where $\rho_{\uparrow}(E_F)$ and $\rho_{\downarrow}(E_F)$ are the spin-dependent density of states at E_F and (\uparrow) and (\downarrow) represent spin-up and spin-dn states, respectively. P equals zero for paramagnetic or antiferromagnetic materials. As shown in Figure.III.6 our studied material is fully spin-polarized (i.e. $P=100\%$), indicating its half-metallic character. However, s and p states of K , Na atoms as well as Rb - d have little contributions to the TDOS for both spin channels, around E_F .

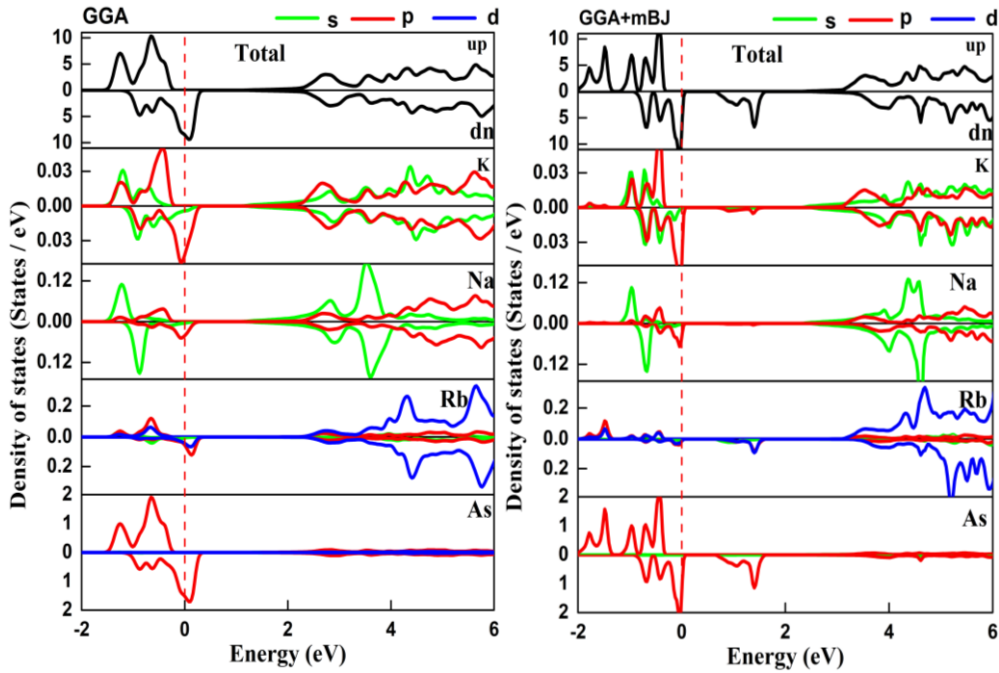


Figure.III.7 Calculated DOS of $K_2NaRbAs_2$ compound in both spin-up and spin-down states by GGA and GGA+mBJ approximations.

III.3.4.1 Magnetic properties:

To describe the spin effect on the considered material, we have computed its magnetic properties. The local, interstitial, and total magnetic moments for the DHH $K_2NaRbAs_2$ alloy, estimated by employing GGA approach are grouped in **Table III.6**. One can see that the total magnetic moment has an integer value of $2\mu_B$ per unit cell which fulfills the necessary condition of the half-metallic behavior for our compound in tetragonal phase. From Table 4, the main contribution, to the total magnetic moment comes from Arsenic atoms, which is

similar to its previously studied parent HH alloys KNaAs and KRbAs, with the participation of the interstitial magnetic moment.

Table.III.5 Calculated total, atom-resolved and interstitial magnetic moments (in μ_B) in the unit cell for $K_2NaRbAs_2$ in its structural and magnetic ground states.

Compound	M_{tot}	M_K	M_{Na}	M_{Rb}	M_{As}	M_{int}
KNaAs ^[6]	1.000	0.017	0.001	//	0.420	0.562
KRbAs ^[6]	1.000	0.010		0.016	0.399	0.575
$K_2NaRbAs_2$	2.000	0.013	-0.004	0.033	0.422	1.100

III.3.5.1 Thermoelectric properties:

Thermoelectricity has recently gained popularity as an “environmentally friendly” technique because it does not use moving parts or chemical reactions resulting in no waste matter. The efficiency of a thermoelectric material is determined by the dimensionless parameter ZT , figure of merit, which is given by $Z_T = \frac{\sigma S^2 T}{\kappa}$, where σ is the electrical conductivity, S is the Seebeck coefficient, κ is the thermal conductivity of the material and T the temperature in K. A substance with a high Seebeck coefficient S , high electric conductivity, and low thermal conductivity is ideal for thermoelectric applications. Many recent investigations on half Heusler alloys demonstrated that they have high energy factors ($S^2\sigma$), leading scientists to concentrate their study on these materials.

In this part, we thoroughly examine the thermoelectric behavior of the considered DHH alloy to determine if it can function as a thermoelectric material. So, we employed semi-classical Boltzmann transport theory, based on a smoothed Fourier interpolation of the bands, as implemented in the BoltzTraP code, to investigate the thermoelectric characteristics of $K_2NaRbAs_2$ DHH alloy. In the same temperature range, from 150 K to 1000 K, thermal (κ/τ), and electrical conductivity (σ/τ), and Seebeck coefficient (S) were calculated. The energy spectral density of electrical conductivity is given by the following equation:

$$\bar{\sigma}_{\alpha\beta}(\varepsilon) = \frac{e^2}{N} \sum_{i,k} \tau_{i,k} v_{\alpha}(i, k) v_{\beta}(i, k) \frac{\delta(\varepsilon - \varepsilon_{i,k})}{\delta(\varepsilon)} \quad (\text{III.26})$$

where α and β are the coordinate components, i is the electronic band number, \mathbf{k} is the wave vector, N is the total number of \mathbf{k} points, e is the elementary charge, τ is the relaxation time of the charge carrier, and ε is the band energy. Also, the group velocity \mathbf{v} is:

$$\mathbf{v}_\alpha(\mathbf{i}, \mathbf{k}) = \frac{1}{\hbar} \frac{\partial \varepsilon_{\mathbf{i}, \mathbf{k}}}{\partial \mathbf{k}_\alpha} \quad (\text{III.27})$$

Using Eq. (III.28), the conductivity tensor $\sigma_{\alpha\beta}$ can be written as a function of temperature T and Fermi level μ as follows:

$$\sigma_{\alpha\beta}(T, \mu) = \frac{1}{\Omega} \int \bar{\sigma}_{\alpha\beta}(\varepsilon) \left[-\frac{\partial f(T, \varepsilon, \mu)}{\partial \varepsilon} \right] d\varepsilon \quad (\text{III.28})$$

In Eq (III.29), Ω is the unit cell volume and f is the Fermi-Dirac distribution. Similarly, the Seebeck coefficient tensor $S_{\alpha\beta}$ can be written as:

$$S_{\alpha\beta}(T, \mu) = \frac{1}{eT\Omega\sigma_{\alpha\beta}(T, \mu)} \int \bar{\sigma}_{\alpha\beta}(\varepsilon)(\varepsilon - \mu) \left[-\frac{\partial f(T, \varepsilon, \mu)}{\partial \varepsilon} \right] d\varepsilon \quad (\text{III.29})$$

The Seebeck coefficient of materials with holes (p-type materials), as dominant charge carriers, is positive whereas it is negative for n-type materials (i.e. electrons as dominant charge carriers). **Figure.III.8** shows that the Seebeck coefficient, in the spin-dn channel, decreases as the temperature rises. In the spin-up channel the opposite occurs. The situation becomes the opposite in the spin- up channel. The Seebeck coefficient (S) is 1259.3. $\mu\text{V/K}$ in the spin-up state at ambient temperature (300°K) confirming the presence of electrons as the majority carriers, while the Seebeck coefficient (S) is 57.9 $\mu\text{V/K}$ in the spin-dn state; these findings show that the $\text{K}_2\text{NaRbAs}_2$ DHH alloy has a high positive spin-up Seebeck coefficient. As a result, This DHH is p-type material.

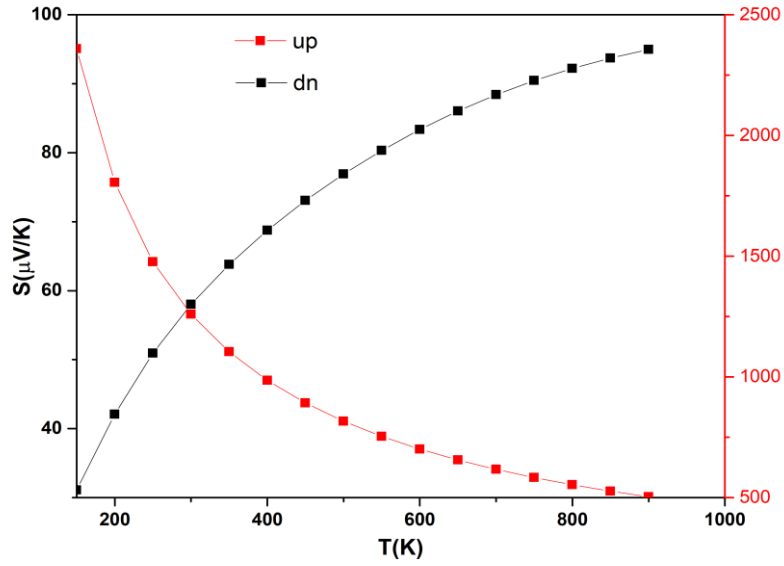


Figure.III.8 Temperature dependence of the Seebeck coefficient of the spin up and spin dn channels of $K_2NaRbAs_2$.

Figure.III.9 depicts the Fermi level plot of the electrical conductivity of the studied compound as a function of temperature for both spin channels is shown. In the spin-up, up to a particular temperature threshold (400 K), the electrical conductivity is nearly constant. After that the electrical conductivity starts to increase; while in the spin-dn, the electronic conductivity (σ/τ) increases as temperature rises.

The value of electrical conductivity per relaxation time in the spin-up state for the DHH at room temperature (300 K) is 0 while, in the spin-dn state, it is $236.4810^{17} \Omega^{-1} m^{-1} s^{-1}$. Due to lower DOS values at Fermi level, the electrical conductivity values for the spin-up channel are lower than those of the spin-down channel. These results demonstrate a high electrical conductivity and, consequently, a low resistivity of this material.

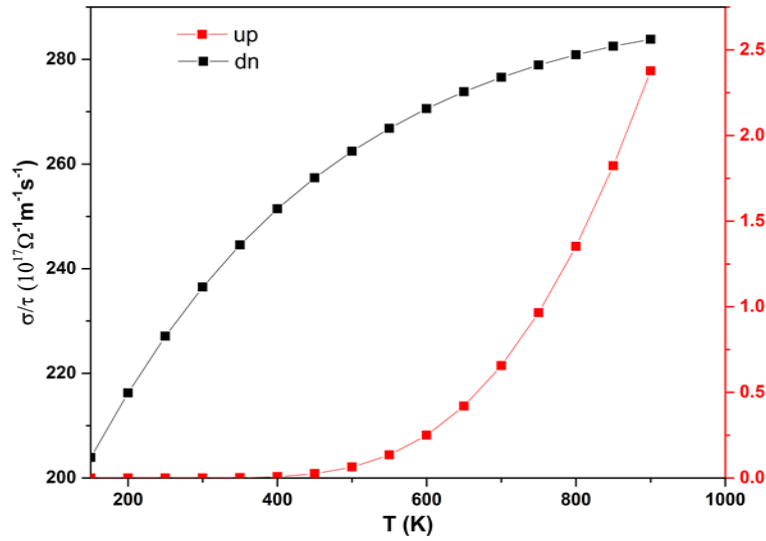


Figure.III.9 Temperature dependence of the electrical conductivity for the spin up and spin dn channels of $K_2NaRbAs_2$.

Figure.III.10 displays the temperature dependence, of the electronic thermal conductivity, scaled by the relaxation time, for spin-up and spin-down channels, of the electronic thermal conductivity, scaled by the relaxation time. The figure shows that the conductivity increases as the electronics become thermally excited with rising temperature and can conduct more heat. This behavior is indicated by a character similar to (σ/τ) . For the examined alloy, a linear increase in κ_e/τ is observed for temperature above approximately 600 K

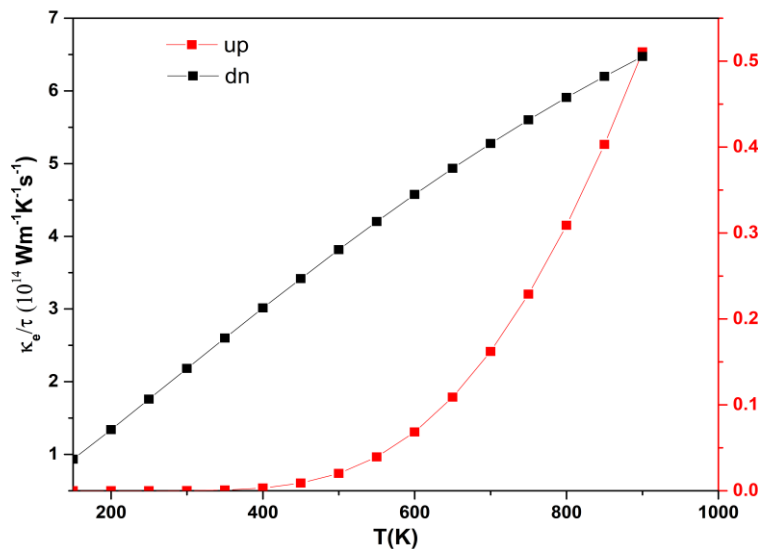


Figure.III.10 Temperature dependence of the electronic thermal conductivity in the spin-up and spin-dn channels of $K_2NaRbAs_2$ DHH alloy.

III.3.2. half-Heusler VMSb (M = Pd, Pt)

III.3.2.1 Structural Properties

III.3.2.1.1 The Crystal Structure of Heusler Alloys and Preferred Sites

Half-Heusler alloys typically consist of transition metals X and Y, and a non-magnetic element Z from groups III, IV, or V in the periodic table. To determine the most stable structural phase and predict ground state properties, the energy minimization method was used to calculate the lattice constants and bulk modulus of a superposition of a rock-salt and zinc-blend structure. This family of compounds has a cubic structure with the space group (no. 216 F-43m), written by $a = b = c$ and $a = \beta = \gamma$ [16, 17] (see **Figure III.11**). Table I summarizes the three equal atomic arrangements possible for this structure type.

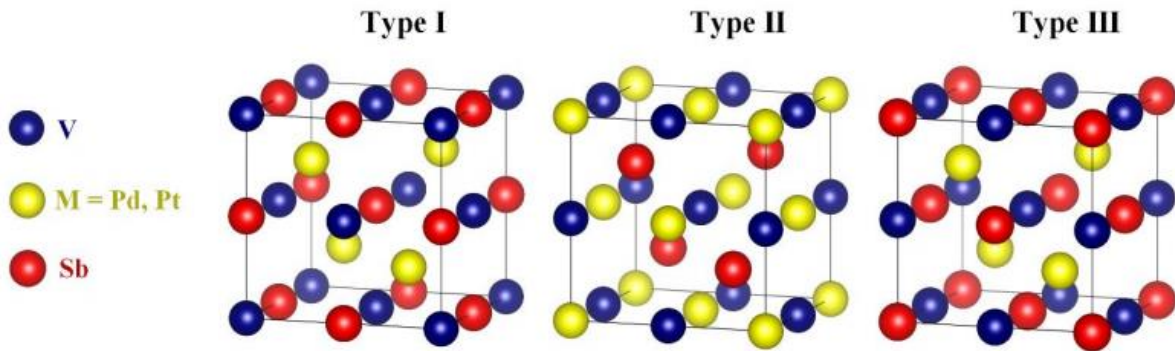


Figure.III.11 Different types of half-Heusler structures.

Table.III.6 Possible atomic arrangements of the half-Heusler compounds VMSb (M= Pd, Pt).

Type	V	M	Sb
Type I	(0, 0, 0)	(1/2, 1/2, 1/2)	(1/4, 1/4, 1/4)
Type II	(1/4, 1/4, 1/4)	(0, 0, 0)	(1/2, 1/2, 1/2)
Type III	(1/2, 1/2, 1/2)	(1/4, 1/4, 1/4)	(0, 0, 0)

III.3.2.1.2 Structural optimizations and magnetic order:

The determination of the most stable structure and equilibrium lattice parameter of a material under study is a crucial step in first principle calculations. This information allows us to subsequently access other physical properties, such as mechanical, electronic, and magnetic properties. **Figure.III.12** presents the total energy curves (**Eq.III.30**) as a function of volume

for VMSb compounds where M is either Pd or Pt . It observed that the ferromagnetic (FM) phase has the lower energy than the non-magnetic (MN) phase for the structure type III . The Bich-Murnaghan equation of state was used to use to obtain the total energy-volume curves for both compounds.

$$E(V) = E_0 + \frac{BV}{B'} \left[\left(\frac{V_0}{V} \right)^{B'} + 1 \right] - \frac{BV}{B'-1} \tag{III.30}$$

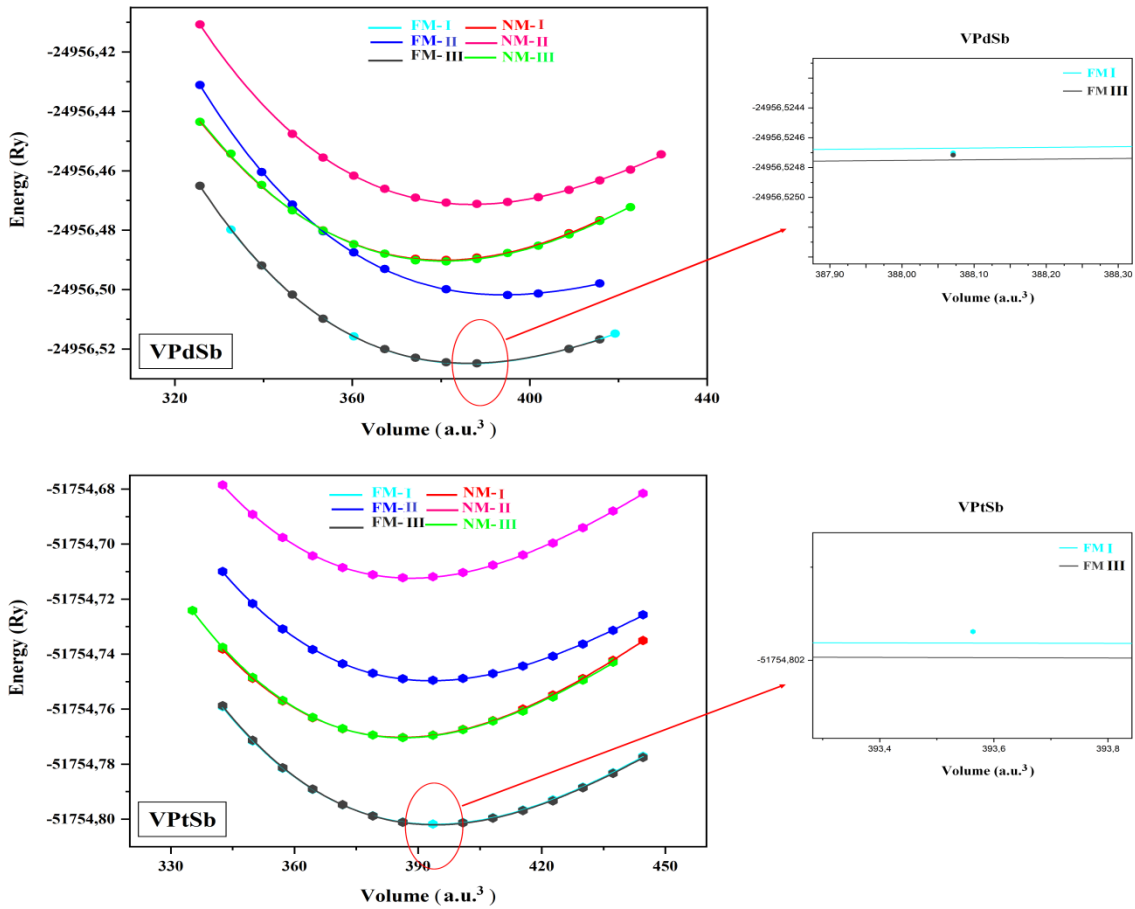


Figure.III.12 Calculated total energy of VPdSb and VPtSb compounds in their FM and NM phases as a function of the volume.

We found that the ferromagnetic phase has the lower energy for both VPdSb (-24956.525) and VPtSb (-51754.802), respectively. **FigureIII.12** affirms the structural stability of VMSb (M= Pd, Pt) composites in FM structures type III. Which are energetically favorable for the experimental fabrication of these alloys. The lattice parameter and bulk modulus of different compounds vary due to the chemical composition and crystal structure of the material. The observed difference in lattice constants between VPdSb and VPtSb can be attributed to the

different atomic radii and electronic structures of Pd and Pt. Pd has a smaller atomic radius than Pt, which can lead to a smaller lattice parameter. The bulk modulus is a measure of a material's resistance to compression and is affected by the strength of the bonds between the atoms. The derivative pressure (B') is a measure of how the bulk modulus changes under pressure. It indicates that the material becomes less compressible at high pressures, while a smaller B' indicates the opposite. The specific values of B' for VPdSb and VPtSb in **Table III.8** can provide insight into how the compounds behave under different pressures. The differences in lattice parameter, bulk modulus, and B' between the two compounds can be attributed to the different atomic and electronic structures of the two compounds.

Table.III.7 The calculated values of lattice parameter (\AA), bulk modulus (GPa), and its pressure derivative, the minimum energy (Ry) of both compounds VMSb (M=Pd, Pt).

Compound	Phase	a_0	B	B'	E_{\min}
VPdSb	FM-III	6.121	129.044	4.672	-24956.525
VPtSb	FM-III	6.160	140.466	4.733	-51754.802

III.3.2.2 Elastic properties:

The elastic constants play an important role in determining a material's mechanical response to external forces, such as stress or strain, C_{11} , C_{12} , and C_{44} are three independent elastic constants that describe the behavior of a cubic crystal under stress. C_{11} represents the stiffness of the crystal along one axis, while C_{12} represents the stiffness between two perpendicular axes. Finally, C_{44} represents the shear modulus which is the measure of the crystal's resistance to shear deformation along a plane parallel to one of its faces. The values of these constants provide information about the stiffness, shear modulus, and bulk modulus of the material, which are important for confirming its mechanical stability. The bulk modulus is a measure of a material's resistance to uniform compression, while the shear modulus is a measure of its resistance to shear deformation. By calculating the elastic constants and moduli of a material, we can predict how it will behave under different types of mechanical stress, and strain.

The elastic constants and moduli of VMSb (M=Pd, Pt) alloys were calculated using the IRelast package integrated into the Wien2k code [18]. These properties are important for understanding how a material responds to external forces, such as stress or strain. The elastic constants for the cubic phases were determined using isotropic strain and volume-conserving

deformations of the cubic primitive cells. The bulk modulus (B) of the VMSb alloys was also calculated and found to be within the range of $C_{12} < B < C_{11}$, consistent with the criteria for mechanical stability. **Eq III.31** shows how the elastic constants affect the total energy of the material as a function of strain (δ), providing insight into the material's mechanical response to external stresses and strains.

$$E(\delta) = E(-\delta) = E(0) + (C_{11} - C_{12})V_0\delta^2 + O(\delta^4) \quad (\text{III.31})$$

Overall, the results suggest that VMSb (M=Pd, Pt) alloys have the potential to exhibit strong mechanical properties due to their elastic constants and moduli.

Where $E(0)$ is the total energy of an undisturbed lattice, V_0 is the equilibrium volume, and C_{ij} are elastic constants.

Applying an orthorhombic strain tensor with conserved volume and the following expression, we can obtain C_{11} and C_{12} **Eq III.32**.

$$\bar{\epsilon} = \begin{bmatrix} \delta & 0 & 0 \\ 0 & -\delta & 0 \\ 0 & 0 & \frac{\delta^2}{(1-\delta^2)} \end{bmatrix} \quad (\text{III.32})$$

The bulk modulus B of an isotropic cubic crystal is written as a function of C_{11} and C_{12} as following:

$$B = \frac{C_{11} + 2C_{12}}{2} \quad (\text{III.33})$$

C_{44} was calculated using a monoclinic strain conserving volume method.

$$\bar{\epsilon} = \begin{bmatrix} 0 & \frac{\delta}{2} & 0 \\ \frac{\delta}{2} & 0 & 0 \\ 0 & 0 & \frac{4}{(4-\delta^2)} \end{bmatrix} \quad (\text{III.34})$$

The total energy is then represented as follows:

$$E(\delta) = E(-\delta) = E(0) + \frac{1}{2}C_{44}V_0\delta^2 + O(\delta^4) \quad (\text{III.35})$$

The results, presented in **Table III.8** show that both VPtSb and VPdSb are mechanically stable according to Born's criteria for the cubic structure[19]. Specifically, the values of C_{11} , C_{12} , and C_{44} satisfy the conditions $C_{11} - C_{12} > 0$, $C_{11} > 0$, and $C_{44} > 0$, as well as $C_{11} + 2C_{12} > 0$ and $C_{12} < B < C_{11}$.

Table.III.8 The elasticity constants C_{ij} (in GPa), the calculated elasticity constants: bulk B , shear G and Young moduli E (in GPa), anisotropy parameter A , B/G ratio, and Poisson's ratio ν , θ_D temperature of Debye for VMSb ($M = Pd$ and Pt) compounds.

Compound	C_{11}	C_{12}	C_{44}	B	G	E	ν	B/G	A	θ_D
VPdSb	147.04	124.98	81.76	132.335	53.47	141.37	0.32	2.47	7.41	272.85
VPtSb	168.73	131.96	89.427	140.221	60.41	160.41	.314	2.36	4.86	266.82

These elasticity constants are used to determine the bulk modulus B , shear modulus G , Young's modulus E , Poisson's ratio ν , and anisotropy factor A **Table III.8**, which can be calculated using the following equations:

$$G = \frac{C_{11} - C_{12} + 3C_{44}}{5} \quad (\text{III.36})$$

$$E = \frac{9BG}{3B + G} \quad (\text{III.37})$$

$$\nu = \frac{(3B - 2G)}{2(3B + G)} \quad (\text{III.38})$$

$$A = \frac{2C_{44}}{C_{11} - C_{12}} \quad (\text{III.39})$$

The bulk modulus values obtained for VPdSb ($B=132.335$ GPa) and VPtSb ($B=140.221$ GPa) compounds are in close agreement with those obtained from the structural properties (129.044 GPa, 140.466 GPa), respectively), which confirms the accuracy of the elasticity constants of VMSb ($M=Pd, Pt$) alloys. The Poisson's ratios (ν) of VMSb ($M = Pd, Pt$) (0.32, 0.31) respectively are higher than (0.25) suggests a high metallic behavior as inter-atomic bonding ,for ductile materials, confirming the ductility of these compounds according to Frantsevich's rule. This could be attributed to the low elasticity constants and bulk modulus B , which promote material ductility. Additionally, the B/G ratios for both VPdSb (2.474) and VPtSb

(2.363) compounds are higher than the critical value of (1.75), which classifies them as ductile materials.

The young modulus of VPtSb (160.4 GPa) is higher than that of VPdSb (141.4 GPa). To describe the elastic properties of different materials, the anisotropy coefficient of expansion as well as the elastic anisotropy are used to cause micro-cracks in ceramics. The elastic anisotropy of VPdSb and VPtSb alloys is demonstrated by the three-dimensional Young's modulus diagrams in **Figure III.13**. The values of the anisotropy parameter A were obtained by applying **Eq III.39** as seen in **Table III.8**. For an isotropic material, $A=1$, whereas values greater or less than one indicate a higher or lower level of anisotropic elastic behavior. Both compounds show an elastic deformation anisotropy ($A \neq 1$), which supports the anisotropic material hypothesis. Further computations are required to fully comprehend the properties of the structural intermetallic compounds.

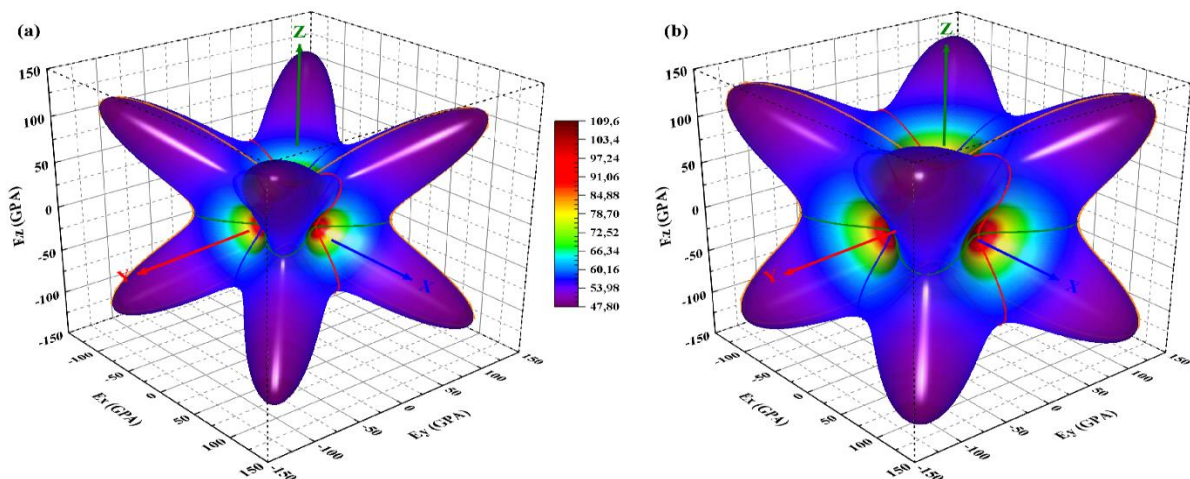


Figure.III.13 3D-representation of Young's modulus of both compounds: a) VPdSb and b) VPtSb.

III.3.2.2.1 Debye temperature Θ_D and elastic wave velocities

The Debye temperature Θ_D is an important physical parameter and is closely related to several physical properties. It is determined from Young's modulus E , the compressibility modulus B , and the shear modulus G . At low temperatures, one of the standard methods for calculating the Debye temperature Θ_D deduced from the elastic constants is the link that exists between the average speed of sound propagation v_m and Θ_D obtained from the Anderson relation [20, 21].

The Debye temperature is given by the following equation:

$$\theta_D = \frac{h}{k_B} \left[\frac{3}{4\pi V_0} \right]^{\frac{1}{3}} v_m \quad (\text{III.40})$$

Where h , k_B and V_0 represent Planck's constant, Boltzmann's constant, and the atomic volume, respectively. V_m is provided for a polycrystalline material by:

$$v_m = \frac{1}{3} \left[\frac{2}{v_t^3} + \frac{1}{v_l^3} \right]^{\frac{-1}{3}} \quad (\text{III.41})$$

Where V_l and V_t are the longitudinal and transverse velocities of sound which are calculated using the bulk modulus B and shear modulus G as follows[22]:

$$v_l = \left(\frac{3B+4G}{3\rho} \right)^{\frac{1}{2}} \quad (\text{III.42})$$

$$v_t = \left(\frac{G}{\rho} \right)^{\frac{1}{2}} \quad (\text{III.43})$$

Furthermore, the melting temperature was deduced, using the expression for cubic metals [23]:

$$T_M = 553 + 5.91C_{11} \quad (\text{III.44})$$

The results of our calculations are shown in **Table III.9**. It should be noted that there are no experimental or theoretical data in the literature for the comparison of our results.

Table.III.9 The calculated transverse and longitudinal elastic wave velocities, the average wave velocity (m.s^{-1}), the temperature of Debye (K), and the melting temperature for VPdSb and VPtSb (K) compounds.

Compounds	v_t	v_l	v_m	θ_D	T_M
VPdSb	2174.16	4762.02	2450.52	272.85	1422.0282
VPtSb	2144.96	4465.21	2411.61	266.82	1550.2285

III.3.2.3 Magnetic properties

The magnetic moment is a crucial property in the field of spintronics, and it was calculated for the Heusler alloys with half-metallic behavior using the optimized lattice parameters. The total magnetic moment of these alloys follows the Slater-Pauling (SP) rule [24], which is one of the methods used for evaluating the magnetic moments of Heusler and half-Heusler compounds. For half-Heusler compounds, the total magnetic moment can be expressed by :

$$M_t = Z_T - 18 \quad (\text{III.45})$$

where M_t represents the spin magnetic moment and Z_T is the total number of valence electrons. **Table III.10** presents the total and local magnetic moments for both VMSb ($M = \text{Pd}$ and Pt) compounds, including contributions from atomically resolved magnetic moments (WC-GGA, LSDA+U, TB-mBJ) and interstitial magnetic moments.

Table.III.10 Total and partial magnetic moments (WC- GGA, LSDA+U, TB-mBJ) in (μ_B) per unit cell.

Compound	Functional	Magnetic moment				
		M_{Int}	M_V	M_M	M_{Sb}	M_T
VPdSb	WC- GGA	0.334	1.715	0.026	-0.076	2.000
	LSDA+U	0.341	1.685	0.037	-0.063	2.000
	TB-Mbj	0.261	1.802	0.007	-0.071	2.000
VPtSb	WC- GGA	0.336	1.694	0.017	-0.047	2.000
	LSDA+U	0.307	1.756	-0.022	-0.041	2.000
	TB-Mbj	0.254	1.731	0.028	-0.014	2.000

According to **Table III.10**, the spin magnetic moment of half-Heusler compounds is calculated by the difference between the spin-up and spin-down states. The compounds have a C_{1b} structure with three atoms in each unit cell [25]. For ternary 1:1:1 half-Heusler compounds such as VMSb ($M = \text{Pd}, \text{Pt}$), we note that in each of the functions (WC-GGA, LSDA + U, TB-mBJ), there is no change. The total magnetic moments are around $2\mu_B$. In these compounds, the V atom has the most significant contribution to the total magnetic moment, with a small presence of an M magnetic moment. The local magnetic moment of the Sb atom is negligible for both alloys and behaves similarly to the s-p element in conventional Heusler alloys.

III.3.2.4 Electronic properties

III.3.2.4.1 Electronic band structure

Electronic structure calculation plays an important role in determining the magnetic properties of half Heusler compounds and, in particular, in predicting half-metallic ferromagnetism. Using electronic structure calculations, one can design materials for specific spintronic applications. For this, we study the band structures of the compounds VPdSb, VPtSb.

The band structures of the VMSb ($M = \text{Pd}$ and Pt) compounds were analyzed by plotting their spin-polarized band structures using WC-GGA, LSDA+U, and TB-Mbj approximations. **Figures III.14** and **III.15** were determined along the high symmetry path of the first Brillouin zone. The analysis revealed that the spin-up channel of VPdSb compound has a metallic nature due to the crossing of the Fermi level by the valence band maximum (VBM) and conduction band minimum (CBM). But for VPtSb compound the electronic properties were found to depend on the computational method used. The WC-GGA, LSDA+U, approximations predicted a metallic nature, while the TB-MBj approximation predicted a semiconductor behavior, with an energy gap of $E_g = 0.48$. This is due to the maximum valence band being located at X, which does not coincide with the minimum conduction band at point L. Overall, the electronic properties of these compounds are important for understanding their potential use in electronic devices, and other applications.

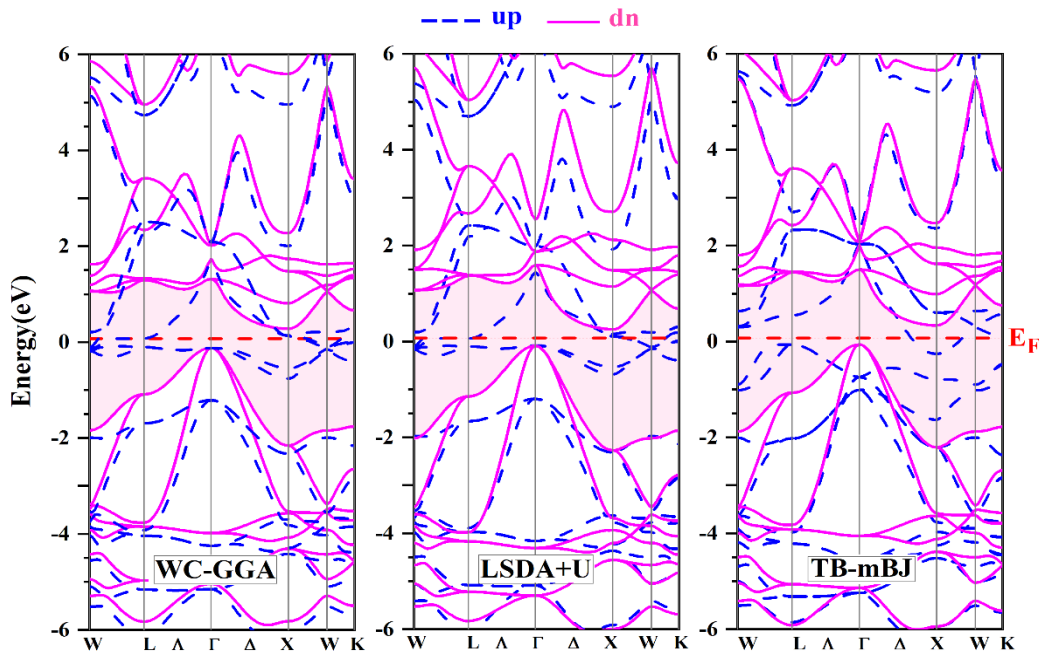


Figure.III.14 The band structure of the VPdSb compound using: WC- GGA, LSDA+U, and TB-mBJ.

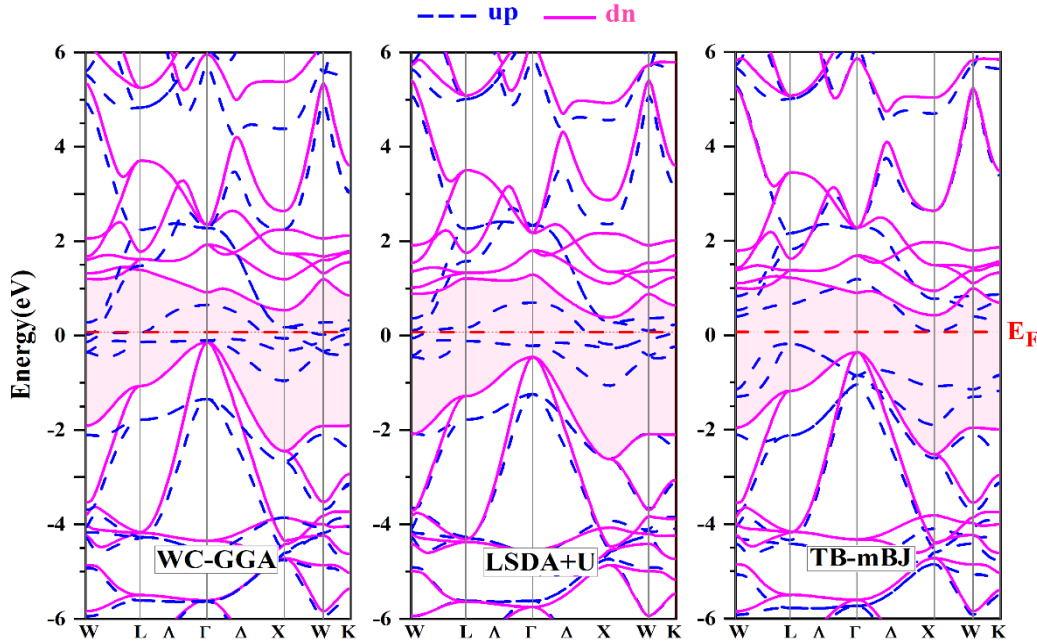


Figure.III.15 The band structure of the VPtSb compound using: WC- GGA, LSDA+U, and TB-mBJ.

III.3.2.4.2 Densities of states:

The electronic density of states (DOS) is a fundamental concept in solid-state physics that describes the distribution of energy levels available to electrons in a material. The DOS is typically represented by the total (TDOS) and partial (PDOS) density of states. The total state density (TDOS) allows access to the electronic conduction properties of a material, while the partial densities of state (PDOS) are used to determine the structure of the chemical bonds between atoms of a crystal or molecule. The projections of the total state density depend on the radii of the spheres on which the partial state densities are projected and therefore only give access to qualitative information [26]. The **Figures III.16**, represent the densities of the electronic states of the half Heusler compounds VPdSb, VPtSb, respectively, they are calculated with Tran-Blaha modified Becke-Johnson (TB-mBJ). The vertical line in red indicates the Fermi level (E_F). DOS of the half Heusler VPdSb VPtSb, reveals that d states of V atom mainly contribute to the total density of states for the spin-up and -down channel states around the Fermi level. But, d states of Pd, and Pt have a contribution to the spin-down and -down channel states between -6 eV and -3 eV, but d states of Sb have no contribution. The total DOS of the compounds show the half-metallic nature.

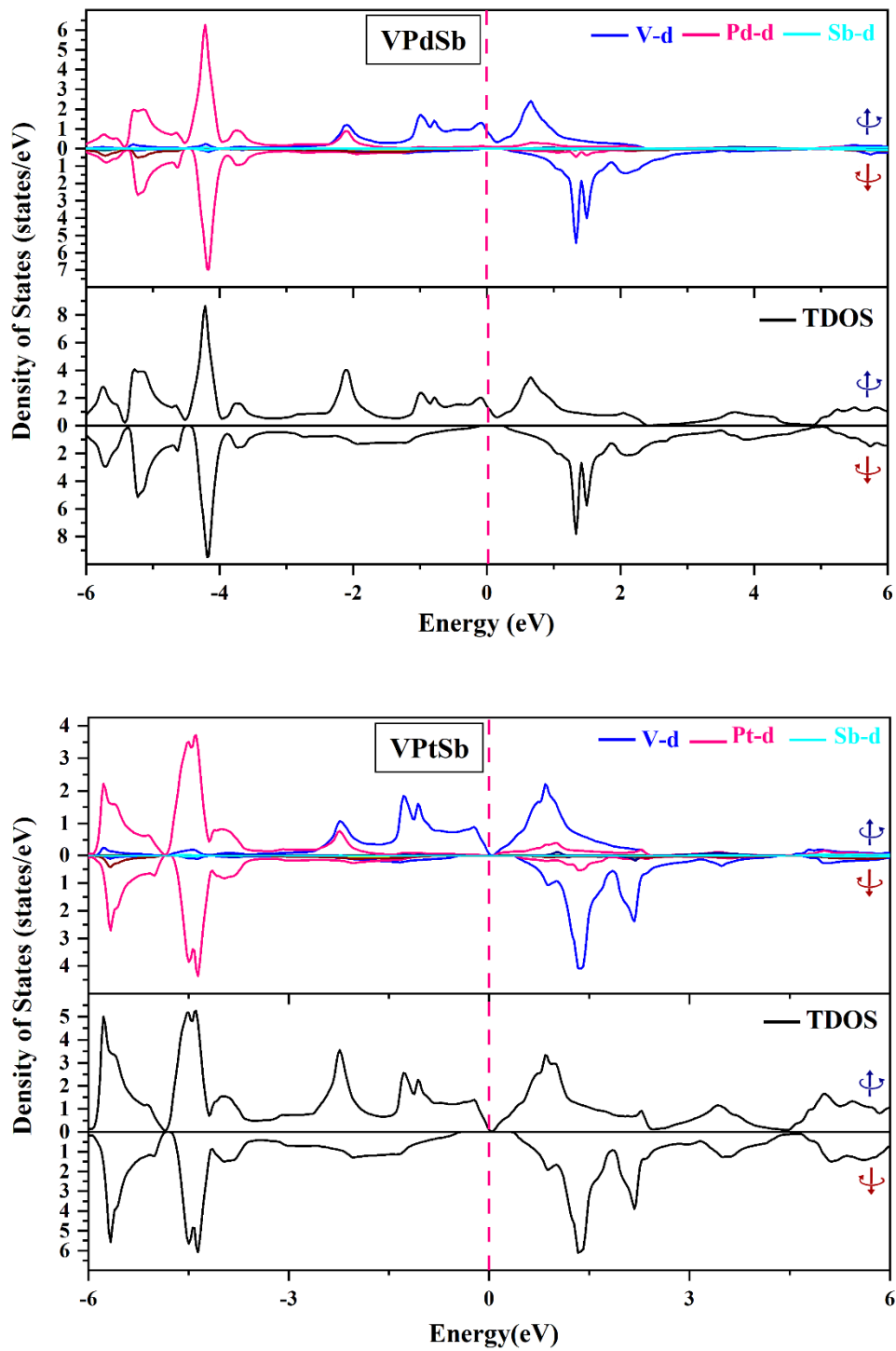


Figure.III.16 Total and Partial DOS of the VPdSb and VPtSb compounds obtained by the TB-mBJ approach.

III.3.2.4.3 Effect of pressure on band structure properties

The study of materials under the effect of hydrostatic pressure is a very important and attractive subject. The most important phenomenon that occurs under the effect of applied pressure is the sudden change in the arrangement of atoms in the crystal.

In order to study the effect of pressure on the electronic properties of our material, we performed FP-LAPW calculations on different volumes at different pressures. Note that the calculations were performed using the WC-GGA approximation. The variation of the lattice parameter as a function of hydrostatic pressure is given by the following expression [27]:

$$P(V) = \frac{B}{B'} \left[\left(\frac{V}{V_0} \right)^{B'} \right] - 1 \quad (\text{III.46})$$

Where B is the modulus of compressibility, B' its first derivative, V is the volume under pressure, and V₀ is the volume at zero pressure. In the present work, we have also studied the electronic properties under the effect of hydrostatic pressure in the range (0–20 GPa) for the materials VPdSb and VPtSb. **Figures III.17,III.18** present the variation The band structures for the spin-up and spin-down channels of both compounds.

Table.III.11 The calculated lattice constant(Å), electronic band gaps for spin down (eV) and the electronic band structure nature of VPdSb and VPtSb compounds.

Material	ressure (GPa)	a (Å)	E _{g_Down} (eV)	Nature of band gap
VPdSb	0	6.121	0.51	Indirect
	5	6.194	0.47	Indirect
	10	6.257	0.44	Indirect
	15	6.313	0.41	Indirect
	20	6.363	0.37	Metal
VPtSb	0	6.160	0.58	Indirect
	5	6.227	0.54	Indirect
	10	6.286	0.51	Indirect
	15	6.339	0.48	Indirect
	20	6.386	0.43	Direct

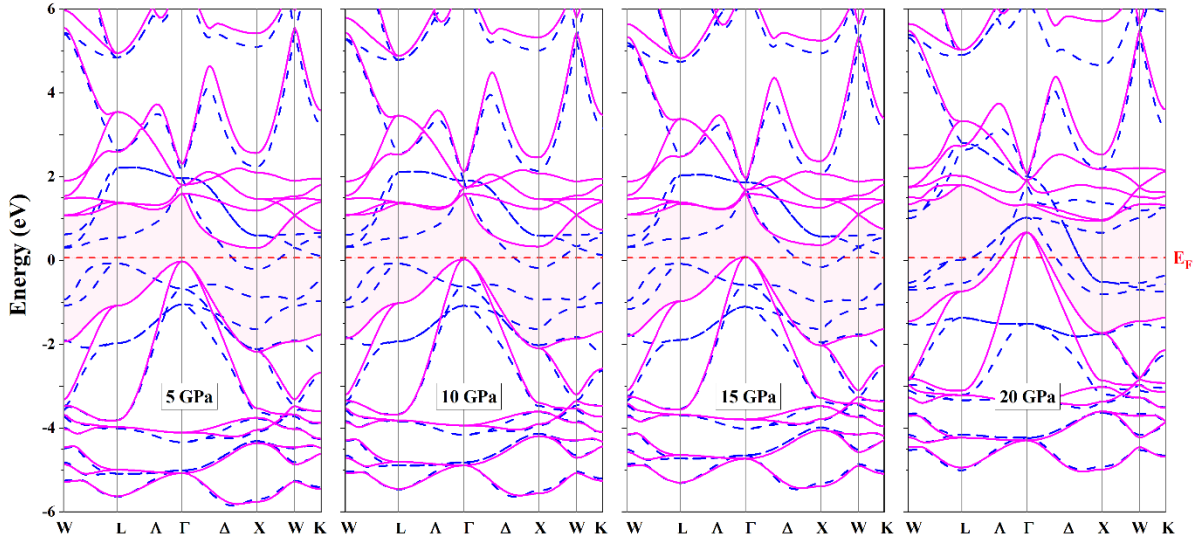


Figure.III.17 Band structure of VPdSb alloy (in the 0–20 GPa range) at optimized lattice constant.

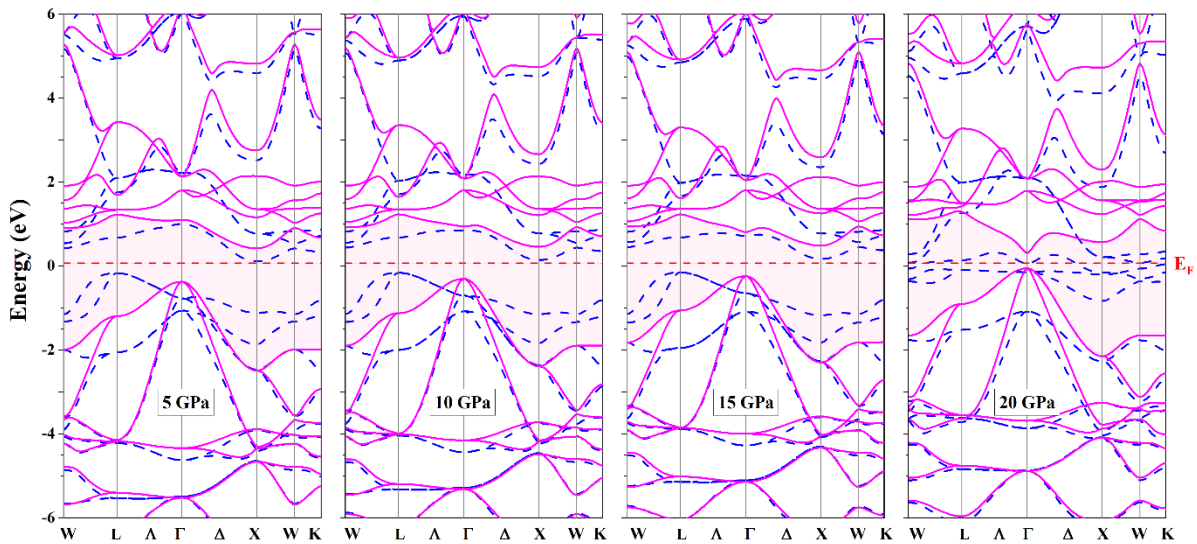


Figure.III.18 Band structure of VPtSb alloy (in the 0–20 GPa range) at optimized lattice constant.

We notice from **Figure (III.17, III 18)**, both compounds exhibit a metallic nature in the spin-up state due to the valence band maximum (VBM) and conduction band minimum (CBM), while the spin-down form shows a semiconducting nature. For the VPdSb compound, the indirect band gap (E_g) gradually decreases from (0.51 eV to 0.41) eV under pressure (0 to 15 GPa). However, the compound loses its half-metallic state at (20 GPa) with $E_g = 0.37$ eV. The calculated band gaps and lattice constants (A) are presented in Table VI. As for VPtSb, the spin-up channel is metallic, while the compound exhibits a semiconductor nature with

indirect gaps of $E_g = (0.58, 0.54, 0.51, \text{ and } 0.48 \text{ eV})$ at pressures ranging from (0 to 15 GPa. At 20 GPa), the compound shows a direct band gap of (0.43 eV) in the spin-down channel. In summary, increasing pressure gradually changes the electronic properties from half-metallic to metallic characters.

References

- [1]. Heusler, F., Magnetic-chemical studies Verh. Dtsch. Phys. Ges, 1903. **5**: p. 219.
- [2]. Schwarz, K. and P. Blaha, Solid state calculations using WIEN2k. Computational Materials Science, 2003. **28**(2): p. 259-273.
- [3]. Bilc D, Orlando R, Shaltaf R, Rignanese G-M, Íñiguez J, Ghosez P. Hybrid exchange-correlation functional for accurate prediction of the electronic and structural properties of ferroelectric oxides. Physical Review B. 2008;**77**(16):165107.
- [4]. Andriotis, A.N., R.M. Sheetz, and M. Menon, LSDA+ U method: A calculation of the U values at the Hartree-Fock level of approximation. Physical Review B, 2010. **81**(24): p. 245103.
- [5]. Perdew JP, Ruzsinszky A, Csonka GI, Vydrov OA, Scuseria GE, Constantin LA, et al. Restoring the density-gradient expansion for exchange in solids and surfaces. Physical review letters. 2008;**100**(13):136406.
- [6]. Lorf A, Boudia K, Khelifaoui F, Amara K, Sadouki O, Ameri M, editors. Structural and Half-Metallic Stabilities of the Half-Heusler Alloys KNaAs, KRbAs and NaRbAs: First Principles Method. Spin; 2021: World Scientific.
- [7]. Birch, F., The effect of pressure upon the elastic parameters of isotropic solids, according to Murnaghan's theory of finite strain. Journal of Applied Physics, 1938. **9**(4): p. 279-288.
- [8]. Clark SJ, Segall MD, Pickard CJ, Hasnip PJ, Probert MI, Refson K, et al. First principles methods using CASTEP. Zeitschrift für kristallographie-crystalline materials. 2005;**220**(5-6):567-70.
- [9]. Mouhat, F. and F.-X. Coudert, Necessary and sufficient elastic stability conditions in various crystal systems. Physical review B, 2014. **90**(22): p. 224104.
- [10]. Pugh, S., XCII. Relations between the elastic moduli and the plastic properties of polycrystalline pure metals. The London, Edinburgh, and Dublin Philosophical Magazine and Journal of Science, 1954. **45**(367): p. 823-843.
- [11]. Cover M, Warschkow O, Bilek M, McKenzie D. A comprehensive survey of M2AX phase elastic properties. Journal of Physics: Condensed Matter. 2009;**21**(30):305403.
- [12]. Naher, M. and S. Naqib, An ab-initio study on structural, elastic, electronic, bonding, thermal, and optical properties of topological Weyl semimetal TaX (X= P, As). Scientific Reports, 2021. **11**(1): p. 1-21.
- [13]. Nordmann, J., M. Aßmus, and H. Altenbach, Visualising elastic anisotropy: theoretical background and computational implementation. Continuum Mechanics and Thermodynamics, 2018. **30**: p. 689-708.

- [14]. Bouafia, H., et al., Insight into elastic anisotropy, mechanical and dynamical stability, electronic properties, bonding and weak interactions analysis of LuAuSn Half-Heusler. *Solid State Sciences*, 2021. **118**: p. 106677.
- [15]. Mehl, M.J., Pressure dependence of the elastic moduli in aluminum-rich Al-Li compounds. *Physical Review B*, 1993. **47**(5): p. 2493.
- [16]. Özdoğan, K., E. Şaşıoğlu, and I. Galanakis, Slater-Pauling behavior in LiMgPdSn-type multifunctional quaternary Heusler materials: Half-metallicity, spin-gapless and magnetic semiconductors. *Journal of Applied Physics*, 2013. **113**(19): p. 193903.
- [17]. Dai X, Liu G, Fecher GH, Felser C, Li Y, Liu H. New quaternary half metallic material CoFeMnSi. *Journal of Applied Physics*. 2009;**105**(7):07E901.
- [18]. Jamal, M. and G. City-Tehran-Iran, *IR ELAST*, 2014.
- [19]. Blaha P, Schwarz K, Madsen GK, Kvasnicka D, Luitz J. wien2k. An augmented plane wave+ local orbitals program for calculating crystal properties. 2001;60:1-302.
- [20]. Anderson, O.L., A simplified method for calculating the Debye temperature from elastic constants. *Journal of Physics and Chemistry of Solids*, 1963. **24**(7): p. 909-917.
- [21]. Watt, J.P. and L. Peselnick, Clarification of the Hashin-Shtrikman bounds on the effective elastic moduli of polycrystals with hexagonal, trigonal, and tetragonal symmetries. *Journal of Applied Physics*, 1980. **51**(3): p. 1525-1531.
- [22]. Haringa, J. and B. Cook. Comparison of different pressing techniques for the preparation of n-type silicon-germanium thermoelectric alloys. in *Fifteenth International Conference on Thermoelectrics. Proceedings ICT'96*. 1996. IEEE.
- [23]. Fine, M., L. Brown, and H. Marcus, Elastic constants versus melting temperature in metals. *Scripta metallurgica*, 1984. **18**(9): p. 951-956.
- [24]. Suzuki T, Chisnell R, Devarakonda A, Liu Y-T, Feng W, Xiao D, et al. Large anomalous Hall effect in a half-Heusler antiferromagnet. *Nature Physics*. 2016;**12**(12):1119-23.
- [25]. Frantsevich I, Kalinovich D, Kovenskii I, Smolin M. Electrotransport and diffusion in molybdenum-tungsten and iron-nickel alloys over wide ranges of temperatures. *Journal of Physics and Chemistry of Solids*. 1969;**30**(4):947-57.
- [26]. OUAHRANI,T.,CALCUL DES PROPRIÉTÉS STRUCTURALES, THERMIQUES ET OPTIQUES DES COMPOSÉS CHALCOPYRITES PAR LA MÉTHODE FP-(L) APW, 2011.
- [27]. Murnaghan, F.D., The compressibility of media under extreme pressures. *Proceedings of the National Academy of Sciences*, 1944. **30**(9): p. 244-247.

GENERAL CONCLUSION

Conclusion

In the present work, we performed a series of first-principal calculations based on the method of linearized augmented plane waves with total potential (FP-LAPW) implemented in Wien2k code. By utilizing the generalized gradient approximation GGA and TB-mBJ as exchange-correlation potential, we determine the structural, electronic, magnetic, and elastic properties of Heusler alloys, namely, ($K_2NaRbAs_2$, VPdSb, and VPtSb).

The structural optimization results showed that $K_2NaRbAs_2$ compounds crystallize in a tetragonal structure with P-4 m2 space group N°115 and VMSb crystallize in a cubic structure with F-43 m space group N°216, respectively. The study of the structural properties of the double half-Heusler $K_2NaRbAs_2$ demonstrated its stability through its negative formation energy. For the half-Heusler VMSb (M = Pd, Pt), compounds are half-metallic ferromagnetic (HMF) and stable in structure type III.

Elastic properties: Our results suggest that $K_2NaRbAs_2$ is a hard material with a high Young's modulus. We investigated the mechanical profile of $K_2NaRbAs_2$ and found it to be a ductile and anisotropic material. Additionally, the study found that both VPdSb and VPtSb compounds exhibit strong anisotropy, with the $\langle 111 \rangle$ direction being more rigid than the $\langle 100 \rangle$ and $\langle 110 \rangle$ directions.

electronic and magnetic properties: to determine these properties, we calculated the band structures and the partial and total densities of states. We have found that $K_2NaRbAs_2$ have a half-metallic ferromagnetic character based on the calculated total magnetic moment and have confirmed this through the band structure and DOS diagrams. Our study shows that the p-orbitals of arsenic atoms play a major role in the half-metallic ferromagnetism of this DHH alloys.

The results of the band structures, and the density of states (DOS) revealed that VPdSb, and VPtSb compounds exhibit a semiconductor with an indirect gap for the spin-down channels, and a metallic character for the spin up channels, which confirm the half-metallic character of the two compounds.

Despite applying pressure ranging from 0–20 GPa, there was no significant effect on the magnetic moments of the two compounds, indicating their resistance to pressure. The

magnetic properties of both compounds were consistent with the Slater-Pauling rule, indicating their ferromagnetic, half-metallic character.

The thermoelectric properties of $\text{K}_2\text{NaRbAs}_2$ DHH determined using the BoltzTraP code within the Wien2k program show that it has a significantly high Seebeck coefficient and excellent electrical conductivity in the spin-up and spin-dn channels at room temperature, suggesting its potential as a promising thermoelectric material.

Our study offers a comprehensive understanding of the properties and potential applications of $\text{K}_2\text{NaRbAs}_2$ DHH. We anticipate that these findings will encourage researchers to do further experimental and theoretical investigations on DHHs.

This work opens perspectives in materials science for the integration of these half-metallic compounds since it is possible to use them, with suitable conditions, as new candidates for applications in the field of spintronic devices.

Publication

Half-metallic character and thermoelectric properties of the $K_2NaRbAs_2$ double half Heusler alloy

F Sofrani^{1,2}, K Boudia^{1,3}, F Khelfaoui^{4*} , M Hamlat⁴, A Bouhemadou⁵, A Lorf⁶, A Hachilif⁷, F Belkharroubi⁸ and A Slamani⁶

¹University Ahmed Ben Yahia El-Wanchrissi, Tissemsilt, Algeria

²Laboratoire d'Etudes Physique Des Matériaux, Université Des Sciences Et de Technologies USTO-MB, BP El M'Naouar, 1505 Oran, Algérie

³Physical Engineering Laboratory, University of Tiaret, 14000 Tiaret, Algeria

⁴Laboratory of Physicochemical Studies, University of Saida-Dr. Moulay Tahar, 20000 Saida, Algeria

⁵Laboratory for Developing New Materials and Their Characterizations, Faculty of Sciences, Department of Physics, University of Ferhat Abbas Setif, 19000 Setif, Algeria

⁶Laboratory of Physico-Chemistry of Advanced Materials, University of Djillali Liabes, BP 89, 22000 Sidi-Bel-Abbes, Algeria

⁷Computational Materials Physics Laboratory (CMPL), University of Djillali Liabes, BP 89, 22000 Sidi-Bel-Abbes, Algeria

⁸Laboratory of Analysis and Application of Radiations (LAAR), Faculty of Physics, University of Science and Technology of Oran Mohamed Boudiaf (USTO-MB), 1505 El Menouar, 31000 Oran, Algeria

Received: 29 October 2022 / Accepted: 29 March 2023

Abstract: This paper presents an investigation of the properties of the double half Heusler alloy (DHH) $K_2NaRbAs_2$. The structural, elastic, electronic, magnetic, and thermoelectric properties of the alloy are studied using the full-potential linearized augmented plane wave method (FP-LAPW) with the generalized gradient GGA approximation, and the GGA + Modified Becke-Johnson (mBJ) correlation potential is used to calculate the band structures and densities of states. The $K_2NaRbAs_2$ DHH alloy is derived from the previously studied parent half Heusler alloys $KNaAs$ and $KRbAs$ in their ferromagnetic phase of type I structure (FM-I). Our findings confirm the thermodynamic stability and synthesizability of $K_2NaRbAs_2$ in normal conditions. The alloy is shown to be resistant to distortion and able to withstand reversible deformation. The calculated elastic constants indicate that $K_2NaRbAs_2$ is mechanically stable, ductile, and anisotropic, as confirmed by 3D representation of its elastic moduli. Furthermore, the total magnetic moment of $2 \mu_B$ demonstrates its half-metallic behavior, which mainly due to arsenic atoms. Like its parent alloys $KNaAs$, and $KRbAs$, the $K_2NaRbAs_2$ DHH alloy could be suitable for use in spintronic technology. Additionally, the thermoelectric characteristics of the $K_2NaRbAs_2$ DHH alloy are investigated using semi-classical Boltzmann transport theory, based on a smoothed Fourier interpolation of the bands, as implemented in the BoltzTraP package.

Keywords: Heusler alloy; Mechanical stability; Half-metallic gap; Spin-polarization; Magnetic properties

1. Introduction

Since its initial theoretical prediction, the Half-Metallic ferromagnetism (HMF) character has attracted enormous interest and has emerged as one of the most interesting areas of research. In recent years, researchers have

attempted to deepen their knowledge of the HMF behavior to understand, predict and create new half-metallic materials, due to their promising potential applications in spintronic devices[1], magnetic tunnel junctions, magnetic disk drives, spin injection devices and nonvolatile magnetic random access memories [2]. Ideal HM ferromagnet exhibits metallic nature in one spin channel (“up” or “down”) and semiconducting(or insulating) nature in the other spin channel, revealing a 100% spin polarization at

*Corresponding author, E-mail: friha.khelfaoui@univ-saida.dz

the Fermi level [3, 4] with an integer value of the magnetic moment. The HMF nature was first determined in NiMnSb and PtMnSb half Heusler alloys [3–5]. Since then the half-metallic character has been theoretically and experimentally discovered in many other materials such as perovskite oxides without transition metal LiBeO₃[6], KBeO₃ [7], KMgO₃ [8], rutile TiO₂ and VO₂ [9], spinels MgFe₂O₄[10], fluoro-perovskites Rb(Co/Fe)F₃ [11], double perovskite Sr₂CrWO₆ [12], and ternary oxides XMg₃O₄ (X = Li, Na, K, and Rb) [13]. Numerous Heusler alloys can be half-metals as quaternary Heusler TiZrIrZ (Z = Al, Ga and In)[14], full Heusler Zr₂PdZ (Z = Al, Ga, and In) [15] and half Heusler KNaAs, KRbAs[16]. Khandy et al. explored the equilibrium electronic structure of the transition-metal atom based Heuslers XTaZ (X = Pd, or Pt, Z = Al, Ga or In) for possible thermoelectric applications[17]. Recently, a novel class of Heusler alloys, named double half Heusler alloys (DHH), has been discovered, inspired by the conception of double perovskites A₂B'B''O₆. They could be thought of as collection of two half Heuslers of formula. It is worth noting that the first prediction of this class of materials was made by Anand et al.[18].

Half-Heusler materials have inherently high thermal conductivities, which limits their thermoelectric efficiency. To address this issue, Anand et al. investigated a large class of relatively unexplored DHH compounds, which have substantially lower lattice thermal conductivities due to their crystal chemistry. Their work presented a reliable method for identifying low-thermal-conductivity half-Heuslers and highlighted a broad composition space for their potential applications. This research has paved the way for the systematic discovery of additional families of sizable intermetallic semiconductors with diverse potential applications. [18].

In the context of predicting new double half Heusler alloys and understanding their physical properties, K₂NaRbAs₂ was investigated as a new compound in this family. This study presents the structural, elastic, electronic, magnetic, and thermoelectric properties of the K₂NaRbAs₂ DHH alloy, and compares them with those of its parent HH alloys KNaAs, KRbAs[16]. This paper is organized as follows: after the introduction, Sect. 2 outlines the used computational method. The results and discussion paragraph are presented in Sect. 3, followed by the conclusion in Sect. 4, where the main points of the paper are summarized.

2. Computational method

The properties of K₂NaRbAs₂ DHH compound, derived from its parent HH alloys KNaAs and KRbAs, were determined using density functional theory (DFT) with the

full potential linearized augmented plane wave (FP-LAPW) method [19], as implemented in the WIEN2k code[20]. The generalized gradient approximation (GGA) was used to treat the exchange and correlation effects [21]. The muffin-tin (MT) radii, chosen for K, Na, Rb, and As atoms, are 2.35 a.u., 2.35a.u., 2.35. a.u., and 2.23 a.u., respectively. The spherical harmonics were developed up to lmax = 10 within the MT spheres, and at 12, the Gaussian value Gmax was used. An energy cut-off value of RMT*Kmax = 8 was used in the interstitial region. The energy and charge convergences for the iteration procedure of self-coherence calculations were taken to be 10⁻⁴ e and 10⁻⁵ Ry, respectively. The First Brillouin zone (BZ) integration was performed using 1000 K-points by the tetrahedral method[22].

3. Results and discussions

3.1. Structural properties

The studied compound K₂NaRbAs₂ crystallizes in a tetragonal structure with P-4m2 space group N°115 (see Fig. 1).

To determine the stable magnetic phase, the optimization of both parent HH alloys was carried out within GGA in their ferromagnetic, non-magnetic, and antiferromagnetic phases [16], as shown in Fig. 2.

As shown in Fig. 2, the ferromagnetic phase of type I structure (FM-I) has the lowest total energy for both compounds, indicating that it is the energetically most stable phase compared to the non-magnetic (NM) and antiferromagnetic (AFM) phases at the equilibrium volume.

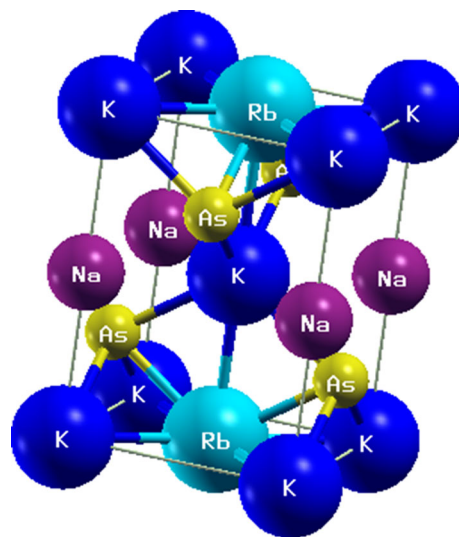


Fig. 1 Crystal structure of K₂NaRbAs₂ DHH alloy

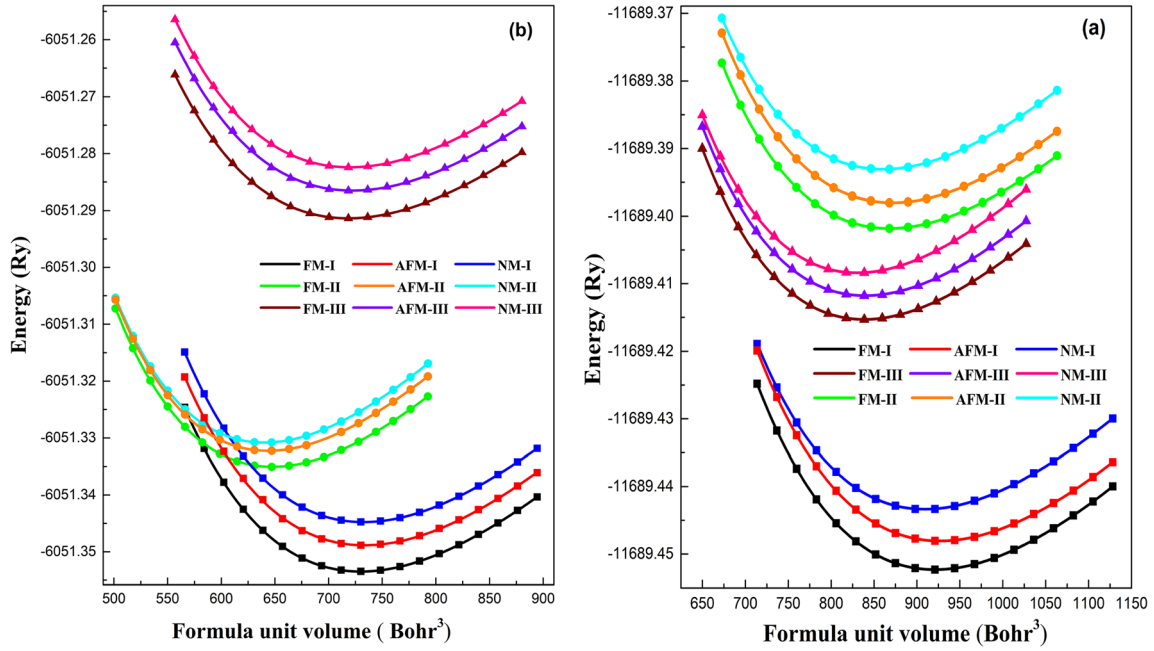


Fig. 2 Calculated Total Energy vs. Volume for FM, NM, and AFM Phases of (a) KRbAs and (b) KNaAs Compounds (color figure online)

From the obtained magnetic and structural ground states of KNaAs and KRbAs (FM-I), $K_2NaRbAs_2$ structure is constructed by substituting, in the conventional lattice of KNaAs, two Na atoms with Rb atoms. Consequently, only the FM phase of this acquired DHH structure is optimized, and as shown in Fig. 3, the optimized volume of $K_2NaRbAs_2$ is 1649.7486 (bohr³).

Then the structural parameters of the equilibrium are calculated by adjusting the total energy as a function of the volume, using the Birch Murnaghan equation of state [23].

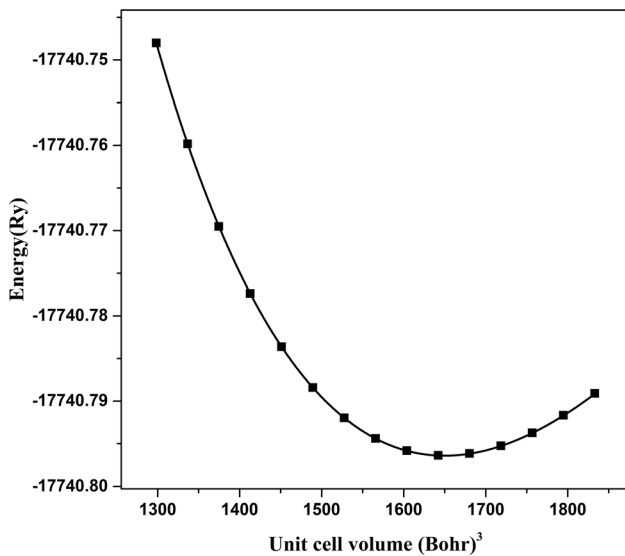


Fig. 3 Calculated total energy vs. Volume of $K_2NaRbAs_2$ compound

$$E(V) = E_0 + \frac{9V_0B_0}{16} \left\{ \left[\left(\frac{V_0}{V} \right)^{2/3} - 1 \right]^3 B'_0 + \left[\left(\frac{V_0}{V} \right)^{2/3} - 1 \right]^2 \left[6 - 4 \left(\frac{V_0}{V} \right)^{2/3} \right] \right\} \quad (1)$$

The resulted structural ground state of DHH has a parent HH with a lattice parameter of a_{HH} , which is equal to c_{DHH} , while $a_{DHH} = b_{DHH} = \frac{a_{HH}}{\sqrt{2}}$, corresponding to a, b and c values, as presented in Table 1.

The obtained parameters corresponding to the optimized structures for different magnetic phases of the equilibrium lattice parameter, bulk modulus, and its derivative, are given in Table 1. The formation energy is a useful norm to examine the synthesizability and stability of $K_2NaRbAs_2$ compound. The formation energy of $K_2NaRbAs_2$ in Table 1 has been evaluated from the following equation:

$$E_f(K_2NaRbAs_2) = E_{tot}(K_2NaRbAs_2) - 2E_{tot}(K) - E_{tot}(Na) - E_{tot}(Rb) - E_{tot}(As) \quad (2)$$

where $E_{tot}(K_2NaRbAs_2)$ is the total energy of $K_2NaRbAs_2$; while, $E_{tot}(K)$, $E_{tot}(Na)$, $E_{tot}(Rb)$ and $E_{tot}(As)$ correspond to the total energy for K, Na, Rb, and As, per atom, respectively. The obtained negative formation energy of -0.0642 Ry, for the studied compound, indicates that this material is thermodynamically stable. Therefore, it can be synthesized in the DHH structure.

Additionally, to verify the dynamic stability of the $K_2NaRbAs_2$ material, we calculated the phonon dispersion

Table 1 Calculated lattice parameter (\AA), B bulk modulus (GPa), B' its derivative pressure, and $E_{\text{formation}}$ formation energies (Ry) for $\text{K}_2\text{NaRbAs}_2$ in their FM phase with structure type I

Alloy	Phase	$a_{\text{HH}}(a_{\text{DHH}} = a_{\text{HH}}/\sqrt{2}, c_{\text{DHH}} = a_{\text{HH}})$	B (GPa)	B'	$E_{\text{formation}}$
HH: KNaAs[16]	FM	7.564	14.835	4.166	- 0.0381
	AFM	7.576	14.881	3.931	
	NM	7.573	14.972	4.086	
HH: KRbAs[16]	FM	8.173	11.117	4.253	- 0.0355
	AFM	10.319	10.931	4.055	
	NM	8.138	11.056	4.443	
DHH: $\text{K}_2\text{NaRbAs}_2$	FM	5.2917	12.6115	4.164	- 0.0642

diagram through the linear response method within the density functional perturbation theory (DFPT) as implemented in the CASTEP computational software [24]. The CASTEP computational code is an implementation of the pseudo potential plane-wave method (PP-PW) in the framework of density functional theory (DFT). To ensure sufficiently accurate total energy calculations, a plane-wave basis set cut-off of 770 eV and a $6 \times 6 \times 4$ Monkhorst–Pack scheme k-point grid for the integration over BZ were applied. The obtained phonon dispersions along lines of high symmetry in BZ are shown in Fig. 4. Note that absence of soft modes (imaginary modes; negative frequencies) in the phonon dispersion curve of a material implies its dynamic stability. Therefore, the absence of soft modes (negative frequencies) in the phonon dispersion curve of the title compound confirms its dynamical stability.

The *equilibrium* lattice constant (a_o), bulk modulus (B), its pressure derivative (B'), and formation energies ($E_{\text{formation}}$) of the compounds are listed in Table 1. The results, presented in Table 1, show that the bulk modulus (measure of compression resistance) diminishes as X atomic number rises.

3.2. Elastic properties

The mechanical behavior of crystals is strongly tied to their elastic properties, which enable us to examine crucial details about mechanical stability and comprehend the kind of forces in materials. Using the IRelast package, integrated into the WIEN2k code, the elastic constants are evaluated in order to check the mechanical stability of our compound.

Compounds, that have a tetragonal structure, have six independent elastic constants, denoted by; C_{11} , C_{12} , C_{13} , C_{33} , C_{44} and C_{66} , are necessary and sufficient to characterize the elastic behavior of the $\text{K}_2\text{NaRbAs}_2$ alloy. The

mechanical stability of a tetragonal structure requires that Born's stability criteria be satisfied [25].

$$(C_{11} - 2C_{12}) > 0,$$

$$(C_{11} + C_{33} - 2C_{13}) > 0,$$

$$(2C_{11} + C_{33} + 2C_{12} + 4C_{13}) > 0,$$

$$C_{11} > 0, C_{33} > 0, C_{44} > 0, C_{66} > 0 \quad (3)$$

The obtained elastic constants satisfied all the Born's stability criteria. So; The $\text{K}_2\text{NaRbAs}_2$ alloy is confirmed to be mechanically stable. The computed C_{ij} constants are given in Table 2. The following formulae can be used to estimate various mechanical quantities such as Bulk (B), shear (G), Young's (E) moduli, anisotropic factor and Poisson's ratio:

$$B = (2C_{11} + C_{33} + 2C_{12} + 4C_{13})/9 \quad (4)$$

$$G = \frac{2C_{11} + C_{33} - C_{12} - 2C_{13} + 6C_{44} + 3C_{66}}{15} \quad (5)$$

$$E = \frac{9BG}{(G + 3B)} \quad (6)$$

$$\nu = \frac{(3B - 2G)}{[2(3B + G)]} \quad (7)$$

It can be observed that the bulk modulus value, determined by Eq. (4), calculated through the elastic constants of the studied alloy is fairly in agreement with that obtained from the total energy optimization.

The estimated data shows that $\text{K}_2\text{NaRbAs}_2$ can resist reversible deformation brought on by shear stress and can endure distortion better than its parent HHs.

To evaluate the brittleness and ductility of a material, it is necessary to calculate B/G ratio, where the critical value which separates the ductile and brittle behavior is equal to 1.75 (brittle $< 1.75 <$ ductile) [26]. According to Pugh's analysis, the B/G ratio, for $\text{K}_2\text{NaRbAs}_2$ DHH alloy, exceeds 1.75, indicating that it falls into the ductile

category. This result is consistent with our previous findings on the KNaAs and KRbAs HH alloys[16], which are the parent materials of the $K_2NaRbAs_2$ DHH alloy.

Machinability is the ability of a metal to be cut to remove material with a satisfactory finish at low cost. Materials with good machinability (free machining materials) require low cutting power, obtaining a good finish and without significant tool wear. Factors that typically improve a material's performance often degrade its machinability, presenting a significant engineering challenge. The machinability index, μ_M of a material is defined by B/C_{44} . The useful material, with a high machinability, should be strong (i.e. high bulk modulus) and malleable (i.e. low C_{44})[27]. The calculated machinability indices are in the sequence: $K_2NaRbAs_2 < KRbAs < KNaAs$, as shown in Table 2.

Hardness (H) is a measure of the resistance to a plastic deformation in the field of materials science, which is the opposite of softness. Strong intermolecular bonds typically describe a macroscopic hardness. Ductility, elastic stiffness, plasticity, deformation, strength, toughness, viscoelasticity, and viscosity are all factors that affect hardness. H is expressed by[28]:

$$H = \frac{(1 - 2\nu)E}{6(1 + \nu)} \quad (8)$$

The $K_2NaRbAs_2$ DHH has a highest hardness of 0.53 GPa, compared to those of their parents HHs, illustrated in Table 2.

The Zener contrast factor is strongly correlated with the possibility of inducing micro cracks in materials, and it is an important physical quantity that informs us about the structural stability. For an isotropic system, A equals the unity, and the divergence from it measures the degree of elastic anisotropy. One may observe, from Table 2, that the $K_2NaRbAs_2$ DHH is more anisotropic than its parent HHs. Poisson's ratio (ν) is a useful parameter for understanding the nature of a compound's bonding forces. The calculated value of ν for the $K_2NaRbAs_2$ DHH alloy is 0.33, which

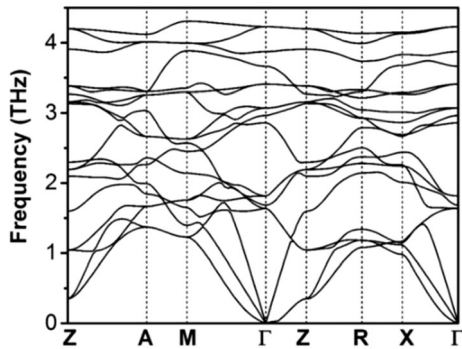


Fig. 4 Phonon dispersion curve of the $K_2NaRbAs_2$ compound

falls within the range of 0.25 to 0.5 observed in its HH parent compounds. This suggests that the bonding in this alloy has an ionic character.

In fact, three-dimensional surfaces can also be used to describe the anisotropy of a material in specific directions. For that, the software MATrix LABORatory, which is made and published by J. Nordmann et al.[29], was used to plot the 3D anisotropic bulk, Young's and shear moduli as well as Poisson's ratio surfaces. It is worth mentioning that this software was used for the first time by H. Bouafia et al. [30] for the LuAuSn HH alloy. For a tetragonal system, the expressions of the elastic moduli are, as follows:

$$\frac{1}{B} = (S_{11} + S_{12} + S_{13}) - (S_{11} + S_{12} - S_{13} - S_{33})l_3^2 \quad (9)$$

$$\frac{1}{E} = S_{11}(l_1^4 + l_2^4) + (2S_{13} - S_{44})(l_1^2l_3^2 + l_2^2l_3^2) + S_{33}l_3^4 + (2S_{12} + S_{66})l_1^2l_2^2 \quad (10)$$

$$\frac{1}{G} = S_{44} + \left[(S_{11} - S_{12}) - \frac{S_{44}}{2} \right] (1 - l_3^2) + 2(S_{11} + S_{33} - 2S_{13} - S_{44})l_3^2(1 - l_3^2) \quad (11)$$

where $\begin{pmatrix} l_1 \\ l_2 \\ l_3 \end{pmatrix} = \begin{pmatrix} \sin\theta\cos\varphi \\ \sin\theta\sin\varphi \\ \cos\theta \end{pmatrix}$, and S_{ij} is compliance coefficient.

$$B_V = [2(C_{11} + C_{12}) + C_{33} + 4C_{13}]/9 \quad (12)$$

$$G_V = [M + 3C_{11} - 3C_{12} + 12C_{44} + 6C_{66}]/30 \quad (13)$$

$$B_R = C^2/M \quad (14)$$

$$G_R = 15\{(18B_V/C^2) + [6/(C_{11} - C_{12})] + (6/C_{44}) + (3/C_{66})\}^{-1} \quad (15)$$

where $C^2 = (C_{11} + C_{12})C_{33} - 2C_{13}^2$; $M = C_{11} + C_{12} + 2C_{33} - 4C_{13}$

$$B_H = (B_V + B_R)/2 \quad (16)$$

$$G_H = (G_V + G_R)/2 \quad (17)$$

The Young's modulus (E), Poisson's ratio (ν) and Zener anisotropic factor are computing with the following equations:

$$E_H = \frac{9B_H G_H}{3B_H + G_H} \quad (18)$$

$$\nu = \frac{3B_H - 2G_H}{2(3B_H + G_H)} \quad (19)$$

$$A^U = 5\frac{G_V}{G_R} + \frac{B_V}{B_R} - 6 \quad (20)$$

The 3D surface of an isotropic system would have a spherical shape; therefore any deviation from that shape reflects the degree of anisotropy. As per Fig. 5, the surfaces

Table 2 Calculated elastic constants C_{11} , C_{12} , C_{13} , C_{33} , C_{44} , C_{66} , bulk B , machinability index B/C_{44} , Shear G , Young E moduli, hardness H (in GPa), anisotropic parameter A , B/G , Poisson's ratio ν , for $K_2NaRbAs_2$ in its structural and magnetic ground states

Compound	B	C_{11}	C_{12}	C_{13}	C_{33}	C_{44}	B/C_{44}	C_{66}	G	E	A	B/G	ν	H
KNaAs[16]	14.20	16.40	13.10	//	//	4.46	3.18	//	2.99	8.39	2.70	4.74	0.40	0.20
KRbAs[16]	12.08	17.96	9.14	//	//	4.16	2.90	//	4.26	11.43	0.94	2.84	0.34	0.45
$K_2NaRbAs_2$	12.20	18.27	7.78	9.90	18.32	5.86	2.08	3.37	4.71	12.53	0.27	2.59	0.33	0.53

of (B), (E) and (G) moduli and (ν) clearly deviate from a spherical shape, which represents the clear elastic anisotropy of $K_2NaRbAs_2$.

Among these mechanical properties, the bulk modulus of $K_2NaRbAs_2$ is nearly isotropic. This is evident in 3D representation (refer to Fig. 5(a)) which appears almost spherical (i.e. not spherical), as expected for a tetragonal structure. For the Young's modulus, we can observe a significant deviation from the sphere shape along the $\langle 111 \rangle$ direction, whereas for the shear modulus and Poisson's ratio, the deformation is along $\langle 001 \rangle$ direction.

The universal anisotropy index A^U , which is determined by the upper and lower limits of the bulk and shear moduli, is expressed by Eq. (20). The crystal displays isotropic behavior when A^U is equal to zero, and any deviation from this value indicates elastic anisotropy. Our compound exhibits elastic anisotropy, as its computed value of A^U was found to be 0.27. As far as we know, there is no theoretical or experimental information about the $K_2NaRbAs_2$ DHH to compare with.

The Calculation of the elastic constants has an impact on how the materials behave when heated; as a result, we can assess several thermal properties, such as the Debye temperature and melting temperature, which are listed in Table 3. The Debye temperature (θ_D) is calculated, using the equation below[26]:

$$\theta_D = \frac{h}{k_B} \left[\frac{3}{4\pi V_0} \right]^{1/3} v_m \quad (21)$$

where h is Planck's constant, k_B is Boltzmann's constant, V_0 is the average atomic volume, and v_m is the average sound wave velocity, which depends on the transverse (v_t) and longitudinal (v_l) sound velocities [31]:

$$v_m = \left[\frac{1}{3} \left(\frac{2}{v_t^3} + \frac{1}{v_l^3} \right) \right]^{-1/3} \quad (22)$$

and these are given by the equations, as follows:

$$v_l = \sqrt{\frac{3B + 4G}{3\rho}} \quad (23)$$

and

$$v_t = \sqrt{\frac{G}{\rho}} \quad (24)$$

where ρ is the density. The outcomes of our calculations are given in Table 3.

3.3. Electronic properties

In order to provide a more accurate description of the electron profile, the following electronic properties were examined at the equilibrium lattice constant using the GGA approach.

3.3.1. Band structures

Figure 6 shows the spin-polarized band structures for the compound $K_2NaRbAs_2$, calculated by GGA and TB-mBJ approximations. These are drawn along the high symmetry points in the first Brillouin zone.

We can see, for the spin down states of $K_2NaRbAs_2$, a metallic character due to the intersection of the valence bands with the Fermi level. On the other hand, for the spin-up channel, the compound exhibits a semiconductor character. In this channel (spin-up), one can observe that the compound $K_2NaRbAs_2$ has indirect band gaps of 1.40 and 2.62 eV, calculated by GGA and TB-mBJ approximations. The half-metallic gap (HMGap) is inferred from the valence band maximum (VBM) which is closer than conduction band minimum (CBM) to the Fermi level. The obtained half-metallic gap values are 0.34 and 0.39 eV for GGA and TB-mBJ methods, respectively. Therefore, we can see that the TB-mBJ method opens the band gap, located at high symmetry points Γ and X, for the valence band maximum (VBM), and conduction band minimum (CBM), respectively.

3.3.2. Densities of electronic states:

To explain the contribution of the different electronic states to the band structures, it is necessary to determine the total (TDOS) and partial (PDOS) densities of states. In order to find out which states are responsible for the bond. The

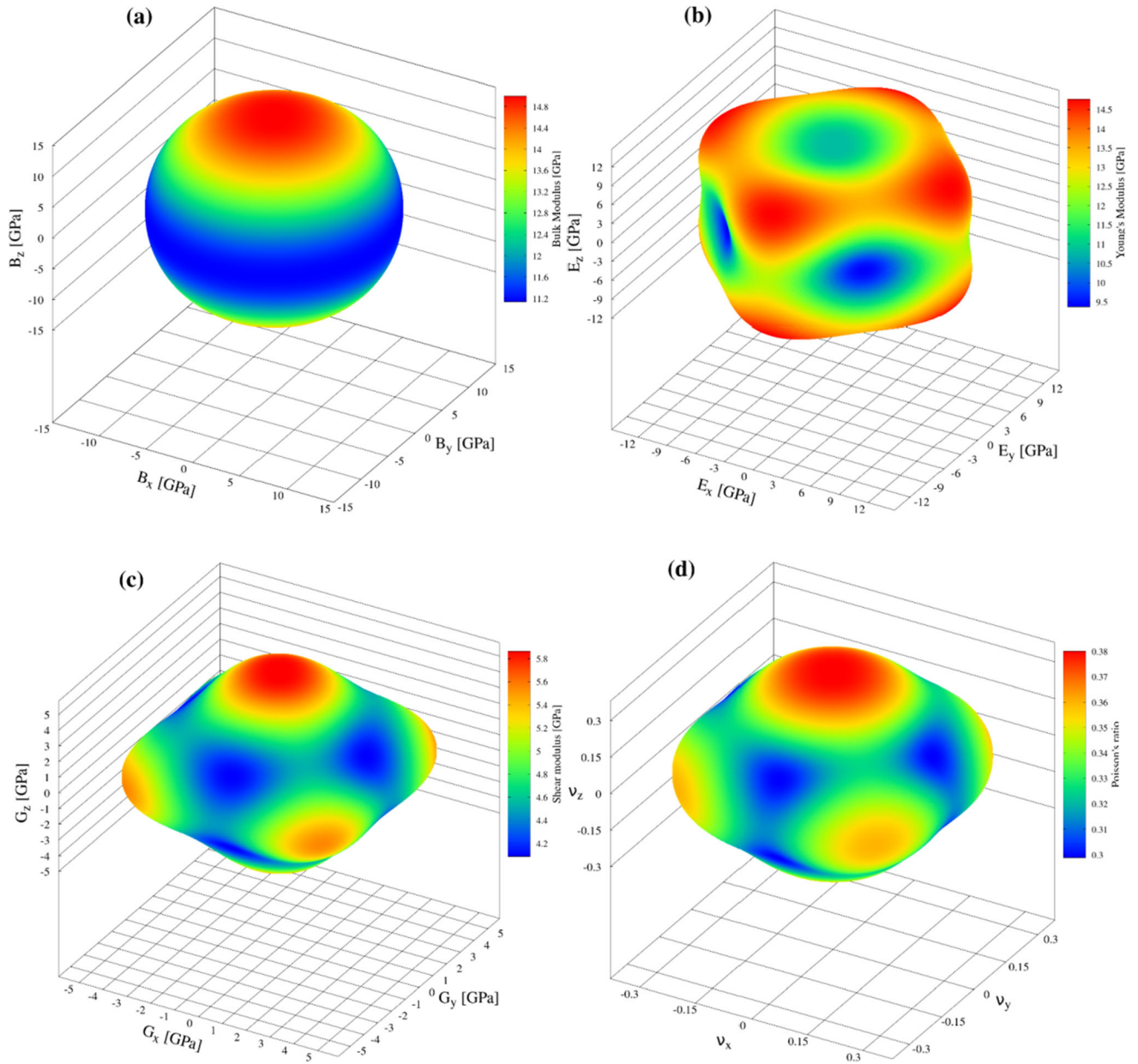


Fig. 5 3D graphical representation of (a) Bulk, (b) Young's and (c) Shear moduli and (d) Poisson's ratio of DHH $K_2NaRbAs_2$ (color figure online)

Table 3 Calculated longitudinal (v_l), transverse elastic wave velocities (v_t), average acoustic (v_m) velocities (in m/s), Debye (θ_D) and melting (T_m) temperatures (in K) of $K_2NaRbAs_2$ in its structural and magnetic ground states

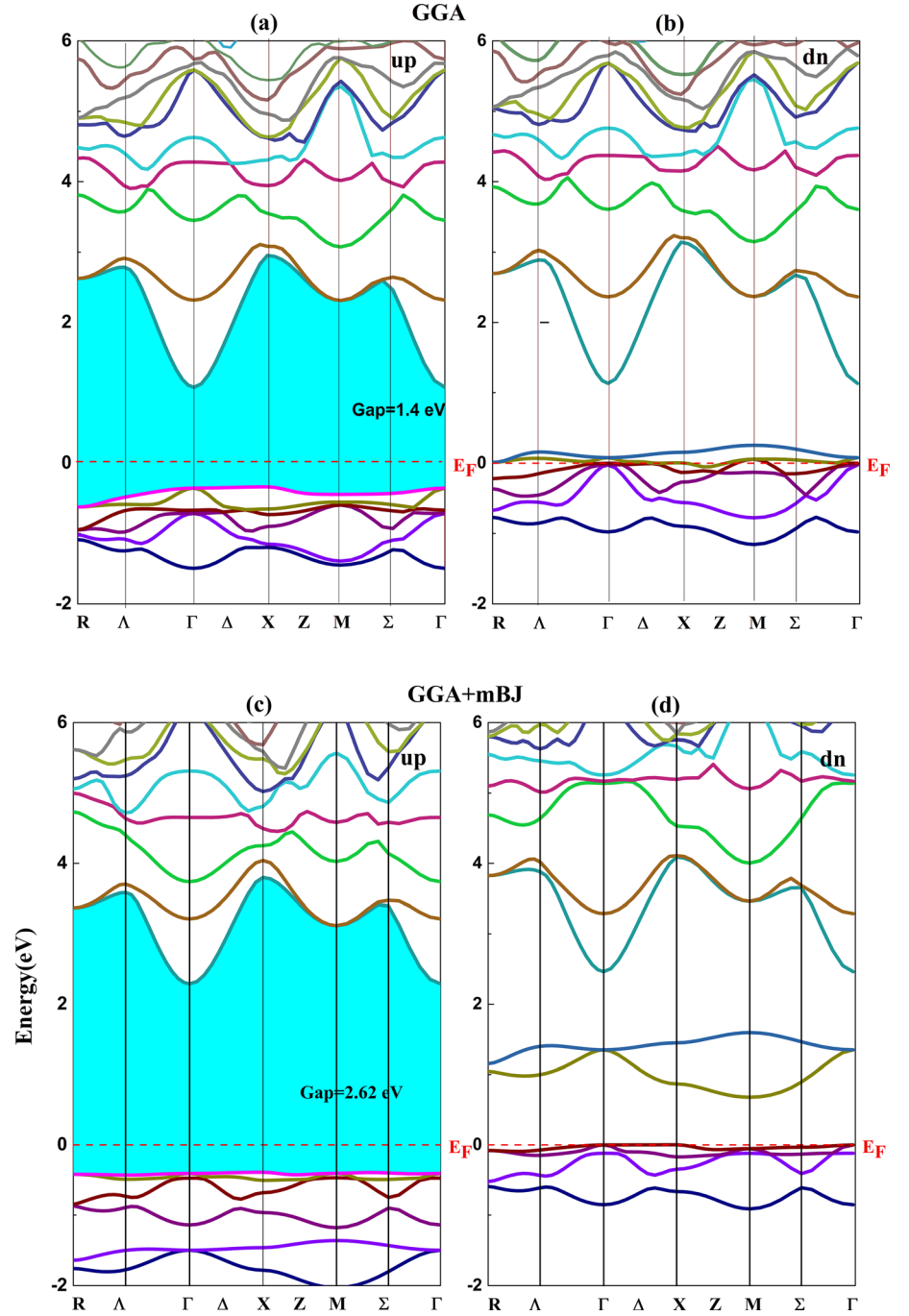
Compound	$v_l(m/s)$	$v_t(m/s)$	$v_m(m/s)$	$\theta_D(K)$	T_m
KNaAs[16]	2941.36	1193.26	1351.07	121.746	649.9393
KRbAs[16]	2705.1	1324.81	1487.96	124.094	622.1995
$K_2NaRbAs_2$	2843.92	1436.11	1610.09	139.307	436.297

TDOS and PDOS are calculated for both spin channels (i.e. spin-up and spin-dn), as shown in Fig. 7.

From both approaches, GGA, and GGA + mBJ, The PDOSs show that spin-exchange splitting, fundamentally originated from p states of Arsenic As atoms, which mainly contribute to the TDOS for the spin-up and-down channels, around the Fermi level.

This exchange splitting causes the spin-polarization of 100%, obtained by:

Fig. 6 Calculated band structure of $K_2NaRbAs_2$ compound in both (a), (c) Spin-up and (b, d) spin-down states by (a, b) GGA and (c), (d) GGA + mBJ approximations



$$P = \frac{|\rho_{\uparrow}(E_F) - \rho_{\downarrow}(E_F)|}{\rho_{\uparrow}(E_F) + \rho_{\downarrow}(E_F)} \quad (25)$$

where $\rho_{\uparrow}(E_F)$ and $\rho_{\downarrow}(E_F)$ are the spin-dependent densities of states at E_F , (\uparrow) and (\downarrow) represent spin-up and spin-down states, respectively. P equals zero for paramagnetic or antiferromagnetic materials. As shown in Fig. 7, our studied material is fully spin-polarized (i.e. $P = 100\%$), indicating a half-metallic character of the studied alloy. However, the s and p states of K , Na atoms as well as $Rb-d$

have little contributions to the TDOS for both spin channels, around E_F .

3.4. Magnetic properties

To describe the spin effect on the considered material, we have computed its magnetic properties. The local, interstitial, and total magnetic moments for the DHH $K_2NaRbAs_2$ alloy, estimated by employing GGA approach are grouped in Table 4. It is noticeable that the total magnetic

Fig. 7 Calculated DOS of $K_2NaRbAs_2$ compound for both spin-up and spin-down states by GGA and GGA + mBJ approximations (color figure online)

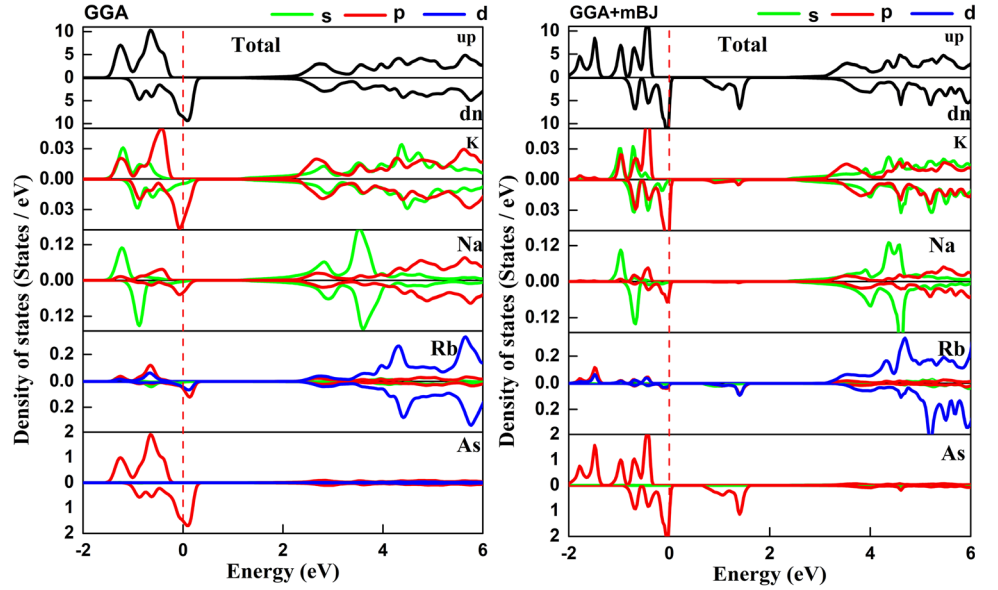


Table 4 Calculated total, atom-resolved and interstitial magnetic moments (in μ_B) in the unit cell for $K_2NaRbAs_2$ in its structural and magnetic ground states

Compound	M_{tot}	M_K	M_{Na}	M_{Rb}	M_{As}	M_{int}
KNaAs[16]	1.000	0.017	0.001	–	0.420	0.562
KRbAs[16]	1.000	0.010	–	0.016	0.399	0.575
$K_2NaRbAs_2$	2.000	0.013	–0.004	0.033	0.422	1.100

moment of the investigated compound has an integer value of $2\mu_B$ per unit cell which fulfills the necessary condition of a half-metallic behavior. According to Table 4, the primary source of the total magnetic moment in $K_2NaRbAs_2$ is the As atom, which is consistent with the findings of previous studies on its parent HH alloys, KNaAs and KRbAs [16].

3.5. Thermoelectric properties:

Thermoelectricity has recently gained popularity as an ‘‘environmentally friendly’’ technique because it does not use moving parts or chemical reactions resulting in no waste matter. The efficiency of a thermoelectric material is determined by the dimensionless parameter ZT , figure of merit, which is given by: $ZT = \frac{\sigma S^2 T}{\kappa}$, where σ is the electrical conductivity, S is the Seebeck coefficient, κ is the thermal conductivity of the material and T is the temperature in K.

A substance with a high Seebeck coefficient S , high electric conductivity, and low thermal conductivity is ideal for thermoelectric applications. Many recent investigations on HHs demonstrated that they have high energy factors

($S^2\sigma$), leading scientists to concentrate their study on these materials.

In this part, we thoroughly examine the thermoelectric behavior of the considered DDH alloy to determine if it can function as a thermoelectric material. So, we employed semi-classical Boltzmann transport theory, based on a smoothed Fourier interpolation of the bands, as implemented in the BoltzTraP code, to investigate the thermoelectric characteristics of $K_2NaRbAs_2$ DDH alloy. In the temperature range, from 150 to 1000 K, thermal (κ_c/τ), electrical conductivity (σ/τ), and Seebeck coefficient (S) were calculated.

The energy spectral density of the electrical conductivity is given by the following equation:

$$\bar{\sigma}_{\alpha\beta}(\varepsilon) = \frac{e^2}{N} \sum_{i,k} \tau_{i,k} v_{\alpha}(i,k) v_{\beta}(i,k) \frac{\delta(\varepsilon - \varepsilon_{i,k})}{\delta(\varepsilon)} \quad (26)$$

where α and β are the coordinate components, i is the electronic band number, k is the wave vector, N is the total number of k points, e is the elementary charge, τ is the relaxation time of the charge carrier, and ε is the band energy. Also, the group velocity v is:

$$v_{\alpha}(i, k) = \frac{1}{\hbar} \frac{\partial \varepsilon_{i,k}}{\partial k_{\alpha}} \quad (27)$$

Using Eq. (27), the conductivity tensor $\sigma_{\alpha\beta}$ can be written as a function of temperature T and Fermi level μ as follows:

$$\sigma_{\alpha\beta}(T, \mu) = \frac{1}{\Omega} \int \tilde{\sigma}_{\alpha\beta}(\varepsilon) \left[-\frac{\partial f(T, \varepsilon, \mu)}{\partial \varepsilon} \right] d\varepsilon \quad (28)$$

In Eq. (28), Ω is the unit cell volume and f is the Fermi-Dirac distribution. Similarly, the Seebeck coefficient tensor $S_{\alpha\beta}$ can be written as:

$$S_{\alpha\beta}(T, \mu) = \frac{1}{eT\Omega\sigma_{\alpha\beta}(T, \mu)} \int \tilde{\sigma}_{\alpha\beta}(\varepsilon) (\varepsilon - \mu) \left[-\frac{\partial f(T, \varepsilon, \mu)}{\partial \varepsilon} \right] d\varepsilon \quad (29)$$

The Seebeck coefficient of materials with holes (p-type materials), as dominant charge carriers, is positive whereas it is negative for n-type materials (i.e. electrons as dominant charge carriers).

Figure 8 shows that the Seebeck coefficient (S), in the spin-dn channel, decreases as the temperature rises, while the opposite trend is observed in the spin-up channel. Specifically, at ambient temperature (300°K), S is 1259.3. $\mu\text{V}/\text{K}$ in the spin-up state, confirming the electrons are the majority carriers. In addition, the S coefficient is 57.9.. $\mu\text{V}/\text{K}$ in the spin-dn state; suggesting a high positive spin-up Seebeck coefficient in the $\text{K}_2\text{NaRbAs}_2$ DDH alloy. These findings indicate that this DDH material is of p-type.

Figure 9 depicts the Fermi level plot of the electrical conductivity per relaxation time (σ/τ) of $\text{K}_2\text{NaRbAs}_2$ as a function of temperature for both spin channels. In the spin-up channel, the electrical conductivity remains relatively

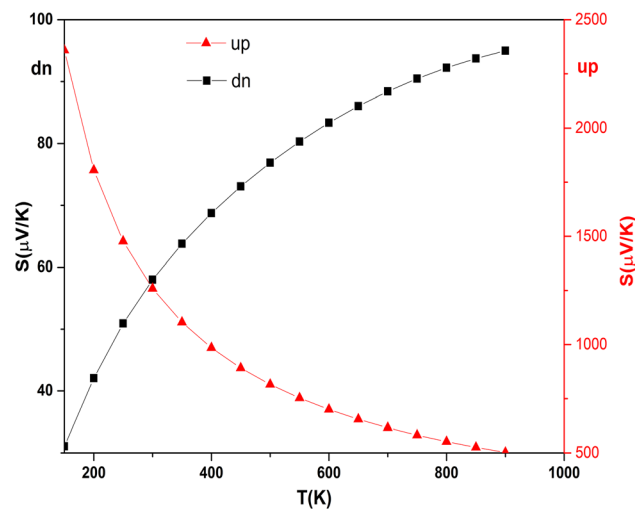


Fig. 8 Temperature dependence of the Seebeck coefficient of the spin-up and spin-dn channels of $\text{K}_2\text{NaRbAs}_2$ (color figure online)

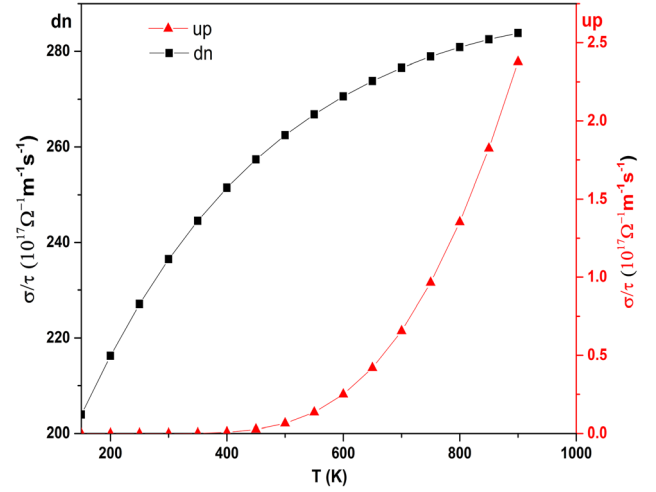


Fig. 9 Temperature dependence of the electrical conductivity for the spin up and spin dn channels of $\text{K}_2\text{NaRbAs}_2$ (color figure online)

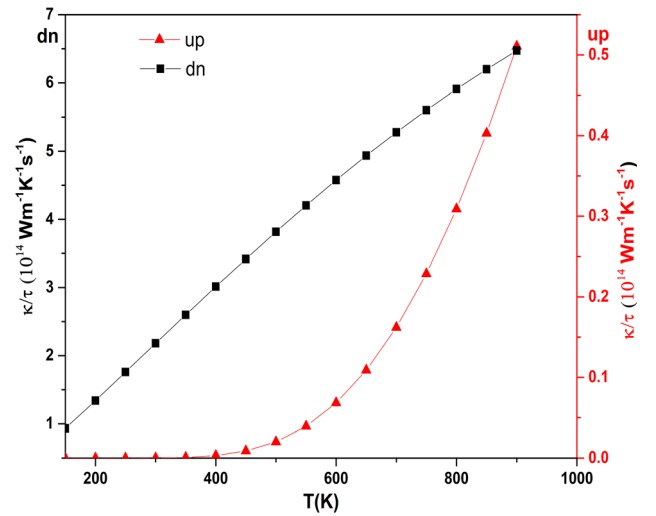


Fig. 10 Temperature dependence of the electronic thermal conductivity in the spin-up and spin-dn channels of $\text{K}_2\text{NaRbAs}_2$ DDH alloy (color figure online)

constant up to a particular temperature threshold (400 °K), after which it starts to increase. In contrast, in the spin-dn channel, the σ/τ value increases with rising temperature.

The σ/τ value in the spin-up state for the DHH at room temperature (300°K) is 0 while, in the spin-dn state, it is $236.4810^{17}\Omega^{-1} \text{m}^{-1} \text{s}^{-1}$. Due to lower DOS values at Fermi level, the electrical conductivity values for the spin-up channel are lower than those of the spin-down channel. These results demonstrate a high electrical conductivity and, consequently, a low resistivity of this material.

Figure 10 displays the temperature dependence, for both spin-up and spin-down channels, of the electronic thermal conductivity, scaled by the relaxation time. This is similar in character to σ/τ , as is due to the thermal excitation of electrons at higher temperatures, leading to increase heat

conduction. In the examined alloy, a linear increase in κ_e/τ' is observed for temperatures above approximately 600 K.

4. Conclusions

In this paper, we have presented a comprehensive theoretical investigation of the structural, elastic, magnetic, and electronic properties of the new DHH alloy $K_2NaRbAs_2$ using the FP-LAPW method with GGA and GGA + mBJ approximations. Our study has yielded several important findings, which are summarized below:

Firstly, we have determined the structural ground state of $K_2NaRbAs_2$ and demonstrated its stability through the negative formation energy and calculated elastic constants. We have also shown that this DHH alloy can withstand distortion better than its reported parent $KNaAs$ and $KRbAs$ HHs, and can resist reversible deformation carried on by shear stress. Our results suggest that $K_2NaRbAs_2$ is a hard material with high Young's modulus. Secondly, we have predicted a half-metallic ferromagnetic character in $K_2NaRbAs_2$ based on the calculated total magnetic moment, and have confirmed this through the band structure and DOS diagrams. Our study shows that the p-orbitals of Arsenic atoms play a major role in the half-metallic ferromagnetism for this DHH alloy. Thirdly, we have investigated the mechanical profile of $K_2NaRbAs_2$ and found it to be a ductile and anisotropic material. Fourthly, the calculation of the thermoelectric properties of $K_2NaRbAs_2$ DHH, using the BoltzTraP code within the Wien2k program, shows that it has a significantly high Seebeck coefficient and excellent electrical conductivity in the spin up and spin-down channels at room temperature, suggesting its potential as a promising thermoelectric material. Finally, we have discussed the potential of $K_2NaRbAs_2$ DHH for future spintronic applications.

Our study offers a comprehensive understanding of the properties and potential applications of $K_2NaRbAs_2$ DHH. We anticipate that these findings will encourage researchers to do further experimental and theoretical investigations on DHHs.

References

- [1] S Wolf, D Awschalom, R Buhrman, J Daughton, V S von Molnár, M Roukes, A Y Chtchelkanova and D Trege *Science*. **294** 1488 (2001)
- [2] S Terkhi, R Bentata, F Bendahma, T Lantri, S Bentata, Z Aziz and B Abbar *Indian J Phys* **95** 833 (2021)
- [3] R De Groot, F Mueller, P Van Engen and K Buschow *Phys Rev Lett* **50** 2024 (1983)
- [4] C Vargas-Hernández and R B Cruz *Comp Condens Matter* **4** 1 (2015)
- [5] R De Groot, F Mueller, P Van Engen and K Buschow *J Appl Phys* **55** 2151 (1984)
- [6] F Khelifaoui, K Amara, H Boutaleb, M Hamlat, K Boudia, Y S Abderrahmane and N Marbough *Comp Condens Matter* **21** e00399 (2019)
- [7] M Hamlat, K Amara, K Boudia and F Khelifaoui *Condens Matter Phys* **23** 33601 (2020)
- [8] M Hamlat, K Boudia, K Amara, F Khelifaoui and N Marbough *Comp Condens Matter* **23** e00456 (2020)
- [9] V Pardo and W E Pickett *Phys Rev Lett* **102** 166803 (2009)
- [10] S Ali, H Ullah and A A AlObaid *Eur Phys J Plus* **136** 1 (2021)
- [11] M R ur rehman Hashmi, M Zafar, M Shakil, A Sattar, SAHmed, S Ahmad *Chin . Phys. B* **.25** 11 7401(2016)
- [12] J Philipp, D Reisinger, M Schonecke, A Marx, A Erb, L Alff and R Gross *Appl Phys Lett* **79** 3654 (2001)
- [13] T Nouri, F Khelifaoui, Y Benallou, H Lakhdari, K Amara, H Boutaleb and M Dahmani *Appl Phys A* **127** 232 (2021)
- [14] H Hocine, K Amara and F Khelfaou *Appl. Phys. A*. **126** 178 (2020)
- [15] F Khelifaoui, A Boudali and A Bentayeb *Acta Phys Pol* **133** 1 (2018)
- [16] A Lorf, K Boudia, F Khelifaoui, K Amara and O Sadouki *M Ameri Spin* **11** 2150010 (2021)
- [17] S A Khandy *Sci. Rep.* **11**(1) 20756 (2021)
- [18] S Anand, M Wood, Y Xia and C Wolverton *Joule*. **3** 1226 (2019)
- [19] P Hohenberg and W Kohn *Phys Rev* **136** B864 (1964)
- [20] P Blaha, K Schwarz and P Sorantin *Comput Phys Commun* **59** 399 (1990)
- [21] Z Wu and R E Cohen *Phys Rev B* **73** 235116 (2006)
- [22] H J Monkhorst and J D Pack *Phys Rev B* **13** 5188 (1976)
- [23] F Birch *J. Appl. Phys.* **9** 279 (1938)
- [24] S J Clark, M D Segall, C J Pickard, P J Hasnip, M I Probert, K Refson, M C Payne, *Z. fur Krist. – Cryst.* **220** 567 (2005)
- [25] F Mouhat and F X Coudert *Phys Rev B* **90** 224104 (2014)
- [26] S Pugh and X C I I Lond *Edinb Dublin Philos Mag J Sci* **45** 823 (1954)
- [27] M Cover, O Warschkow, M Bilek and D McKenzie *J Phys Condens Matter* **21** 305403 (2009)
- [28] M Naher and S Naqib *Sci Rep* **11** 1 (2021)
- [29] J Nordmann and M Aßmus *Contin Mech Thermodyn* **30** 689 (2018)
- [30] H Bouafia, B Sahli, M Bousmaha, B Djebour, A Dorbane and S Mokrane *Solid State Sci.* **118** 106677 (2021)
- [31] M J Mehl *Phys. Rev. B* **47** 2493 (1993)

Publisher's Note Springer Nature remains neutral with regard to jurisdictional claims in published maps and institutional affiliations.

Springer Nature or its licensor (e.g. a society or other partner) holds exclusive rights to this article under a publishing agreement with the author(s) or other rightsholder(s); author self-archiving of the accepted manuscript version of this article is solely governed by the terms of such publishing agreement and applicable law.



Theoretical Study of the Structural, Magnetic, Electronic and Elastic Properties of VSb-Based Half-Heusler Alloys

Fatima Sofrani^{1,2} · Keltouma Boudia^{1,3} · Abderrahmane Cheriet⁴ · Akram Alhussiene⁵ · Linda Aissani⁶

Received: 25 February 2023 / Accepted: 19 April 2023
© The Minerals, Metals & Materials Society 2023

Abstract

Using density functional theory (DFT), the equilibrium structural parameters, electronic, magnetic, and elastic properties of VMSb (M = Pd, Pt) half-Heusler compounds were investigated in this study. Calculations were performed using the full-potential linearized augmented plane wave (FP-LAPW) method, with the Wu-Cohen generalized gradient approximation (WC-GGA). Additionally, the electronic band structures and density of states were calculated using exchange and correlation potentials such as Tran-Blaha modified Becke-Johnson (TB-mBJ) and local spin density approximation with the on-site Coulomb interaction parameter U (LSDA+U). The theoretical results showed that the two half-Heusler compounds VMSb (M = Pd, Pt) exhibit half-metallic ferromagnetism with a total magnetic moment of $2.000 \mu_B$ per formula unit, consistent with the Slater-Pauling rule. The electronic calculations revealed that VPdSb and VPtSb have spin-down band gaps of 0.45 eV, 0.51 eV and 0.54 eV, 0.58 eV, respectively, by LSDA+U, TB-mBJ. These half-Heusler compounds are promising candidates for potential applications in spintronic devices, as they offer an effective approach for magnetic and electronic appliances.

Keywords FP-LAPW · LSDA+U · TB-mBJ · half-metallicity · magnetic properties

Introduction

The development of new materials with 100% spin polarization around the Fermi surface has become a significant research area, as these materials have potential applications in spintronics,¹ superconductivity,² shape memory,³ and spin injection in semiconductors.^{4,5} Heusler alloys, which consist

of non-magnetic metals in their pure state, are a promising candidate for achieving such properties. In 1903, Fritz Heusler first proposed the idea of producing ferromagnetic alloys composed of non-ferromagnetic elements such as manganese and group B elements such as aluminium and antimony.⁶ The discovery of the first half-metallic ferromagnetic material, NiMnSb, by Groot in 1983, marked a significant milestone in the research of Heusler alloys.⁷

Recently, researchers have studied the electronic, magnetic, half-metallic, and structural properties of various Heusler alloys, including CoTiSb and TiNiSn.^{8,9} These alloys exhibit different physical characteristics, and they are classified as intermetallic compounds with the stoichiometric composition X_2YZ , which crystallize in the L_{21} structure. In addition, the half-Heusler type XYZ compounds, which crystallize in the C_{1b} phase, have also been widely investigated. These compounds have Wyckoff positions, with X in position 4a, Y in position 4c, and Z in position 4b.^{10,11} The half-Heusler phase has attracted the attention of many researchers because of its ability to easily adopt a ternary composition.¹²

In this study, the authors used full-potential linearized augmented plane wave (FP-LAPW) and generalized gradient approximation (GGA) within density functional theory

✉ Abderrahmane Cheriet
ab.cheriet@lagh-univ.dz

- 1 Department of Materials Science, Faculty of Science and Technology, Tissemsilt University, 38000 Tissemsilt, Algeria
- 2 Laboratory of Physical Studies of Materials, University of Science and Technology of Mohamed Boudiaf, 31000 Oran, Algeria
- 3 Physical Engineering Laboratory, University of Ibn Khladoun, 14000 Tiaret, Algeria
- 4 Laboratory of Physico-Chemistry of Materials, University of Amar Telidji, 03000 Laghouat, Algeria
- 5 Department of Matter Sciences, University of Abbes, 40004 Khenchela, Algeria
- 6 LASMIS, Technological Pole of South Champagne, University of Technology of Troyes, 52800 Nogent, France

(DFT) to investigate the structural, electronic, elastic, and magnetic properties of two half-Heusler VMSb compounds ($M = \text{Pd}, \text{Pt}$).^{13–16} The results showed that both VMSb compounds exhibited half-metallicity, making them excellent candidates for spintronic applications.

Computational Details

First-principles calculations were performed using the full-potential linearized augmented plane wave (FP-LAPW) method^{17,18} in WIEN2k code.¹⁹ Exchange–correlation effects were represented using the Wu–Cohen generalized gradient approximation (WC-GGA)²⁰ and the local spin density approximation with interaction parameter U (LSDA+ U).²¹ To obtain more precise results of the magnetic and electronic properties, the Tran–Blaha modified Becke–Johnson (TB-mBJ) exchange–correlation potential²² was applied, as this functional is considered to be more accurate than the standard (WC-GGA, LSDA+ U) approaches for reproducing band gap results. To calculate the composite size (convergence), the parameters R_{MT} and $K_{\text{max}} = 8$ were used, where K_{max} is the plane wave cut-off, and R_{MT} is the lowest radii of all atomic spheres. The Fourier charge density expansion of the potential in the interstitial area was chosen using unique K -point sampling from a $15 \times 15 \times 15$ grid and $G_{\text{max}} = 12 \text{ a.u.}^{-1}$. The charge density and potential inside the interstitial zone are lower. Muffin-tin spheres were enlarged in terms of spherical harmonics up to $l_{\text{max}} = 10$.

Results and Discussion

Structural Properties

The stoichiometric composition of half-Heusler alloys typically consists of transition metals X and Y , and a non-magnetic element Z from group III, IV, or V in the periodic table. These alloys have a face-centred cubic (FCC) Bravais structure. To determine the most stable structural phase and predict ground

state properties, we employed the energy minimization method by calculating the total energy as a function of the unit-cell volume. We calculated the lattice constants and bulk modulus of a superposition of a rock-salt and zinc-blend structure. This family of compounds has a cubic structure with the space group 216 F-43m, written by $a = b = c$ and $a = b = c = \gamma$ ^{23,24} (see Fig. 1). The structure type is characterized by correspondingly occupied Wyckoff positions 4a (0, 0, 0), 4b (1/2, 1/2, 1/2), and 4c (1/4, 1/4, 1/4).²⁵ Table I summarizes the three equivalent atomic arrangements possible for this structure type,²⁶ and the atomic arrangements of VPtSb and VPdSb using WC-GGA. The birch–murnaghan equation of state was used to obtain the total energy–volume curves for both compounds.^{27–29}

Figure 2 presents the total energy curves (Eq. 1) as a function of the volume. It is seen that the ferromagnetic (FM) state is more favourable than the non-magnetic (NM) state in energy. For the type III structure, we found that the ferromagnetic state has lower energy in both VPdSb (−24956.525) and VPtSb (−51754.802), respectively.

On the other hand, the negative value of the total energy (Fig. 2) confirms that the structural stability of VMSb ($M = \text{Pd}, \text{Pt}$) composites in the FM type III structures are energetically favourable for the experimental fabrication of these alloys.

$$E(V) = E_0 + \frac{BV}{B'} \left[\frac{\left(\frac{v_0}{v}\right)^{B'}}{B' - 1} + 1 \right] - \frac{BV}{B' - 1} \quad (1)$$

It is common for the lattice parameter and bulk modulus to vary among different compounds, as they are

Table I Possible atomic arrangements of the half-Heusler compounds VMSb ($M = \text{Pd}, \text{Pt}$)

Type	V	M	Sb
Type I	(0, 0, 0)	(1/2, 1/2, 1/2)	(1/4, 1/4, 1/4)
Type II	(1/4, 1/4, 1/4)	(0, 0, 0)	(1/2, 1/2, 1/2)
Type III	(1/2, 1/2, 1/2)	(1/4, 1/4, 1/4)	(0, 0, 0)

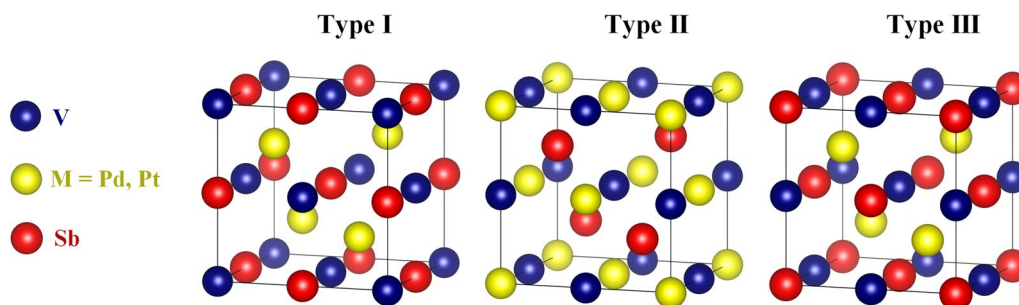


Fig. 1 Different arrangements of half-Heusler structures.

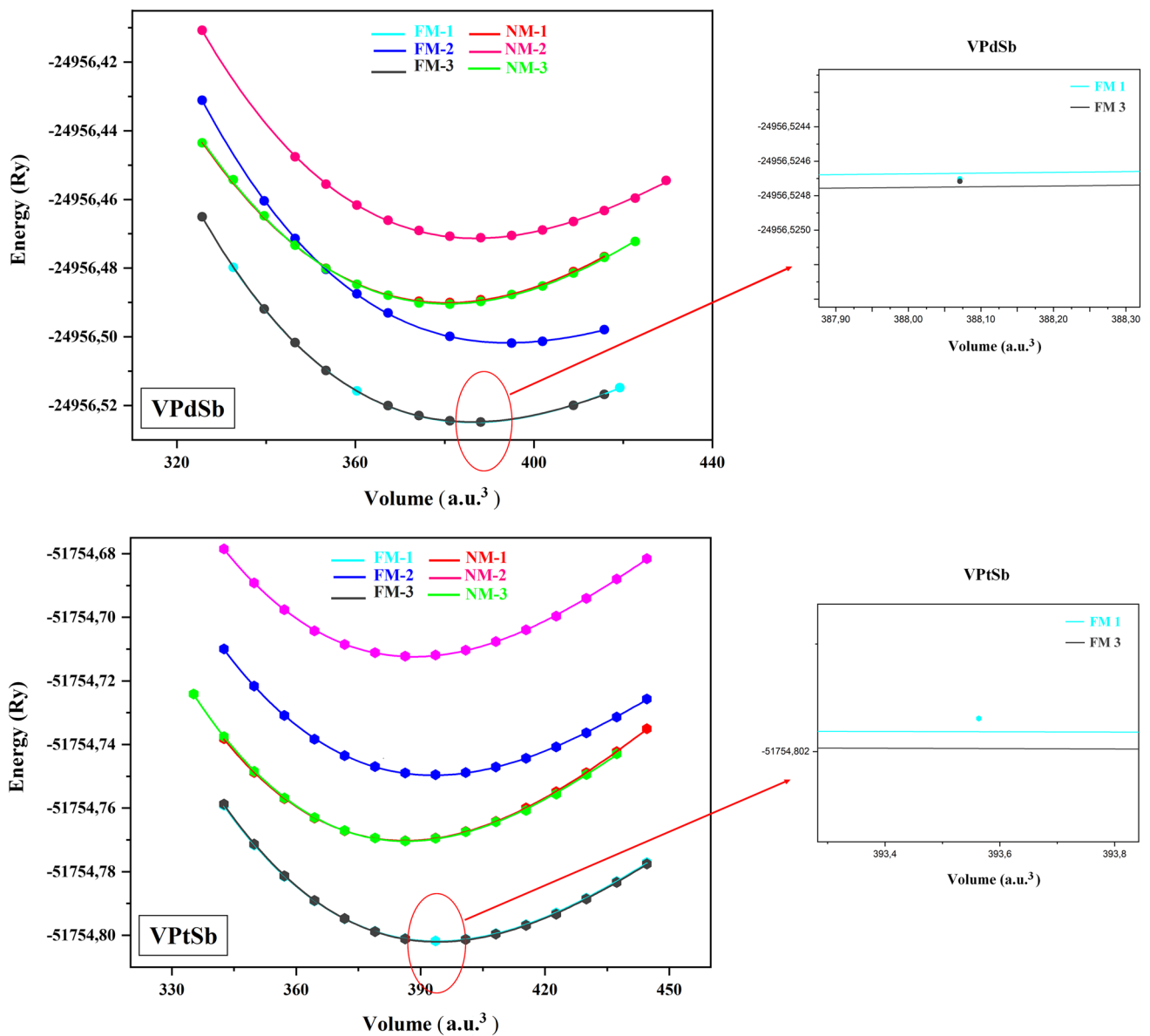


Fig. 2 Calculated total energy of VPdSb and VPtSb compounds in their FM and NM phases as a function of the volume.

determined by the chemical composition and crystal structure of the material. In this case, the observed difference in lattice constants and bulk modulus between VPdSb and VPtSb can be attributed to the different atomic radii and electronic structures of Pd and Pt.

Pd has a smaller atomic radius than Pt, which can lead to a smaller lattice parameter for VPdSb compared to VPtSb. The bulk modulus, on the other hand, is a measure of a material's resistance to compression and is affected by the strength of the bonds between the atoms. Since Pd and Pt have different electronic structures and bonding characteristics, they can have different effects on the bulk modulus of the compound.

The derivative of pressure (B') is a measure of how the bulk modulus changes under pressure. A larger B' indicates that the material becomes less compressible at high pressures, while a smaller B' indicates the opposite. The specific values of B' for VPdSb and VPtSb in Table II can provide insight into how the compounds behave under different pressures.

Overall, the differences in lattice parameter, bulk modulus, and B' between VPdSb and VPtSb can be attributed to the different atomic and electronic structures of the two compounds.

Elastic Properties

In materials science, elastic constants are parameters that describe the response of a material to applied mechanical stresses or strains. C_{11} , C_{12} , and C_{44} are three independent elastic constants that describe the behaviour of a cubic crystal under stress. C_{11} represents the stiffness of the crystal along one axis, while C_{12} represents the stiffness between two perpendicular axes. Finally, C_{44} represents the shear modulus, which is the measure of the crystal's resistance to shear deformation along a plane parallel to one of its faces. The values of these elastic constants provide valuable information about the mechanical stability and strength of the crystal, as well as its ability to withstand stress and strain without undergoing plastic deformation or failure. Additionally, the elastic constants can be used to predict the behaviour of the material under different mechanical loads, which is essential in many engineering applications. The elastic constants and moduli of VMSb (M = Pd, Pt) alloys were calculated using the IRelast package integrated into the Wien2k code.^{30,31} These properties are important for understanding how a material responds to external forces, such as stress or strain. The elastic constants for the cubic phases of the VMSb alloys were determined using isotropic strain and volume-conserving deformations of the cubic primitive cells.

These conditions ensure that the material is able to resist deformation under external forces. The bulk modulus (B) of the VMSb alloys was also calculated and found to be within the range of $C_{12} < B < C_{11}$, which is consistent with the criteria for mechanical stability. Equation 2³² shows how the elastic constants affect the total energy of the material as a function of strain (δ), providing insight into the material's mechanical response to external stresses and strains.

$$E(\delta) = E(-\delta) = E(0) + (C_{11} - C_{12})V_0\delta^2 + O(\delta^4) \quad (2)$$

where $E(0)$ is the total energy of an undisturbed lattice, V_0 is the equilibrium volume, and C_{ij} are elastic constants.

Table II The calculated values of lattice parameter (Å), bulk modulus (GPa) and its pressure derivative, the minimum energy (Ry) of both VMSb compounds (M = Pd, Pt)

	Phase	a_0 (Å)	B (GPa)	B' (GPa)	E_{\min} (Ry)
VPdSb	FM-III	6.121	129.044	4.672	-24,956.525
VPtSb	FM-III	6.160	140.466	4.733	-51,754.802

Table III The elasticity constants C_{ij} (in GPa), the calculated elasticity constants: bulk B , shear G and Young's moduli E (in GPa), anisotropy parameter A , B/G ratio, Poisson's ratio ν , and Debye temperature θ_D for VMSb (M = Pd and Pt) compounds

	C_{11}	C_{12}	C_{44}	B	G	E	ν	B/G	A	Θ_D
VPdSb	147.04	124.98	81.76	132.33	53.47	141.37	0.32	2.47	7.41	272.85
VPtSb	168.73	131.96	89.42	144.22	61.41	160.41	0.31	2.36	4.86	266.82

Overall, the results suggest that VMSb (M = Pd, Pt) alloys have the potential to exhibit strong mechanical properties due to their elastic constants and moduli.

Applying an orthorhombic strain tensor with conserved volume and the following expression, we can obtain C_{11} and C_{12} (Eq. 3).

$$\bar{\epsilon} = \begin{bmatrix} \delta & 0 & 0 \\ 0 & -\delta & 0 \\ 0 & 0 & \frac{\delta^2}{(1-\delta^2)} \end{bmatrix} \quad (3)$$

The bulk modulus B of an isotropic cubic crystal is written as a function of C_{11} and C_{12} as follows:

$$B = \frac{C_{11} + 2C_{12}}{2} \quad (4)$$

C_{44} was calculated using a monoclinic strain-conserving volume method.

$$\bar{\epsilon} = \begin{bmatrix} 0 & \frac{\delta}{2} & 0 \\ \frac{\delta}{2} & 0 & 0 \\ 0 & 0 & \frac{4}{(4-\delta^2)} \end{bmatrix} \quad (5)$$

The total energy is then represented as follows:

$$E(\delta) = E(-\delta) = E(0) + \frac{1}{2}C_{44}V_0\delta^2 + O(\delta^4) \quad (6)$$

The results presented in Table III show that both VPtSb and VPdSb are mechanically stable according to Born's criteria for a cubic structure.³³ Specifically, the values of C_{11} , C_{12} , and C_{44} satisfy the conditions $C_{11} - C_{12} > 0$, $C_{11} > 0$, and $C_{44} > 0$, as well as $C_{11} + 2C_{12} > 0$ and $C_{12} < B < C_{11}$.

These elasticity constants are used to determine the bulk modulus B , shear modulus G , Young's modulus E , Poisson's ratio ν , and anisotropy factor A (Table III), which can be calculated using the following equations:

$$G = \frac{C_{11} - C_{12} + 3C_{44}}{5} \quad (7)$$

$$E = \frac{9BG}{3B + G} \quad (8)$$

$$\nu = \frac{(3B - 2G)}{2(3B + G)} \quad (9)$$

$$A = \frac{2C_{44}}{C_{11} - C_{12}} \quad (10)$$

The bulk modulus values obtained for VPdSb ($B = 132.335$ GPa) and VPtSb ($B = 132.335$ GPa) compounds are in close agreement with those obtained from the structural properties (129.044 GPa, 140.466 GPa), respectively, which confirms the accuracy of the elasticity constants of VMSb ($M = \text{Pd, Pt}$) alloys. The Poisson ratios (ν) of VMSb ($M = \text{Pd, Pt}$) (0.32, 0.31, respectively) are higher than that for ductile materials (0.26), confirming the ductility of these compounds according to Frantsevich's rule. This can be attributed to the low elasticity constants and bulk modulus B , which promote the ductility of the material. Additionally, the B/G ratios for both the VPdSb (2.474) and VPtSb (2.363) compounds are higher than the critical value of 1.75, which classifies them as ductile materials.

Young's modulus of VPtSb (160.4 GPa) is higher than that of VPdSb (141.4 GPa). To describe the elastic properties of different materials, the anisotropy coefficient of expansion and the elastic anisotropy are used to cause micro-cracks in ceramics. The elastic anisotropy of VPdSb and VPtSb alloys is demonstrated by the two- and three-dimensional Young's modulus diagrams in Fig. 3. The values of anisotropy parameter A_3 were obtained by applying Eq. 6 as seen in Table III. For an isotropic material, $A = 1$, whereas values greater or less than one indicate a higher or lower level of anisotropic elastic behaviour. Both compounds show an elastic deformation anisotropy ($A \neq 1$), which supports the anisotropic material hypothesis. Further computations are required to fully understand the properties of the structural intermetallic compounds.

The Debye temperature is an important physical property given by the following equation:

$$\theta_D = \frac{h}{k_B} \left[\frac{3}{4\pi V_0} \right]^{\frac{1}{3}} v_m \quad (11)$$

where h , k_B and V_0 represent Planck's constant, Boltzmann's constant, and the atomic volume, respectively. V_m is provided for a polycrystalline material by:

$$v_m = \frac{1}{3} \left[\frac{2}{v_l^3} + \frac{1}{v_t^3} \right]^{-\frac{1}{3}} \quad (12)$$

where v_l and v_t are the longitudinal and transverse velocities of sound which are calculated using the bulk modulus B and shear modulus G as follows³⁴:

$$v_l = \left(\frac{3B + 4G}{3\rho} \right)^{\frac{1}{2}} \quad (13)$$

$$v_t = \left(\frac{G}{\rho} \right)^{\frac{1}{2}} \quad (14)$$

Table IV shows the velocity and temperature values for both compounds. We can see that the Debye temperature and melting temperature decrease as the atomic size increases. Furthermore, the Θ_D values calculated for the VPdSb and VPtSb alloys are 272.85 K and 266.82 K, which is close to room temperature and has a significant impact on spintronics device applications.

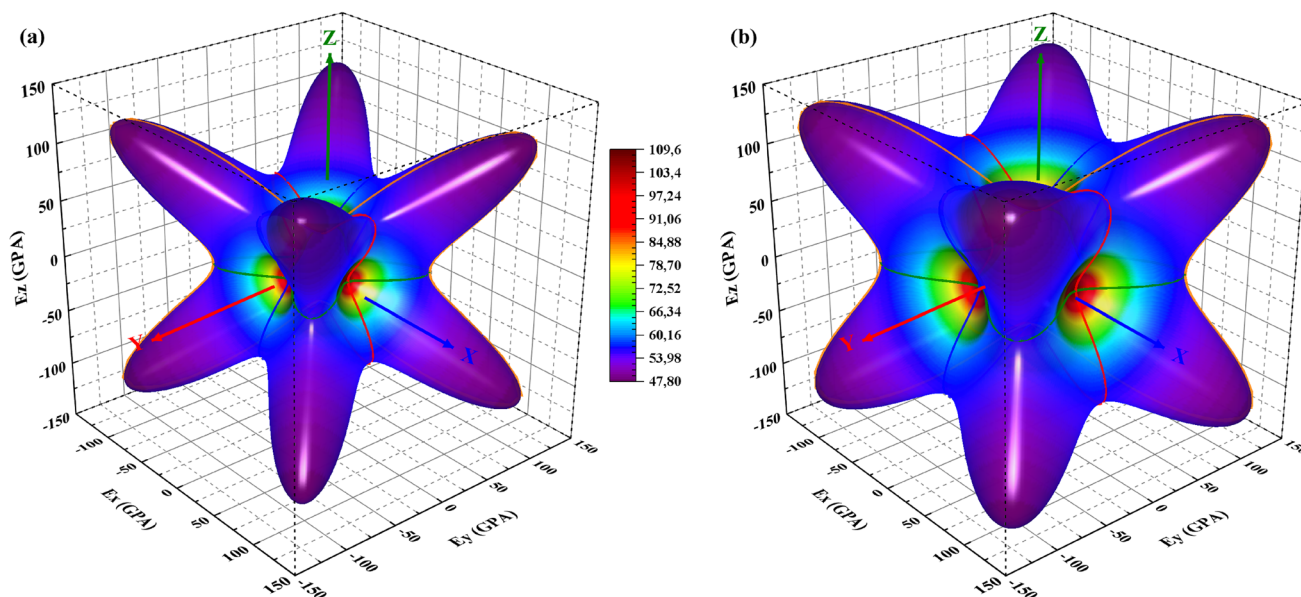


Fig. 3 3D representation of Young's modulus for both compounds: (a) VPdSb and (b) VPtSb.

Table IV The calculated transverse and longitudinal elastic wave velocities, the average wave velocity, the temperature of Debye, and the melting temperature for VPdSb and VPtSb compounds

	vt (m s ⁻¹)	vl (m s ⁻¹)	vm (m s ⁻¹)	θD (K)	TM (K)
VPdSb	2174.16	4762.02	2450.52	272.85	1422.0282
VPtSb	2144.96	4465.21	2411.61	266.82	1550.2285

Magnetic Properties

The magnetic moment is a crucial property in the field of spintronics, and it was calculated for the Heusler alloys with half-metallic behaviour using the optimized lattice parameters. The total magnetic moment of these alloys follows the Slater-Pauling (SP) rule,³⁵ which is one of the methods used for evaluating the magnetic moments of Heusler and half-Heusler compounds. For half-Heusler compounds, the total magnetic moment can be expressed by $M_T = Z_T - 18$,³⁶ where M_T represents the spin magnetic moment and Z_T is the total number of valence electrons. The spin magnetic moment of half-Heusler compounds is calculated by the difference between the spin-up and spin-down states. The compounds have a C_{1b} structure with three atoms in each unit cell.³⁷ For ternary 1:1:1 half-Heusler compounds such as VMSb ($M = Pd, Pt$), no change is observed in any of the functions (WC-GGA, LSDA+U, TB-mBJ). The total magnetic moments are around $2\mu_B$. In these compounds, the V atom has the most significant contribution to the total magnetic moment, with a small presence of an M magnetic moment. The local magnetic moment of the Sb atom is negligible for both alloys and behaves similarly to the sp element in conventional Heusler alloys. Table V presents the total and local magnetic moments for both VMSb ($M = Pd$ and Pt) compounds, including contributions from atomic resolved magnetic moments (WC-GGA, LSDA+U, TB-mBJ) and interstitial magnetic moments.

Table V Total and local magnetic moments (WC-GGA, LSDA+U, TB-mBJ) in (μ_B) per unit cell

Compounds	Functional	Magnetic moment				
		MInt	MV	MM	MSb	MT
VPdSb	WC-GGA	0.334	1.715	0.026	-0.076	2.000
	LSDA+U	0.341	1.685	0.037	-0.063	2.000
	TB-mBJ	0.261	1.802	0.007	-0.071	2.000
VPtSb	WC-GGA	0.336	1.694	0.017	-0.047	2.000
	LSDA+U	0.307	1.756	-0.022	-0.041	2.000
	TB-mBJ	0.254	1.731	0.028	-0.014	2.000

Electronic Properties

The electronic properties of the VMSb ($M = Pd$ and Pt) compounds were analysed by plotting their spin-polarized band structures using WC-GGA, LSDA+U, and TB-mBJ approximations Figs. 4 and 5. The band structures were determined along the high symmetry path of the first Brillouin zone. The analysis revealed that the spin-up channel of the VPdSb compound has a metallic nature because the valence band maximum (VBM) crosses the conduction band minimum (CBM) at the Fermi level. Contrary to the results of the other methods, the TB-mBJ approximation shows a semiconductor character with an indirect band gap for the VPtSb compound. The transformed and increased nature of the band gap causes an apparent change in the physical properties with an energy gap $E_g = 0.48, 0.45, \text{ and } 0.51$ eV and $E_g = 0.55, 0.54, \text{ and } 0.58$ eV for VPdSb and VPtSb, respectively. The energy gap occurs between the VBM at the Γ point and the CBM at the X point, validating the half-metallic characteristics of the VPdSb and VPtSb compounds.

Table VI The calculated lattice constant (\AA), electronic band gaps for the spin-down state (eV) and the electronic band structure nature of VPdSb and VPtSb compounds

Material	Pressure (GPa)	a (\AA)	Eg_Down (eV)	Nature of band gap
VPdSb	0	6.121	0.51	Indirect
	5	6.194	0.47	Indirect
	10	6.257	0.44	Indirect
	15	6.313	0.41	Indirect
	20	6.363	0.37	Metal
VPtSb	0	6.160	0.58	Indirect
	5	6.227	0.54	Indirect
	10	6.286	0.51	Indirect
	15	6.339	0.48	Indirect
	20	6.386	0.43	Direct

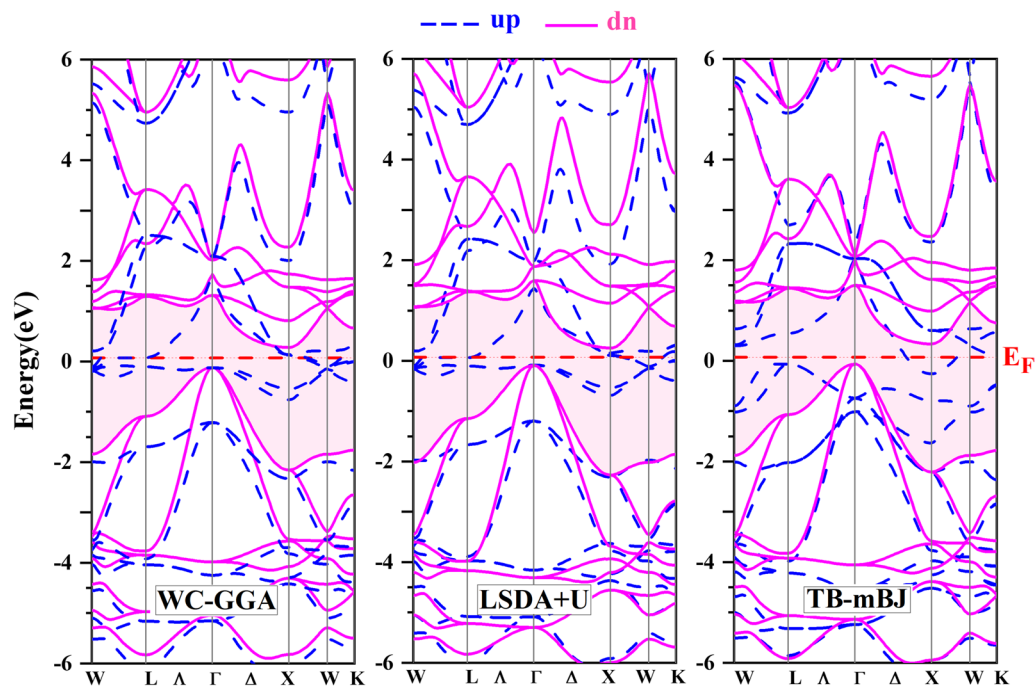


Fig. 4 The band structure of the VPdSb compound using: WC-GGA, LSDA+U, and TB-mBJ.

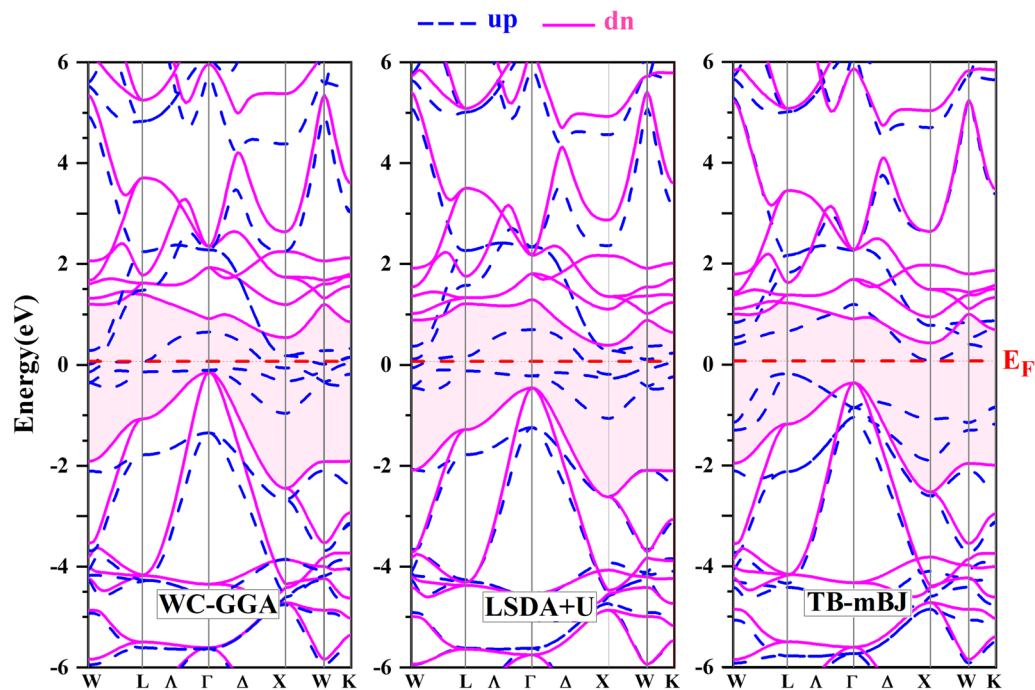
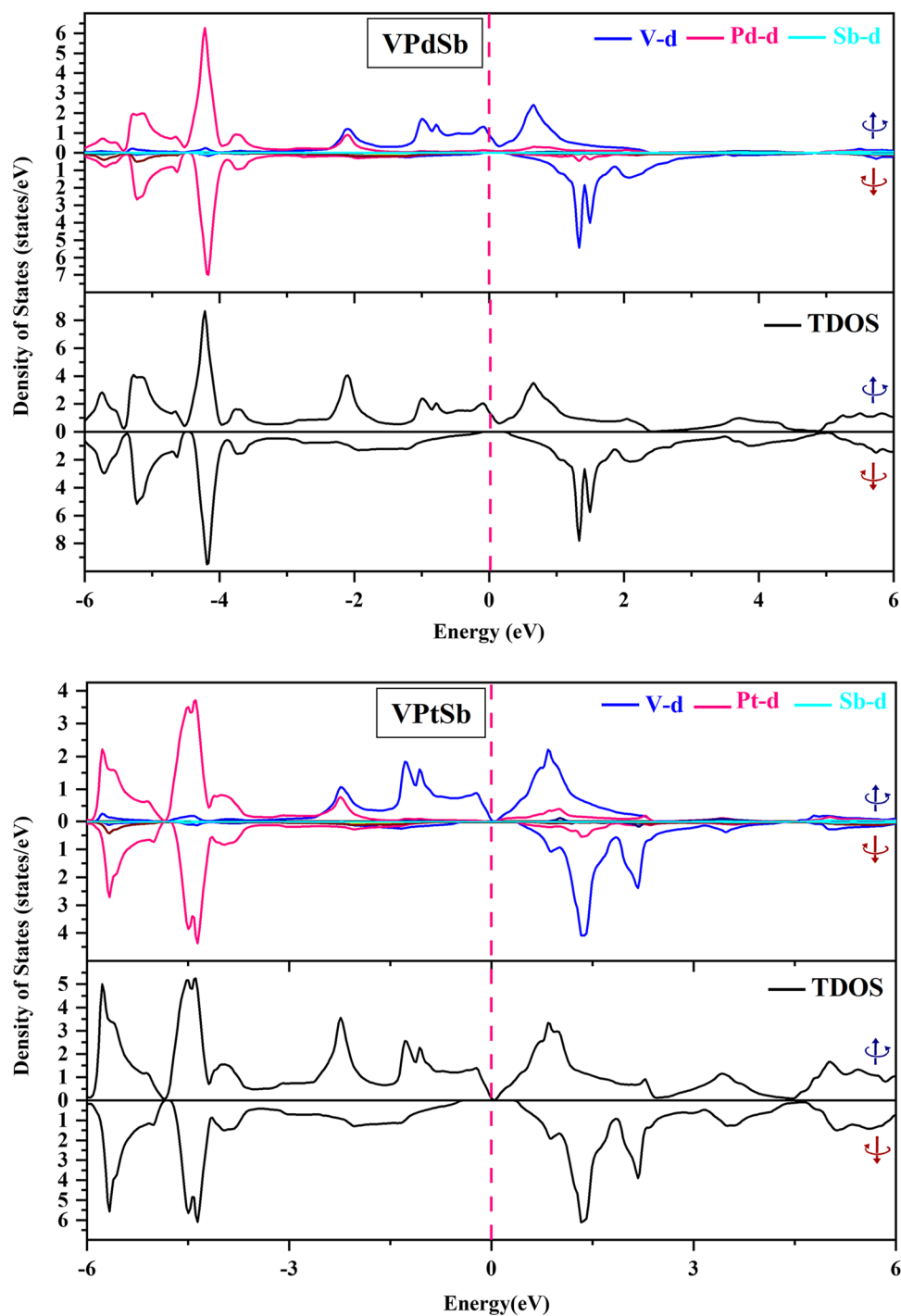


Fig. 5 The band structure of the VPtSb compound using: WC-GGA, LSDA+U, and TB-mBJ.

The electronic properties of a material provide important information about the behaviour of electrons at the Fermi level, and the presence of an energy gap is a key factor in determining a material's suitability for certain applications such as spintronics. In this study, the TB-mBJ method was

used to calculate the total and partial densities of states (DOS) for the spin channels of both VPdSb and VPtSb at two different lattice parameters. The analysis revealed that both compounds exhibit half-metallic behaviour with an energy range of -6.0 to 6.0 eV, as shown in Fig. 6. The DOS

Fig. 6 Total and partial DOS of the VPdSb and VPtSb compounds obtained by the TB-mBJ approach.



plots indicate that the hybridization of the Pd-d and Pt-d atoms in both the spin-up and spin-down channels results in an excess of states between -6 eV and -1 eV. The calculations also show the presence of hybridization induced by the V-d atom in all compounds between -1 eV and 3 eV.

Effect of Pressure on Band Structure Properties

The electronic properties of VPdSb and VPtSb compounds were investigated under different pressures ranging from 0 to 20 GPa using the generalized gradient approximation (WC-GGA). The band structures for the

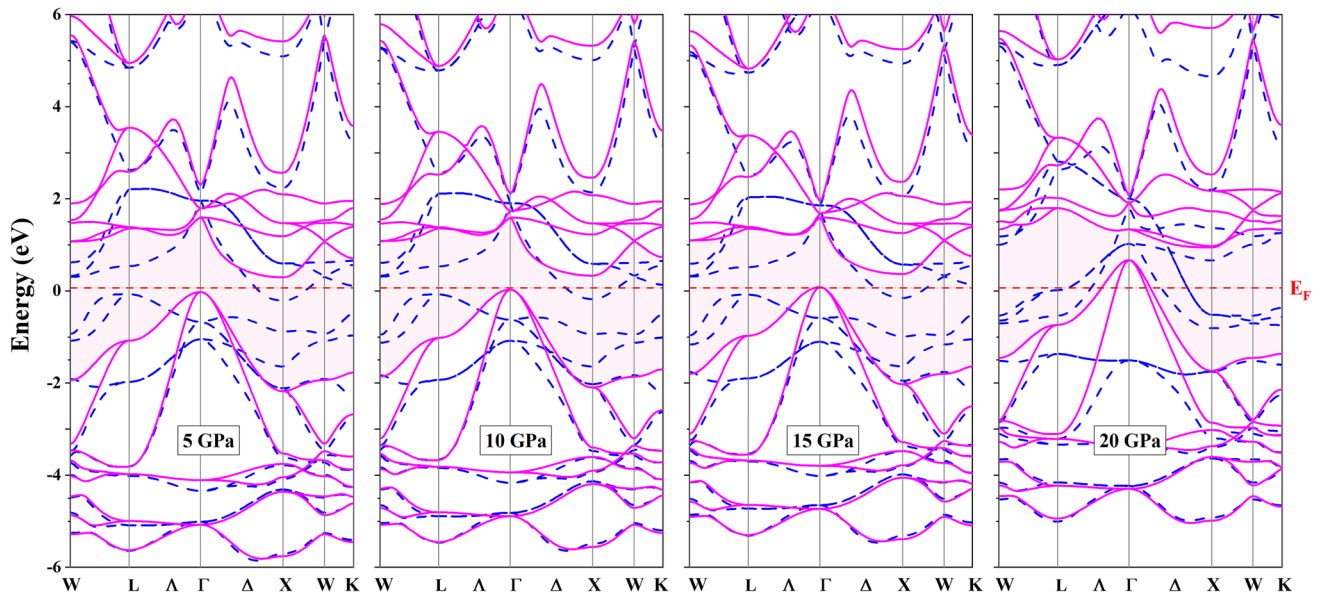


Fig. 7 Band structure of VPdSb alloy (in the 0–20 GPa range) at optimized lattice constant.

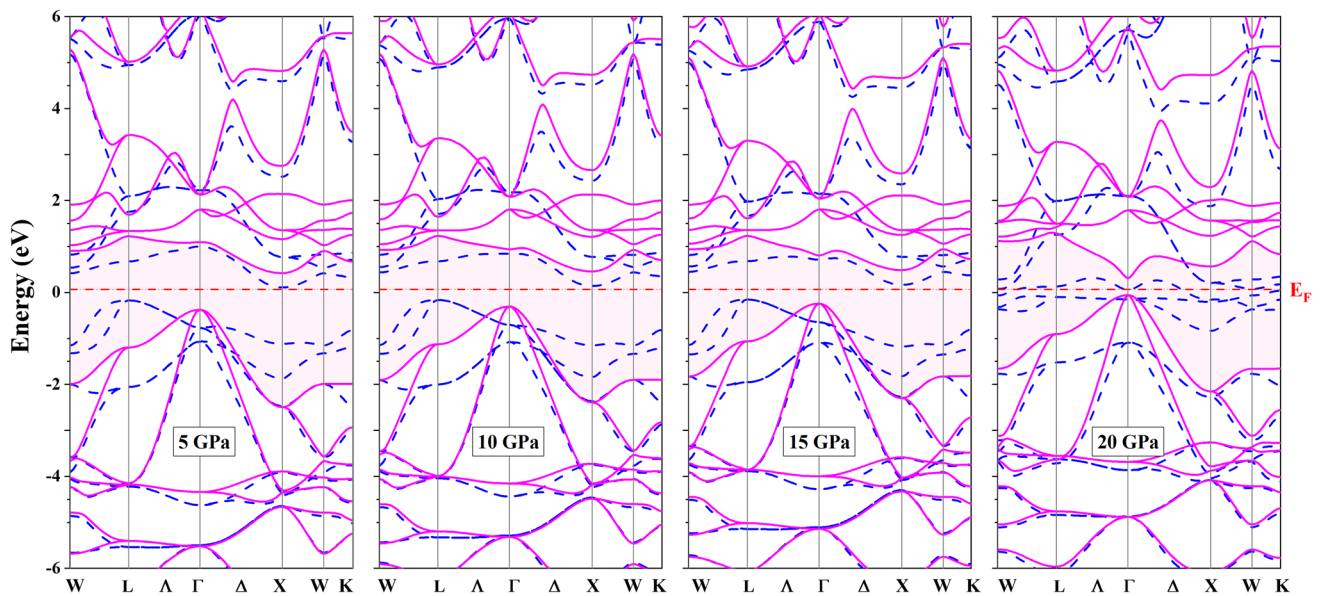


Fig. 8 Band structure of VPtSb alloy (in the 0–20 GPa range) at optimized lattice constant.

spin-up and spin-down channels of both compounds are presented in Figs. 7 and 8. Under pressure, both compounds exhibit a metallic nature in the spin-up state due to the valence band maximum (VBM) and conduction band minimum (CBM), while the spin-down form shows a semiconducting nature. For the VPdSb compound, the

indirect band gap (E_g) gradually decreases from 0.51 to 0.41 eV under a pressure range of 0–15 GPa. However, the compound loses its half-metallic state at 20 GPa with $E_g = 0.37$ eV. The calculated band gaps and lattice constants (A) are presented in Table VI. For VPtSb, the spin-up channel is metallic, while the compound exhibits

a semiconductor nature with indirect gaps of $E_g = 0.58, 0.54, 0.51,$ and 0.48 eV at pressures ranging from 0 to 15 GPa. At 20 GPa, the compound shows a direct band gap of 0.43 eV in the spin-down channel. In summary, increasing pressure gradually changes the electronic properties from half-metallic to metallic characters.

Conclusions

The purpose of the study was to investigate the structural, elastic, electronic, and magnetic properties of VMSb ($M = \text{Pd}, \text{Pt}$) alloys using first-principles calculations based on density functional theory with the addition of the Hubbard-U approximation. The results indicated that the VMSb ($M = \text{Pd}, \text{Pt}$) compounds are half-metallic ferromagnetic (HMF) and stable in structure type III, with optimized lattice constants of 6.121 and 6.160, respectively.

The electronic properties of the density of states (DOS) and band structures revealed that the compounds exhibit half-metallicity with indirect gap spin-down E_g values of 0.51 eV for VPdSb and 0.58 eV for VPtSb. The band structures gradually changed from half-metallic to metallic for VPdSb, while VPtSb exhibited a half-metallic indirect gap. The magnetic properties of both compounds were consistent with the Slater-Pauling rule, confirming their ferromagnetic half-metallic character. Additionally, even an applied pressure ranging from 0 to 20 GPa had no significant effect on the magnetic moment of the two compounds, indicating their resistance to pressure.

Based on these results, the VMSb ($M = \text{Pd}, \text{Pt}$) alloys are considered good candidates for the design and development of spintronics devices.

Conflict of interest On behalf of all authors, the corresponding author states that there is no conflict of interest.

References

1. F. Casper, T. Graf, S. Chadov, B. Balke, and C. Felser, Half-Heusler compounds: novel materials for energy and spintronic applications. *Semicond. Sci. Technol.* 27(6), 063001 (2012).
2. J. Winterlik, G.H. Fecher, A. Thomas, and C. Felser, Superconductivity in palladium-based Heusler compounds. *Phys. Rev. B.* 79(6), 064508 (2009).
3. V. Alijani, S. Ouardi, G.H. Fecher, J. Winterlik, S.S. Naghavi, X. Kozina et al., Electronic, structural, and magnetic properties of the half-metallic ferromagnetic quaternary Heusler compounds CoFeMnZ ($Z = \text{Al}, \text{Ga}, \text{Si}, \text{Ge}$). *Phys. Rev. B.* 84(22), 224416 (2011).
4. R. Farshchi and M. Ramsteiner, Spin injection from Heusler alloys into semiconductors: a materials perspective. *J. Appl. Phys.* 113(19), 7 (2013).
5. F. Heusler, W. Starck, and E. Haupt, Magnetisch-chemische studien. *Verh. Dtsch. Phys. Ges* 5, 219 (1903).
6. M. Yin, J. Hasier, and P. Nash, A review of phase equilibria in Heusler alloy systems containing Fe Co or Ni. *J. Mater. Sci.* 51, 50 (2016).
7. R. De Groot, F. Mueller, P. Engen, and K.H.J. Buschow, New class of materials: Half-metallic ferromagnets. *Phys. Rev. Lett.* 50(25), 2024 (1983).
8. S. Ouardi, G.H. Fecher, C. Felser, M. Schwall, S.S. Naghavi, A. Gloskovskii et al., Electronic structure and optical, mechanical, and transport properties of the pure, electron-doped, and hole-doped Heusler compound CoTiSb . *Phys RevB.* 86(4), 045116 (2012).
9. L. Wang, L. Miao, Z. Wang, W. Wei, R. Xiong, H. Liu et al., Thermoelectric performance of half-Heusler compounds TiNiSn and TiCoSb . *J. Appl. Phys.* 105(1), 013709 (2009).
10. K.-U. Neumann, J. Crangle, J. Smith, N. Zayer, and K. Ziebeck, Magnetic order in ternary intermetallic compounds containing palladium and titanium. *J. Magn. Magn. Mater.* 140, 185 (1995).
11. K. Prokeš, M. Diviš, P. Mohn, K. Schwarz, V. Sechovský, P. Svoboda et al., Reduced magnetic moments in UNiSi . *J. Alloys Compd.* 269(1–2), 43 (1998).
12. C.S. Birkel, J.E. Douglas, B.R. Lettiere, G. Seward, N. Verma, Y. Zhang et al., Improving the thermoelectric properties of half-Heusler TiNiSn through inclusion of a second full-Heusler phase: microwave preparation and spark plasma sintering of $\text{TiNi}_{1+x}\text{Sn}$. *Phys. Chem. Chem. Phys.* 15(18), 6990–6997 (2013).
13. P. Hohenberg and W. Kohn, Inhomogeneous electron gas. *Phys Rev.* 136(3B), B864 (1964).
14. W. Kohn and L.J. Sham, Self-consistent equations including exchange and correlation effects. *Phys. Rev.* 140(4A), A1133 (1965).
15. H. Rozale, A. Amar, A. Lakdja, A. Moukadem, and A. Chahed, Half-metallicity in the half-Heusler RbSrC , RbSrSi and RbSrGe compounds. *J. Magn. Magn. Mater.* 336, 83 (2013).
16. J.P. Perdew, K. Burke, and M. Ernzerhof, Generalized gradient approximation made simple. *Phys. Rev. Lett.* 77(18), 3865 (1996).
17. W. Kohn, Density functional and density matrix method scaling linearly with the number of atoms. *Phys. Rev. Lett.* 76(17), 3168 (1996).
18. M. Petersen, F. Wagner, L. Hufnagel, M. Scheffler, P. Blaha, and K. Schwarz, Improving the efficiency of FP-LAPW calculations. *Comput. Phys. Commun.* 126(3), 294 (2000).
19. P. Blaha, K. Schwarz, G.K. Madsen, D. Kvasnicka, and J. Luitz, wien2k. *An Augment. Plane Wave Local Orbitals Progr. Calc Cryst Prop.* 60, 1 (2001).
20. D. Bilc, R. Orlando, R. Shaltaf, G.-M. Rignanese, J. Íñiguez, and P. Ghosez, Hybrid exchange-correlation functional for accurate prediction of the electronic and structural properties of ferroelectric oxides. *Phys. Rev. B.* 77(16), 165107 (2008).
21. A.N. Andriotis, R.M. Sheetz, and M. Menon, LSDA+ U method: a calculation of the U values at the Hartree-Fock level of approximation. *Phys. Rev. B.* 81(24), 245103 (2010).
22. J.P. Perdew, A. Ruzsinszky, G.I. Csonka, O.A. Vydrov, G.E. Scuseria, L.A. Constantin et al., Restoring the density-gradient expansion for exchange in solids and surfaces. *Phys. Rev. Lett.* 100(13), 136406 (2008).
23. K. Özdoğan, E. Şaşıoğlu, and I. Galanakis, Slater-Pauling behavior in LiMgPdSn -type multifunctional quaternary Heusler materials: half-metallicity, spin-gapless and magnetic semiconductors. *J. Appl. Phys.* 113(19), 193903 (2013).
24. X. Dai, G. Liu, G.H. Fecher, C. Felser, Y. Li, and H. Liu, New quaternary half metallic material CoFeMnSi . *J. Appl. Phys.* 105(7), 07E901 (2009).
25. A. Missoum, T. Seddik, G. Murtaza, R. Khenata, A. Bouhemadou, Y. Al-Douri et al., Ab initio study of the structural and

- optoelectronic properties of the half-Heusler CoCr Z (Z= Al, Ga). *Can. J. Phys.* 92(10), 1105–1112 (2014).
26. D. Fruchart, Alloys and compounds of D-elements with main group elements. *Magn. Prop. Met.* 19, 24 (1988).
 27. Y. Ohno, D. Young, B. Ba, F. Matsukura, H. Ohno, and D. Awschalom, Electrical spin injection in a ferromagnetic semiconductor heterostructure. *Nature* 402(6763), 790–792 (1999).
 28. J.-B. Gu, C.-J. Wang, Y. Cheng, L. Zhang, L.-C. Cai, and G.-F. Ji, Structural, elastic, thermodynamic, electronic properties and phase transition in half-Heusler alloy NiVSb at high pressures. *Comput. Mater. Sci.* 96, 72 (2015).
 29. F.D. Murnaghan, The compressibility of media under extreme pressures. *Proc. Natl. Acad. Sci. USA* 30(9), 244 (1944).
 30. M. Jamal and G. City-Tehran-Iran, IR ELAST (2014)
 31. M. Jamal, M. Bilal, I. Ahmad, and S. Jalali-Asadabadi, IRelast package. *J. Alloys Compd.* 735, 569 (2018).
 32. I. Galanakis and P.H. Dederichs, *Half-Metallic Alloys: Fundamentals and Applications*, Vol. 676 (Berlin: Springer, 2005).
 33. H. Joshi, D. Rai, L. Hnamte, A. Laref, and R. Thapa, A theoretical analysis of elastic and optical properties of half Heusler MCoSb (M= Ti, Zr and Hf). *Heliyon.* 5(3), e01155 (2019).
 34. J. Haringa and B. Cook, Comparison of different pressing techniques for the preparation of n-type silicon-germanium thermoelectric alloys. in *Fifteenth International Conference on Thermoelectrics. Proceedings ICT'96*. IEEE. (1996)
 35. T. Suzuki, R. Chisnell, A. Devarakonda, Y.-T. Liu, W. Feng, D. Xiao et al., Large anomalous Hall effect in a half-Heusler antiferromagnet. *Nat. Phys.* 12(12), 1119 (2016).
 36. V. Tyuterev and N. Vast, Murnaghan's equation of state for the electronic ground state energy. *Comput. Mater. Sci.* 38(2), 350 (2006).
 37. I. Frantsevich, D. Kalinovich, I. Kovenskii, and M. Smolin, Electrotransport and diffusion in molybdenum-tungsten and iron-nickel alloys over wide ranges of temperatures. *J. Phys. Chem. Solids.* 30(4), 947 (1969).

Publisher's Note Springer Nature remains neutral with regard to jurisdictional claims in published maps and institutional affiliations.

Springer Nature or its licensor (e.g. a society or other partner) holds exclusive rights to this article under a publishing agreement with the author(s) or other rightsholder(s); author self-archiving of the accepted manuscript version of this article is solely governed by the terms of such publishing agreement and applicable law.

Half-metallic character and thermoelectric properties of the $K_2NaRbAs_2$ double half Heusler alloy

F Sofrani^{1,2}, K Boudia^{1,3}, F Khelifaoui^{4*} , M Hamlat⁴, A Bouhemadou⁵, A Lorf⁶, A Hachilif⁷, F Belkharroubi⁸ and A Slamani⁶

¹University Ahmed Ben Yahia El-Wanchrissi, Tissemsilt, Algeria

²Laboratoire d'Etudes Physique Des Matériaux, Université Des Sciences Et de Technologies USTO-MB, BP El M'Naouar, 1505 Oran, Algérie

³Physical Engineering Laboratory, University of Tiaret, 14000 Tiaret, Algeria

⁴Laboratory of Physicochemical Studies, University of Saida-Dr. Moulay Tahar, 20000 Saida, Algeria

⁵Laboratory for Developing New Materials and Their Characterizations, Faculty of Sciences, Department of Physics, University of Ferhat Abbas Setif, 19000 Setif, Algeria

⁶Laboratory of Physico-Chemistry of Advanced Materials, University of Djillali Liabes, BP 89, 22000 Sidi-Bel-Abbes, Algeria

⁷Computational Materials Physics Laboratory (CMPL), University of Djillali Liabes, BP 89, 22000 Sidi-Bel-Abbes, Algeria

⁸Laboratory of Analysis and Application of Radiations (LAAR), Faculty of Physics, University of Science and Technology of Oran Mohamed Boudiaf (USTO-MB), 1505 El Menouar, 31000 Oran, Algeria

Received: 29 October 2022 / Accepted: 29 March 2023

Abstract: This paper presents an investigation of the properties of the double half Heusler alloy (DHH) $K_2NaRbAs_2$. The structural, elastic, electronic, magnetic, and thermoelectric properties of the alloy are studied using the full-potential linearized augmented plane wave method (FP-LAPW) with the generalized gradient GGA approximation, and the GGA + Modified Becke-Johnson (mBJ) correlation potential is used to calculate the band structures and densities of states. The $K_2NaRbAs_2$ DHH alloy is derived from the previously studied parent half Heusler alloys $KNaAs$ and $KRbAs$ in their ferromagnetic phase of type I structure (FM-I). Our findings confirm the thermodynamic stability and synthesizability of $K_2NaRbAs_2$ in normal conditions. The alloy is shown to be resistant to distortion and able to withstand reversible deformation. The calculated elastic constants indicate that $K_2NaRbAs_2$ is mechanically stable, ductile, and anisotropic, as confirmed by 3D representation of its elastic moduli. Furthermore, the total magnetic moment of $2 \mu_B$ demonstrates its half-metallic behavior, which mainly due to arsenic atoms. Like its parent alloys $KNaAs$, and $KRbAs$, the $K_2NaRbAs_2$ DHH alloy could be suitable for use in spintronic technology. Additionally, the thermoelectric characteristics of the $K_2NaRbAs_2$ DHH alloy are investigated using semi-classical Boltzmann transport theory, based on a smoothed Fourier interpolation of the bands, as implemented in the BoltzTraP package.

Keywords: Heusler alloy; Mechanical stability; Half-metallic gap; Spin-polarization; Magnetic properties

1. Introduction

Since its initial theoretical prediction, the Half-Metallic ferromagnetism (HMF) character has attracted enormous interest and has emerged as one of the most interesting areas of research. In recent years, researchers have

attempted to deepen their knowledge of the HMF behavior to understand, predict and create new half-metallic materials, due to their promising potential applications in spintronic devices[1], magnetic tunnel junctions, magnetic disk drives, spin injection devices and nonvolatile magnetic random access memories [2]. Ideal HM ferromagnet exhibits metallic nature in one spin channel (“up” or “down”) and semiconducting(or insulating) nature in the other spin channel, revealing a 100% spin polarization at

*Corresponding author, E-mail: friha.khelifaoui@univ-saida.dz

the Fermi level [3, 4] with an integer value of the magnetic moment. The HMF nature was first determined in NiMnSb and PtMnSb half Heusler alloys [3–5]. Since then the half-metallic character has been theoretically and experimentally discovered in many other materials such as perovskite oxides without transition metal LiBeO₃[6], KBeO₃ [7], KMgO₃ [8], rutile TiO₂ and VO₂ [9], spinels MgFe₂O₄[10], fluoro-perovskites Rb(Co/Fe)F₃ [11], double perovskite Sr₂CrWO₆ [12], and ternary oxides XMg₃O₄ (X = Li, Na, K, and Rb) [13]. Numerous Heusler alloys can be half-metals as quaternary Heusler TiZrIrZ (Z = Al, Ga and In)[14], full Heusler Zr₂PdZ (Z = Al, Ga, and In) [15] and half Heusler KNaAs, KRbAs[16]. Khandy et al. explored the equilibrium electronic structure of the transition-metal atom based Heuslers XTaZ (X = Pd, or Pt, Z = Al, Ga or In) for possible thermoelectric applications[17]. Recently, a novel class of Heusler alloys, named double half Heusler alloys (DHH), has been discovered, inspired by the conception of double perovskites A₂B'B''O₆. They could be thought of as collection of two half Heuslers of formula. It is worth noting that the first prediction of this class of materials was made by Anand et al.[18].

Half-Heusler materials have inherently high thermal conductivities, which limits their thermoelectric efficiency. To address this issue, Anand et al. investigated a large class of relatively unexplored DHH compounds, which have substantially lower lattice thermal conductivities due to their crystal chemistry. Their work presented a reliable method for identifying low-thermal-conductivity half-Heuslers and highlighted a broad composition space for their potential applications. This research has paved the way for the systematic discovery of additional families of sizable intermetallic semiconductors with diverse potential applications. [18].

In the context of predicting new double half Heusler alloys and understanding their physical properties, K₂NaRbAs₂ was investigated as a new compound in this family. This study presents the structural, elastic, electronic, magnetic, and thermoelectric properties of the K₂NaRbAs₂ DHH alloy, and compares them with those of its parent HH alloys KNaAs, KRbAs[16]. This paper is organized as follows: after the introduction, Sect. 2 outlines the used computational method. The results and discussion paragraph are presented in Sect. 3, followed by the conclusion in Sect. 4, where the main points of the paper are summarized.

2. Computational method

The properties of K₂NaRbAs₂ DHH compound, derived from its parent HH alloys KNaAs and KRbAs, were determined using density functional theory (DFT) with the

full potential linearized augmented plane wave (FP-LAPW) method [19], as implemented in the WIEN2k code[20]. The generalized gradient approximation (GGA) was used to treat the exchange and correlation effects [21]. The muffin-tin (MT) radii, chosen for K, Na, Rb, and As atoms, are 2.35 a.u., 2.35a.u., 2.35. a.u., and 2.23 a.u., respectively. The spherical harmonics were developed up to lmax = 10 within the MT spheres, and at 12, the Gaussian value Gmax was used. An energy cut-off value of RMT*Kmax = 8 was used in the interstitial region. The energy and charge convergences for the iteration procedure of self-coherence calculations were taken to be 10⁻⁴ e and 10⁻⁵ Ry, respectively. The First Brillouin zone (BZ) integration was performed using 1000 K-points by the tetrahedral method[22].

3. Results and discussions

3.1. Structural properties

The studied compound K₂NaRbAs₂ crystallizes in a tetragonal structure with P-4m2 space group N^o115 (see Fig. 1).

To determine the stable magnetic phase, the optimization of both parent HH alloys was carried out within GGA in their ferromagnetic, non-magnetic, and antiferromagnetic phases [16], as shown in Fig. 2.

As shown in Fig. 2, the ferromagnetic phase of type I structure (FM-I) has the lowest total energy for both compounds, indicating that it is the energetically most stable phase compared to the non-magnetic (NM) and antiferromagnetic (AFM) phases at the equilibrium volume.

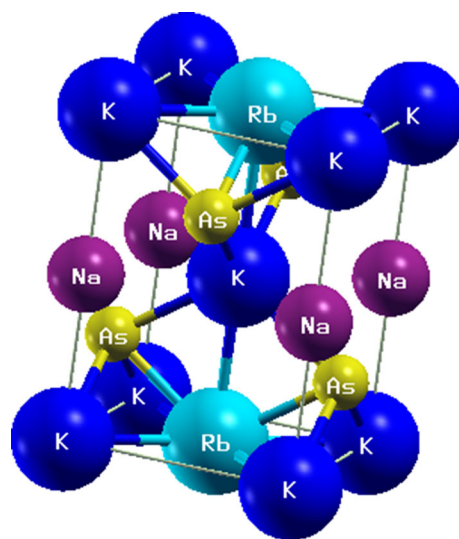


Fig. 1 Crystal structure of K₂NaRbAs₂ DHH alloy

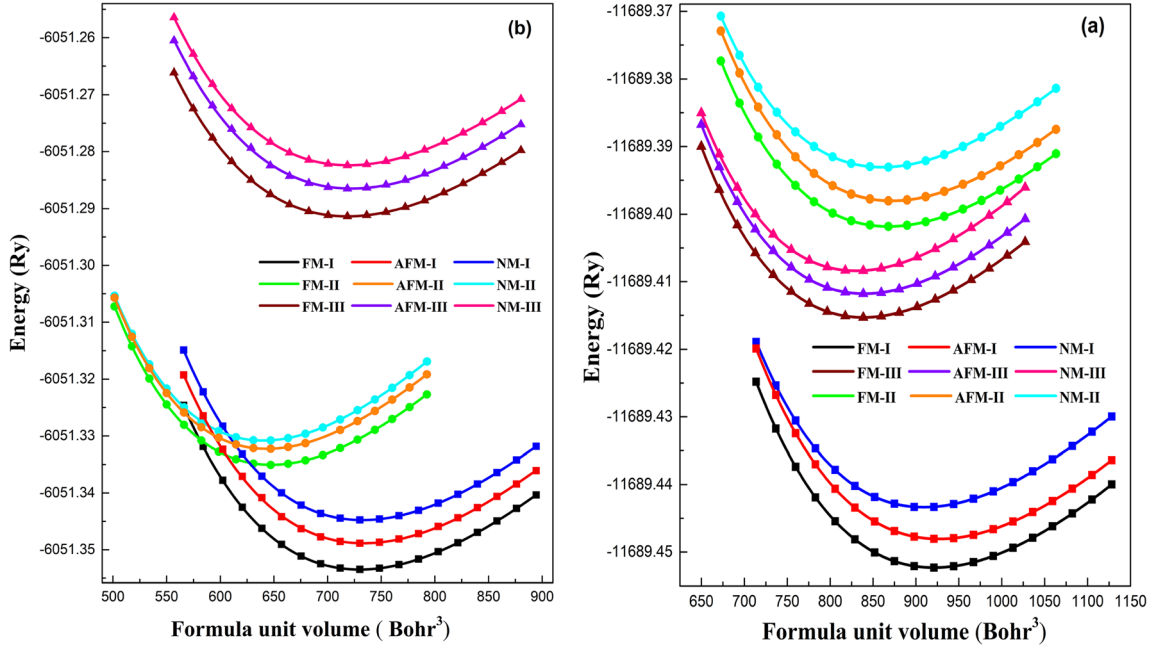


Fig. 2 Calculated Total Energy vs. Volume for FM, NM, and AFM Phases of (a) KRbAs and (b) KNaAs Compounds (color figure online)

From the obtained magnetic and structural ground states of KNaAs and KRbAs (FM-I), $K_2NaRbAs_2$ structure is constructed by substituting, in the conventional lattice of KNaAs, two Na atoms with Rb atoms. Consequently, only the FM phase of this acquired DHH structure is optimized, and as shown in Fig. 3, the optimized volume of $K_2NaRbAs_2$ is 1649.7486 (bohr³).

Then the structural parameters of the equilibrium are calculated by adjusting the total energy as a function of the volume, using the Birch Murnaghan equation of state [23].

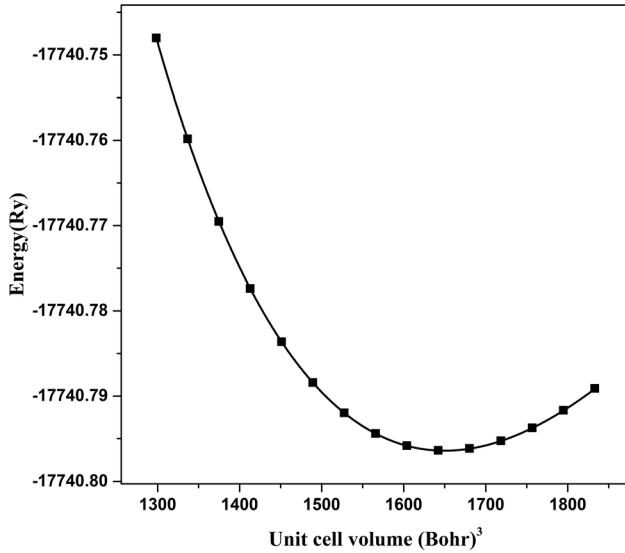


Fig. 3 Calculated total energy vs. Volume of $K_2NaRbAs_2$ compound

$$E(V) = E_0 + \frac{9V_0B_0}{16} \left\{ \left[\left(\frac{V_0}{V} \right)^{2/3} - 1 \right]^3 \dot{B}_0 + \left[\left(\frac{V_0}{V} \right)^{2/3} - 1 \right]^2 \left[6 - 4 \left(\frac{V_0}{V} \right)^{2/3} \right] \right\} \quad (1)$$

The resulted structural ground state of DHH has a parent HH with a lattice parameter of a_{HH} , which is equal to c_{DHH} , while $a_{DHH} = b_{DHH} = \frac{a_{HH}}{\sqrt{2}}$, corresponding to a, b and c values, as presented in Table 1.

The obtained parameters corresponding to the optimized structures for different magnetic phases of the equilibrium lattice parameter, bulk modulus, and its derivative, are given in Table 1. The formation energy is a useful norm to examine the synthesizability and stability of $K_2NaRbAs_2$ compound. The formation energy of $K_2NaRbAs_2$ in Table 1 has been evaluated from the following equation:

$$E_f(K_2NaRbAs_2) = E_{tot}(K_2NaRbAs_2) - 2E_{tot}(K) - E_{tot}(Na) - E_{tot}(Rb) - E_{tot}(As) \quad (2)$$

where $E_{tot}(K_2NaRbAs_2)$ is the total energy of $K_2NaRbAs_2$; while, $E_{tot}(K)$, $E_{tot}(Na)$, $E_{tot}(Rb)$ and $E_{tot}(As)$ correspond to the total energy for K, Na, Rb, and As, per atom, respectively. The obtained negative formation energy of -0.0642 Ry, for the studied compound, indicates that this material is thermodynamically stable. Therefore, it can be synthesized in the DHH structure.

Additionally, to verify the dynamic stability of the $K_2NaRbAs_2$ material, we calculated the phonon dispersion

Table 1 Calculated lattice parameter (\AA), B bulk modulus (GPa), B' its derivative pressure, and $E_{\text{formation}}$ formation energies (Ry) for $\text{K}_2\text{NaRbAs}_2$ in their FM phase with structure type I

Alloy	Phase	$a_{\text{HH}}(a_{\text{DHH}} = a_{\text{HH}}/\sqrt{2}, c_{\text{DHH}} = a_{\text{HH}})$	B (GPa)	B'	$E_{\text{formation}}$
HH: KNaAs[16]	FM	7.564	14.835	4.166	- 0.0381
	AFM	7.576	14.881	3.931	
	NM	7.573	14.972	4.086	
HH: KRbAs[16]	FM	8.173	11.117	4.253	- 0.0355
	AFM	10.319	10.931	4.055	
	NM	8.138	11.056	4.443	
DHH: $\text{K}_2\text{NaRbAs}_2$	FM	5.2917	12.6115	4.164	- 0.0642

diagram through the linear response method within the density functional perturbation theory (DFPT) as implemented in the CASTEP computational software [24]. The CASTEP computational code is an implementation of the pseudo potential plane-wave method (PP-PW) in the framework of density functional theory (DFT). To ensure sufficiently accurate total energy calculations, a plane-wave basis set cut-off of 770 eV and a $6 \times 6 \times 4$ Monkhorst–Pack scheme k-point grid for the integration over BZ were applied. The obtained phonon dispersions along lines of high symmetry in BZ are shown in Fig. 4. Note that absence of soft modes (imaginary modes; negative frequencies) in the phonon dispersion curve of a material implies its dynamic stability. Therefore, the absence of soft modes (negative frequencies) in the phonon dispersion curve of the title compound confirms its dynamical stability.

The *equilibrium* lattice constant (a_o), bulk modulus (B), its pressure derivative (B'), and formation energies ($E_{\text{formation}}$) of the compounds are listed in Table 1. The results, presented in Table 1, show that the bulk modulus (measure of compression resistance) diminishes as X atomic number rises.

3.2. Elastic properties

The mechanical behavior of crystals is strongly tied to their elastic properties, which enable us to examine crucial details about mechanical stability and comprehend the kind of forces in materials. Using the IRelast package, integrated into the WIEN2k code, the elastic constants are evaluated in order to check the mechanical stability of our compound.

Compounds, that have a tetragonal structure, have six independent elastic constants, denoted by; C_{11} , C_{12} , C_{13} , C_{33} , C_{44} and C_{66} , are necessary and sufficient to characterize the elastic behavior of the $\text{K}_2\text{NaRbAs}_2$ alloy. The

mechanical stability of a tetragonal structure requires that Born's stability criteria be satisfied [25].

$$(C_{11} - 2C_{12}) > 0,$$

$$(C_{11} + C_{33} - 2C_{13}) > 0,$$

$$(2C_{11} + C_{33} + 2C_{12} + 4C_{13}) > 0,$$

$$C_{11} > 0, C_{33} > 0, C_{44} > 0, C_{66} > 0 \quad (3)$$

The obtained elastic constants satisfied all the Born's stability criteria. So; The $\text{K}_2\text{NaRbAs}_2$ alloy is confirmed to be mechanically stable. The computed C_{ij} constants are given in Table 2. The following formulae can be used to estimate various mechanical quantities such as Bulk (B), shear (G), Young's (E) moduli, anisotropic factor and Poisson's ratio:

$$B = (2C_{11} + C_{33} + 2C_{12} + 4C_{13})/9 \quad (4)$$

$$G = \frac{2C_{11} + C_{33} - C_{12} - 2C_{13} + 6C_{44} + 3C_{66}}{15} \quad (5)$$

$$E = \frac{9BG}{(G + 3B)} \quad (6)$$

$$\nu = \frac{(3B - 2G)}{[2(3B + G)]} \quad (7)$$

It can be observed that the bulk modulus value, determined by Eq. (4), calculated through the elastic constants of the studied alloy is fairly in agreement with that obtained from the total energy optimization.

The estimated data shows that $\text{K}_2\text{NaRbAs}_2$ can resist reversible deformation brought on by shear stress and can endure distortion better than its parent HHs.

To evaluate the brittleness and ductility of a material, it is necessary to calculate B/G ratio, where the critical value which separates the ductile and brittle behavior is equal to 1.75 (brittle $< 1.75 <$ ductile) [26]. According to Pugh's analysis, the B/G ratio, for $\text{K}_2\text{NaRbAs}_2$ DHH alloy, exceeds 1.75, indicating that it falls into the ductile

category. This result is consistent with our previous findings on the KNaAs and KRbAs HH alloys[16], which are the parent materials of the $K_2NaRbAs_2$ DHH alloy.

Machinability is the ability of a metal to be cut to remove material with a satisfactory finish at low cost. Materials with good machinability (free machining materials) require low cutting power, obtaining a good finish and without significant tool wear. Factors that typically improve a material's performance often degrade its machinability, presenting a significant engineering challenge. The machinability index, μ_M of a material is defined by B/C_{44} . The useful material, with a high machinability, should be strong (i.e. high bulk modulus) and malleable (i.e. low C_{44})[27]. The calculated machinability indices are in the sequence: $K_2NaRbAs_2 < KRbAs < KNaAs$, as shown in Table 2.

Hardness (H) is a measure of the resistance to a plastic deformation in the field of materials science, which is the opposite of softness. Strong intermolecular bonds typically describe a macroscopic hardness. Ductility, elastic stiffness, plasticity, deformation, strength, toughness, viscoelasticity, and viscosity are all factors that affect hardness. H is expressed by[28]:

$$H = \frac{(1 - 2\nu)E}{6(1 + \nu)} \quad (8)$$

The $K_2NaRbAs_2$ DHH has a highest hardness of 0.53 GPa, compared to those of their parents HHs, illustrated in Table 2.

The Zener contrast factor is strongly correlated with the possibility of inducing micro cracks in materials, and it is an important physical quantity that informs us about the structural stability. For an isotropic system, A equals the unity, and the divergence from it measures the degree of elastic anisotropy. One may observe, from Table 2, that the $K_2NaRbAs_2$ DHH is more anisotropic than its parent HHs. Poisson's ratio (ν) is a useful parameter for understanding the nature of a compound's bonding forces. The calculated value of ν for the $K_2NaRbAs_2$ DHH alloy is 0.33, which

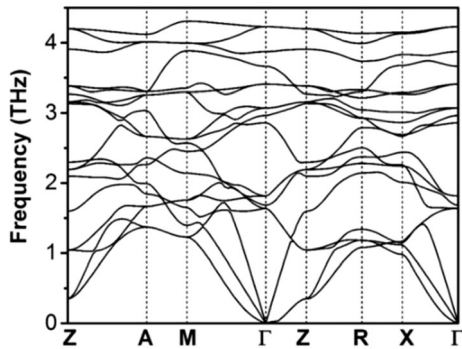


Fig. 4 Phonon dispersion curve of the $K_2NaRbAs_2$ compound

falls within the range of 0.25 to 0.5 observed in its HH parent compounds. This suggests that the bonding in this alloy has an ionic character.

In fact, three-dimensional surfaces can also be used to describe the anisotropy of a material in specific directions. For that, the software MATrix LABORatory, which is made and published by J. Nordmann et al.[29], was used to plot the 3D anisotropic bulk, Young's and shear moduli as well as Poisson's ratio surfaces. It is worth mentioning that this software was used for the first time by H. Bouafia et al. [30] for the LuAuSn HH alloy. For a tetragonal system, the expressions of the elastic moduli are, as follows:

$$\frac{1}{B} = (S_{11} + S_{12} + S_{13}) - (S_{11} + S_{12} - S_{13} - S_{33})l_3^2 \quad (9)$$

$$\frac{1}{E} = S_{11}(l_1^4 + l_2^4) + (2S_{13} - S_{44})(l_1^2l_3^2 + l_2^2l_3^2) + S_{33}l_3^4 + (2S_{12} + S_{66})l_1^2l_2^2 \quad (10)$$

$$\frac{1}{G} = S_{44} + \left[(S_{11} - S_{12}) - \frac{S_{44}}{2} \right] (1 - l_3^2) + 2(S_{11} + S_{33} - 2S_{13} - S_{44})l_3^2(1 - l_3^2) \quad (11)$$

where $\begin{pmatrix} l_1 \\ l_2 \\ l_3 \end{pmatrix} = \begin{pmatrix} \sin\theta\cos\varphi \\ \sin\theta\sin\varphi \\ \cos\theta \end{pmatrix}$, and S_{ij} is compliance coefficient.

$$B_V = [2(C_{11} + C_{12}) + C_{33} + 4C_{13}]/9 \quad (12)$$

$$G_V = [M + 3C_{11} - 3C_{12} + 12C_{44} + 6C_{66}]/30 \quad (13)$$

$$B_R = C^2/M \quad (14)$$

$$G_R = 15\{(18B_V/C^2) + [6/(C_{11} - C_{12})] + (6/C_{44}) + (3/C_{66})\}^{-1} \quad (15)$$

where $C^2 = (C_{11} + C_{12})C_{33} - 2C_{13}^2$; $M = C_{11} + C_{12} + 2C_{33} - 4C_{13}$

$$B_H = (B_V + B_R)/2 \quad (16)$$

$$G_H = (G_V + G_R)/2 \quad (17)$$

The Young's modulus (E), Poisson's ratio (ν) and Zener anisotropic factor are computing with the following equations:

$$E_H = \frac{9B_H G_H}{3B_H + G_H} \quad (18)$$

$$\nu = \frac{3B_H - 2G_H}{2(3B_H + G_H)} \quad (19)$$

$$A^U = 5\frac{G_V}{G_R} + \frac{B_V}{B_R} - 6 \quad (20)$$

The 3D surface of an isotropic system would have a spherical shape; therefore any deviation from that shape reflects the degree of anisotropy. As per Fig. 5, the surfaces

Table 2 Calculated elastic constants C_{11} , C_{12} , C_{13} , C_{33} , C_{44} , C_{66} , bulk B , machinability index B/C_{44} , Shear G , Young E moduli, hardness H (in GPa), anisotropic parameter A , B/G , Poisson's ratio ν , for $K_2NaRbAs_2$ in its structural and magnetic ground states

Compound	B	C_{11}	C_{12}	C_{13}	C_{33}	C_{44}	B/C_{44}	C_{66}	G	E	A	B/G	ν	H
KNaAs[16]	14.20	16.40	13.10	//	//	4.46	3.18	//	2.99	8.39	2.70	4.74	0.40	0.20
KRbAs[16]	12.08	17.96	9.14	//	//	4.16	2.90	//	4.26	11.43	0.94	2.84	0.34	0.45
$K_2NaRbAs_2$	12.20	18.27	7.78	9.90	18.32	5.86	2.08	3.37	4.71	12.53	0.27	2.59	0.33	0.53

of (B), (E) and (G) moduli and (ν) clearly deviate from a spherical shape, which represents the clear elastic anisotropy of $K_2NaRbAs_2$.

Among these mechanical properties, the bulk modulus of $K_2NaRbAs_2$ is nearly isotropic. This is evident in 3D representation (refer to Fig. 5(a)) which appears almost spherical (i.e. not spherical), as expected for a tetragonal structure. For the Young's modulus, we can observe a significant deviation from the sphere shape along the $\langle 111 \rangle$ direction, whereas for the shear modulus and Poisson's ratio, the deformation is along $\langle 001 \rangle$ direction.

The universal anisotropy index A^U , which is determined by the upper and lower limits of the bulk and shear moduli, is expressed by Eq. (20). The crystal displays isotropic behavior when A^U is equal to zero, and any deviation from this value indicates elastic anisotropy. Our compound exhibits elastic anisotropy, as its computed value of A^U was found to be 0.27. As far as we know, there is no theoretical or experimental information about the $K_2NaRbAs_2$ DHH to compare with.

The Calculation of the elastic constants has an impact on how the materials behave when heated; as a result, we can assess several thermal properties, such as the Debye temperature and melting temperature, which are listed in Table 3. The Debye temperature (θ_D) is calculated, using the equation below[26]:

$$\theta_D = \frac{h}{k_B} \left[\frac{3}{4\pi V_0} \right]^{1/3} v_m \quad (21)$$

where h is Planck's constant, k_B is Boltzmann's constant, V_0 is the average atomic volume, and v_m is the average sound wave velocity, which depends on the transverse (v_t) and longitudinal (v_l) sound velocities [31]:

$$v_m = \left[\frac{1}{3} \left(\frac{2}{v_t^3} + \frac{1}{v_l^3} \right) \right]^{-1/3} \quad (22)$$

and these are given by the equations, as follows:

$$v_l = \sqrt{\frac{3B + 4G}{3\rho}} \quad (23)$$

and

$$v_t = \sqrt{\frac{G}{\rho}} \quad (24)$$

where ρ is the density. The outcomes of our calculations are given in Table 3.

3.3. Electronic properties

In order to provide a more accurate description of the electron profile, the following electronic properties were examined at the equilibrium lattice constant using the GGA approach.

3.3.1. Band structures

Figure 6 shows the spin-polarized band structures for the compound $K_2NaRbAs_2$, calculated by GGA and TB-mBJ approximations. These are drawn along the high symmetry points in the first Brillouin zone.

We can see, for the spin down states of $K_2NaRbAs_2$, a metallic character due to the intersection of the valence bands with the Fermi level. On the other hand, for the spin-up channel, the compound exhibits a semiconductor character. In this channel (spin-up), one can observe that the compound $K_2NaRbAs_2$ has indirect band gaps of 1.40 and 2.62 eV, calculated by GGA and TB-mBJ approximations. The half-metallic gap (HMGap) is inferred from the valence band maximum (VBM) which is closer than conduction band minimum (CBM) to the Fermi level. The obtained half-metallic gap values are 0.34 and 0.39 eV for GGA and TB-mBJ methods, respectively. Therefore, we can see that the TB-mBJ method opens the band gap, located at high symmetry points Γ and X, for the valence band maximum (VBM), and conduction band minimum (CBM), respectively.

3.3.2. Densities of electronic states:

To explain the contribution of the different electronic states to the band structures, it is necessary to determine the total (TDOS) and partial (PDOS) densities of states. In order to find out which states are responsible for the bond. The

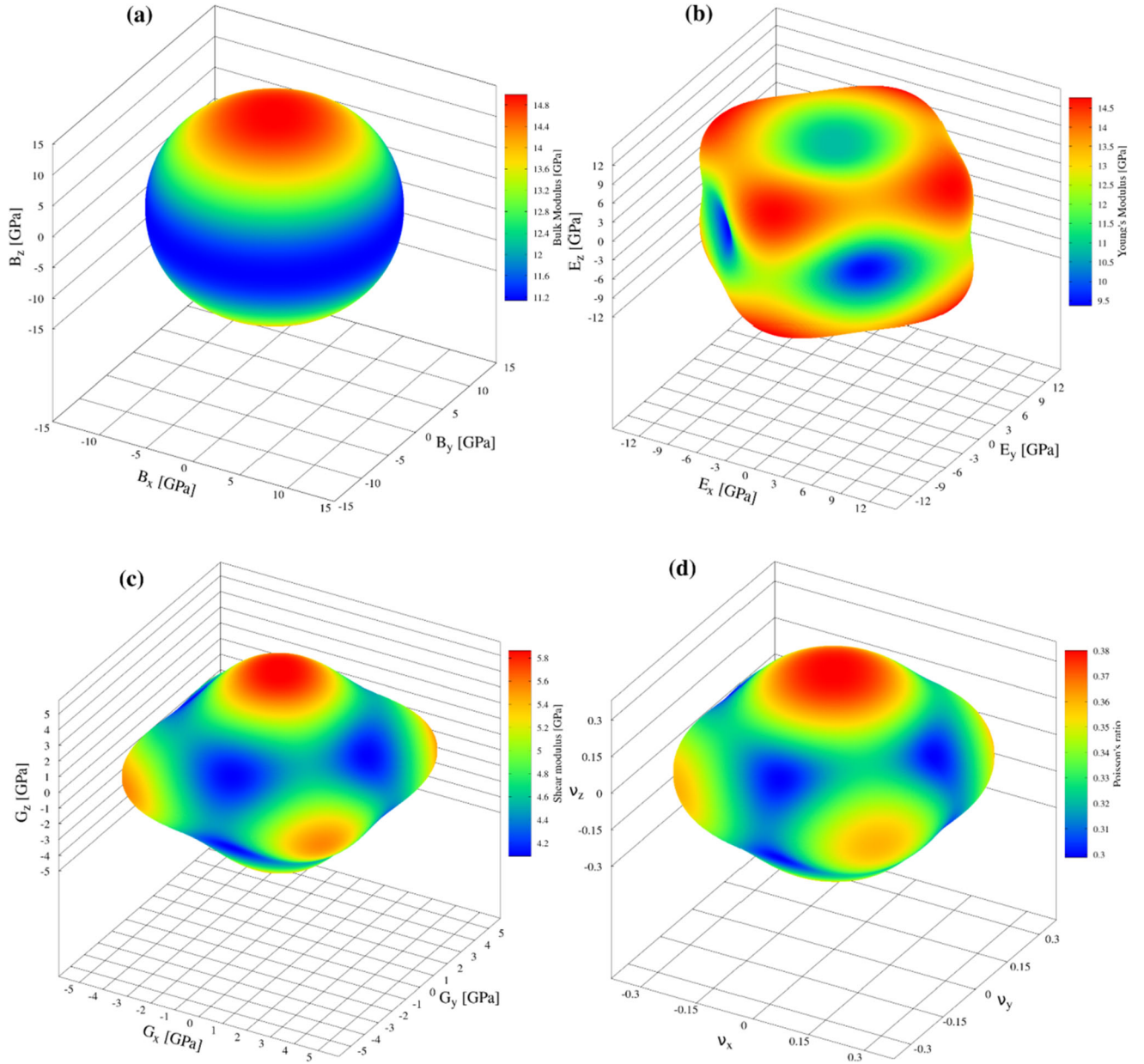


Fig. 5 3D graphical representation of (a) Bulk, (b) Young's and (c) Shear moduli and (d) Poisson's ratio of DHH $K_2NaRbAs_2$ (color figure online)

Table 3 Calculated longitudinal (v_l), transverse elastic wave velocities (v_t), average acoustic (v_m) velocities (in m/s), Debye (θ_D) and melting (T_m) temperatures (in K) of $K_2NaRbAs_2$ in its structural and magnetic ground states

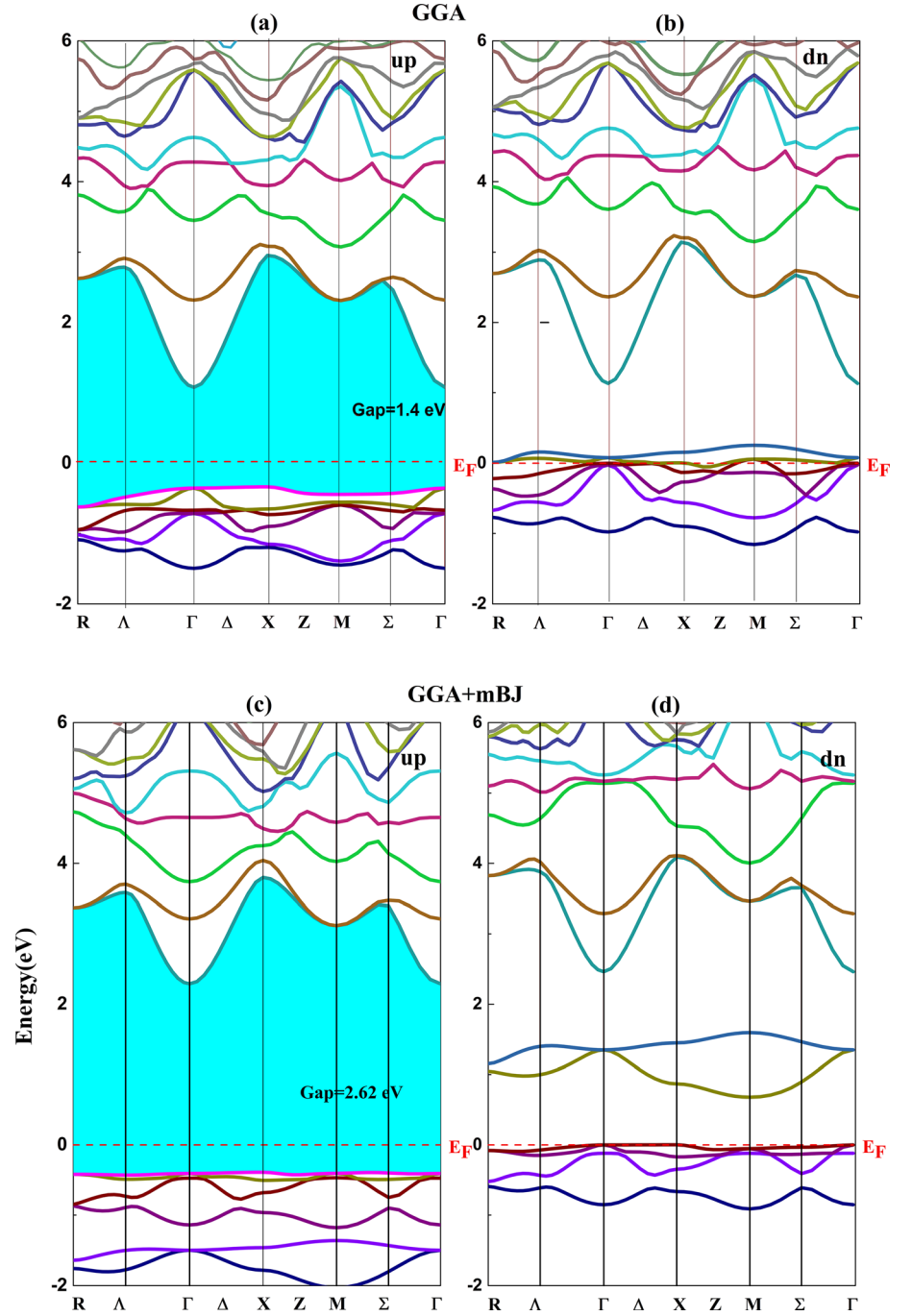
Compound	$v_l(m/s)$	$v_t(m/s)$	$v_m(m/s)$	$\theta_D(K)$	T_m
KNaAs[16]	2941.36	1193.26	1351.07	121.746	649.9393
KRbAs[16]	2705.1	1324.81	1487.96	124.094	622.1995
$K_2NaRbAs_2$	2843.92	1436.11	1610.09	139.307	436.297

TDOS and PDOS are calculated for both spin channels (i.e. spin-up and spin-dn), as shown in Fig. 7.

From both approaches, GGA, and GGA + mBJ, The PDOSs show that spin-exchange splitting, fundamentally originated from p states of Arsenic As atoms, which mainly contribute to the TDOS for the spin-up and-down channels, around the Fermi level.

This exchange splitting causes the spin-polarization of 100%, obtained by:

Fig. 6 Calculated band structure of $K_2NaRbAs_2$ compound in both (a), (c) Spin-up and (b, d) spin-down states by (a, b) GGA and (c), (d) GGA + mBJ approximations



$$P = \frac{|\rho_{\uparrow}(E_F) - \rho_{\downarrow}(E_F)|}{\rho_{\uparrow}(E_F) + \rho_{\downarrow}(E_F)} \quad (25)$$

where $\rho_{\uparrow}(E_F)$ and $\rho_{\downarrow}(E_F)$ are the spin-dependent densities of states at E_F , (\uparrow) and (\downarrow) represent spin-up and spin-dn states, respectively. P equals zero for paramagnetic or antiferromagnetic materials. As shown in Fig. 7, our studied material is fully spin-polarized (i.e. $P = 100\%$), indicating a half-metallic character of the studied alloy. However, the s and p states of K, Na atoms as well as Rb-d

have little contributions to the TDOS for both spin channels, around E_F .

3.4. Magnetic properties

To describe the spin effect on the considered material, we have computed its magnetic properties. The local, interstitial, and total magnetic moments for the DHH $K_2NaRbAs_2$ alloy, estimated by employing GGA approach are grouped in Table 4. It is noticeable that the total magnetic

Fig. 7 Calculated DOS of $K_2NaRbAs_2$ compound for both spin-up and spin-down states by GGA and GGA + mBJ approximations (color figure online)

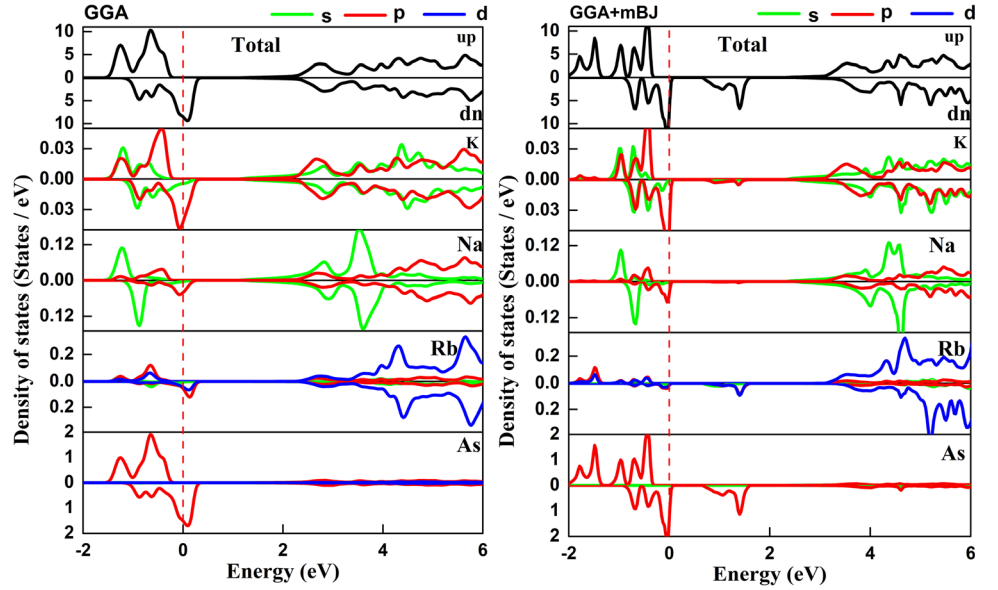


Table 4 Calculated total, atom-resolved and interstitial magnetic moments (in μ_B) in the unit cell for $K_2NaRbAs_2$ in its structural and magnetic ground states

Compound	M_{tot}	M_K	M_{Na}	M_{Rb}	M_{As}	M_{int}
KNaAs[16]	1.000	0.017	0.001	–	0.420	0.562
KRbAs[16]	1.000	0.010	–	0.016	0.399	0.575
$K_2NaRbAs_2$	2.000	0.013	–0.004	0.033	0.422	1.100

moment of the investigated compound has an integer value of $2\mu_B$ per unit cell which fulfills the necessary condition of a half-metallic behavior. According to Table 4, the primary source of the total magnetic moment in $K_2NaRbAs_2$ is the As atom, which is consistent with the findings of previous studies on its parent HH alloys, KNaAs and KRbAs [16].

3.5. Thermoelectric properties:

Thermoelectricity has recently gained popularity as an ‘‘environmentally friendly’’ technique because it does not use moving parts or chemical reactions resulting in no waste matter. The efficiency of a thermoelectric material is determined by the dimensionless parameter ZT , figure of merit, which is given by: $ZT = \frac{\sigma S^2 T}{\kappa}$, where σ is the electrical conductivity, S is the Seebeck coefficient, κ is the thermal conductivity of the material and T is the temperature in K.

A substance with a high Seebeck coefficient S , high electric conductivity, and low thermal conductivity is ideal for thermoelectric applications. Many recent investigations on HHs demonstrated that they have high energy factors

($S^2\sigma$), leading scientists to concentrate their study on these materials.

In this part, we thoroughly examine the thermoelectric behavior of the considered DDH alloy to determine if it can function as a thermoelectric material. So, we employed semi-classical Boltzmann transport theory, based on a smoothed Fourier interpolation of the bands, as implemented in the BoltzTraP code, to investigate the thermoelectric characteristics of $K_2NaRbAs_2$ DDH alloy. In the temperature range, from 150 to 1000 K, thermal (κ_c/τ), electrical conductivity (σ/τ), and Seebeck coefficient (S) were calculated.

The energy spectral density of the electrical conductivity is given by the following equation:

$$\bar{\sigma}_{\alpha\beta}(\varepsilon) = \frac{e^2}{N} \sum_{i,k} \tau_{i,k} v_{\alpha}(i,k) v_{\beta}(i,k) \frac{\delta(\varepsilon - \varepsilon_{i,k})}{\delta(\varepsilon)} \quad (26)$$

where α and β are the coordinate components, i is the electronic band number, k is the wave vector, N is the total number of k points, e is the elementary charge, τ is the relaxation time of the charge carrier, and ε is the band energy. Also, the group velocity v is:

$$v_{\alpha}(i, k) = \frac{1}{\hbar} \frac{\partial \varepsilon_{i,k}}{\partial k_{\alpha}} \quad (27)$$

Using Eq. (27), the conductivity tensor $\sigma_{\alpha\beta}$ can be written as a function of temperature T and Fermi level μ as follows:

$$\sigma_{\alpha\beta}(T, \mu) = \frac{1}{\Omega} \int \tilde{\sigma}_{\alpha\beta}(\varepsilon) \left[-\frac{\partial f(T, \varepsilon, \mu)}{\partial \varepsilon} \right] d\varepsilon \quad (28)$$

In Eq. (28), Ω is the unit cell volume and f is the Fermi-Dirac distribution. Similarly, the Seebeck coefficient tensor $S_{\alpha\beta}$ can be written as:

$$S_{\alpha\beta}(T, \mu) = \frac{1}{eT\Omega\sigma_{\alpha\beta}(T, \mu)} \int \tilde{\sigma}_{\alpha\beta}(\varepsilon) (\varepsilon - \mu) \left[-\frac{\partial f(T, \varepsilon, \mu)}{\partial \varepsilon} \right] d\varepsilon \quad (29)$$

The Seebeck coefficient of materials with holes (p-type materials), as dominant charge carriers, is positive whereas it is negative for n-type materials (i.e. electrons as dominant charge carriers).

Figure 8 shows that the Seebeck coefficient (S), in the spin-dn channel, decreases as the temperature rises, while the opposite trend is observed in the spin-up channel. Specifically, at ambient temperature (300°K), S is 1259.3. $\mu\text{V}/\text{K}$ in the spin-up state, confirming the electrons are the majority carriers. In addition, the S coefficient is 57.9. $\mu\text{V}/\text{K}$ in the spin-dn state; suggesting a high positive spin-up Seebeck coefficient in the $\text{K}_2\text{NaRbAs}_2$ DDH alloy. These findings indicate that this DDH material is of p-type.

Figure 9 depicts the Fermi level plot of the electrical conductivity per relaxation time (σ/τ) of $\text{K}_2\text{NaRbAs}_2$ as a function of temperature for both spin channels. In the spin-up channel, the electrical conductivity remains relatively

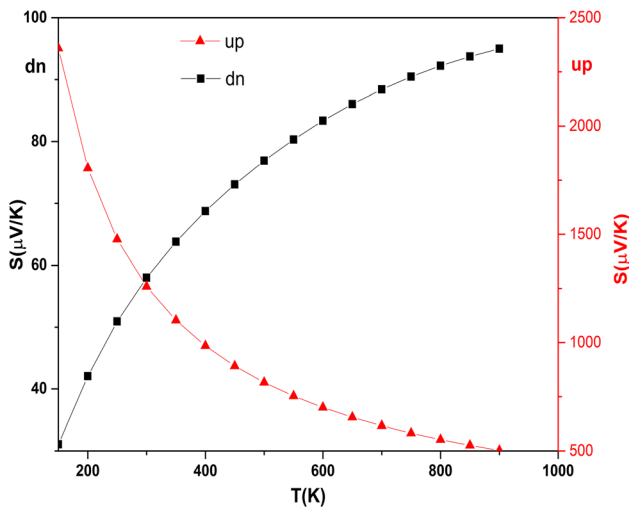


Fig. 8 Temperature dependence of the Seebeck coefficient of the spin-up and spin-dn channels of $\text{K}_2\text{NaRbAs}_2$ (color figure online)

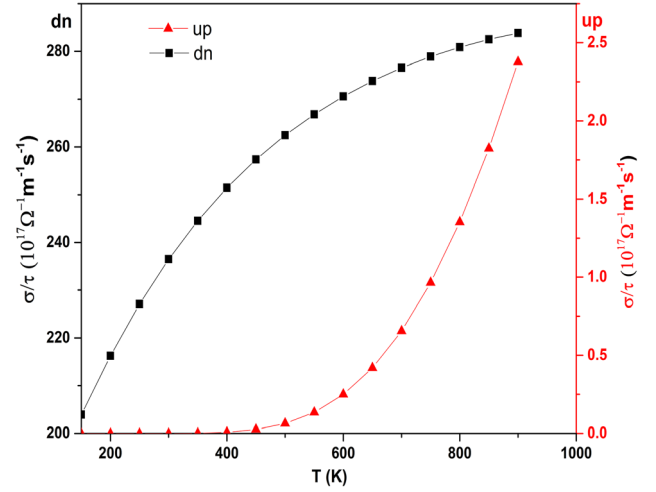


Fig. 9 Temperature dependence of the electrical conductivity for the spin up and spin dn channels of $\text{K}_2\text{NaRbAs}_2$ (color figure online)

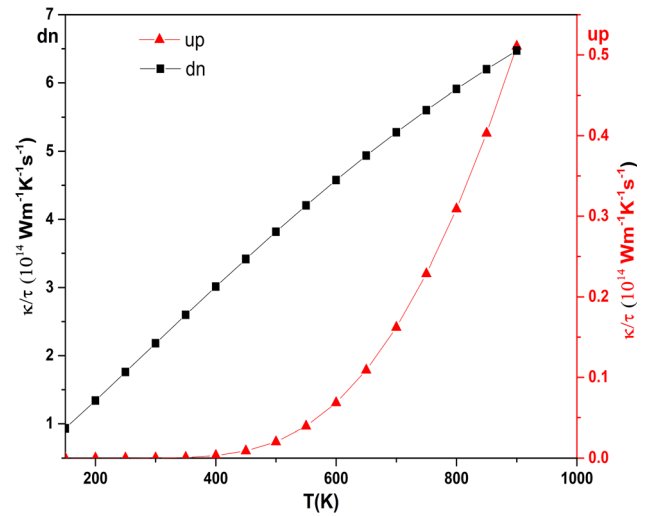


Fig. 10 Temperature dependence of the electronic thermal conductivity in the spin-up and spin-dn channels of $\text{K}_2\text{NaRbAs}_2$ DDH alloy (color figure online)

constant up to a particular temperature threshold (400 °K), after which it starts to increase. In contrast, in the spin-dn channel, the σ/τ value increases with rising temperature.

The σ/τ value in the spin-up state for the DHH at room temperature (300°K) is 0 while, in the spin-dn state, it is $236.4810^{17}\Omega^{-1} \text{m}^{-1} \text{s}^{-1}$. Due to lower DOS values at Fermi level, the electrical conductivity values for the spin-up channel are lower than those of the spin-down channel. These results demonstrate a high electrical conductivity and, consequently, a low resistivity of this material.

Figure 10 displays the temperature dependence, for both spin-up and spin-down channels, of the electronic thermal conductivity, scaled by the relaxation time. This is similar in character to σ/τ , as is due to the thermal excitation of electrons at higher temperatures, leading to increase heat

conduction. In the examined alloy, a linear increase in κ_e/τ' is observed for temperatures above approximately 600 K.

4. Conclusions

In this paper, we have presented a comprehensive theoretical investigation of the structural, elastic, magnetic, and electronic properties of the new DHH alloy $K_2NaRbAs_2$ using the FP-LAPW method with GGA and GGA + mBJ approximations. Our study has yielded several important findings, which are summarized below:

Firstly, we have determined the structural ground state of $K_2NaRbAs_2$ and demonstrated its stability through the negative formation energy and calculated elastic constants. We have also shown that this DHH alloy can withstand distortion better than its reported parent $KNaAs$ and $KRbAs$ HHs, and can resist reversible deformation carried on by shear stress. Our results suggest that $K_2NaRbAs_2$ is a hard material with high Young's modulus. Secondly, we have predicted a half-metallic ferromagnetic character in $K_2NaRbAs_2$ based on the calculated total magnetic moment, and have confirmed this through the band structure and DOS diagrams. Our study shows that the p-orbitals of Arsenic atoms play a major role in the half-metallic ferromagnetism for this DHH alloy. Thirdly, we have investigated the mechanical profile of $K_2NaRbAs_2$ and found it to be a ductile and anisotropic material. Fourthly, the calculation of the thermoelectric properties of $K_2NaRbAs_2$ DHH, using the BoltzTraP code within the Wien2k program, shows that it has a significantly high Seebeck coefficient and excellent electrical conductivity in the spin up and spin-down channels at room temperature, suggesting its potential as a promising thermoelectric material. Finally, we have discussed the potential of $K_2NaRbAs_2$ DHH for future spintronic applications.

Our study offers a comprehensive understanding of the properties and potential applications of $K_2NaRbAs_2$ DHH. We anticipate that these findings will encourage researchers to do further experimental and theoretical investigations on DHHs.

References

- [1] S Wolf, D Awschalom, R Buhrman, J Daughton, V S von Molnár, M Roukes, A Y Chtchelkanova and D Trege *Science*. **294** 1488 (2001)
- [2] S Terkhi, R Bentata, F Bendahma, T Lantri, S Bentata, Z Aziz and B Abbar *Indian J Phys* **95** 833 (2021)
- [3] R De Groot, F Mueller, P Van Engen and K Buschow *Phys Rev Lett* **50** 2024 (1983)
- [4] C Vargas-Hernández and R B Cruz *Comp Condens Matter* **4** 1 (2015)
- [5] R De Groot, F Mueller, P Van Engen and K Buschow *J Appl Phys* **55** 2151 (1984)
- [6] F Khelifaoui, K Amara, H Boutaleb, M Hamlat, K Boudia, Y S Abderrahmane and N Marbough *Comp Condens Matter* **21** e00399 (2019)
- [7] M Hamlat, K Amara, K Boudia and F Khelifaoui *Condens Matter Phys* **23** 33601 (2020)
- [8] M Hamlat, K Boudia, K Amara, F Khelifaoui and N Marbough *Comp Condens Matter* **23** e00456 (2020)
- [9] V Pardo and W E Pickett *Phys Rev Lett* **102** 166803 (2009)
- [10] S Ali, H Ullah and A A AlObaid *Eur Phys J Plus* **136** 1 (2021)
- [11] M R ur rehman Hashmi, M Zafar, M Shakil, A Sattar, SAHmed, S Ahmad *Chin . Phys. B* **.25** 11 7401(2016)
- [12] J Philipp, D Reisinger, M Schonecke, A Marx, A Erb, L Alff and R Gross *Appl Phys Lett* **79** 3654 (2001)
- [13] T Nouri, F Khelifaoui, Y Benallou, H Lakhdari, K Amara, H Boutaleb and M Dahmani *Appl Phys A* **127** 232 (2021)
- [14] H Hocine, K Amara and F Khelfaou *Appl. Phys. A*. **126** 178 (2020)
- [15] F Khelifaoui, A Boudali and A Bentayeb *Acta Phys Pol* **133** 1 (2018)
- [16] A Lorf, K Boudia, F Khelifaoui, K Amara and O Sadouki *M Ameri Spin* **11** 2150010 (2021)
- [17] S A Khandy *Sci. Rep.* **11**(1) 20756 (2021)
- [18] S Anand, M Wood, Y Xia and C Wolverton *Joule*. **3** 1226 (2019)
- [19] P Hohenberg and W Kohn *Phys Rev* **136** B864 (1964)
- [20] P Blaha, K Schwarz and P Sorantin *Comput Phys Commun* **59** 399 (1990)
- [21] Z Wu and R E Cohen *Phys Rev B* **73** 235116 (2006)
- [22] H J Monkhorst and J D Pack *Phys Rev B* **13** 5188 (1976)
- [23] F Birch *J. Appl. Phys.* **9** 279 (1938)
- [24] S J Clark, M D Segall, C J Pickard, P J Hasnip, M I Probert, K Refson, M C Payne, *Z. fur Krist. – Cryst.* **220** 567 (2005)
- [25] F Mouhat and F X Coudert *Phys Rev B* **90** 224104 (2014)
- [26] S Pugh and X C I I Lond *Edinb Dublin Philos Mag J Sci* **45** 823 (1954)
- [27] M Cover, O Warschkow, M Bilek and D McKenzie *J Phys Condens Matter* **21** 305403 (2009)
- [28] M Naher and S Naqib *Sci Rep* **11** 1 (2021)
- [29] J Nordmann and M Aßmus *Contin Mech Thermodyn* **30** 689 (2018)
- [30] H Bouafia, B Sahli, M Bousmaha, B Djebour, A Dorbane and S Mokrane *Solid State Sci.* **118** 106677 (2021)
- [31] M J Mehl *Phys. Rev. B* **47** 2493 (1993)

Publisher's Note Springer Nature remains neutral with regard to jurisdictional claims in published maps and institutional affiliations.

Springer Nature or its licensor (e.g. a society or other partner) holds exclusive rights to this article under a publishing agreement with the author(s) or other rightsholder(s); author self-archiving of the accepted manuscript version of this article is solely governed by the terms of such publishing agreement and applicable law.